

**ADVERTIMENT.** L'accés als continguts d'aquesta tesi queda condicionat a l'acceptació de les condicions d'ús establertes per la següent llicència Creative Commons:  <https://creativecommons.org/licenses/?lang=ca>

**ADVERTENCIA.** El acceso a los contenidos de esta tesis queda condicionado a la aceptación de las condiciones de uso establecidas por la siguiente licencia Creative Commons:  <https://creativecommons.org/licenses/?lang=es>

**WARNING.** The access to the contents of this doctoral thesis it is limited to the acceptance of the use conditions set by the following Creative Commons license:  <https://creativecommons.org/licenses/?lang=en>

# **Advances in depolarization techniques for applications in biomedicine: unveiling brain structures**

*Mónica Canabal Carbia*

Submitted in fulfillment of  
the requirements for the degree of  
Doctor of Physics

Thesis supervisors:

**Dr. Angel Lizana**

**Dra. Irene Estévez**

**Prof. Dr. Juan Campos**

Departament de Física  
Universitat Autònoma de Barcelona  
Bellaterra, 2025



This work has been financed by the following research projects:

- i) Optical Polarimetry Technology for IMAGING BIOsamples (OPTIMA-BIO). Spanish Science and Innovation Ministry, Proofs of concept (PDC2022-133332-C21).
- ii) Surface metrology, imaging polarimetry and data processing combination for biomedical and botanical applications. European Regional Development Funds (FEDER) (PID2021-126509OB-C21).
- iii) Grup de Reserca Consolidat – SGR (2021SGR00138).

M. Canabal-Carbia thanks the Universitat Autònoma de Barcelona for the grant “Personal Investigador en Formació (PIF) 2021-2022”. Ref. B21P0046.





*La física contemporánea...se encamina hacia el único método atinado, hacía la única filosofía certera de las Ciencias Naturales, no en línea recta, sino en zigzag, no sabiendo adónde va, sino por impulso natural, no viendo con claridad su "objetivo final", sino acercándose a él a tientas, titubeando y, a veces, hasta reculando.*

*V.I. Lenin*



# Abstract

This thesis focuses on the analysis of polarimetric techniques as valuable tools for the inspection of biological samples. These methods benefit from taking advantage of polarimetric response of samples, which can be englobed in three main physical features: dichroism, birefringence and depolarization. Importantly, these polarimetric properties can be linked to physical characteristics (such as composition, density, orientation...) of samples, that in turn, are responsible for such polarimetric behavior. Advantageously, the experimental obtaining of these features can be readily extracted from the experimental measurement of their Mueller matrices, where the polarimetric information is encoded. Note that the Mueller matrix measurement of samples is non-invasive and non-destructive, making the polarimetric techniques we present in this thesis excellent candidates to be applied for biological tissues imaging.

In literature, it is demonstrated that among these properties, the study of the depolarizing behavior of biological tissues is especially suitable to characterize such samples. In this context, the Indices of Polarimetric Purity show very good performance for imaging purposes. In thesis, we make advances in the fundamental comprehension of the information provided by the Indices of Polarimetric Purity as well as, their connection with inherent structures within samples. Such fundamental knowledge is used to implement polarimetric based tools helping for the identification and contrast enhancement of biological structures. Additionally, other relevant depolarization parameters are also investigated in this thesis in the framework of biophotonics applications, as it is the case of some observables derived from the Arrow decomposition.

In particular we describe for the first time different origins of depolarization in samples. To this aim, we conduct a series of simulations mimicking depolarizers based on different polarimetric characteristics. This leads to the identification of two depolarization sources, named anisotropic and isotropic depolarization. Whereas the first one is related to statistical processes involving the polarimetric elements from which samples are composed of, the second one is related to random scattering processes produced in light-matter interactions, which led to a complete loss of sample polarimetric information. The thorough understanding of such depolarizing mechanisms lead us to the implementation of a digital depolarization filter that eliminates the isotropic depolarization content of

samples, highlighting the anisotropic one. The application of this filter on biological samples yields to a significant image enhancement of relevant structures.

Taking profit of the filter potential for imaging applications, we apply it in the study of animal and human brain samples. The analysis of filtered polarimetric channels lead to excellent results in terms of structure identification when comparing with both conventional polarimetric methods and commonly used medical techniques. As a result, the depolarization filter presented in this work arises as an excellent tool with great potential for *in-vivo* surgeries in the medical field and fundamental neurological research and pathology detection.

## List of publications of Mónica Canabal-Carbia

Publications contained in this thesis:

1. José J. Gil, Ignacio San José, **Mónica Canabal-Carbia**, Irene Estévez, Emilio González-Arnay, Jordi Luque, Teresa Garnatje, Angel Lizana and Juan Campos. *Polarimetric Images of Biological Tissues Based on the Arrow Decomposition of Mueller matrices*, Photonics **10**(6), 669 (2023). DOI: [10.3390/photonics10060669](https://doi.org/10.3390/photonics10060669).
2. **Mónica Canabal-Carbia**, Irene Estévez, Esther Nabadda, Enrique García-Caurel, José J. Gil, Razvigor Ossikovski, Andrés Márquez, Ignacio Moreno, Juan Campos and Angel Lizana. *Connecting the microscopic depolarizing origin of simples with macroscopic measures of the Indices of Polarimetric Purity*, Opt. Laser Eng. **172**, 107530 (2024). DOI: [10.1016/j.optlaseng.2023.107830](https://doi.org/10.1016/j.optlaseng.2023.107830).
3. **Mónica Canabal-Carbia**, Irene Estévez, Emilio González-Arnay, Ivan Montes-González, José J. Gil, Arnau Barrera, Enrique García-Caurel, Razvigor Ossikovski, Ignacio Moreno, Juan Campos and Angel Lizana. *Revealing hidden bioimaging information by isotropic depolarization filter*, Opt. Laser Technol. **188**, 112956 (2025). DOI: [j.optlastec.2025.112956](https://doi.org/10.1016/j.optlastec.2025.112956).

Other publications of Mónica Canabal-Carbia not contained in this thesis:

4. Dekui Li, Ivan Montes-González, **Mónica Canabal-Carbia**, Irene Estévez, Octavi López-Coronado, Zhongyi Guo, Juan Campos and Angel Lizana. *Combined use of the Purity and the Polarizance-Reflection-Transformation Spaces as a suitable tool for depolarizing samples enhanced characterization and discrimination*, Adv. Photon. Nexus **4**(1), 016009 (2025). DOI: [10.1117/1.APN.4.1.016009](https://doi.org/10.1117/1.APN.4.1.016009).
5. Ivan Montes-Gonzalez, Irene Estévez, **Mónica Canabal-Carbia**, Angel Lizana and Juan Campos. *Generalized eigenvalue calibration method for Mueller imaging polarimeter based on micropolarized sensors*, Photonic Sens **15**, 250320 (2025). DOI: [10.1007/s13320-025-0767-z](https://doi.org/10.1007/s13320-025-0767-z)
6. **Mónica Canabal-Carbia**, Albert Van Eeckhout, Carla Rodríguez, Emilio González-Arnay, José J. Gil, Enrique García-Caurel, Razvigor Ossikovski, Juan Campos and Angel Lizana. *Depolarizing metrics in the biomedical field: vision enhancement and classification of*

*biological tissue*, J. Innov. Opt. Health Sci. **16**(5), 2330004 (2023). DOI: [10.1142/S1793545823300045](https://doi.org/10.1142/S1793545823300045).

## List of acronyms

Acronym	Meaning
<b>Polarimetric-related acronyms</b>	
CN	Condition Number
CP	Components of Purity
DoP	Degree of Polarization
DOLP	Degree of Linear Polarization
IDF	Isotropic Depolarization Filter
IPP	Indices of Polarimetric Purity
LD	Linear Diattenuator
LED	Light Emitting Diode
LP	Linear Polarizer
LR	Linear Retarder
M	Mueller matrix
PA-LC	Parallel Aligned Liquid Crystal
PS-OCT	Polarization Sensitive-Optical Coherence Tomography
PSHG	Polarization Sensitive Second Harmonic Generation
PSA	Polarization State Generator
PSG	Polarization State Analyzer
M-S	Mueller Stokes
SoP	State of Polarization
<b>Biological structure-related acronyms</b>	



---

ad	Adventita walls
al	Ansa lenticularis
alv	alvelus
BCC	Basal Cel Carcinoma
CA	Cornu Amonis
cs	Collateral suculus
e	Endocardium
ec	Entorhinal cortex
ep	epicardium
gm	Gray matter
hc	Hippocampal formation
ic	Internal capsule
iml	Internal medullary lamina
l	lumen
mgf	Medial frontal gyrus
ml	Medial lemniscus
my	myocardium
pcl	Pyramidal cell layer
sb	subiculum
se	subepicardium
St	Subthalamic nucleus
Str	Stratum
so	Stratum oriens
t	thalamus

---

vpn	Ventral posterior nucleus
-----	---------------------------

wm	White matter
----	--------------

---

---

Other acronyms	
----------------	--

---

CCD	Charged-Coupled Device
-----	------------------------

CLSM	Confocal Laser Scanning Microscopy
------	------------------------------------

ML	Machine Learning
----	------------------

MRI	Magnetic Resonance Imaging
-----	----------------------------

OCT	Optical Coherence Tomography
-----	------------------------------

RGB	Red-Green-Blue
-----	----------------

ROI	Region of Interest
-----	--------------------

SHG	Second Harmonic Generation
-----	----------------------------

SPE	Surgical Polarization Endoscope
-----	---------------------------------

# Contents

<b>Advances in depolarization techniques for applications in biomedicine: unveiling brain structures .....</b>	<b>2-1</b>
Abstract .....	iii
List of publications of Mónica Canabal-Carbia .....	v
List of acronyms.....	vii
Contents .....	10
<b>Chapter 1 Introduction .....</b>	<b>13</b>
1.1 Optical technologies in the medical field .....	14
1.1.1 Polarimetry applications .....	15
1.1.2 Polarimetry in biomedicine .....	18
1.1.3 Polarimetry in Neurological Applications.....	29
1.2 Main goals of this thesis .....	32
1.3 Structure of this thesis .....	33
<b>Chapter 2 Mathematical formalism.....</b>	<b>35</b>
2.1 Mueller-Stokes formalism .....	35
2.1.1 Stokes vector .....	36
2.1.2 Poincaré Sphere .....	37
2.1.3 Mueller matrix.....	39
2.2 Mueller matrix decompositions and Polarimetric Observables.....	40
2.2.1 Block form of a Mueller matrix .....	40
2.2.2 Parallel and Serial decompositions of a Mueller matrix .....	42
2.2.3 Arrow decompositions of a Mueller matrix .....	42
2.2.4 Spectral and Characteristic decompositions of a Mueller matrix.....	45

2.2.5 Summary .....	49
2.3 Polarimetric Spaces .....	50
2.3.1 Purity Space .....	51
2.3.2 Components of Purity Space .....	52
<b>Chapter 3 Materials and Methods.....</b>	<b>55</b>
3.1 Complete Image Mueller polarimeter.....	55
3.1.1 Experimental set-up .....	55
3.1.2 PSG and PSA calibration and optimization.....	58
3.1.3 Polarimeter Measuring Principle: Measurement of the Mueller images .....	61
3.2 Sample description .....	62
3.2.1 Heart and tongue samples .....	63
3.2.2 Brain samples .....	64
<b>Chapter 4 Discovering anisotropic and isotropic depolarization sources.....</b>	<b>72</b>
4.1 Depolarizers simulations $P3 = 1$ .....	73
4.1.1 Linear diattenuators .....	76
4.1.2 Linear retarders .....	81
4.1.3 Addition of linear retarders and linear diattenuators.....	84
4.2 Depolarizers simulations with $P3 < 1$ .....	86
4.2.1 Simulation results.....	88
4.3 Experimental results.....	93
4.4 Interpretation of the results in the Purity Space and Characteristic decomposition .....	96
<b>Chapter 5 Depolarization Filter .....</b>	<b>99</b>
5.1 Isotropic Depolarization Filter .....	100
5.1.1 Non-depolarizing channels: Dichroic and Retardance properties .....	102
5.1.2 Depolarizing channels .....	103
5.1.3 Dichroic and depolarizing Arrow parameters .....	105
5.1.4 Polarimetric Spaces after IDF .....	106
5.2 Applications of IDF to biological samples.....	109

5.2.1 Filtered vs non-filtered images: application of the IDF to biological samples imaging .....	111
5.2.2 IDF in Polarimetric Spaces .....	117
<b>Chapter 6 Polarimetric tools applied to brain analysis .....</b>	<b>121</b>
6.1 Animal Samples: Preliminary studies .....	122
6.2 Human Samples: Polarimetric parcellation of the human prosencephalon .....	126
<b>Chapter 7 Conclusions .....</b>	<b>137</b>
7.1 Summary and conclusions .....	137
7.1.1 Mathematical formalism .....	137
7.1.2 Materials and methods .....	138
7.1.3 Discovering anisotropic and isotropic depolarization sources.....	138
7.1.4 Isotropic Depolarization Filter (IDF) .....	140
7.1.5 Polarimetric tools applied to brain analysis .....	142
7.2 Proposal for future research .....	143
<b>Bibliography.....</b>	<b>145</b>
<b>Papers of this doctoral thesis .....</b>	<b>157</b>

# Chapter 1 Introduction

This thesis proposes an in-depth study of depolarization, one of the key polarimetric features of samples. The interest in studying this property arises from the interesting results when analyzing the depolarization characteristics of biological samples in terms of contrast enhancement and structure identification. There exist in specialized literature different polarimetric observables derived from samples Mueller matrix to extract the depolarization information and in this thesis, we will analyze some of them. However, we will focus on one set of depolarization parameters named the Indices of Polarimetric Purity (IPP). The IPP are an excellent source of information when inspecting highly scattering samples, as is the case of soft biological samples. In this work, we present an analysis of each one of the indices comprising the IPP to find a connection between them and the intrinsic physical properties (composition, densities, orientation...) of depolarizing samples. In this sense, we performed a series of depolarizers simulations to study their depolarization characteristics as a function of different physical control parameters. This has led to the identification of two different depolarization sources in samples (isotropic and anisotropic) which can be related to different physical processes leading to depolarization, and also to different values for the IPP parameters. We found that isotropic depolarization has the information of scattering processes in samples, while anisotropic depolarization relates to intrinsic features of samples such as elemental composition and structures orientation. This distinction enables to analyze samples separating these two depolarization sources, anisotropic depolarization being a richer source of information. In this thesis we also present a digital polarimetric filter to isolate anisotropic depolarization leading to outstanding results in terms of the polarimetric visualization and analysis of biological samples, surpassing the results of standard polarimetric techniques and other common optical techniques. To conclude, we take advantage of these new polarimetric tools for their application in the study of brain samples.

In this introductory chapter, we present the scientific context in which this thesis is framed. First, we provide an overview of various optical techniques commonly employed in biomedical applications (section 1.1.1). Among these, the technique used throughout this work is polarimetry; therefore, we review the current state of the art in medical polarimetry (section 1.1.2).

Given that one of the central applications of this thesis involves polarization-based imaging techniques for the study of brain structures, section 1.1.3 is dedicated to previous research conducted in the field of polarimetry applied to brain studies. Additionally, sections 1.2 and 1.3 outline the main objectives of this thesis and its overall structure, respectively.

## **1.1 Optical technologies in the medical field**

Light and light-matter interactions constitute a fundamental and valuable source of information in science and technology. Optical technologies, based on light properties, are very synergistic with current societal trends, including manufacturing, telecommunications, digitalization, IoT, big data, artificial intelligence or autonomous transportation.

The fundamental physical properties of light, such as intensity distribution, spectrum, phase and polarization, are modified through light-matter interactions. In biomedicine, optics and photonics play a key role in applications ranging from diagnostic imaging and non-invasive procedures to surgical tools, biosensors, and augmented vision systems, biomarkers, etc. Numerous biomedical techniques have been developed based on measuring and interpreting changes in these fundamental properties of light, allowing the study and characterization of biological tissue [1–3].

Among these properties, intensity is the most straightforward to measure. Many biomedical imaging techniques and instruments rely on intensity-based contrast, including magnifying glass-based systems in otoscopy and rhinoscopy, optical microscopies in pathology and hematology, and confocal microscopy in cell research. Fiber optics are also crucial for endoscopy and minimal invasive surgery [4,5]. Moreover, augmented reality is increasingly applied in surgery, medical training, rehabilitation and patient education [6,7].

Spectroscopic techniques are also significant, as tissue responses vary with the illumination wavelength [8,9]. The absorption and reflection spectra of different biological

components make spectroscopy a vital tool for medical studies, and it is often combined with other optical or medical systems [10–12]. For instance, the presence and concentration of hemoglobin can be used to quantify the response to some cancer therapies [13]. In addition, fluorescence-based methods are used in cytokinesis, dermatopathology and optogenetics, among others.

Beyond spectral and intensity information, the phase information of light provides valuable contrast in transparent and weakly scattering samples and can be of interest in medicine. Techniques such as phase-contrast microscopy, interferometry and optical coherent tomography (OCT) are widely used for clinical applications [14,15]. For instance, OCT has become a gold-standard technique in ophthalmology in the detection of ocular related pathologies; also, for vascular and neurological diseases, sclerosis, and drug-induced retinopathies [16–18].

Complementarily, polarization state of light has also proved to be highly valuable in biomedical applications. The dependence on the response of tissue to polarized light has led to the emergence of polarimetry as a useful tool in medicine. The way polarized light interacts with tissue—depending on structural anisotropy, composition, and organization—has led to the development of polarimetric imaging techniques for diagnosis and tissue characterization. Applications range from simple devices such as dermatoscopes, used by dermatologists to assess skin lesions, to advanced techniques such as the OCT or second harmonic generation microscopy in cancer detection [15,19,20].

In the next section, we focus on the role of the polarization properties of light in the study of light-matter interactions and describe its applications across various disciplines. We make special emphasis on the biomedical field, the central topic of this dissertation.

### **1.1.1 Polarimetry applications**

Polarimetric based methods are a valuable and powerful tool in a wide range of applications, as in astronomy, advanced materials characterization, biology, geology, climate and environmental science, chemistry, pharmaceuticals, among others [21–25]. In the following, we review some representative examples of applications in relevant fields such as remote sensing, material characterization or botany. Moreover, we briefly introduce the current state of polarimetric data-driven methods. Then, we focus more on the use of polarimetry for biomedical applications, this being the aim of this thesis.

- Remote sensing

Polarimetry has been commonly used in remote sensing applications for enhancing or detecting certain objects that are otherwise not identified by means of other conventional imaging techniques [26]. Most remote sensing applications are based on passive illumination, where samples are illuminated by sunlight. By analyzing how objects alter the polarization state of the scattered light, it is possible to extract valuable information about their physical and chemical properties. The combination of this technique with multi-



spectral and multi-angle measurements are used to characterize aerosols (optical thickness, size and distribution, chemical composition and particle shape), this being very valuable for characterizing the health hazards of aerosols [27,28]. In addition, the combination with lidar and radar techniques are used for atmospheric and oceanic remote sensing [29–32] and classification of vegetation, smoke and urban objects in the remote sensing of Earth [33–35], among others.

- Material characterization

The use of polarimetric techniques in material science is traditionally called ellipsometry, polarimetry being a generalized ellipsometry. When combined with spectroscopy, ellipsometry becomes a powerful technique for the inspection of optical properties and thickness of various materials, with widespread applications in crucial areas, including the characterization of thin films, surfaces and interfaces. Spectroscopic ellipsometry analyzes the change in the polarization state of the incident light after its interaction with the sample, deriving from this information essential parameters [36]. For instance, ellipsometry can determine critical parameters such as layer thickness, composition and optical properties in the semiconductor industry [37]. Moreover, in thin film characterization also plays a crucial role in various industries such as microelectronics, photovoltaics, optical coating and sensors [23,38,39].

- Botany

In botany, polarimetry has been mostly used to study dichroic and birefringence properties of plant samples. The inspection of these polarimetric features in imaging polarimetric techniques provide enhancement and detection of structures in the plants [40–44]. Dichroism metrics can reveal concentration and organization of plants organelles and the detection of specific molecules. Birefringence is produced by some structures and macromolecules such as cellulose and allows us to investigate cell wall composition, among other characteristics [45,46]. More recently, depolarization response of plant samples has been studied, demonstrating their ability to highlight different structural components [43] and for the detection and classification of different pathological stages in the samples [41]. The structural changes occurring in the plant when is affected by different stages of a pathology (healthy, chlorotic and necrotic) are translated into different depolarization responses, presenting depolarization inspection of vegetal samples as a tool for pathology inspection.

These promising results in the use of imaging polarimetry to study botanic samples lead to the development of set-ups for the direct measurement of the plants in crops for monitoring [47]. This could help in the future to prevent the infections in crops by means of early pathology detection or monitoring water content of the plants and therefore aiding to reduce the number of pesticides or water needed to maintain the crops. That is, providing environmental and economic benefits.

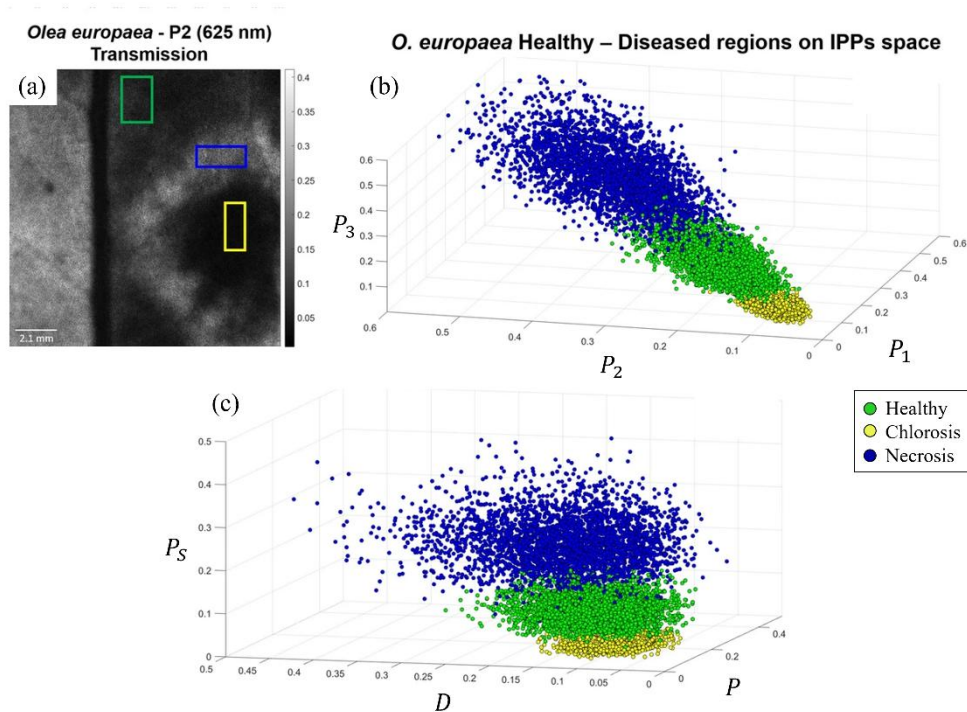


Figure 1-1 Polarimetric analysis of olea europea sample. (a) Polarimetric observable image with healthy and unhealthy regions marked, (b) and (c) scatter plots of points correspondent to the different regions of the leaf in the Purity and Components of Purity Space, respectively. Image adapted from [41].

- Data-driven methods: Machine Learning

We have described some of the numerous applications of polarimetry. Lately, the appearance of machine learning, based on the use of large datasets to extract features of samples, has become an essential tool in various fields representing a transversal research area. In this sense, the combination of polarimetric information and data-driven algorithms have opened new perspectives in the applications of polarimetric techniques for tasks as above described.

Traditionally, image analysis has relied on intensity images. However, integrating polarimetric data has demonstrated great performance when included in detection or classification algorithms. For instance, in urban object classification by including polarimetric data the results are improved even in adverse weather conditions [48,49]. Medical diagnosis techniques such as the inspection and characterization of features in pathological samples and damaged tissue inspection [50–53]. Also, fields such as industrial quality inspection [54,55] and remote sensing [56,57] are proactively using polarimetric data in their machine learning models.

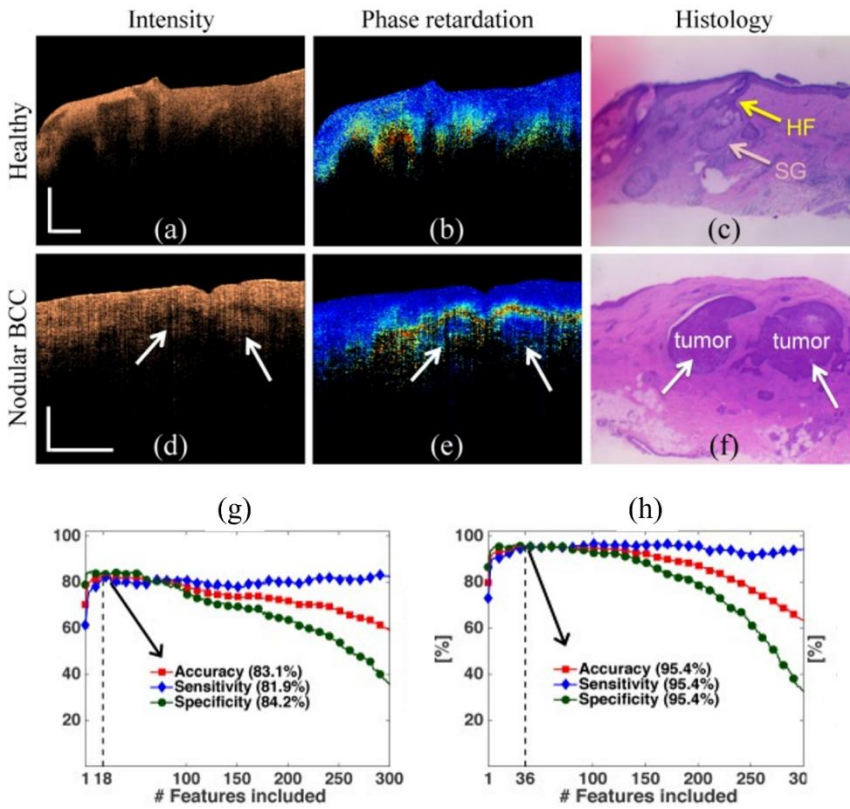


Figure 1-2 (a)-(f) Intensity (left), phase retardation (middle) and histology (right) images of healthy and pathological human skin. (g) and (h) Accuracy, sensitivity and specificity at each iteration of the classifier process; (g) based on only intensity features and (h) using both intensity and phase retardation information. Image adapted from [51].

In [51], they acquire data from 42 samples for the detection of basocellular carcinoma, using OCT techniques measuring both intensity and phase. In addition to this information, they also have histological images to identify the regions with tumor. In Figure 1-2 (g) they show the results of training a Support Vector Machine classification model using only intensity information and (h) shows the results of the models where phase and intensity information were combined, leading to the best results.

In the next subsection we focus on the applications of polarimetry in the field of medicine, which represents the major focus of this thesis.

### 1.1.2 Polarimetry in biomedicine

Polarimetry presents valuable advantages for the inspection of biological tissue in the biomedical field. The non-invasive and non-destructive nature of these techniques makes it suitable for several biomedical applications. Since polarimetric images do not require

physical contact or chemical alteration of the sample, it enables complementary medical analyses—such as histology—to be performed on the same tissue. Furthermore, most polarimetric systems employ “cold” light sources, harmless to patients, allowing the use of polarimetry for *in-vivo* examination during intra-operative procedures.

Biological tissue, especially bulk soft tissue, has very interesting polarimetric response. Spatial variations of the components of a sample due to different densities, orientation or components of the structures comprising the tissue will have characteristic polarimetric responses leading to contrast enhancement and the detection of structures invisible with naked eye or other common optical techniques. In the following, we present the relation between physical characteristics of the biological samples leading to response in the polarimetric channels (dichroism, birefringence and depolarization).

The most common polarimetric effects observed in the polarimetric analysis of tissue samples are retardance and depolarization. The composition and organization of tissue are very commonly made of fibrous components, such as collagen and elastin [58,59], leading to retardance response. In addition, the microstructure of samples and the instrumentation led to an important depolarization response. Also, dichroism can be an interesting channel for some biological samples, but it is not commonly used due to the weak response of tissues.

- Dichroism in biomedical samples

Polarimetric observables related to samples, as diattenuation and polarizance, present weak response in biological tissue. Therefore, they are not commonly used in the study of biological samples [60]. Even though, they have demonstrated to be helpful for some applications such as tissue classification [52,61]. In addition, diattenuation has recently been used for the study of brain tractography [62]. Also, dichroic properties are of interest in the study of plant samples, helping in the detection of chloroplasts and related organelles in plant species [45].

- Birefringence in biomedical samples

Retardance, a measure of birefringence, is a central polarimetric parameter in biomedical imaging [63–68]. Biological tissues are collagen rich structures and collagen fibers are birefringent materials. The retardance channels are related to collagen density and orientation. This determines the magnitude, direction, and alignment of birefringence in biological tissues. For instance, the relationship between collagen organizations and birefringent properties has been used to detect and monitor the progression of various types of cancer [69,70]; also, nerve fibers and certain proteins also exhibit significant

birefringent responses [71]. In [72], Nielsen P. M. group, use the birefringent properties to study bovine pericardial membranes used in valvular prosthesis. The measured retardance maps enabled non-destructive evaluation of crucial tissue characteristics such as tissue uniformity that allows to detect regional variations of anisotropy that could be dangerous for prosthesis performance (see Figure 1-3).

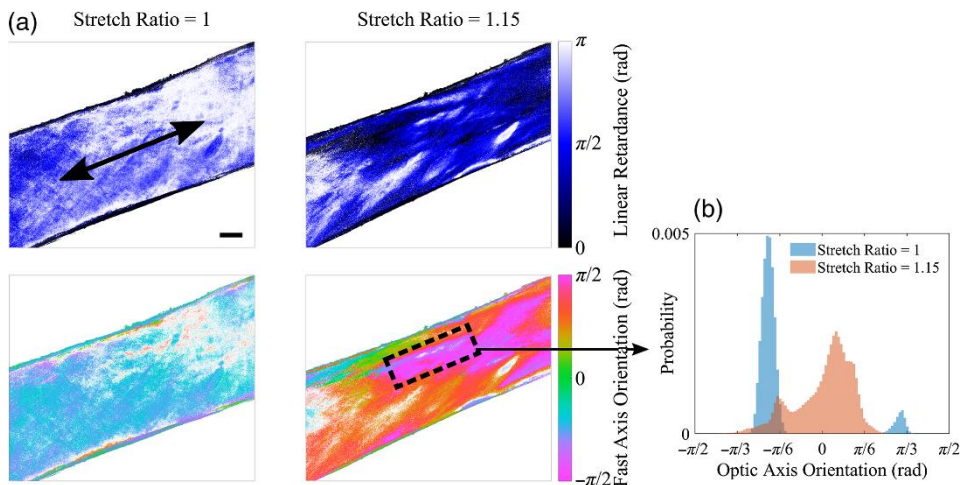


Figure 1-3 (a) Linear retardance (first row) and fast axis orientation (second row) for the bovine pericardium sample mounted in a uniaxial tester at stretch ratios of 1 and 1.5. (b) Histograms distributions of the region correspondent to the black-dashed rectangle for both stretch ratios. Image adapted from [72].

- Depolarization in biomedical samples

Depolarization was initially understood as a characteristic with little value in biomedical applications and often regarded as noise to be minimized. In the past decade, studies have shown that the depolarizing properties of a sample contain valuable information. It reflects microscopic structural disorder, scattering strength, and compositional inhomogeneities in tissue. In this context, due to the high scattering response of biological samples and the structural changes that occur in tissues during many pathological processes, depolarization has become a powerful tool for studying and characterizing various human diseases [73–77]. For example, changes in tissue cellular concentration associated with the progression from pre-cancerous to cancerous states can be assessed through depolarization variations [75]. Similarly, alterations in anisotropy and orientation disorder have been directly linked to pathologies such as myocardial infarction [73] and different cancer stages in tissues like *ex-vivo* human colon, skin, cervix, and larynx [74,75,77]. Therefore, the anisotropic properties of samples can be correlated with specific pathological stages. In this

regard, depolarization metrics derived from experimental Mueller matrix measurements have proven to be valuable for such diagnostic applications. In [67], they use the study of depolarization features of samples for the early detection of abnormal tissue morphology aiding tissue characterization and diagnosis of ductal carcinoma, an early stage of breast cancer. They study show the degree of depolarization (DoP) and the degree of linear depolarization (DOLP) for both healthy and pathological tissue correspondent to breast sections. In Figure 1-4 the results show the different responses in DoP and DOLP for normal and tumorous tissue. This information is used to train Machine Learning models for the early detection of this pathology.

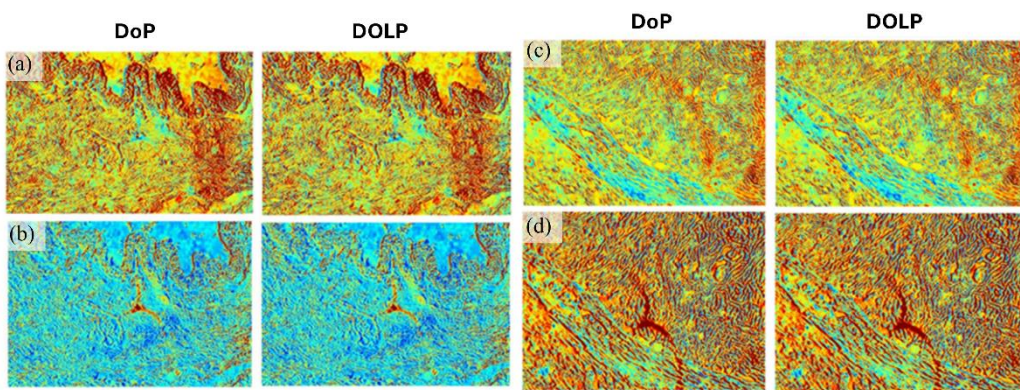


Figure 1-4 Depolarization parameters of healthy (a, b) and tumor (c, d) regions of ductal carcinoma sample. Image adapted from [67].

The mentioned characteristics -dichroism, retardance and depolarization- are useful in the inspection of biological tissue to achieve contrast enhancement and the detection of regions within samples that cannot be detected by common imaging techniques. In addition, it is worth noting that the spatial variation observed in the response of different tissue regions is linked to specific physical characteristics of the tissue structure, such as differences in composition, density or orientation of its components. Importantly, pathological changes in tissues often alter their structural organization, which in turn affects their polarimetric response. Several studies have demonstrated not only the capability of polarimetric channels to detect pathologies but also to detect them in early stages, when other techniques are not able to detect them. In the following, we present different imaging optical techniques used in the medical field where polarimetry can play an important role.

There exist some very common techniques in medicine where polarimetry plays a key role. For instance, dermatoscopes are well-established tools for dermatologists. The newest generation of these devices are comprised of a light source, a magnifying glass and

crossed polarizers. This device is used in the context of general dermatological disorders, including inflammatory dermatosis, pigmentary dermatosis, infectious dermatosis, and disorders of the hair, scalp and nails, among other [19,78]. In addition, microscopy with cross-polarizers is a standardized method in medicine, it allows to analyze features in tissues without the necessity of dyes or labels [79].

In recent years, a variety of medical imaging diagnosis instruments have incorporated polarization-based optical techniques. In this framework, we can cite very common medical techniques where optics play a key role: Optical Coherence Tomography (OCT), endoscopy, multispectral imaging, mass spectrometry, glucose detection, Raman spectroscopy and different types of microscopies (fluorescence, confocal, second harmonic generation,...) [80]. Some of them are already being applied, others are in clinical trial or in the experimental phase.

In the following, we present a more detailed discussion of some of the cases mentioned in the previous paragraph, due to their relevance in the medical field and their potential impact when combined with polarimetric methods: (1) Optical Coherence Tomography, (2) endoscopy, (3) multispectral imaging, and (4) microscopy.

1) Optical coherence tomography performs high resolution cross-sectional imaging; it can provide cross-sectional images of tissue structures on the micron scale *in situ* and real time. This technique has shown its potential in biomedical and clinical applications [14,15,17,18,81]. For instance, some applications of OCT in clinical research are in retinal disease, coronary atherosclerosis, aiding during cancer interventions and the study of bones, muscles, tendons and skin imaging. Then, also imaging of cardiac and vascular tissue has shown good performance. In addition, clinical polariscopes is an ophthalmic device that utilizes birefringence analysis to assess corneal structure, helping in the diagnosis of conditions such as keratoconus and cataracts [82,83].

A more advanced technique, polarization sensitive optical coherence tomography (PS-OCT), enables depth-resolved imaging with polarization information. This technique has demonstrated its utility in a vast range of applications: ophthalmology, dermatology, oncology, cardiovascular imaging and neuroimaging, among other [15,84]. PS-OCT is used in clinical research for some applications in ophthalmology, coronary atherosclerosis and the lungs. More applications are in the preclinical phase and await integration into commercial instruments. PS-OCT stands out as a versatile functional extension of OCT that requires relatively minor hardware modifications, providing a powerful qualitative and quantitative polarization-based imaging. As an example, in Figure 1-5 we can see the difference between the conventional OCT image (a) and the results obtained from PS-OCT



(b)-(d) where the regions of healthy and pathological (basal cell carcinoma; BCC) tissue can be identified [85].

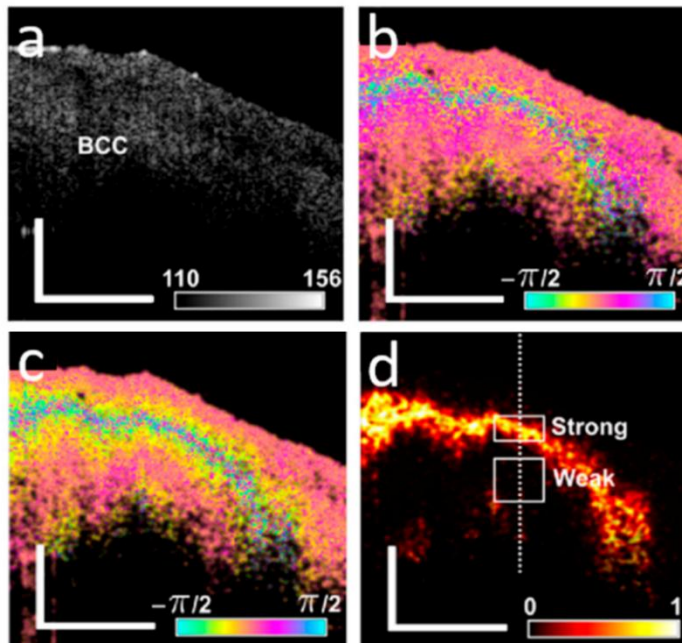


Figure 1-5 PS-OCT of cancerous tissue. (a) Intensity information, (b), (c) and (d) phase and depolarization information from the PS-OCT of basal cell carcinoma in human skin. Adapted with permission from [85] © Optical Society of America.

2) Polarimetric endoscopy is also an emerging technology, offering enhanced tissue contrast by detecting changes in surface polarization properties—showing promise in the early detection of gastrointestinal cancers and precancerous lesions. The addition of polarization in endoscopy can be very helpful for adding birefringence and depolarization information in diagnosis. This helps to improve the visualization of fine microstructural features in superficial tissues. The integration of polarization capabilities into endoscopes is relatively straightforward in the case of rigid endoscopes, as it requires minimal modifications to commercially available systems [86]. However, since rigid endoscopes limit the possible medical applications of this technique, there are several trials for the inclusion of polarimetry in flexible fibers [87,88]. In [89] they show the use of a polarimetric endoscope for the assessment of surgical polarimetric endoscope (SPE) in an *in-vivo* laryngectomy case, showing the potential of this apparatus in the laryngeal cancer detection (see Figure 1-6).



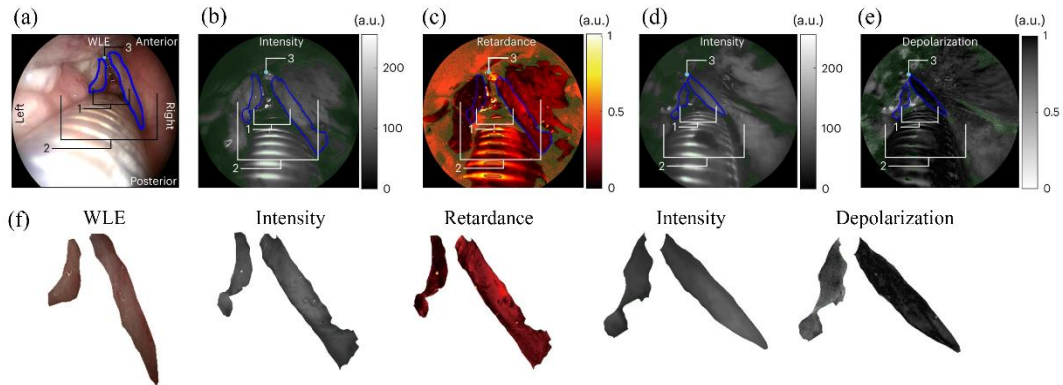


Figure 1-6 (a) Intensity image of the larynx (b), (c), Retardance and its intensity-reference image of the larynx. (d), (e) Depolarization and its intensity-reference image of the larynx. (f), Magnified images of the cancerous and normal vocal cord (for those of the supraglottis). Image adapted from [89].

3) Multispectral polarimetric imaging combines spectral information with polarization. The combination of spectral and polarization data enables the visualization of biological structures and lesions that can be hard to discern with conventional methods. In [84,90,91], they have shown the usefulness of this method for the analysis of brain samples.

For instance, in Figure 1-7, Conde Portilla's group study different regions of lamb brain by multispectral polarimetric technique. In the figure, they present the results of one of cerebral hemisphere for depolarization and retardance. They inspect different recognized regions within the brain with the aid of depolarization and retardance characteristics including multispectral information, obtaining very interesting results in terms of structure identification.

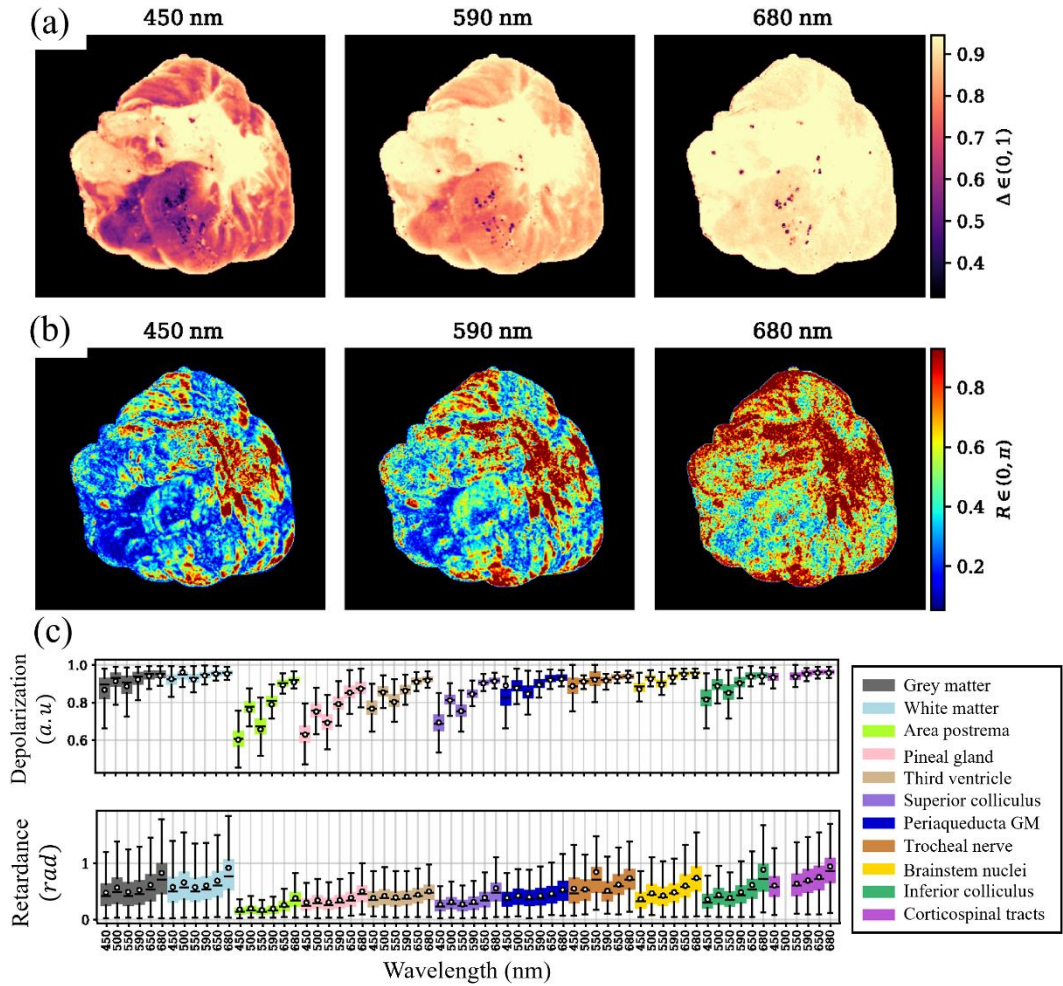


Figure 1-7 (a) Depolarization and (b) retardance images of lamb brain for different wavelengths. (c) Shows the boxplots for both polarimetric observables for different wavelengths from 450 nm to 680 nm. Each color indicates a different region in the brain. Image adapted from [84].

Finally, the inclusion of polarization in 4) microscopy also enables contrast enhancement and structure detection in biological tissues. The addition of polarization in different microscopy techniques adds information of polarimetric related properties such as birefringence, dichroism and depolarization. As previously mentioned, conventional polarized light microscopy is broadly used for diagnosis purposes, for instance, in the identification of birefringent crystals that can be indicators of gout [92] or assessing histological analysis [93]. In addition, more advanced polarimetric techniques have been introduced in microscopy devices. For instance, the addition of polarimetric features to

confocal scanning laser microscopy, Confocal Scanning Laser Polarimetric Microscopy (CLSM), allows to add information about the spatially resolved structure of the sample including polarimetric characteristics to the conventional microscopy information. Moreover, as demonstrated in several of the presented examples that incorporate polarization, the measurement of polarimetric features has contributed to enhanced contrast. Some examples are shown by Wang et al. in [94], where CLSM has allowed to perform visualization of cytomembranes and image amyloidosis, also Gareau et al. in [95] image melanoma in malignant tissue. Additionally, Second Harmonic Generation microscopy (SHG) is used for non-invasive high-resolution imaging in different kinds of biological samples, for instance, the visualization of bone, skin or cornea [96–98]. The implementation of Polarization sensitive second harmonic generation microscopy (PSGH) allows to measure the resulting SHG signal as a function of polarization. This can reveal orientation and structural properties of anisotropic molecules like collagen, myosin, or microtubules. In the literature we can find applications of PSGH in collagen studies for cancer detection [98,99], hepatic and pulmonary fibrosis, osteoarthritis, and investigation of muscle contraction dynamics, among others [80]. Therefore, PSGH offers impressive results and presents itself as a technique that can enable automated cancer diagnosis and earlier diagnosis of pathologies.

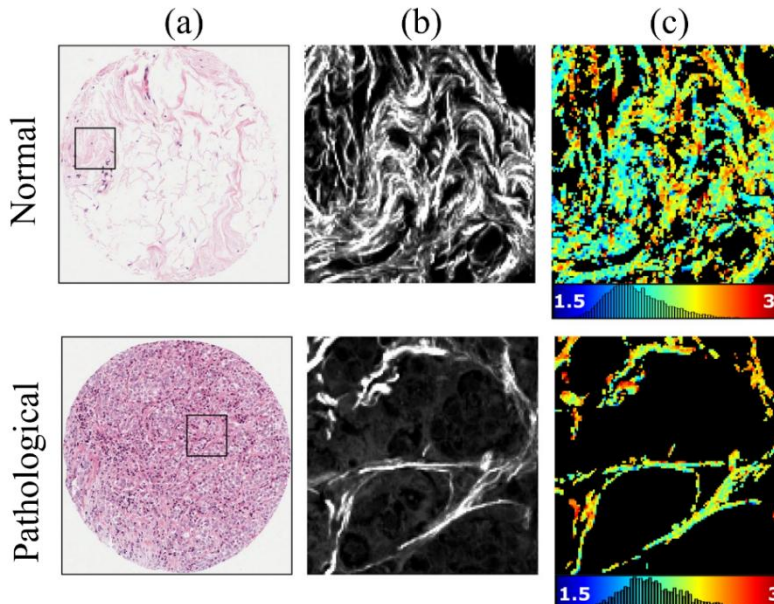


Figure 1-8 Healthy (first row) and pathological images for breast tissue samples sections. (a) Microscopic histological images, (b) standard SHG images and (c) PSGH images. Image adapted from [20].

Figure 1-8, presents the results for healthy and pathological breast tissue samples. (a) Shows the histological image, (b) the correspondent SHG image of the black squared indicated in (a) and (c) displays polarization information obtained from the PSHG. When comparing normal (first row) and pathological (second row) results, the polarimetric parameter presents more yellow pixels, whereas the health has more blue pixels, showing that the collagen in normal breast tissue has lower values than for malignant. Therefore, the addition of polarimetry to SGH leads to a detection of slight changes in tumor development.

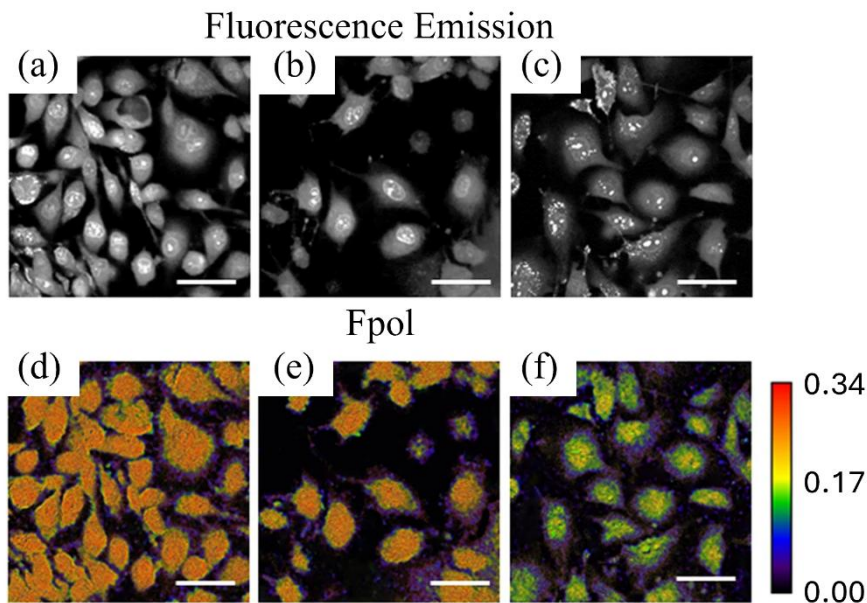


Figure 1-9 Standard (first row) and polarimetric (second row) fluorescence emission microscopy images of breast healthy ((a) (b) (d) (e)) and cancerous ((c) (f)) cells. Image adapted from [100].

In addition, polarization was also added to other microscopy techniques such as fluorescence, total reflection, optical scanning or nonlinear microscopy [100–103]. As an example, in Figure 1-9 the fluorescence emission images are shown; the first row corresponds to standard fluorescence microscopy and second row to fluorescence polarization microscopy (Fpol). Images of different normal ((a), (b), (d), (e)) and cancerous ((c), (f)) cells are shown. The Fpol images demonstrate notable differences between the healthy ((d), (e)) and the pathological cells ((f)).

It is also noteworthy that a recent advancement in medical technology has incorporated polarimetric information: the development of a portable hybrid colposcope, designed as a snapshot Mueller matrix polarimeter, by Ramella-Roman's group. Colposcopy tests are



medical devices used as the first step in cervical cancer screening, which consist of collecting epithelial cells from the cervix and examining them under microscope. However, it is difficult to correctly locate the possible affected regions, and this usually implies a low sensitivity and specificity. The hybrid colposcope device or Mueller polarimetric colposcope can be used as a conventional colposcope and provide reliable polarimetric images, making the location of the possible pathological regions easier with the aid of polarimetric information [104]. In Figure 1-10 they demonstrate the performance of the polarimetric information obtained with the hybrid polarimetric colposcope in the inspection of two cervix samples. Zones 1 and 2 correspond to normal cervix, while zone 3 is the pathological part where the polyp is located. Both in the polarimetric images ((b)-(i)) and in their correspondent histograms show a clear contrast between the healthy and pathological part of the tissue, demonstrating the utility of the proposed device for the cervix inspection [105].

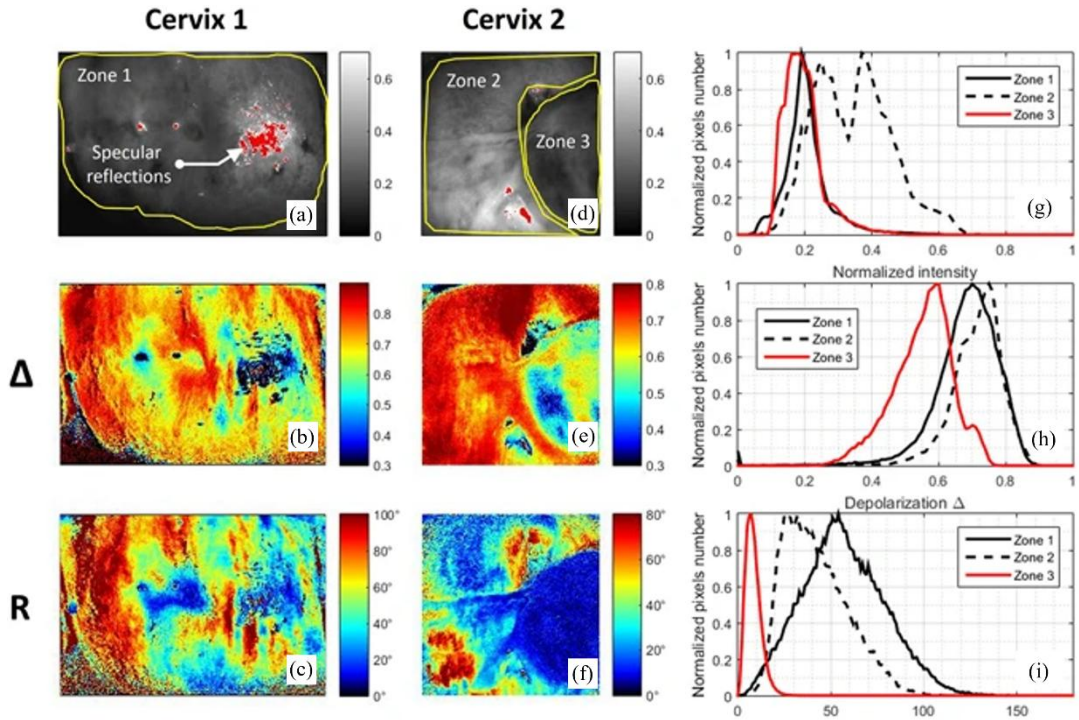


Figure 1-10 Comparison between the intensity (first row) and polarimetric (depolarization, second row and retardance third row) images of *in-vivo* uterine cervix 1 and 2. (i)-(k) show the correspondent histograms of intensity, depolarization and retardance images of both samples. Image adapted from [105].

Summarizing, these instruments present the importance of polarization optics in advancing polarimetric diagnostics. Some of these instruments or methods have already reached the clinical stage while others are in active research or early development, facing the challenges of integrating polarization-based technologies into medical practice.

### 1.1.3 Polarimetry in Neurological Applications

As previously mentioned, one of the central pillars of the polarimetric knowledge and methods developed in this thesis is their application to the study of brain structures. For this reason, in the following subsection, we aim to present the current state of the art regarding the techniques currently used for the characterization of this biological organ.

The brain can be divided into two main regions: gray matter (*gm*) and white matter (*wm*). Gray matter (*gm*) is a 2-4 mm thick outer layer of the brain, conformed by cell bodies of neurons and is organized in six sub-layers, each with distinct functions related to sensory processing, motor control and cognition. In contrast, white matter (*wm*) is a more fibered structure composed of a large number of axons linked together that form fiber tracts and it connects different *gm* regions. The different fiber tracts are related to different brain functions, such as memory, vision, smell, voluntary movements, among others. The study of white matter is highly valuable for understanding brain connectivity and for the diagnosis of neurological disorders. For instance, abnormalities in white matter are associated with conditions such as schizophrenia, chronic depression, bipolar disorder, Alzheimer's disease, among other [106,107]. In the case of gray matter, its study is essential for understanding brain processes related to sensory and motor information. In addition, *gm* analysis is especially useful in the early detection of neurodegenerative diseases like Alzheimer, semantic dementia and some types of epilepsy [108].

Both fundamental research on specific brain regions and the study of brain pathologies — such as tumors and neurological disorders — remain active areas of investigation because of the challenges of studying the brain *in-vivo*. Interestingly, the variety and complexity of brain tissue structures lead to very interesting polarimetric properties. Recently, polarimetric imaging has emerged as a useful tool for inspecting brain pathology and microstructure, particularly due to its sensitivity to anisotropic optical properties related to fiber organization (for the case of *wm*) and cell composition (for the case of *gm*). In addition, the sensitivity of polarimetry to structural changes has led to potential results in pathological detection in brain tissue [109].

Currently, only a few groups are working in this field (polarization applied to the study of brain structure), and thus, its full potential remains largely unexplored. In literature we can find very promising results not only in terms of structure identification for fundamental

analysis but also the first trials to adapt polarimetric technologies for surgery assistant environments. In the following, we will present a brief review of the latest results in the use of polarimetry for brain analysis.

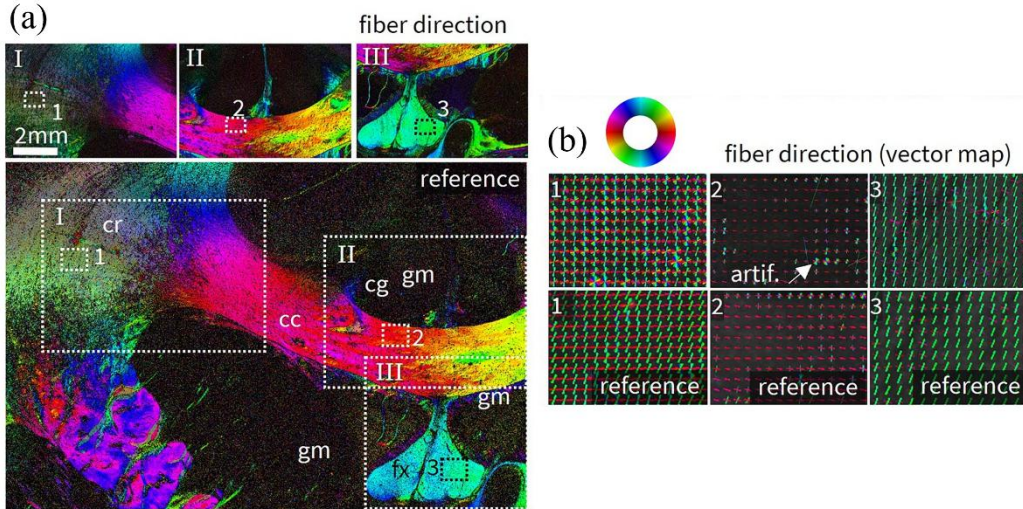


Figure 1-11 (a) Fiber direction map for a vervet brain sample obtained by the polarimetric measurement in [113]. Smaller rectangles marked with 1, 2, 3 indicate the regions for which the vector maps are visualized in (b): corpus callosum (cc), corona radiata (cr), cingulum (cg), fornix (fx), gray matter (gm). Image adapted from [113].

The study of *wm* directionality has been addressed by several research groups, primarily studying the birefringence properties of the myelinated axons comprising *wm*. This study helps not only to the pathway mapping of white matter in brain, this being a fundamental study in medicine, but also to the possible detection of neurological pathologies directly related to *wm* directionality and functionality. Imaging polarimetry has been extensively used to study fiber orientations, comparing the results with known anatomical trajectories. For instance, Menzel et al. in [62] proposed a method based on the study of birefringence to improve angular precision in the study of birefringence; wide-field Mueller matrix polarimetry has also shown promising results in mapping white matter directionality in thick, unstained sections [110–112]. In addition, in [90] they have demonstrated that these methods outperform common medical techniques such as diffusion MRI in spatial resolution, highlighting their capability to resolve microscale directionality features in complex regions of the brain. More recently, Heiden et al. in [113] they developed a high-speed scattering polarimeter that integrates 3D-PLI with Combined Structured Light Imaging (ComSLI), enabling precise mapping of fiber crossings and orientation dispersion in both human and primate brains (see Figure 1-11). In addition to the study of *wm*, the

information given by the polarimetric studies of the brain result in a contrast enhancement between structures of the brain difficult to detect by means of other techniques [84,112,114].

Tatiana Novikova's group and collaborators have performed extensive research in the use of wide-field Mueller matrix polarimetry for brain analysis. In [115], they demonstrated the correlation between the azimuth of the optical axis and histologically validated fiber tract orientation in fixed and fresh brain samples, highlighting the capacity of polarimetry for label-free identification of white matter structures relevant to tumor margin detection. In addition, they perform studies in *ex-vivo* samples under surgery-like conditions confirmed that the technique remains robust even in the presence of factors such as surface irregularities, blood, and topographic complexity, maintaining accurate orientation mapping of fiber tracts [111,116]. Finally, they introduced a near real time, AI-driven process that yields high-quality fiber orientation maps compatible with intraoperative neurosurgical workflows [117].

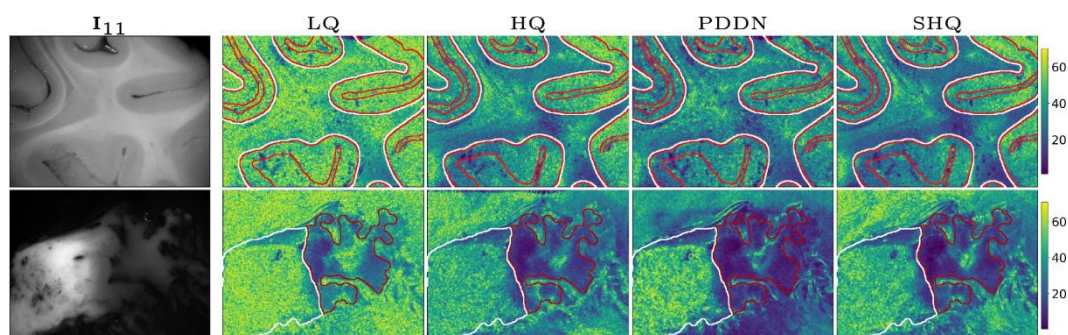


Figure 1-12 Top and bottom rows correspond to healthy and pathological brain samples, respectively. Low quality (LQ), high quality (HQ), polarimetric denoising diffusion network (PDDN) and Super high quality (SHQ) images of both samples show the potential of the polarimetric technique proposed in [117] for its use in real time medical applications. Image adapted from [117].

Additionally, our group has explored the use of depolarization and birefringent channels for biological tissue inspection, and the studies have yielded to very promising results in the detection of brain structures (see Figure 1-12). In [118], we describe for the first time the presence of two depolarization sources in samples, that we label as isotropic and anisotropic depolarization. Following this study, we introduced a polarimetric filter which allows to isolate only the anisotropic part of depolarization, containing the information of the microscopic structure of samples. After the application of this filter, the results of wide-field Mueller matrix polarimetry in high depolarizing samples, including brain samples,



yields to excellent results in terms of tissue discrimination and structure unveiling in brain samples, surpassing both common optical techniques and conventional polarimetric imaging [110,112]. The preliminary results presented in the mentioned articles were performed in animal samples, in this thesis we extend this study to human brain samples.

Summarizing, polarimetry provides a complementary and often unique perspective of neural tissue organization and pathology. The integration of this technique in medical imaging and computational models paves the way for advancing both basic neuroscience and clinician practice. The integration of polarimetric systems into *in-vivo* and minimally invasive settings could open novel frontiers for brain imaging, intraoperative decision-making and pathological detection.

## 1.2 Main goals of this thesis

The use of polarimetric imaging techniques in biological samples gives excellent results in terms of enhanced samples imaging and structure unveiling. The main goal of this thesis is to present a comprehensive and in-depth study of depolarization, one of the polarimetric characteristics of samples, for its application in the study of biological tissues. Some of the main goals of the thesis are listed below:

1. Deep study of depolarization sources of samples: to establish a connection between macroscopic polarimetric measurements (specifically the Indices of Polarimetric Purity) and the underlying microscopic depolarization mechanism. This provides a methodology for interpreting the physical origin of depolarization in different samples, distinguishing two depolarization sources: isotropic depolarization (associated with multiple scattering) and anisotropic depolarization (linked to intrinsic structural properties).
2. Use of new Arrow decomposition derived polarimetric observables: to design and implement a novel polarimetric imaging approach based on the Arrow decomposition of Mueller matrices, enabling enhanced spatial characterization of biological tissues. This methodology yields significant improvements in contrast and structure detection compared to conventional Mueller matrix imaging, particularly in the context of biological tissue inspection.
3. Development of the Isotropic Depolarization Filter (IDF): to isolate the depolarization sources, isotropic and anisotropic. Anisotropic depolarization contains the intrinsic information of samples, whereas isotropic is related to multiple

scattering processes that veil structural information in polarimetric measurements. The isolation of both sources by the application of the IDF allows to obtain highly improved results when compared with standard polarimetric observables.

4. Application of the IDF for the study of biological medical samples: to demonstrate the practical utility of the IDF in the analysis of biological samples, particularly in medical imaging. The filter highly improves image quality in terms of contrast enhancement and structure detection. These advances open promising avenues for the non-invasive polarimetric study of brain tissues, including the study of white and gray matter.

### 1.3 Structure of this thesis

The outline of this thesis is as follows:

In Chapter 2, we explain in detail the mathematical formalism used in this thesis to study the interaction between polarized light and matter. In particular, we describe the Mueller Stokes formalism which allows us to describe partially and totally depolarized states and polarimetric samples. In addition, we also provide several decompositions of the Mueller matrices for the study of the polarimetric characteristics of samples related to the physical properties of samples.

Chapter 3 is divided in two main sections; in section 3.1 we describe the experimental set-up of the Complete Mueller matrix Image polarimeter used to obtain the experimental Mueller matrices of samples shown in this work. Then, in section 3.2 we also provide a detailed explanation of the physiological characteristics of the biological samples inspected through the following sections of this manuscript.

Afterwards, Chapter 4 focuses on the study of the depolarization sources of samples. To do so, we perform a series of simulations to analyze the effect of the depolarization sources in the Indices of Polarimetric Purity. In section 4.1 we provide the detailed explanation for the obtention of the different depolarizers by means of pure diattenuators, pure retarders and the combination of both, where the value of  $P_3$  is always equal to 1. Section 4.2 includes the depolarizers simulations with  $P_3 < 1$ . Finally, we also provide some experimental proofs for the simulations and a visual interpretation of the simulated results in the Purity Space.

Chapter 5 is divided into two sections. The first section presents the implementation of a digital filter (the isotropic depolarization filter) to the Mueller matrix, separating the depolarization sources. We also inspect the effect of the application of this filter in the

polarimetric observables and polarimetric spaces described in previous sections as well as a visual interpretation of the filter in the polarimetric spaces. Then, the second section shows the effect of the filter application in real biological samples, comparing the results obtained with standard polarimetric images and the filtered ones.

Chapter 6 is devoted to the application of the isotropic depolarization filter in the inspection of brain samples. We present results obtained from animal brain samples, focusing on the study of white matter regions, as well as from human brain samples, where the application of filtered polarimetric data has led to an excellent identification of different regions within gray matter. We also describe the potential of the detection of these structures for possible applications in medical and neurological applications.

Finally, the conclusions of the present work are summarized and a proposal for future research is presented.

## Chapter 2 Mathematical formalism

This chapter presents the mathematical formalism used in this thesis to describe the light-matter interactions in terms of their polarimetric response. The mathematical basis of this study is the Mueller-Stokes formalism, where the polarimetric characteristics of light can be described by means of the Stokes vector and the polarimetric response of samples is encoded in the Mueller matrix ( $M$ ).

First, the concepts related to the Mueller-Stokes formalism are described in section 2.1. In particular, Stokes vector and related Poincaré Sphere are presented in subsections 2.1.1 and 2.1.2, respectively. Next, in subsection 2.1.3 the Mueller matrix main characteristics are presented. In section 2.2 we deeply analyze  $M$ , introducing different matrix decompositions, such as, the block form (sec. 2.2.1), Parallel decomposition and Serial compositions (sec. 2.2.2 to 2.2.4). These decompositions allow us to obtain polarimetric observables related to dichroism, birefringence and depolarization. All the polarimetric observables obtained are summarized in section 2.2.5. To conclude, in the last section 2.3 we present two 3D polarimetric spaces, generated by triplets of polarimetric observables, the Purity Space (generated by the Indices of Polarimetric Purity) and the Components of Purity Space (generated by the Components of Purity) which are useful tools for depolarizers visualization and discrimination.

### 2.1 Mueller-Stokes formalism

Polarization is a fundamental property of light related to its vectorial nature, describing the behavior of light when it propagates. The description of polarized light and the result of its interaction with matter can be described by using different mathematical approaches.

Historically, different formalisms such as the Jones calculus [119], based on the complex components of the electric field, the Bareman formalism [120], which considers the magnetic field, or the Mueller-Stokes (*M-S*) formalism [119,121] based on light flux measurements, were used to describe this characteristic, among others. For the framework of this thesis, the study of the interaction between polarized light and biological samples, the most suitable approach is the *M-S* formalism. In contrast with other formalisms, this approach is valid when working with depolarized or partially polarized light and is based on magnitudes that can be easily measured in the laboratory.

### 2.1.1 Stokes vector

In 1852, Sir George Gabriel Stokes discovered that the polarization nature of light could be represented in terms of observables [122]. He described the four terms comprising the Stokes vector ( $\mathbf{S}$ ) as four measurable quantities known as the Stokes polarization parameters ( $S_0, S_1, S_2, S_3$ ). These parameters are derived from statistical treatment of the polarization ellipse [123], based on the amplitudes of the electric field, that can be experimentally obtained by means of radiometric measurements:

$$\mathbf{S} = \begin{pmatrix} S_0 \\ S_1 \\ S_2 \\ S_3 \end{pmatrix} = \begin{pmatrix} I_{0^\circ} + I_{90^\circ} \\ I_{0^\circ} - I_{90^\circ} \\ I_{45^\circ} - I_{135^\circ} \\ I_R - I_L \end{pmatrix}, \quad (2-1)$$

where  $S_0$  is associated with the total intensity of the light beam and  $S_1$ ,  $S_2$  and  $S_3$  parameters state for the fully polarized content of the beam. In particular,  $S_1$  corresponds to the amount of light with horizontal ( $0^\circ$ ) or vertical ( $90^\circ$ ) linear polarization,  $S_2$  indicates the light polarized in diagonal ( $45^\circ$ ) or anti-diagonal ( $145^\circ$ ) linear polarization and,  $S_3$  represents the amount of light correspondent to right-handed or left-handed circular polarization. The values of these parameters are obtained by means of different intensity measurements:  $I_{0^\circ}$ ,  $I_{90^\circ}$ ,  $I_{45^\circ}$ ,  $I_{135^\circ}$ ,  $I_R$ ,  $I_L$ , corresponding to the amount of flux light polarized in horizontal, vertical, diagonal, antidiagonal linear polarization and right-handed and left-handed circular polarization, respectively.

Moreover, when the light beam contains certain depolarization content, the relation  $S_0 > \sqrt{S_1^2 + S_2^2 + S_3^2}$  is accomplished, and it can be quantified by using the degree of polarization (DoP) metric, that can be calculated as follows [124]:

$$\text{DoP} = \frac{\sqrt{S_1^2 + S_2^2 + S_3^2}}{S_0}, \quad (2-2)$$

where a fully polarized light beam corresponds to a  $DoP = 1$  ( $S_0 = \sqrt{S_1^2 + S_2^2 + S_3^2}$  i.e., all the intensity of the light correspond to different polarization states), a totally unpolarized state is represented by a  $DoP = 0$  ( $\sqrt{S_1^2 + S_2^2 + S_3^2} = 0$  i.e., none of the measured intensity correspond to polarized light), and a partially polarized state have values  $0 < DoP < 1$  ( $0 < \sqrt{S_1^2 + S_2^2 + S_3^2} < S_0$  i.e., only part of the light is polarized).

In addition, these parameters can be normalized to eliminate the intensity dependence of the beam and compare the polarization characteristics of SoPs with different intensities. So, to eliminate the intensity contribution to the Stokes vector parameters, each of the elements is divided by  $S_0$  and we will note it as  $(s_1, s_2, s_3)$ .

### 2.1.2 Poincaré Sphere

In 1982 Henri Poincaré introduced the so-called Poincaré Sphere [125]. This sphere contains the graphical representation of any physically realizable SoP, from fully polarized to totally depolarized light, represented by the value of their normalized Stokes vector  $(s_1, s_2, s_3)$ . These parameters can be written in terms of the spherical coordinates [123]:

$$s = \begin{pmatrix} s_1 \\ s_2 \\ s_3 \end{pmatrix} = DoP \begin{pmatrix} \cos 2\varphi \cos 2\chi \\ \sin 2\varphi \cos 2\chi \\ \sin 2\chi \end{pmatrix}, \quad (2-3)$$

where  $\varphi$  and  $\chi$  correspond, respectively, to the azimuth and ellipticity angles of the polarization ellipse describing the fully polarized content of the SoP, and where the values of the normalized Stokes parameter can take values from 1 to -1. Moreover, we can identify the modulus of the normalized Stokes vector as the value of its DoP (see Eq. (2-2)), that is, the distance from the vector position to the center (modulus) is directly related to its degree of polarization. Therefore, the position of the vector in the sphere has complete information about the polarimetric characteristics of light; the modulus of the vector represents the degree of polarization and the position in the sphere corresponds to the polarization angles.

Some interesting properties of the spherical representation depicted in Figure 2-1 are:

- Points in the external surface ( $\hat{S}$ ) of the sphere correspond to fully polarized SoPs ( $s_1^2 + s_2^2 + s_3^2 = 1$ ;  $DoP = 1$ ).
- Totally unpolarized states are in the center of the sphere ( $s_1 = s_2 = s_3 = 0$ ;  $DoP = 0$ ).

- Points located inside the sphere correspond to partially polarized states, the DoP decreases as points get closer to the origin. For instance, pink sphere in Figure 2-1 represents partially polarized states with  $0 < DoP < 1$ .
- Linear states ( $\chi = 0$ ) are located in the equator of the sphere (see black dashed lines in the figure).  $\hat{S}_H$ ,  $\hat{S}_V$ ,  $\hat{S}_{45}$  and  $\hat{S}_{135}$  are the horizontal (1,1,0,0), vertical (1,-1,0,0), diagonal (1,0,1,0) and antidiagonal (1,0,-1,0) linear polarized states cases.
- Circular polarized states correspond to the poles of the sphere  $\hat{S}_L$  (1,0,0,1) and  $\hat{S}_D$  (1,0,0,-1).
- Any other arbitrary SoP in the Poincaré sphere is an elliptically polarized SoP characterized by the azimuth and ellipticity angles ( $\varphi$ ,  $\chi$ ).

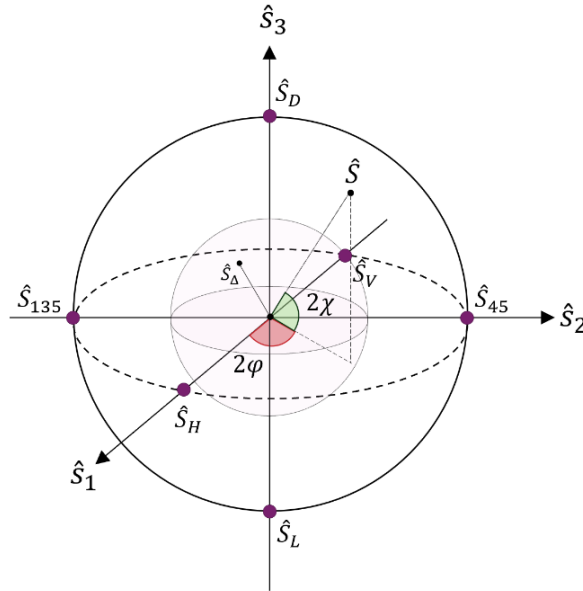


Figure 2-1 Representation of the Poincaré sphere and a totally polarized SoP ( $\hat{S}$ ) characterized by  $\varphi$  and  $\chi$  angles. Horizontal ( $\hat{S}_H$ ), vertical ( $\hat{S}_V$ ), diagonal ( $\hat{S}_{45}$ ) and antidiagonal ( $\hat{S}_{135}$ ) linear SoPs are represented by the purple points located in the equator of the sphere; left ( $\hat{S}_L$ ) and right ( $\hat{S}_D$ ) circular totally polarized SoPs are represented by the purple points located in the poles of the sphere. The pink sphere represents partially polarized SoPs, ( $\hat{S}_\Delta$ ;  $DoP < 1$ ).

This representation is not only highly useful for the representation of SoPs, but also for representing the change of polarized light in light-matter interactions.

### 2.1.3 Mueller matrix

When a sample is illuminated with polarized light, this light interacts with the sample and this interaction can make changes in its state of polarization (SoP). To measure these changes, that is, the variations in the Stokes vector before ( $S_{in}$ ) and after ( $S_{out}$ ) interacting with a sample, Hans Mueller introduced the so-called Mueller matrix ( $M$ ), which acts as a transfer function between Stokes vectors:

$$S_{out} = MS_{in}. \quad (2-4)$$

The Mueller matrix is defined as a 4x4 real matrix where all the variations that a sample can produce in the polarization state of light are encoded. That is, the elements of  $M$  describe how the polarization of any SoP interacting with a sample can be changed. These changes can be related to the intrinsic characteristics of the sample (dichroism, birefringence, composition, orientations, randomness, etc.), which some of them, in turn, also depend on the wavelength of the illuminating light and the direction of incidence [123,124]. In this sense, the Mueller matrix allows us to classify the polarimetric properties of materials depending on how they modify the SoP of an incident light beam. The properties of the samples affecting the polarimetric state of light can be divided into three features: (1) dichroism, representing asymmetries in light components absorption, (2) birefringence, accounting for components relative phase changes; and (3) depolarization, corresponding to the capability of the samples to transform polarized light into unpolarized states.

- (1) Dichroism manifests in two physical effects: diattenuation and polarizance. Diattenuation represents the amount of light that is absorbed in a light-matter interaction process depending on the polarization state of the incident SoP whereas polarizance quantifies the capacity of the sample to polarize an incident unpolarized light beam [123,124].
- (2) Birefringence describes the capability of samples to introduce certain relative retardance between the electromagnetic components of the input light without changing either the DoP of the incident beam or the input light flux. It is associated with materials exhibiting some refractive index anisotropy.
- (3) Depolarization is the capability of a material to reduce the DoP of the incident SoP, that is, to depolarize light, and it is associated with physical and statistical processes introducing SoP randomization.

The combined effect of these three properties is encoded in the 16 Mueller matrix elements. To decode this information and obtain polarimetric observables related to



dichroism, birefringence and depolarization separately we can perform different decompositions of  $M$ .

## 2.2 Mueller matrix decompositions and Polarimetric Observables

Polarimetric features encoded in the Mueller matrix are related to physical properties of the samples, such as intrinsic components, densities and/or organization. To obtain the polarimetric observables associated with these properties, we need to further process the  $M$  elements.

There are different mathematical treatments that can be applied to the raw  $M$  for the obtention of polarimetric observables with physical meaning. Some of them can be directly associated with certain sets of  $M$  elements, whereas others need further mathematical processing of the Mueller matrix data. For instance, dichroic-related parameters such as the diattenuation ( $\mathbf{D}$ ) and polarizance ( $\mathbf{P}$ ) vectors can be directly extracted from  $M$  structure. However, for the obtention of depolarizing and birefringent parameters there are different decompositions allowing them to isolate these properties and extract the parameters.

In the following we review certain approaches to obtain a representative set of polarimetric observables from  $M$ . We first describe the block form of the  $M$ , from which the dichroism and some depolarization features of the sample can be directly obtained from its elements or simple combinations of them (sec. 2.2.1). In secs. 2.2.2 to 2.2.4, we introduce the general Serial and Parallel decompositions of  $M$  as well as some particular examples retrieving polarimetric observables of special interest in the inspection of biological tissues.

### 2.2.1 Block form of a Mueller matrix

Let us start with the block form of  $M$ , one of the simplest decompositions of the Mueller matrix [126]:

$$M = m_{00} \begin{pmatrix} 1 & \mathbf{D}^T \\ \mathbf{P} & m \end{pmatrix}, \quad (2-5)$$

$$\mathbf{D} = \frac{1}{m_{00}} (m_{10}, m_{20}, m_{30})^T, \quad \mathbf{P} = \frac{1}{m_{00}} (m_{01}, m_{02}, m_{03}), \quad (2-6)$$

$$m = \frac{1}{m_{00}} \begin{pmatrix} m_{11} & m_{12} & m_{13} \\ m_{21} & m_{22} & m_{23} \\ m_{31} & m_{32} & m_{33} \end{pmatrix}, \quad (2-7)$$

where  $m_{00}$  is the element of the Mueller matrix corresponding to the mean intensity coefficient (MIC); the three component vectors  $\mathbf{D}$  and  $\mathbf{P}$  represent the diattenuation and polarizance vectors and  $m$  is a 3x3 sub-matrix encoding in a more complex way other polarimetric properties of the samples (birefringence and depolarization). The modulus of  $\mathbf{D}$  and  $\mathbf{P}$  vectors ( $D = |\mathbf{D}|, P = |\mathbf{P}|$ ) correspond to the magnitude values for the diattenuation and polarizance of the sample. Directly from the raw elements of  $M$ , we can also obtain the Depolarization index parameter,  $P_\Delta$ , which measures the total capacity of a sample to depolarize light [127,128], and can be understood as a generalization of the DoP concept to matrices:

$$P_\Delta = \sqrt{\frac{(\sum_{i,j=0}^3 m_{ij}^2) - m_{00}^2}{3m_{00}^2}} = \sqrt{\frac{P^2}{3} + \frac{D^2}{3} + \frac{\|m\|_2}{3}}, \quad (0 \leq P_\Delta \leq 1). \quad (2-8)$$

where  $\|m\|_2$  is the 2-norm of the sub-matrix  $m$  and the depolarization index is restricted between 0 and 1;  $P_\Delta = 0$  corresponds to a totally depolarizing system whereas  $P_\Delta = 1$  represent pure, non-depolarizing systems. The third term in Eq. (2-8) is defined as the degree of spherical purity ( $P_s$ ) [129]:

$$P_s = \frac{\|m\|_2}{\sqrt{3}}, \quad (0 \leq P_s \leq 1). \quad (2-9)$$

This parameter relates to the birefringent sources behind depolarization processes. Equation (2-8) represents the overall depolarization capacity of samples and can be determined by the dichroic ( $P$ ,  $D$ ) and birefringent ( $P_s$ ) effects resulting in depolarization. The three mentioned polarimetric observables ( $P$ ,  $D$  and  $P_s$ ) define a triplet of metrics, the-called Components of Purity (CP).

The Depolarization index,  $P_\Delta$ , is a global depolarization parameter; to obtain more specific information of different depolarization sources and characteristics of a sample it is necessary to perform further mathematical treatment of  $M$ . In the following sections, we show different decompositions of  $M$  to obtain depolarization and birefringence related metrics.

### 2.2.2 Parallel and Serial decompositions of a Mueller matrix

In the literature, we can find different decompositions and related metrics describing polarimetric properties of samples. In this sense, it is important to note that when performing decompositions and Mueller matrix analysis, we reduce the complexity of real samples (such as biological samples) by modeling them as combinations of simpler systems. This modeling allows to extract some physical features from them, such as dichroism, birefringence and depolarization. Therefore, depending on the kind of samples under study and the measurement conditions, we can choose to study them by means of different polarimetric observables and/or decompositions.

In general, a Mueller matrix can be decomposed into two kinds of decompositions: Parallel and Serial decompositions (or combinations of them) [124,130].

Parallel decompositions consist of dividing a  $M$  in a convex sum of  $M_s$ . This decomposition represents the polarized light-matter interaction as a physical process where the incident beam is divided into a set of pencils that interact with different optical components spatially distributed in the illuminated area without overlapping. The pencils after the interaction are incoherently recombined into an output beam. Some decompositions belonging to this group are the Spectral [124] and Characteristic [127] decompositions.

Serial decompositions consist of representing a general Mueller matrix as a product of particular Mueller matrices. In this decomposition the whole system is considered as a cascade of simpler polarimetric components where the incoming light interacts sequentially with them. Well known decompositions such as the Lu-Chipman [131] and the Arrow [132] decompositions belong to this category.

### 2.2.3 Arrow decompositions of a Mueller matrix

The Arrow decomposition is a Serial decomposition inspired on the arrow form of the Mueller matrix,  $M_A(M)$  [124,132]. This decomposition is based on the singular value decomposition of the 3x3 submatrix,  $m$  (see Eq. (2-7)):

$$m = m_{RO} m_A m_{RI}, \quad (2-10)$$

where,

$$\left\{ \begin{array}{l} m_{RI}^{-1} = m_{RI}^T \quad \det m_{RI} = +1 \quad (i = O, I), \\ m_A = \text{diag}(a_1, a_2, \epsilon a_3), \quad 1 \geq a_1 \geq a_2 \geq a_3 \geq 0, \quad \epsilon = \frac{\det m}{|\det m|}, \end{array} \right\} \quad (2-11)$$

and

$$M_{Ri} = \begin{pmatrix} 1 & 0^T \\ 0 & m_{Ri} \end{pmatrix} \quad (i = O, I), \quad (2-12)$$

where  $a_1, a_2$  and  $a_3$  are the singular values of  $m$ ,  $m_A$  corresponds to the 3x3 submatrix of the arrow form of  $(M_A)$  of the Mueller matrix, and  $m_{RO}$ , and  $m_{RI}$  are the submatrix forms of a pure entrance ( $M_{RI}$ ) and exiting ( $M_{RO}$ ) retarder, respectively. Thus, we can define the arrow form of  $M$  as:

$$M = M_{RO} M_A(M) M_{RI} \quad (2-13)$$

This decomposition considers the polarimetric interaction of the system described by  $M$  as a combined effect of an initial entrance retarder ( $M_{RI}$ ), a dichroic and depolarizing system described by the Arrow form ( $M_A$ ) of  $M$  and, finally, an exit retarder ( $M_{RO}$ ). To obtain the arrow form of  $M$ , we can rewrite the equation as:

$$M_A(M) = M_{RO}^T M M_{RI}^T = m_{00} \begin{pmatrix} 1 & D_A^T \\ P_A & m_A \end{pmatrix}; \quad P_A \equiv m_{RO}^T P, \quad D_A \equiv m_{RI} D. \quad (2-14)$$

From this decomposition, we separate the contributions of the retardance properties ( $M_{RI}$ ) from the dichroism and depolarization ( $M_A$ ). In this sense, from the arrow form of  $M$ ,  $M_A$ , we can extract the arrow polarizance and diattenuation ( $P_A$  and  $D_A$ ) as shown in Eq. (2-14). In addition, the 3x3 submatrix  $m_A$  represent a diagonal matrix (see Eq. (2-11)) conformed by the three arrow indices ( $a_1, a_2, a_3$ ). These indices encode a mixture of depolarization and dichroic properties of the media.

The retardance parameters are encoded in the entrance and exiting retarder matrices ( $M_{RI}, M_{RO}$ ). To characterize the birefringent properties of a sample, we can apply on them operations already described for a general retarder  $M_{Ri}$  [123,124], this giving rise to the following set of observables:

$$\Delta_i = \cos^{-1} \left| \frac{\text{tr}(m_{Ri})}{2} - 1 \right|, \quad 0 \leq \Delta_i \leq \pi; \quad (2-15)$$

$$R_i = \frac{\Delta_i}{2\pi \sin \Delta_i} \begin{pmatrix} m_{Ri23} - m_{Ri32} \\ m_{Ri31} - m_{Ri13} \\ m_{Ri12} - m_{Ri21} \end{pmatrix} = R_i \begin{pmatrix} \cos 2\varphi_{Ri} \cos 2\chi_{Ri} \\ \sin 2\varphi_{Ri} \cos 2\chi_{Ri} \\ \sin 2\chi_{Ri} \end{pmatrix}, \quad (2-16)$$

$$\varphi_{Ri} = \frac{1}{2} \tan^{-1} \left( \frac{m_{Ri31} - m_{Ri13}}{m_{Ri23} + m_{Ri32}} \right), \quad \chi_{Ri} = \frac{1}{2} \sin^{-1} (R_i (m_{Ri12} - m_{Ri21}))$$

$$\left[ 0 < R_i \leq 1, \quad 0 \leq \varphi_{Ri} < \pi, \quad -\pi/4 \leq \chi_{Ri} < \pi/4 \right],$$

where  $\Delta_i$  is the total retardance, describing the global behavior of a general retarder,  $\mathbf{R}_i$  is the retardance vector, the modulus ( $R_i$ ) indicates the phase shift introduced between the electromagnetic components of the light and  $(\varphi_{Ri}, \chi_{Ri})$  are the azimuth and ellipticity angles of the fast eigenstate. In addition to the general retardance vector ( $\mathbf{R}_i$ ), we can extract additional information related to birefringence, such as the linear retardance ( $\delta$ ) and the optical rotation ( $\psi$ , rotation applied to the linear retarder) [133]:

$$\delta_{Ri} = \cos^{-1} \left( \sqrt{(m_{Ri11} + m_{Ri22})^2 + (m_{Ri21} - m_{Ri12})^2} - 1 \right), \quad (2-17)$$

$$\psi_{Ri} = \tan^{-1} \left( \frac{m_{Ri21} - m_{Ri12}}{m_{Ri11} + m_{Ri22}} \right). \quad (2-18)$$

For the Arrow decomposition particular case, we can obtain the retardance parameters related to the entrance and exiting retarders:

#### Entrance retardance

$$M_{RI} = \begin{pmatrix} 1 & 0^T \\ 0 & m_{RI} \end{pmatrix} \rightarrow (R_I, \varphi_{RI}, \chi_{RI}, \delta_{RI}, \psi_{RI}), \quad (2-19)$$

#### Exit retardance

$$M_{RO} = \begin{pmatrix} 1 & 0^T \\ 0 & m_{RO} \end{pmatrix} \rightarrow (R_O, \varphi_{RO}, \chi_{RO}, \delta_{RO}, \psi_{RO}). \quad (2-20)$$

In this decomposition, we consider the light-matter interaction as a combinative effect of an entrance retarder ( $M_{RI}$ ), a matrix representing the dichroic and depolarizing properties of the sample ( $M_A$ ) and an exiting retarder ( $M_{RO}$ ). Therefore, birefringent, dichroic and depolarizing properties of the samples are represented by different matrices, making easiest the calculation of the observables. As previously explained, dichroic and depolarization properties are not completely isolated; the three arrow indices have mainly depolarization information but also contain dichroism features and the arrow diattenuation ( $\mathbf{D}_A$ ) and polarizance ( $\mathbf{P}_A$ ) vectors are also related to retardance. However, as we show in sections 5.2 and Chapter 6, the polarimetric arrangements specifically of this decomposition demonstrate extremely good performance for different tissue identification in image polarimetry.

### 2.2.4 Spectral and Characteristic decompositions of a Mueller matrix

Spectral decomposition of a matrix is based on the spectral theorem, this theorem states that a diagonalizable matrix can be decomposed in a pondered sum of matrices obtained from its eigenvectors and weighted by its eigenvalues [124].

To perform the Spectral decomposition of the Mueller matrix we need to transform  $M$  to the covariance matrix ( $H$ ). This is because  $H$  is a positive Hermitian matrix that can be always diagonalized [134], whereas  $M$  does not always fulfil this condition. The covariance matrix can be defined from  $M$  elements as:

$$H(M) = \frac{1}{4} \sum_{k,l=0}^3 m_{kl} (\sigma_k \otimes \sigma_l), \quad (2-21)$$

where  $\sigma_i$  are the Dirac matrices and the symbol  $\otimes$  represents the Kronecker product. The above-mentioned characteristics of  $H$  matrix make it diagonalizable through a unitary transformation:

$$H = \mathbf{U} \text{diag}(\lambda_0, \lambda_1, \lambda_2, \lambda_3) \mathbf{U}^t, \quad (2-22)$$

where  $\lambda_i$ , are the four eigenvalues of  $H$  fulfilling  $0 \leq \lambda_0 \leq \lambda_1 \leq \lambda_2 \leq \lambda_3 \leq 1$  and  $\sum_{i=1}^4 \lambda_i = 1$ ,  $\mathbf{U}$  is the unitary matrix conformed by the orthonormal eigenvectors ( $\mathbf{u}_i, i = 0,1,2,3$ ) of  $H$ . For each  $\mathbf{u}_i$  eigenvector associated to  $H$ , we can construct a rank=1 covariance matrix correspondent to a pure system. By considering these four pure matrices, the Spectral decomposition of  $H$  can be expressed as:

$$H = \sum_{i=0}^3 \frac{\lambda_i}{\text{tr}H} H_i; \quad H_i = (\text{tr}H)(\mathbf{u}_i \otimes \mathbf{u}_i^\dagger), \quad (2-23)$$

where  $\text{tr}H = m_{00}$ . By applying the relation between  $M$  and  $H$  (see Eq. (2-21)), we can now obtain the Spectral decomposition in terms of  $M$  (see relation in Eq. (2-23)):

$$M = \sum_{i=0}^3 \frac{\lambda_i}{m_{00}} (m_{00} \hat{M}_{ji}) = \sum_{i=0}^3 \hat{\lambda}_i (m_{00} \hat{M}_{ji}), \quad (2-24)$$

where  $\hat{\lambda}_i$  are the normalized eigenvalues of  $H$  and  $\hat{M}_{ji}$  are the normalized Mueller matrices of pure systems.

Considering these expressions, it is very interesting to reorder the terms of the Spectral decomposition in different terms representing not only pure but also non-pure (or depolarizing) systems. In this way, we can obtain the Characteristic decomposition [127] :

$$H = \frac{\lambda_0 - \lambda_1}{trH} H_0 + 2 \frac{\lambda_1 - \lambda_2}{trH} H_1 + 3 \frac{\lambda_2 - \lambda_3}{trH} H_2 + 4 \frac{\lambda_3}{trH} H_3, \quad (2-25)$$

where each one of the covariance matrices ( $H_i, i = 0,1,2,3$ ) are obtained as follows:

$$H_0 = (trH)[Udiag(1,0,0,0)U^t] = (trH)(u_0 \otimes u_0^\dagger), \quad (2-26)$$

$$H_1 = \frac{1}{2}(trH)[Udiag(1,1,0,0)U^t] = \frac{1}{2}(trH) \sum_{i=0}^1 u_i \otimes u_i^\dagger, \quad (2-27)$$

$$H_2 = \frac{1}{3}(trH)[Udiag(1,1,1,0)U^t] = \frac{1}{3}(trH) \sum_{i=0}^2 u_i \otimes u_i^\dagger, \quad (2-28)$$

$$H_3 = \frac{1}{4}(trH)[Udiag(1,1,1,1)U^t] = \frac{1}{4}(trH) \sum_{i=0}^3 u_i \otimes u_i^\dagger. \quad (2-29)$$

$H_0$  is a pure component and  $H_i$  ( $i = 1,2,3$ ) are non-pure components, with rank=1,2,3 and 4, respectively. As in the case of the Spectral decomposition, we can also obtain the Characteristic decomposition in terms of  $M$ :

$$M = (\hat{\lambda}_0 - \hat{\lambda}_1)(m_{00}\hat{M}_{J0}) + 2(\hat{\lambda}_1 - \hat{\lambda}_2)(m_{00}\hat{M}_1) + 3(\hat{\lambda}_2 - \hat{\lambda}_3)(m_{00}\hat{M}_2) + 4\hat{\lambda}_3(m_{00}\hat{M}_3), \quad (2-30)$$

$$[m_{00}\hat{M}_{J0} = M(H_0), m_{00}\hat{M}_i = M(H_i) i = 1,2,3].$$

The Characteristic decomposition allows to write the  $M$  of any depolarizer as the incoherent addition of different Mueller matrices weighted by  $H$  eigenvalues or linear combinations of them. Each one of these matrices has a physical interpretation describing polarizing ( $\hat{M}_{J0}$ ) or depolarizing properties ( $\hat{M}_1, \hat{M}_2$  and  $\hat{M}_3$ ):

- $\hat{M}_{J0}$ : represents the non-depolarizing features of the medium.
- $\hat{M}_1$ : represents the part of the medium that behaves as a 2D depolarizer, containing an equiprobable mixture of two pure components.
- $\hat{M}_2$ : represents the part of the medium that behaves as a 3D depolarizer, containing an equiprobable mixture of three pure components.
- $\hat{M}_3$ : corresponds to the part of the medium behaving as a total depolarizer ( $\hat{M}_3 = diag(1,0,0,0)$ ), a fully random component.

In order to fully describe the depolarization or non-pure characteristics of a sample, we can conveniently define a new set of metrics from combinations of the  $H$  eigenvalues, the

so-called Indices of Polarimetric Purity (IPP). In the following section we explicitly describe these parameters.

### 2.2.4.1 The Indices of Polarimetric Purity

The Indices of Polarimetric Purity are defined from  $\lambda_i$  as follows [135,136]:

$$P_1 = \frac{\lambda_0 - \lambda_1}{\text{tr}H}, \quad P_2 = \frac{\lambda_0 + \lambda_1 - 2\lambda_2}{\text{tr}H}, \quad P_3 = \frac{\lambda_0 + \lambda_1 + \lambda_2 - 3\lambda_3}{\text{tr}H}, \quad (2-31)$$

The constraints among the eigenvalues of  $H$  are translated in the IPP as:

$$0 \leq P_1 \leq P_3 \leq P_2 \leq 1. \quad (2-32)$$

Also, the eigenvalues of  $H$  can be written as:

$$\lambda_0 = \frac{1}{4} \text{tr}H \left( 1 + 2P_1 + \frac{2}{3}P_2 + \frac{1}{3}P_3 \right), \quad (2-33)$$

$$\lambda_1 = \frac{1}{4} \text{tr}H \left( 1 - 2P_1 + \frac{2}{3}P_2 + \frac{1}{3}P_3 \right), \quad (2-34)$$

$$\lambda_2 = \frac{1}{4} \text{tr}H \left( 1 - \frac{4}{3}P_2 + \frac{1}{3}P_3 \right), \quad (2-35)$$

$$\lambda_3 = \frac{1}{4} \text{tr}H (1 - P_3). \quad (2-36)$$

With this relation between the IPP and  $H$  eigenvalues described above, the Characteristic decomposition (Eq. (2-30)) can be rewritten in terms of  $P_1, P_2, P_3$  in the following way:

$$M = P_1(m_{00}\hat{M}_{J0}) + (P_2 - P_1)(m_{00}\hat{M}_1) + (P_3 - P_2)(m_{00}\hat{M}_2) + (1 - P_3)(m_{00}\hat{M}_3). \quad (2-37)$$

Therefore, these indices can be directly interpreted through the Characteristic decomposition of the system:

- **$P_1$**  quantifies the extent to which a single pure polarimetric component dominates the system. It reaches its maximum value when the largest eigenvalue is significantly greater than the others, indicating that the system behaves almost entirely as a non-depolarizing medium.
- **$P_2$**  builds on this by comparing the two largest eigenvalues to the third. When both are dominant over the third, the system presents a statistical mixture of two



distinct pure polarimetric behaviors, this incoherent addition introducing depolarization which is associated with a two-dimensional polarimetric space (two significant eigenvalues).

- $P_3$  measures the combined contribution of the first three eigenvalues relative to the fourth. A high  $P_3$  value suggests that part of the system's behavior can be described using only three pure components, this introducing depolarization associated with a three-dimensional polarimetric sub-space (three significant eigenvalues), and with minimal contribution from fully random depolarization.

It is also interesting to consider the fraction,  $1 - P_3$ , represents complete randomness—where any information related to the input polarization is lost.

To exemplify this relation of the Characteristic decomposition of  $M$  with the IPP, some representative cases are further analyzed with the help of following Table 2-1:

$P_1$	$P_2$	$P_3$	$M$	Characteristics
1	1	1	$m_{00}\hat{M}_{J0}$	pure Mueller matrix
0	1	1	$m_{00}\hat{M}_1$	only 2D depolarizer
0	0	1	$m_{00}\hat{M}_2$	only 3D depolarizer
0	0	0	$m_{00}\hat{M}_3$	pure depolarizing component

Table 2-1 Table showing the elements of the  $M$  Characteristic decomposition in terms of possible IPP values.

With this table we can clearly see the relation between the IPP and the different depolarization sources conforming the Characteristic decomposition of the Mueller matrix. For intermediate values of the IPP, depolarization is divided into different terms of the decomposition. In Chapter 4 we will deeply inspect the interest of this decomposition for depolarization behavior analysis.

It is also interesting to relate the IPP with the depolarization index ( $P_\Delta$ ) [128,137]:

$$P_\Delta = \sqrt{\frac{2P_1^2}{3} + \frac{2P_2^2}{9} + \frac{P_3^2}{9}}, \quad (2-38)$$

From Eq. (2-38) we can see that different combinations of IPP can lead to the same value for  $P_\Delta$  [138]. Therefore, it is clear the interest on inspecting the IPP parameters when studying depolarization of samples, as a more comprehensive source of information [118].

### 2.2.5 Summary

To summarize, in section 2.2 we have shown several methods to decompose the Mueller matrix to extract the polarimetric characteristics related to physical properties of samples. These properties are divided into three main groups: dichroism, depolarization and birefringence. In the following tables we summarize all the polarimetric observables extracted from  $M$  as well as a brief description.

Dichroism		
Diattenuation ( $D$ ) [123,124]	$D =  \mathbf{D}  = \frac{\sqrt{m_{01}^2 + m_{02}^2 + m_{03}^2}}{m_{00}}$ ( $0 \leq D \leq 1$ )	Selective absorption of polarized light depending on the incident polarization state of light.
Arrow Diattenuation ( $D_A$ ) [110,132]	$D_A \equiv m_{Ri} D$ ( $0 \leq D_A \leq 1$ )	
Polarizance ( $P$ ) [123,124]	$P =  \mathbf{P}  = \frac{\sqrt{m_{10}^2 + m_{20}^2 + m_{30}^2}}{m_{00}}$ ( $0 \leq P \leq 1$ )	Selective polarization of light into a particular polarization state.
Arrow Polarizance ( $P_A$ ) <sup>60,69</sup>	$P_A \equiv m_{Ro}^T P$ ( $0 \leq P_A \leq 1$ )	

Table 2-2 Table summarizing the principal dichroic features of  $M$ .

Birefringence		
Total retardance ( $\Delta$ ) [123,124]	$\Delta = \cos^{-1} \left  \frac{\text{tr}(m_{Ri})}{2} - 1 \right $ ( $0 \leq \Delta_i \leq \pi$ )	Phase change introduced between the components of light without intensity attenuation.
Azimuth angle ( $\varphi_R$ ) [123,124]	$\varphi_{Ri} = \frac{1}{2} \tan^{-1} \left( \frac{m_{Ri31} - m_{Ri13}}{m_{Ri23} + m_{Ri32}} \right)$ ( $0 \leq \varphi_{Ri} < \pi$ )	Azimuth angle of total retardance in the Poincaré Sphere.
Ellipticity angle ( $\chi_R$ ) [123,124]	$\chi_{Ri} = \frac{1}{2} \sin^{-1} (R_i (m_{Ri12} - m_{Ri21}))$ ( $-\pi/4 \leq \chi_{Ri} \leq \pi/4$ )	Ellipticity angle of total retardance in the Poincaré Sphere.
Linear retardance ( $\delta$ ) [133]	$\delta_i = \cos^{-1} \left( \sqrt{(m_{Ri11} + m_{Ri22})^2 + (m_{Ri21} - m_{Ri12})^2} - 1 \right)$	Phase change introduced between the linear polarized components of light without intensity attenuation.
Optical rotation ( $\psi_i$ ) [133]	$\psi_i = \tan^{-1} \left( \frac{m_{Ri21} - m_{Ri12}}{m_{Ri11} + m_{Ri22}} \right)$	Optical rotation of the linear retarder.

Table 2-3 Table summarizing the principal birefringent features of  $M$ .

Depolarization		
Depolarization Index ( $P_\Delta$ ) [127,128]	$P_\Delta = \sqrt{\frac{P^2}{3} + \frac{D^2}{3} + P_S^2} = \sqrt{\frac{2P_1^2}{3} + \frac{2P_2^2}{9} + \frac{P_3^2}{9}},$ ( $0 \leq P_\Delta \leq 1$ )	Overall depolarization capacity of the sample.
Spherical Purity ( $P_s$ ) [129]	$P_s = \frac{\ m\ _2}{\sqrt{3}}, (0 \leq P_s \leq 1)$	Connects depolarization with birefringent sources.
Arrow parameters ( $a_1, a_2, a_3$ ) [110,132]	$m_A = \text{diag}(a_1, a_2, \epsilon a_3),$ $1 \geq a_1 \geq a_2 \geq a_3 \geq 0$	Depolarization information mixed with dichroic characteristics.
Indices of Polarimetric Purity ( $P_1, P_2, P_3$ ) [135,136]	$P_n = \frac{1}{trH} \sum_{k=1}^n k(\lambda_{k-1} - \lambda_k), k = 1,2,3$ $0 \leq P_1 \leq P_3 \leq P_3 \leq 1$	Depolarization capability of samples, each one of the indices can be related to different depolarization sources.

Table 2-4 Table summarizing the principal depolarization features of  $M$ 

## 2.3 Polarimetric Spaces

As evidenced in the state of the art [61–65,75–77], with some contributions within the framework of this thesis [112,118,139], the relation between the polarimetric observables and physical properties of the samples lead to excellent results in terms of discriminatory capability of polarimetric techniques based on the Mueller matrix analysis. For instance, biological tissues are complex structures with spatial variations of their physical properties due to different intrinsic compositions, densities and/or organization. Interestingly, pathologies usually change the internal structure of the tissue, and these changes can be detected by means of polarimetry. In recent years, the above-described polarimetric observables have been used for the study, detection and classification of structures of interest in biological tissues, paving the way for applications in the early detection of pathologies [41,76,140,141].

Among the different observables proposed in the specialized literature, depolarization related metrics have demonstrated excellent results in the study of a vast number of biological tissue samples [73–77,140]. This ability of depolarizing metrics, such as the IPP and the CP parameters, to characterize and distinguish between biological structures, makes them particularly appealing for grouping them in the construction of depolarization spaces, by associating, for instance, a specific observable with each Cartesian axis. This idea led to the generation of different 3D polarimetric spaces [124,136], arising as excellent visual tools aiding identification and classification of different tissue types. That is, different

samples featuring different polarimetric properties will occupy different positions within the volumes associated with such polarimetric spaces.

In this section we focus on two depolarizing spaces specially interesting for biological sample studies: the IPP or Purity Space (conformed by  $P_1$ ,  $P_2$  and  $P_3$ ) and the Components of Purity Space (conformed by  $D$ ,  $P$  and  $P_S$ ). Since these pair of triplets are mutually related by certain constraints, it is worth representing them graphically in order to get a visual representation of the volume that different experimental Mueller matrices can occupy.

### 2.3.1 Purity Space

The Purity Space is the volume generated by the triplet  $(P_1, P_2, P_3)$ . The constraints among the three variables (see Eq. (2-32)) generate a tetrahedron containing all physical realizable depolarizers inside its volume [124,136]. Figure 2-2 provides a representation of the Purity Space, where the  $P_3$  metric corresponds to the z axis (height of the tetrahedron) and  $P_1$  and  $P_2$  correspond to the x and y axes, respectively.

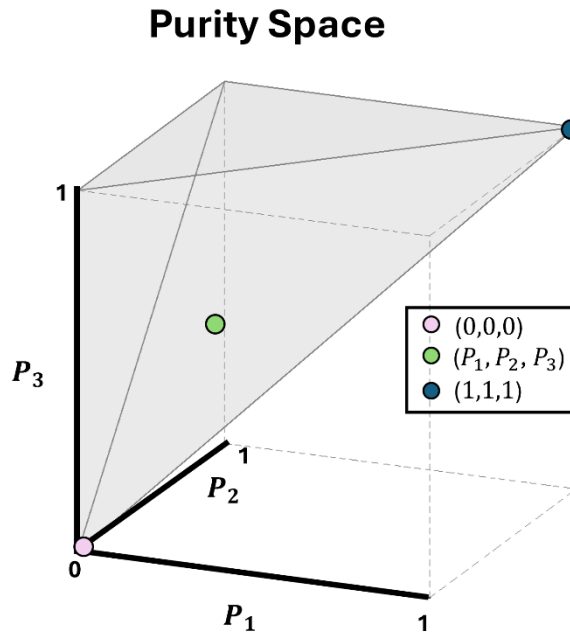


Figure 2-2 Representation of the IPP Space, where all the physically realizable depolarizers are contained.

In Figure 2-2 we provide a representation of the Purity Space. The points illustrated in the tetrahedron represent three different samples: the blue point corresponds to a pure, non-depolarizing system ( $P_1 = P_2 = P_3 = 1$ ) that is located to a vertex within the top face of the figure (this is the only point in the space which does not represent a depolarizer).

The purple point represents an ideal depolarizer ( $P_1 = P_2 = P_3 = 0$ ) (any input polarization is fully depolarized), which is located at the origin and, lastly, the green point ( $0 \leq P_1 \leq P_2 \leq P_3 \leq 1$ ) represents a partial depolarizer (the depolarization induced to incident light depends on the input state of polarization).

It is worth noting that,  $P_1$  and  $P_2$  set the position of the depolarizer in a plane for a constant value of  $P_3$  and,  $P_3$  represents the height of such a plane in the Purity Space ( $z$  axis). Under this scenario, giving a value of  $P_3$ , the possible values that the other two IPP,  $P_1$  and  $P_2$ , are allowed to achieve decrease as  $P_3$  gets close to (0,0,0), as evidenced by the constrain given in Eq. (2-32).

### 2.3.2 Components of Purity Space

In analogy to Purity Space, we can also define a space conformed by the Components of Purity. These variables constitute the Components of Purity Space or Purity Figure, which contains complementary information about the depolarization properties of a sample [142]. The CP space consists of: diattenuation ( $D$ ), polarizance ( $P$ ) and the degree of spherical purity ( $P_S$ ) metrics. The Components of Purity space represents a volume where all the possible depolarizers are contained. The constraint between the three components (see Eqs. (2-8) and (2-9)) giving rise to this space is the following [129]:

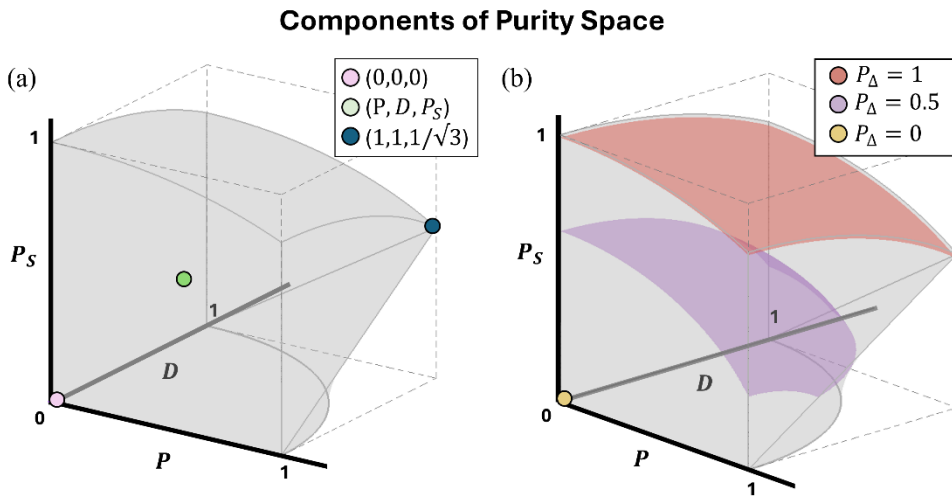


Figure 2-3 Representation of the volume generated by the CP triplet, leading to the Components of Purity Space. In (a) different points are represented in the volume, correspondent to three polarimetric scenarios. (b) shows surfaces which correspond to constant values of  $P_\Delta$ ; red, purple and yellow surfaces correspond to  $P_\Delta$  values of (1, 0.5, 0).

$$P^2 + D^2 \leq 1 + 3P_S^2 . \quad (2-39)$$

Figure 2-3 (a) represents the volume generated by the CP triplet  $(P, D, P_S)$ . These parameters are related to dichroic and birefringent parameters of  $M$ . The CP provide complementary depolarization information with respect to the IPP. From the IPP we can extract the depolarization capability and depolarizing anisotropies (depolarization capability with respect to the input SoP) of the samples and study the weight of different depolarizing sources leading to depolarization. Additionally, the CP are also capable of relating measured depolarizing values with non-depolarizing sources (and related physical features) originating such depolarization (in Chapter 4 we explain how incoherent combination of pure elements can produce depolarization). In Figure 2-3 (a) we represent three cases: blue point  $(1,1,1/\sqrt{3})$  corresponds to a system with depolarization; the pink point  $(0,0,0)$  represents a pure depolarizer and, green point  $(P, D, P_S)$  represents a system where both dichroism and birefringence share the depolarizing effect.

In addition, in Figure 2-3 (b) we present the Components of Purity Space where different surfaces of constant  $P_\Delta$  values are shown. Since the CPs are related by the Depolarization Index metric, representing the total amount of depolarization present in a sample, it is interesting to study how the points in the CP Space are located depending on this parameter.  $P_\Delta = 1$  represents the case of no-depolarization, being the higher surface in the figure (red surface in Figure 2-3 (b)). Whereas, as more depolarization is present in the sample ( $P_\Delta$  decrease), the correspondent surface in the figure decreases until the limit point  $P_\Delta = 0$ .

Further analysis of the relationship between these spaces has been done by A. Van Eeckhout in [143]. Moreover, section 2.3 and Chapter 6 we show the utility of both spaces (or metrics comprising the spaces) for the discrimination of different tissues within a sample, explicitly demonstrating the potential of 3D Depolarization Spaces for the classification of biological structures.



## Chapter 3 Materials and Methods

In this chapter we present the materials and methods of this thesis. Firstly, section 3.1 presents the experimental procedure used to obtain the experimental Mueller matrices. The experimental set-up of the Complete Mueller matrix polarimeter is explained in subsection 3.1.1, where all the optical elements comprising the set-up are introduced. Then, subsection 3.1.2 explains the calibration and optimization procedure of the polarimeter. Lastly, subsection 3.1.3 shows how, once we have the set-up calibrated, which is the protocol to obtain the experimental Mueller matrices of the samples under measurement. In addition, in section 3.2 we provide a detailed anatomical description of the biological samples analyzed through this work. These samples correspond to *ex-vivo* heart, tongue and brain sections from cow and cattle specimens and *ex-vivo* human brain samples.

### 3.1 Complete Image Mueller polarimeter

In this subsection, we describe the experimental set-up of the imaging Mueller polarimeter, as well as its calibration and optimization procedures. This system being the main device used for obtaining the Mueller matrix measurements of the samples studied.

#### 3.1.1 Experimental set-up

To obtain the experimental  $M$  of the samples inspected in this text we use a complete image Mueller polarimeter prototype developed at the Optics Group of the UAB. These kinds of polarimeters are comprised by two main parts: the polarization state generator



(PSG) and the polarization state analyzer (PSA), which allow us to control the generation and analysis, respectively, of the state of polarization of light illuminating or exiting the sample.

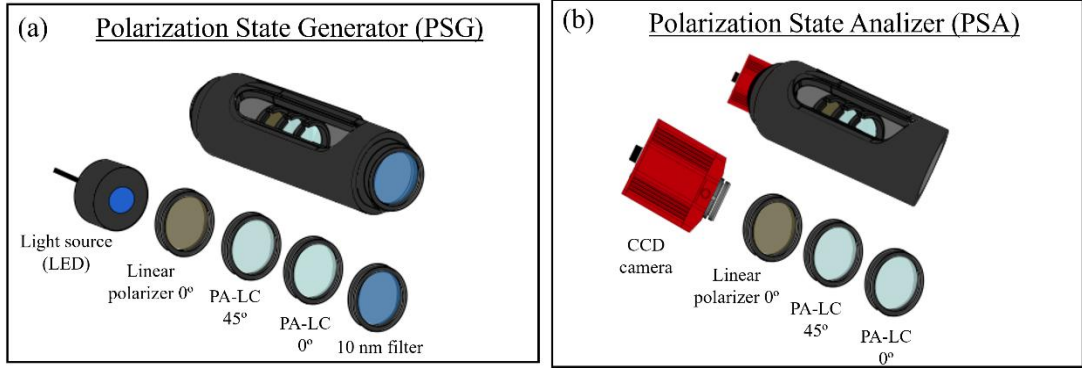


Figure 3-1 Representation of the polarization state generator (PSG; a) and polarization state analyzer (PSA; b) optical components arrangement.

The PSG (Figure 3-1 (a)) is comprised of a linear polarized oriented at 0° with respect to the laboratory vertical and two parallel aligned liquid crystal (PA-LC) retarders oriented at 45° and 0°, respectively. By modelling this system with the Mueller-Stokes formalism, the following out Stokes vector is obtained [124]:

$$\mathbf{S} = DoP \begin{pmatrix} 1 \\ \cos 2\varphi \cos 2\chi \\ \sin 2\varphi \cos 2\chi \\ \sin 2\chi \end{pmatrix}, \quad (3-1)$$

where  $\varphi$  and  $\chi$  are the polarimetric angles (azimuth and ellipticity of the polarization ellipse, respectively). We can note that such a vector is defined in sphere coordinates, where any point at the surface of the Poincaré sphere (see section 2.1.2) is obtained by setting the proper values of  $(\varphi, \chi)$ . Under such scenario, any fully polarized Stokes vector can be generated by properly addressing the voltages to the PA-LC. This requires proper calibration of the polarimetric elements as explained in the following sub-section.

In the case of the PSA (Figure 3-1 (b)), the elements conforming this system are the same as in the PSG but located in inverse order. Again, by properly setting the voltages to the PA-LCs within the PSA, any fully polarized SoP can be set as analyzer (i.e., as polarization

where the polarization of the light exiting from the sample is projected). As in the case of the PSG, for adequate operation of the PSA, it requires adequate experimental calibration.

Moreover, the system also includes a CCD camera located after the PSA system, allowing the imaging capability to the polarimeter. The CCD camera has incorporated an objective lens at the entrance of the camera, which allows to image the sample to the CCD. Under this optical scheme, we can obtain the intensity distribution (image) of the sample corresponding to different combinations of PSG-PSA polarizations. As it explained in more detail in following subsections, by using a proper set of PSG-PSA polarizations combinations, after having been calibrated, the Mueller image of the sample can be retrieved from corresponding intensity images acquired at the CCD.

In addition, the system is provided with a LED (Light Emitting Diode) light source located before the PSG for illumination of the sample; this source can work at four illumination wavelengths in the visible range (625 nm, 530 nm, 590 nm and 470 nm) allowing to inspect different characteristics of the samples. This capability is very interesting as the Mueller matrix of samples (i.e., the light-matter polarimetric interaction) depends on this parameter. For instance, light penetration depth in biological samples or samples birefringence depends on the illumination wavelength. As an example, the penetration length of visible light (400 nm – 750 nm) in human skin varies from 0.01 mm to 1 mm [9]. Both arms comprising the polarimeter are located in rotation stages, therefore the angle configuration for the measures can be changed. This is another crucial parameter as Mueller matrices also depends on this parameter (note that the optical path within the samples, or the Fresnel coefficients, changes with the measuring configuration). In this work, we set a reflection configuration for measuring light exiting from samples. It should be noted that most biological tissues are opaque, which prevents transmission-based measurements in most cases, except, for instance, in the case of certain thin-layer histological sections. In most measurements provided in this thesis, the measuring configuration used corresponds to: the sample is illuminated with the PSG located at  $34^\circ$  with respect to the laboratory horizontal and the PSA is located at  $0^\circ$  with respect to the laboratory vertical to avoid direct reflections. This configuration avoids ballistic measurements and focuses on light scattered by samples, this being of interest in biological samples analysis. A 3D schematic representation and a photographic image of the set-up are shown in Figure 3-2 (a) and (b) respectively.

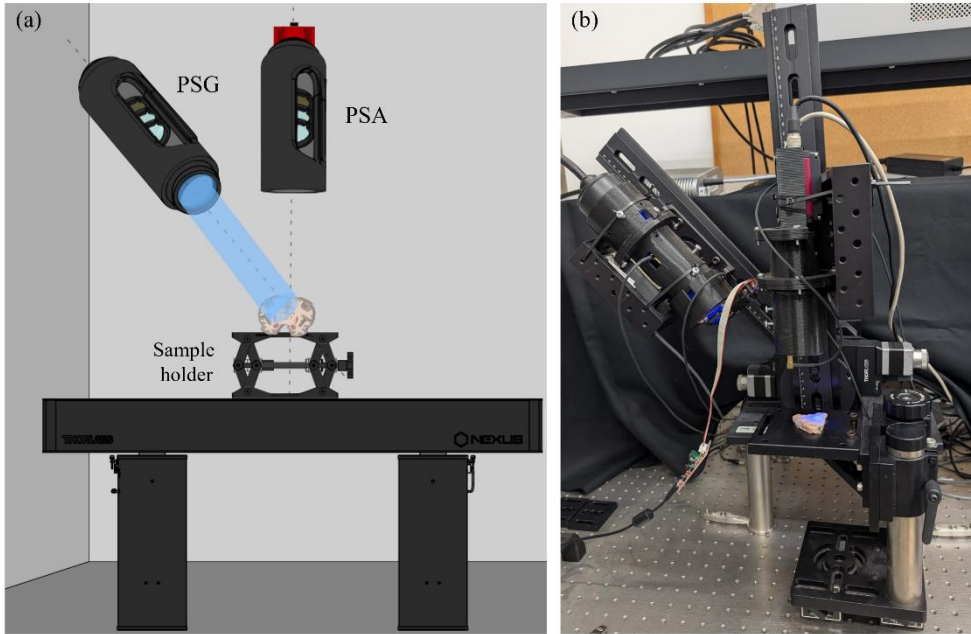


Figure 3-2 Representation of the complete image Mueller polarimeter at scattering configuration; (a) schematic image and (b) photographic image.

In the following, we also provide commercial information about the components comprising the polarimeter: the illumination is provided by a Thorlabs LED source (LED4D211, operated by DC4104 drivers distributed by Thorlabs) complemented with a 10 nm dielectric bandwidth distributed by Thorlabs: FB530-10 and FB470-10 for green and blue wavelengths, respectively. The linear polarizer located in the PSG is a Glam–Thompson prism-based CASIX whereas the one placed in the PSA is a dichroic sheet polarizer distributed by Meadowlark Optics. The four PA-LC retarders are variable retarders with temperature control (LVR-200-400-700-1LTSC distributed by Meadowlark Optics). Finally, imaging is performed by means of a 35 mm focal length Edmund Optics TECHSPEC® high resolution objective followed by an Allied Vision manta G-504B CCD camera, with 5 Megapixel GigE Vision and Sony ICX655 CCD sensor, 2452(H)×2056(V) resolution, and cell size of  $3.45\mu\text{m} \times 3.45\mu\text{m}$ , so a spatial resolution of  $22\mu\text{m}$  is achieved.

### 3.1.2 PSG and PSA calibration and optimization

In this section, we briefly describe the procedure to calibrate the experimental set-up to minimize the experimental errors affecting the measurements and optimizing the obtention of accurate Mueller matrix images.

To determine the experimental  $M$  of a sample by means of the mentioned set-up, at least 16 radiometric measurements are required, as we are dealing with  $4 \times 4$  real matrices. These radiometric measurements correspond to four well-determined input and output states of polarization. The illumination and analyzing SoPs are set by the PSG and PSA, respectively (see Figure 3-3). In our measurements, we add redundancy data to reduce statistical noise, as shown in Ref. [144]. We generate 6 states of polarization for generation and the same states for analysis (we use 36 measurements instead of the minimum required 16 measurements). The specific 6 SoPs basis used in this work is represented in Figure 3-3 at the surface of the Poincaré sphere, and it is a well-known basis in specialized literature for its suitability to conduct polarimetric metrology [145]. It includes four linear polarizations ( $0^\circ$ ,  $45^\circ$ ,  $90^\circ$  and  $135^\circ$  orientations) and two circular (left and right) handed polarizations, corresponding to the poles of the sphere. In Ref. [144] it is demonstrated that the bases with lower noise amplification are those where the SoPs are distributed uniformly over the surface of the Poincaré Sphere, and the rhombohedron set by this polarimetric basis (see Figure 3-3) accomplishes this condition, being a Platonic solid [145].

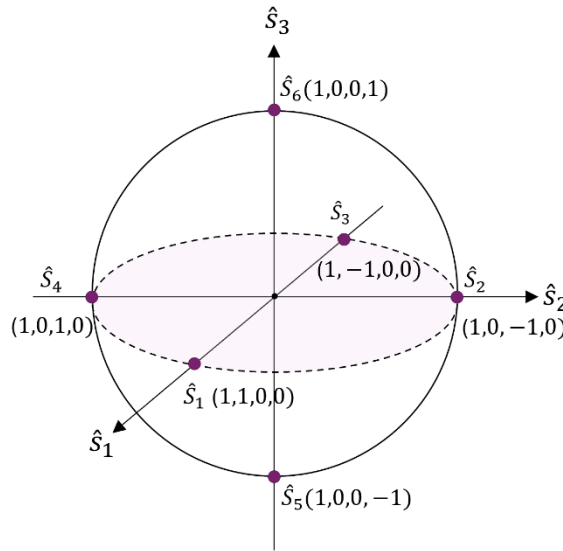


Figure 3-3 Representation of the Poincaré sphere with an ideal calibration basis. Polarimetric states  $\hat{S}_1$ ,  $\hat{S}_2$ ,  $\hat{S}_3$  and  $\hat{S}_4$  are the four linear polarized states distributed in a uniform way in the equator of the sphere.  $\hat{S}_5$  and  $\hat{S}_6$  represent the two circular polarized states.

The method for calibrating the PSG aims experimentally generating the 6 above-stated SoPs as close as possible to the ideal ones. These desired SoPs form the generation base  $S_G$ ,

4x6 matrix consisting of the 6 input generators. The calibration procedure is performed with the aid of a commercial Thorlabs polarimeter (PAX5710VIS-T) as reference. The elements comprising the PSG allow us to generate any fully polarized SoP and, with the commercial polarimeter we are able to test the exact state that we are experimentally generating. Therefore, the procedure consists of changing the voltages controlling the PA-LC within an iterative approach until achieving the desired SoPs. The Thorlabs polarimeter also allows us to obtain the exact experimental SoP values, this ensuring accurate polarimetric metrology.

In turn, the calibration of the PSA is conducted by illuminating the PSA with the previously calibrated PSG states ( $S_G$ ) and retrieving the experimental analyzers base ( $S_A$ ) by following an inversion method [143].

The PSG is located directly illuminating the PSA (i.e., in transmission configuration where the PSG is in front of the PSA). This process can be described as:

$$I = S_A M_{air} S_G, \quad (3-2)$$

where  $M_{air}$  is the Mueller matrix of the air (i.e., no-sample place between PSG and PSA systems) and  $I$  is a matrix containing the radiometric measurements related to all the PSG-PSA polarization configurations used. Considering the ideal value for  $M_{air}$ ,  $M_{air} = \text{diag}(1,1,1,1)$ , we can obtain the analyzers base as:

$$S_A = I \cdot (\tilde{S}_G^{-1}). \quad (3-3)$$

With this, we obtain the 6 polarization analyzers (rows in  $S_A$  matrix) we set with the PSA. The next step of the calibration process is to check if the obtained SoPs correspond with the desired ones. If the values do not correspond with the ones conforming the optimal base described above, we conduct an iterative approach by varying the voltages of the PSA PA-LC until achieving those experimentally obtained analyzers as close as possible to the theoretical ones.

Of course, the calibrated values for  $S_A$  and  $S_G$  are not exactly the ideal SoPs due to experimental issues. Therefore, to evaluate how optimal are the experimental PSG and PSA bases we obtained, we use the Condition Number (CN) as a figure of merit [146]. Condition Number analyzes how far a matrix is from a singular matrix and it is connected to its error amplification after the inversion [147]. For a given matrix  $X$ , the  $CN$  is obtained as:

$$CN = \|X\|_2 \cdot \|X^{-1}\|_2, \quad (3-4)$$

where  $\| \cdot \|_2$  represents the Frobenius. Even mathematically the minimum value of  $CN$  (optimum in terms of noise amplification) is equal to  $CN=1$ , corresponding to orthogonal matrices  $U$  ( $\text{norma2}(U) = \text{norma2}(U^{-1}) = 1$ ), due to restrictions of Stokes vectors in polarimetric systems, the ideal value is  $CN = \sqrt{3} \sim 1.73$  [148], correspondent to polarimetric matrices as far as possible from singularity. Therefore, after the described calibration process for the PSG and PSA, the experimental condition number of  $S_A$  and  $S_G$  is evaluated. The values obtained for the  $CN$  in the measurements presented in this manuscript oscillate between 1.85-1.95, these values considered excellent  $CN$  values and ensuring a high-quality performance of the polarimeter. In this way, PSG and PSA are optimized for the reduction of error amplification to the calculated  $M$  elements. This optimization process is performed before every set of experimental measurements, and if the  $CN$  value is not acceptable, the calibration process is repeated.

Importantly, this calibration process, both for PSG and PSA is conducted for all the used wavelengths. The retardance of the liquid crystals depends on the illumination wavelength therefore, the values of the voltages to obtain the generators and analyzers variate between them.

In addition to this calibration of the experimental system, the conditions of measurement in the laboratory are adapted to minimize any kind of external noise source. For instance, the measurements are carried out in a totally dark room, where the only light recorded by the camera is the polarized light generated by the PSG that interacts with the sample. Also, to eliminate the thermal noise or any electrical noise that can affect the intensity measurement of the pixels in the camera, before each measurement we took a background image; that is, an image of the pixel value in the camera when the illumination light is off. These values are subtracted from the sample intensity images measured before the obtention of the Mueller matrices.

### 3.1.3 Polarimeter Measuring Principle: Measurement of the Mueller images

For the experimental obtention of  $M$ , we consider that the polarization of the light illuminating the sample ( $S_G$ ) is modified by the polarimetric characteristics of the sample ( $M_{Sample}$ ), resulting in a new state of polarization that is projected into the different

analyzers ( $S_A$ ) set by the PSA, leading to a collection of intensity measurements. Mathematically, this situation can be written as:

$$I = S_A M_{Sample} S_G, \quad (3-5)$$

where  $I$  is a 6x6 intensities matrix related to the 36 possible combinations of  $S_A$  and  $S_G$  systems. To obtain the measure of  $M_{Sample}$ , we perform the pseudo-inverse matrices of  $S_G$  and  $S_A$ :

$$M_{Sample} = (\tilde{S}_A^{-1}) \cdot I \cdot (\tilde{S}_G^{-1}), \quad (3-6)$$

where  $\tilde{S}_A^{-1}$  and  $\tilde{S}_G^{-1}$  are the pseudo-inversed matrices of  $S_A$  and  $S_G$ , respectively. The pseudo-inverse form of matrix  $X$  can be given by:

$$\tilde{X}^{-1} = (X^T X)^{-1} X^T, \quad (3-7)$$

$$\tilde{X}^{-1} = X^T (X X^T)^{-1}. \quad (3-8)$$

Depending on the properties of  $X$ , where (3-7) corresponds to the left inverse ( $\tilde{X}^{-1} X = I$ ) and (3-8) is a right inverse ( $X \tilde{X}^{-1} = I$ ).

For the calculation of the pseudo-inversed matrix and further obtention of  $M_{Sample}$ , it is important to study the singularity of the matrices. This property of matrices can be characterized by means of the  $CN$  obtained in the calibration process.

## 3.2 Sample description

In this section we provide a detailed anatomical description of the different samples analyzed through this work. In section 5.2 we show the polarimetric results obtained for three *ex-vivo* animal samples. The animal samples correspond to two regions of heart and tongue from an *ex-vivo* cattle, obtained from a local slaughterhouse. In Chapter 6 we focus our attention on the brain; the inspected samples correspond to both fresh animal tissue and formalin fixed human tissue. The anatomical description of the two groups of samples is provided in subsections 3.2.1 and 0, respectively.

### 3.2.1 Heart and tongue samples

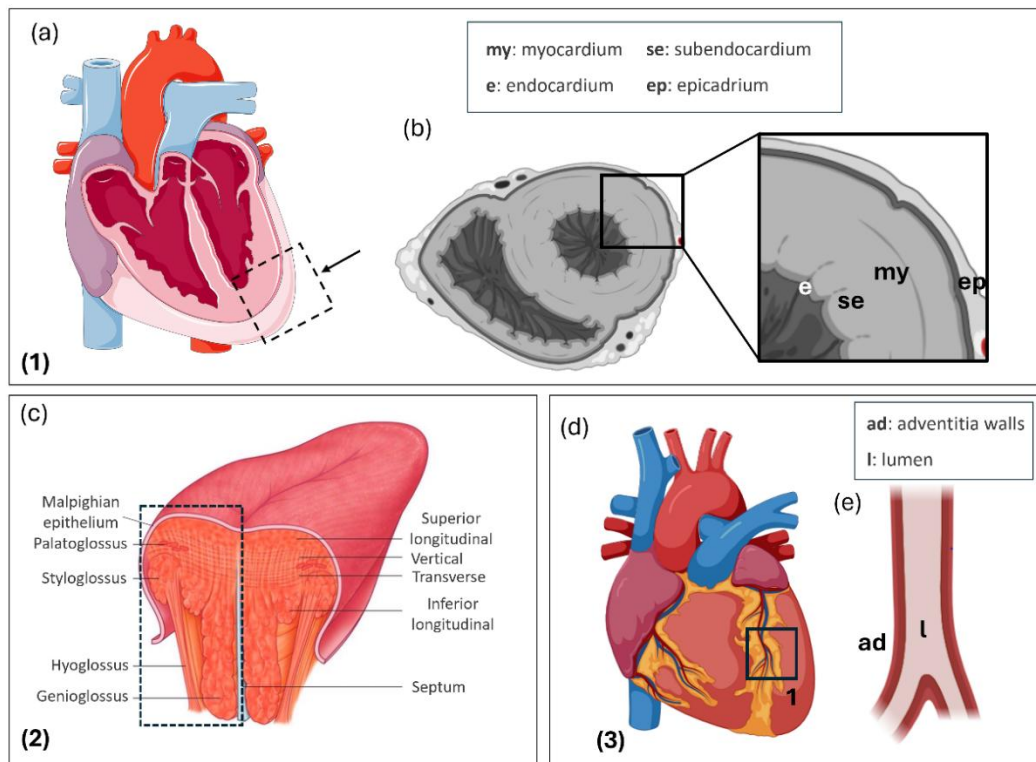


Figure 3-4 Anatomical context for measurements shown in section 5.2 depicted in humanized schematic drawings. (1) and (3) correspond to the sections of ex-vivo cattle heart, representing a transversal and an external section. (2) corresponds to the ex-vivo cattle tongue, where the region inspected is a transversal section. Figures obtained created with BioRender.com.

In Figure 3-4 (a) we show a coronal cut of a mammalian heart where the region marked by the black dashed rectangle corresponds to the section in (b). This part of the heart shows the direction of a section of both ventricles transverse to the heart axis resulting in an image close to the one depicted in (b). In this image the left ventricle appears lined by the endocardium (*en*) and surrounded by the subendocardium (*se*), the myocardium (*my*) and the epicardium (*ep*).

The tongue sample is shown in Figure 3-4 (c), the black dashed rectangle corresponds to the part of the tissue analyzed in section 5.2. This corresponds to a transversal section of the tissue shown in frontal view. In the image we can observe all the muscles comprising the tongue anatomy, the layer recovering all the tongue structure which is a kind of epithelium called Malpighian epithelium and the central part of the tongue which is the septum formed by myotendinous tissue.



Figure 3-4 (d) shows a frontal view of a mammalian heart showing the interventricular sulcus containing the interventricular branch of the left coronary artery surrounded by subepicardial fatty tissue. (1) Indicates the location of a longitudinal section of the coronary vessel, shown in (e), where (l) and (ad) correspond to its lumen and adventitia (external wall) respectively.

The thickness of the samples is around 2 cm in the case of the heart and tongue samples. Note that the length of light is significantly lower than the thickness and all the measurements presented in this work were done in the reflection configuration of the system shown in Figure 3-2.

### 3.2.2 Brain samples

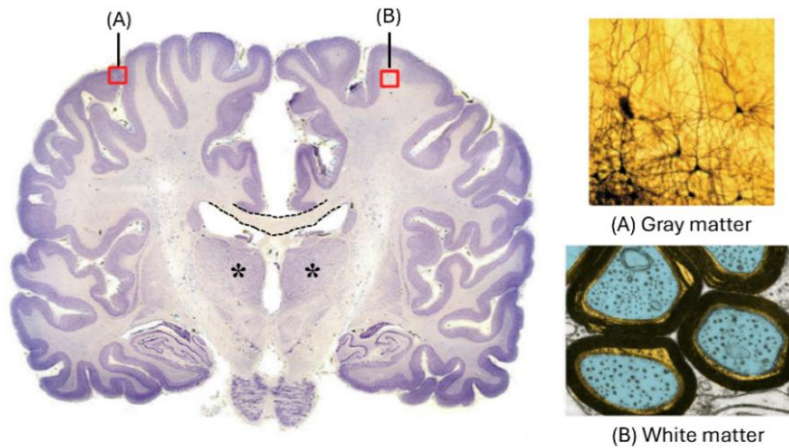


Figure 3-5 Histology of a coronal section of human brain where we can differentiate between gray matter (A), white matter (B), the corpus callosum delimited by the black dashed lines and the thalamus marked with the black arrows. (A) Golgi-stained pyramidal cells of the gray matter and (B) to electron microscopy image of the white matter axons and myelin shell. Image adapted from<sup>146,147</sup>.

The brain can be divided into two main regions: the gray matter (or cortex) and the white matter. Gray matter (*gm*) is a 2-4 mm thick outer layer of the brain, conformed by cell bodies of neurons. At the same time, this layer is divided into different sub-layers corresponding to different brain functionalities and connections. In contrast, white matter (*wm*) is a more fibered structure composed of axons linked together that form fiber tracts that are related to brain functions, such as memory, vision or voluntary movement.

### White matter

White matter is composed of bundles, which connect various gray matter areas of the brain to each other and carry nerve impulses between neurons. The exploration of white matter directionality is of high potential in fundamental studies but also for the detection of various neurological diseases directly related to brain connectivity. Variations in *wm* associated to schizophrenia, chronic depression, bipolar disorder, obsessive-compulsive disorder, Alzheimer's disease, and post-stroke diaschisis [106,107].

Corpus callosum is a region of the brain connecting the cerebral hemispheres and it is composed of white matter tracts (see black dashed lines in Figure 3-5). The primary function of the corpus callosum is to integrate and transfer information from both cerebral hemispheres to process sensory, motor, and high-level cognitive signals [149].

### Gray matter

Gray matter plays the most significant part in allowing humans to function normally daily. It is formed by many neurons, allowing to process and release new information through axon signaling found in white matter. The *gm* throughout the central nervous system allows to make connections between different parts of the brain and thus, it is responsible for muscle movement and sensory information, among others. We can identify six different sub-layers within *gm*. Layers in *gm* are named by roman numbers, from I (being the most outer layer) to VI (being the inner layer, just before *wm*). In the following we describe the composition and functionality of each layer [150]:

- **Layer I:** also called molecular layer, includes thalamocortical ascending projections and intercortical connections, appears weak on staining due to its relative paucity of cells [151].
- **Layer II/III:** both are formed by poorly delineated laminae of highly heterogeneous excitatory neurons involved cortico-cortical connections, including interhemispheric ones [152].
- **Layer IV:** also known as internal granular layer, is populated by relatively medium sized rounded excitatory neurons that receives afferent (ascending) sensory inputs (visual, auditory, somatosensorial) in many cases from the sensory relay nuclei of the thalamus.
- **Layer V:** the internal pyramidal layer, populated by large projection cells, that convey the main extra-cortical outputs.

- **Layer VI:** Thalamo-cortical reciprocal connections input, and cortico-cortical connections that include both short-range U-shaped connections and longer horizontal axons through the deep cortical layers [150,153,154].

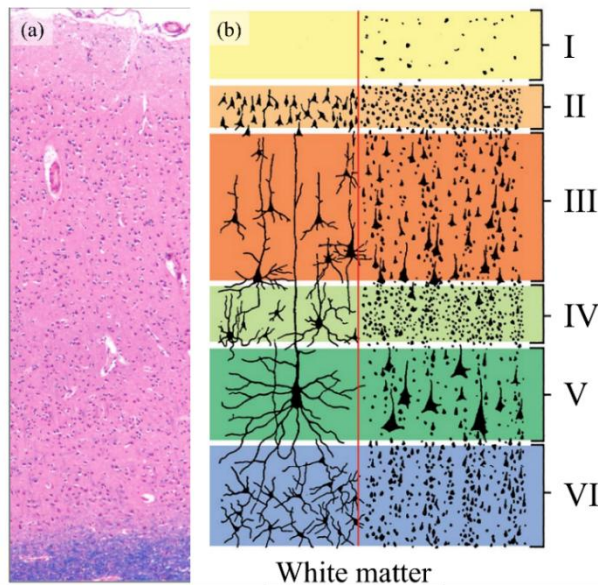


Figure 3-6 (a) Histology of a brain showing mainly the layers of neocortical gray matter. (b) Schematic picture of the location and composition of layers I to VI in gray matter.

The study of the cortical area of the brain and the detection of the different layers can be very useful in the study and/or early detection of some neurodegenerative disorders. For instance, Alzheimer's disease primarily affects periallocortical areas and then spreads to further neocortical areas interrupting the flux of information from the sensory neocortex to the temporal allocortex and the prefrontal neocortex that is essential for situational awareness and memory formation. Damage to the cortices of temporal lobe results in semantic dementia, which is the loss of memory of information (semantic memories). Also related to disruptions in the temporal cortical layering are some forms of epilepsy. Finally, the hippocampus (i.e the archicortex) is a long ridge of gray matter tissue located into the medial temporal lobe of the brain and is responsible for memory and learning. Atrophies of human hippocampus can be related to Alzheimer's disease, depression and schizophrenia [108].

In addition to the cortical structures, the telencephalon is composed of the basal ganglia (caudate nucleus, putamen and globus pallidus) that form reciprocal circuits with the

cortex and are primarily involved in movement and emotional regulation. Deep in the encephalic mass is the diencephalon, composed by the hypothalamus, the epithalamus, the thalamus and the subthalamus, the latter also involved in the motor regulation circuit. Thalamus is a large mass of gray matter located on the lateral wall of the third ventricle (see the asterisks in Figure 3-5). The nerve fibers of the thalamus project out to the cerebral cortex in all directions, connecting the information between different subcortical areas and the cerebral cortex. It plays an important role in the regulation of sleeping and consciousness or many of the sensory systems, such as the visual, auditory and gustatory systems.

### 3.2.2.1 Brain samples analyzed in this work

The fresh brain sections correspond to animal samples (*ex-vivo* cow and cattle specimens).

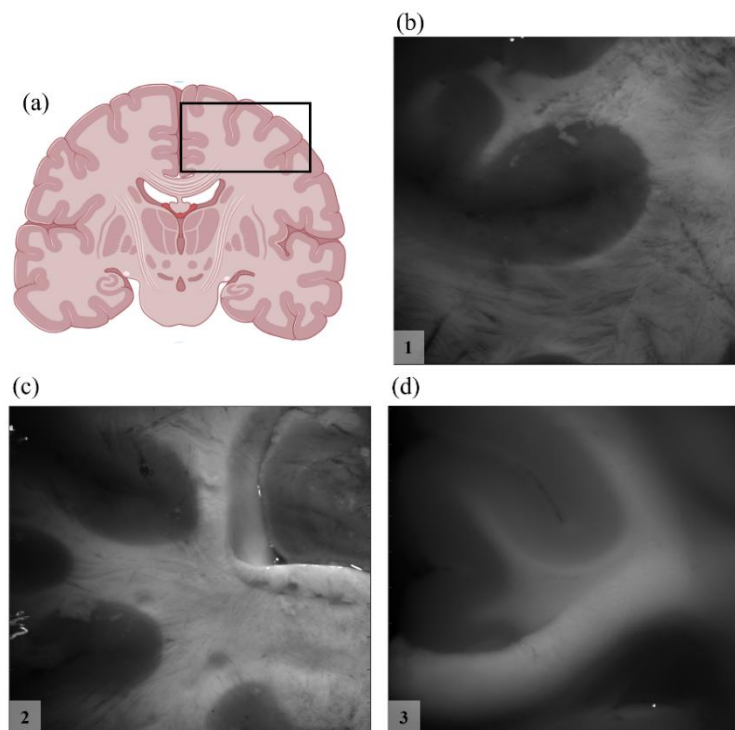


Figure 3-7 (a) Schematic drawing of a brain coronal section. (b) and (c) are the intensity images of the sections obtained from cow brain and (d) is the sample obtained from the cattle brain.

Figure 3-7 (a) corresponds with a schematic drawing of a coronal view of a human brain sample, black rectangle shows the equivalent region to the animal brains where the three samples were obtained, from (b) to (d) the regions are from right to left (outer from inner part of the brain). Figures (b) and (c) are the intensity images of the *ex-vivo* cow brain and

(d) the *ex-vivo* cattle brain. Sample 1 corresponds to a coronal section taken in the crossroad between the posterior parietal lobe and the occipital lobe of a cow, approximately 2 cm from the rostral to the occipital pole, whereas sample 2 was obtained across the frontal lobe. These sections are composed of cortical grey matter (*gm*), which is a layered cell-rich structure, and subcortical white matter (*wm*), which is sparsely cellular and composed of bundles of nerve fibers that connect the cortex with other cortical areas or with subcortical structures (at this level, mainly thalamus). Finally, sample 3 is taken across the frontal lobe of cattle, closer to the medial region of the brain. This region is also composed of *wm*, *gm* and includes a region of corpus callosum.

Note that all the samples studied in this section were obtained from a local slaughterhouse and no laboratory animals were used for the experiments; previous treatment and commercial use of the animal tissue were in accordance with Spanish legislation. The samples were stored at -16°C after acquisition and until the measurements.

The two female *ex-vivo* human brain samples were facilitated by Dr. Emilio Gonzalez-Arnan obtained from the Universidad de la Laguna and preserved in formalin. We select a coronal section from each one of the brains (ULLA621 and ULLA251) and we carry out the sectioning obtaining fragments of interest for its polarimetric study (noted as 11, 31, 22, 32 and 12). The use of these samples was approved by the ethics committee CHUC with registration number CEIBA2019-0353 and CEIBA 2021–3113.

Figure 3-8 shows a coronal section of ULLA621 (a), where the three selected regions for analyzing are marked with a white square (11, 22 and 31). A standard intensity image of these regions is provided in Figure 3-8 (b), (c) and (d), respectively.

In the frontal lobe we centered our analysis in the paracentral gyrus (11), which at the analyzed level is mainly composed of Brodmann area 6, a relatively agranular (sparse layer IV, see A2-A4) cortex that sometimes exhibits a prominent layer V (A4). Region 31 corresponds to the inferior temporal lobe, also predominantly neocortical. Finally, region 22 corresponds to a deep region of the human prosencephalon, which is composed by the thalamus (*t*) separated by the stratum (*str*) by the internal capsule (*ic*). The thalamus is a structure segregated into different nuclei by the internal medullary lamina (*iml*), being highlighted the predominantly somatosensorial ventral posterior nuclei (*vpn*), which receives the medial lemniscus (*ml*). The ventral posterior thalamus is separated from the subthalamic nucleus (*st*) through a complicated area that includes Forel fields H1 and H2 and the *zona incerta* (*zi*). Forel field H2 is, in turn, formed by the *ansa lenticularis* (*al*) that surrounds the subthalamic nucleus.

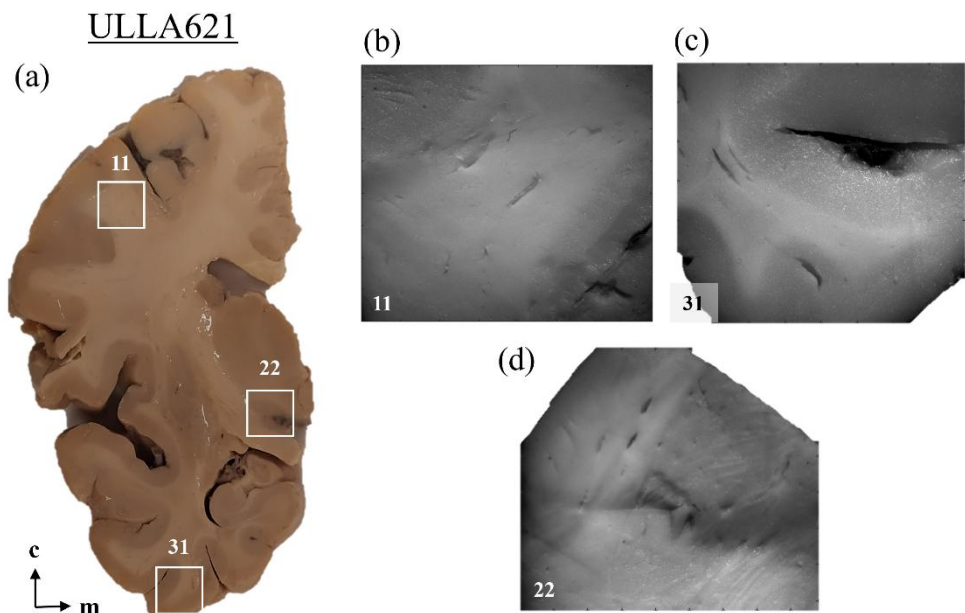


Figure 3-8 (a) Coronal section of the female human brain noted as ULLA621. This section corresponds to the frontal lobe of the brain. White squares in (a) denote the regions selected for further analysis, the intensity images of 11, 31 and 22 are zoomed in (b), (c) and (d), respectively. c and m indicate cephalic coronal and media directions, respectively.

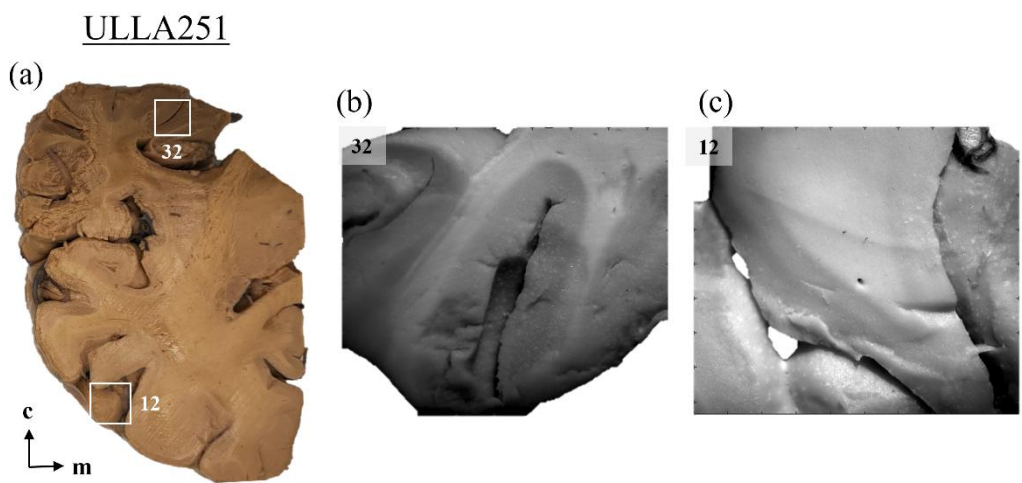


Figure 3-9 (a) Coronal section of the female human brain noted as ULLA251. This section is taken at the AP (anterior posterior) +2 plane of the brain. White squares in (a) denote the regions selected for further analysis, the intensity images of 32 and 12 are zoomed in (b) and (c), respectively. (b) and (c) correspond to the parahippocampal gyrus (pg) and the posterior middle frontal gyrus (mfg), respectively.

In Figure 3-9 we present the second section of *ex-vivo* human brain inspected in this work. (a) corresponds to the full coronal section of ULLA251, where the two selected regions for analysis are indicated with the white squares (denoted as 32 and 12). These two regions correspond to the intensity images (b) and (c). Figure 3-9 (b) is the parahippocampal gyrus, which is defined medial to the collateral sulcus (*cs*) and composed by the entorhinal cortex (*ec*) and the hippocampal formation (*hc*). The *ec* is a periarchicortex with a relatively homogeneous layering at the level in which it was analyzed and the *hc* is at three layered structure with a cell-rich pyramidal cell layer (*pcl*, in the *subiculum* –Sb- and *cornu ammonis* –CA-), a stratum *lacunosum moleculare* (*slm*), and a stratum *oriens* (*so*) both cell-poor. The *hc* is coated laterally by the alveus (*alv*), a white matter tract. The region noted as 12 corresponds to the posterior middle frontal gyrus (*mfg*).

To conclude this section, we provide an explanation of the processes applied to the brain samples: the formalin fixation for the preservation of the human brain samples and the posterior histochemical processes to histologically identify the structures of interest.

Formalin fixation: The immersion brains were obtained from cadaveric donors to the University of La Laguna, perfused through the carotid arteries with 4% paraformaldehyde and then extracted following a standard protocol including opening of the cranial vault and careful sectioning of the cranial nerves, the tentorium and the medulla oblonga from anterior to posterior. Afterwards, brains were fixed by immersion in 4% paraformaldehyde at 4 °C for 4–5 days and transported to the UAB laboratory, where they were manually cut into 1 cm. thick slices using the posterior edge of the anterior white commissure as reference for the first cut. From these major sections, regions of interest were selected and 1,5 x 1,5 cm blocks were extracted. After polarimetric analysis, the tissue blocks were dehydrated using successive overnight baths in 70°, 80°, 90° and 100° ethanol, one last final overnight bath in xylene, embedded in paraffin, and cut in 5 µm-thick sections.

Histochemical process: Cresyl violet (Nissl) was used for histological staining, previously prepared as a solution of 1 g/l of cresyl acetate in crystals and 2.5 g/l of 100% glacial acetate. Samples intended to be stained with violet were deparaffinized by overnight heating at 60°C and brought to 100°, 96°, and 90° alcohol in successive baths, before being subjected to a preheated Cresyl Violet bath for 30 seconds and two 5-second baths in a mixture of Acetic Acid and 96° alcohol. They were then dehydrated with alcohols of increasing concentration and covered with Eukitt® before microscopic analysis.





## Chapter 4 Discovering anisotropic and isotropic depolarization sources

This chapter introduces a fundamental study that serves as the basis for the development of new analytical tools, providing deeper insight into the depolarizing characteristics of samples. Importantly, using the Indices of Polarimetric Purity as framework, we describe two origins of depolarization sources, namely isotropic and anisotropic depolarization. The analysis provided in this section relates to the results presented in one of the articles comprising this thesis (Ref. [118]).

In this section we study the role of each one of the IPP in depolarizing processes, with special interest in showing the connection between inherent physical properties of samples and measurable macroscopic depolarization data. To do so, we simulate different kinds of depolarizers originated by the action of pure polarimetric elements (linear diattenuators, linear retarders or combinations of both), providing diverse cases of study leading to depolarization and being easy to interpret. With these simulations, we found very interesting results. In particular, depolarizers generated by these pure polarimetric elements only show response in  $P_1$  and  $P_2$  indices, being  $P_3 = 1$  in all cases. To get a response in the  $P_3$  index different kinds of depolarizers are needed, the so-called isotropic depolarizers. However, these depolarizers are not achieved by the mentioned simulations. In this sense, as stated before, we can divide depolarization into two different terms (1) the one affecting only to  $P_1$  and  $P_2$  that is originated by microscopic constituent elements of samples showing polarimetric anisotropy and (2) depolarization produced by isotropic depolarizers that affect also the  $P_3$  index, in this case it is related mainly to scattering processes that losses any polarimetric information of the system. We have decided to

name anisotropic depolarization to the process (1) and isotropic depolarization to the process described in (2).

To conclude, we also provide an experimental part of the study to verify the results of the simulations (section 4.3) and further interpretation of the results in terms of the Purity Space (section 4.4).

## 4.1 Depolarizers simulations $P_3 = 1$

To study the effect of depolarization in the indices comprising the IPP we simulate different depolarizers constituted by means of well-known (clear physical interpretation) pure polarimetric elements such as linear diattenuators, linear retarders and combinations of them. The idea behind the simulations and studies developed in this chapter is based on Mueller's additive decomposition theory, where several decompositions of this category demonstrate that a Mueller matrix representing a depolarizing system can be constructed as the incoherent sum of simpler or even pure matrices [124].

In section 2.2, we introduced diverse decompositions of  $M$ ; among them, the Parallel decomposition allows us to decompose a depolarizing Mueller matrix in a convex sum of  $M$  that can be pure, non-pure or a mixture of them. This decomposition allows building Mueller matrices of depolarizers by means of the stated pure polarimetric elements. As a first approach, by constructing a space of simulations obtained from different control parameters (main characteristics of the constitutive pure elements) and analyzing the related Parallel decomposition of the resulting Mueller matrices, we can relate the intrinsic characteristics of the constitutive components of samples with the physical interpretation of depolarization sources. In addition, they also relate different physical processes directly with the magnitude of the different IPP.

Thus, the Mueller matrices constructed and inspected in this chapter are analyzed on basis of the Parallel decomposition:

$$M = m_{00} \sum_{i=1}^n \alpha_i \hat{M}_i ; \alpha_i \geq 0; \sum_{i=0}^n \alpha_i = 1 , \quad (4-1)$$

where  $\alpha_i$  is the weight of each  $\hat{M}_i$  comprising the summation. These simulations pretend to mimic complex systems presenting dichroic and/or birefringent properties producing depolarization.

In addition to the dichroic and birefringent characteristics introduced in the model by including the pure elements, to approach more the simulations to real samples, we also

aim to introduce certain dispersion in the orientation of such constituent elements, which is highly representative, for example, of biological structures. For this reason, we add different orientations to each element in the summation. That is, each one of the  $\hat{M}_i$  conforming our simulated sample is oriented at a given angle ( $\theta$ ):

$$\hat{M}_i(x, \theta) = M_{rot}(-\theta)\hat{M}_i(x)M_{rot}(\theta), \quad (4-2)$$

where  $M_{rot}(\theta)$  represent the rotation Mueller matrix ( $\theta$ ) and  $\hat{M}_i(x)$  the normalized  $M$  of the polarimetric pure element under study that can be a linear diattenuator (LD) or a linear retarder (LR) [124]:

$$M_{rot}(\theta) = \begin{pmatrix} 1 & 0 & 0 & 0 \\ 0 & \cos 2\theta & \sin 2\theta & 0 \\ 0 & -\sin 2\theta & \cos 2\theta & 0 \\ 0 & 0 & 0 & 1 \end{pmatrix}; 0 \leq \theta \leq \pi, \quad (4-3)$$

$$M_{LD}(p_x, p_y) = \frac{1}{2} \begin{pmatrix} p_x^2 + p_y^2 & p_x^2 - p_y^2 & 0 & 0 \\ p_x^2 - p_y^2 & p_x^2 + p_y^2 & 0 & 0 \\ 0 & 0 & 2p_x p_y & 0 \\ 0 & 0 & 0 & 2p_x p_y \end{pmatrix}; 0 \leq p_{x,y} \leq 1, \quad (4-4)$$

where  $p_x$  and  $p_y$  are the amplitude attenuation coefficients for the  $x$  and  $y$  components, respectively. In addition to these parameters, we can also compute the diattenuation value of a linear diattenuator in terms of  $p_x$  and  $p_y$  as (see Eq. (2-6)):

$$D = \frac{|p_x^2 - p_y^2|}{p_x^2 + p_y^2}. \quad (4-5)$$

$$M_{LR}(\phi) = \begin{pmatrix} 1 & 0 & 0 & 0 \\ 0 & 1 & 0 & 0 \\ 0 & 0 & \cos \phi & \sin \phi \\ 0 & 0 & -\sin \phi & \cos \phi \end{pmatrix}; 0 \leq \phi \leq \pi, \quad (4-6)$$

the angle  $\phi$  is the phase shift introduced to the orthogonal components of the incident light field. The matrices  $M_{LD}$  and  $M_{LR}$  correspond to the Mueller matrices of linear diattenuator and retarder oriented at  $0^\circ$ , respectively.

At this point, we presented the Mueller matrices of the different elements used to build the depolarizers. With the above presented physical parameters, diattenuation characteristics ( $p_x, p_y$ ), retardance ( $\phi$ ) and orientation ( $\theta$ ) angles of the different terms comprising the incoherent addition (Eq. (4-1)), we can control the depolarizers characteristics. In addition, to make a more accurate approximation into the simulations

and real samples present in nature such as, for instance, biological samples, we also decided to add some more control parameters. Instead of assigning random values to the parameters for each term in the summation, we chose to restrict their domain of variation. We consider a group of dichroic, birefringent or combinations of them, with a privileged value or direction and with deviations from this value or direction following a gaussian distribution. This approach is justified by the fact that normal distributions are frequently observed in nature, a phenomenon supported by the Central Limit Theorem, which explains how the aggregation of many independent random factors often leads to normally distributed outcomes. Therefore, the values of the parameters under control in the simulations ( $A$ ) are characterized by a mean value ( $\bar{A}$ ) and a variance ( $\sigma_A$ ) that follow the Gaussian distribution.

Here we provide a description of the control parameters in the simulations:

- $n$ : number of matrices in the summation.
- $\alpha_i$ : weight of every term in the summation. We chose the same weight for all terms.
- $\bar{p}_{xi}, \bar{p}_{yi}$ : mean values of the amplitude coefficients of the diattenuators in each interaction ( $0 \leq \bar{p}_{x,y} \leq 1$ ).
- $\bar{\theta}$ : mean value of the orientation angle of the polarimetric element (diattenuator and retarder) in each interaction ( $0 \leq \bar{\theta} \leq \pi$ ). This angle is arbitrary fixed to  $\bar{\theta} = 60^\circ$  for all the simulations, the mean value of the rotation angle does not affect the simulations. It can be interpreted as a rotation of the system, and thus, the polarimetric properties of the samples are not affected
- $\bar{\phi}$ : mean value of the retarder total retardance ( $0^\circ \leq \bar{\phi} \leq 360^\circ$ ).
- $\sigma_{p_x}, \sigma_{p_y}, \sigma_{\phi}, \sigma_{\theta}$ : variance value for the amplitude coefficients and the orientation angle.

We want to note that the number of components in the incoherent addition is fixed to  $n = 1500$  in all cases. The depolarizing (and enpolarizing) response of the simulated systems was not affected by increasing the number of simulations ( $n$ ) from a given limit value. In this sense, by selecting low values of  $n$  ( $n < 20$ ), the response was sensible to this factor, but from  $n > 1000$  the system was very robust. Our main goal was to reproduce real biological systems, here we are talking about millions of unitary elements. However, the computation time for such a number was too large and we realized that with lower  $n$  values the response was the same. Therefore, we chose lower (but representative)  $n$  values ( $n = 1500$  in our case) to study the systems.

In the following sections, we present the results for the depolarization response of different sorts of depolarizers, through the analysis of the IPP, for different values of the control parameters. In particular, depolarizers generated by means of the incoherent

addition of diattenuators are described in sec. 4.1.1, sec. 4.1.2 show those corresponding to retarders and in sec. 4.1.3 we present the results of the combination of retarders and diattenuators.

#### 4.1.1 Linear diattenuators

The first depolarizers we describe are constituted by the incoherent addition of diattenuators ( $M_{LD}$ ). Therefore, Eq. (4-1) for this case is given by:

$$M(p_{xi}, p_{yi}, \theta) = m_{00} \sum_{i=1}^n \alpha_i \hat{M}_{LDi}(p_{xi}, p_{yi}, \theta). \quad (4-7)$$

To obtain depolarizers by means of linear diattenuators we obtain a model where we can control the mean value and variance of several parameters ( $p_{xi}, p_{yi}, \theta$ ) as well as the number of interactions in the simulation ( $n$ ) and the weight of each component ( $\alpha_i$ ).

To simplify, we decided to vary only one of the amplitude coefficients, since both are equivalent, we arbitrary chose  $p_y$ , fixing the value of  $p_x$ . Therefore, for each of the simulated depolarizers, we set a constant value for  $(\bar{p}_x, \bar{\theta})$  and for each term in the summation we vary the values of  $\bar{p}_y$ , and,  $\sigma_\theta$ . To conduct the simulations, for a fixed value of  $\bar{p}_x$ , we perform a series of simulations varying the values of  $\bar{p}_y$  between 0 and 1 with steps of 0.003 and a null variance ( $\sigma_{p_y} = 0$ ). The mean value of the orientation angle is fixed to  $\bar{\theta} = 60^\circ$  and its variance ( $\sigma_\theta$ ) takes values between  $0^\circ$  and  $180^\circ$  with steps of  $0.6^\circ$ . Therefore, for each value of  $p_x$ , we perform  $300 \times 300 = 90.000$  simulations. That is, we simulate 90.000 depolarizers with characteristics given by the correspondent inherent parameters.

To study the depolarization features of the implemented systems, we calculate the IPP corresponding to each simulated Mueller matrix. The results for the  $P_1, P_2$  and  $P_3$  parameters are shown in Figure 4-1 and Figure 4-2 corresponds to the  $P_3$  index, where we see that the behavior of  $P_3$  as a function of  $\sigma_\theta$  ( $y$  axis) and  $\bar{p}_y$  ( $x$  axis) is constant ( $P_3 = 1$ ) independently of the value set for  $p_x$ . In Figure 4-2 (a)-(f)), each row corresponds to the  $P_1$  and  $P_2$  values for different  $\bar{p}_x$  values (1, 0.5, 0.1; from top to bottom). In both cases, the  $x$  axis provides the values for the  $\bar{p}_y$  parameter,  $y$  axis show the values for the variance of the orientation angle ( $\sigma_\theta$ ) and the colorbar indicates the color code representing the value of the IPP (from red (0) indicating total depolarization and dark blue no depolarization at all (1)).

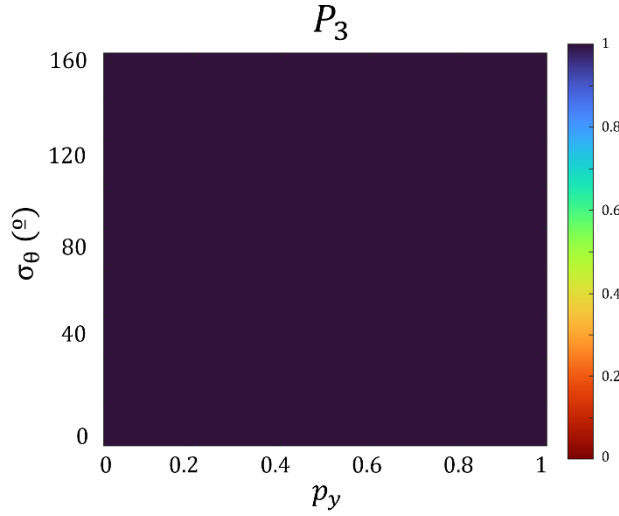


Figure 4-1  $P_3$  value of the simulated  $M$  composed by the incoherent addition of linear diattenuators. The  $x$  axis represents the value of  $p_y$  from 0 to 1, and the  $y$  axis corresponds to  $\sigma_\theta$ , taking values from  $0^\circ$  to  $180^\circ$ .

The first interesting result is the behavior of  $P_3$ . Figure 4-1 shows that the response in the  $P_3$  index is independent of the simulation control parameters, ( $\bar{p}_x$  control in the  $\bar{p}_y, \sigma_\theta$ ), and it is always equal to 1. We can conclude that, by means of the incoherent addition of linear diattenuators the value of the  $P_3$  parameter is not affected. This result leads us to understand that the depolarization caused by dichroic structures cannot be assessed through the  $P_3$  channel, which must contain information distinct from this mechanism (as will be discussed later).

In contrast, we find interesting dependencies between the  $P_1$  and  $P_2$  channels with the studied control parameters, as shown in Figure 4-2, where both show very similar function distribution with  $\bar{p}_x, \bar{p}_y$  and  $\sigma_\theta$ . The general dependence of  $P_1$  and  $P_2$  in the control parameters ( $\bar{p}_y, \sigma_\theta$ ) is equivalent, however we find a vertical shift in  $P_2$  channel as  $\bar{p}_x$

increases. This situation is explained by the inequality shown in Eq. (2-32), which forces  $P_2$  to have larger or equal values than  $P_1$ .

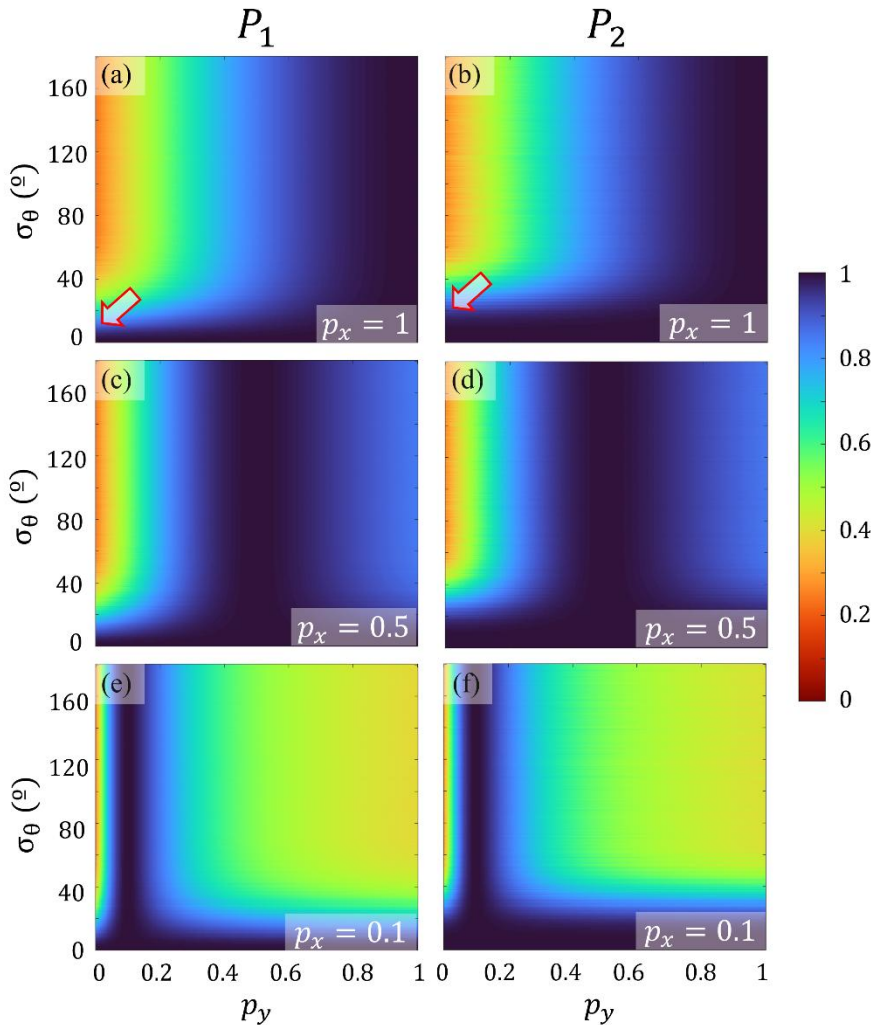


Figure 4-2 Results for the  $P_1$  and  $P_2$  indices of the simulated  $M$  composed by the incoherent addition of linear diattenuators. The  $x$  axis represents the value of  $p_y$  from 0 to 1, and the  $y$  axis corresponds to  $\sigma_\theta$ , taking values from  $0^\circ$  to  $180^\circ$ . Each row corresponds to a  $p_x$  value (1, 0.5, 0.1; from top to bottom).

Interestingly, the depolarization response is very dependent on  $\sigma_\theta$ , this parameter represents the disorganization of the elements, in this case the diattenuators, forming the depolarizer. In Figure 4-2 (a) to (f), for low values of  $\sigma_\theta$  the system does not present depolarization ( $P_1 = P_2 = P_3 = 1$ , dark blue in the images). Depolarization is achieved for values of  $\sigma_\theta \sim 18^\circ$  (see red arrow in Figure 4-2 (a)), when values of  $P_1$  start to decrease from the non-depolarization case ( $P_1 = 1$ ). In the  $P_2$  channel this effect starts for larger values

of  $\sigma_\theta$  ( $\sigma_\theta \sim 22^\circ$ ; see red arrow in Figure 4-2 (b)). This situation corresponds to  $M$  of samples constituted by a substantial disorganization of the linear diattenuators. The disorganization, represented by  $\sigma_\theta$  parameter, has a threshold around  $50^\circ$ , where the maximum depolarization in  $P_1$  and  $P_2$  is achieved ( $P_1 = P_2 = 0$ ) and these values are maintained when increasing  $\sigma_\theta$ . These conditions also depend on the values of the attenuation parameters ( $\bar{p}_x, \bar{p}_y$ ), we analyze these dependences in the following.

We can further analysis the IPP regarding the similarities between the  $P_1$  and  $P_2$  channels and the dependence with  $\bar{p}_x$  and  $\bar{p}_y$  parameters. In Figure 4-3 we present the results for  $P_1$  for a range of  $\bar{p}_x$  values (1 (a), 0.9 (b), 0.7 (c), 0.5 (d), 0.3 (e), 0.1 (f)). As shown in Figure 4-2, the behavior of  $P_2$  is the same but, with a vertical shift. In this case, we reduce the representation range of  $\sigma_\theta$  ( $0^\circ - 90^\circ$ ) since the threshold for this parameter is around  $50^\circ$ .

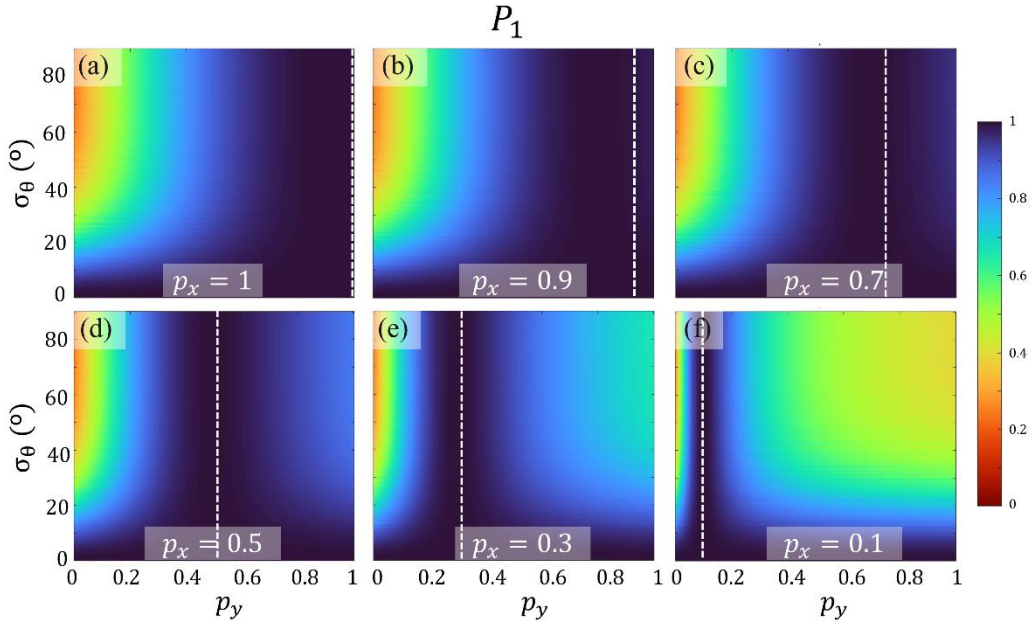


Figure 4-3 (a)-(f)  $P_1$  values for simulated samples composed by the incoherent addition of diattenuators, with  $p_x = 1, 0.9, 0.7, 0.5, 0.3, 0.1$ . The  $x$  axis represents the value of  $p_y$  from 0 to 1, and the  $y$  axis corresponds to  $\sigma_\theta$ , taking values from  $0^\circ$  to  $90^\circ$ .

Figure 4-3 from (a) to (f) represents the decrease in the value of  $\bar{p}_x$  of the simulated samples. This increase represents a higher depolarization response in the images, see how the dark blue zone (no depolarization) decreases as  $\bar{p}_x$  takes lower values. Moreover, it is interesting to study the non-depolarizing zones; the white dashed line in the figures represents the  $\bar{p}_x = \bar{p}_y$  situation and corresponds to  $P_1 = P_2 = P_3 = 1$ . Recalling Eq. (4-4), for this case, the Mueller matrix of a diattenuator becomes the identity



( $diag(1,1,1,1)$ ) which acts as a neutral polarimetric element (i.e., we are representing a non-dichroic element). Depolarization starts appearing as  $\bar{p}_x$  and  $\bar{p}_y$  values separate and  $M$  differs from the identity. The appearance of depolarization with respect both  $\bar{p}_y$  and  $\sigma_\theta$  occurs earlier as  $\bar{p}_x$  value is lower. For instance, Figure 4-3 (e) and (f) with  $\bar{p}_x = 0.3$  and  $\bar{p}_y = 0.1$  we see two high depolarization zones. In Figure 4-3 (e), the zone  $0 < \bar{p}_y < 0.1$  have values of  $P_1$  from 0 to 0.65 and for  $0.7 < \bar{p}_y < 1$ ,  $P_1$  achieves depolarization values in  $P_1$  between 0.7 and 0.5. In Figure 4-3 (f),  $P_1$  decreases until 0 – 0.5 in the range  $0 < \bar{p}_y < 0.1$  and for  $0.4 < \bar{p}_y < 1$   $P_1$  is around 0.6 – 0.4. The values of  $P_2$  are almost the same and,  $P_2 = 1$  for all cases. These corresponds to  $\sigma_\theta > 18^\circ$  for  $P_1$  and  $\sigma_\theta > 22^\circ$  for  $P_2$ .

Regarding the above-stated results, we observe that the depolarizing effect becomes more pronounced as the relative difference between  $\bar{p}_x$  and  $\bar{p}_y$  increases — that is, when the diattenuation effects of the constituent elements become more significant. For this reason, it is of interest to perform the same analysis in terms of the diattenuation parameter ( $D$ , see Eq. (2-6)), where the effect of  $\bar{p}_x$  and  $\bar{p}_y$  is combined. Figure 4-4 shows the values of  $D$  obtained from the Mueller matrices resultant from the incoherent addition of linear diattenuators with  $\sigma_\theta = 0$  and values of the attenuation coefficients ranging from 0 to 1. The colormap corresponding to the diattenuation values goes from red color ( $D = 0$ ) when no diattenuation is present in the sample to dark blue color ( $D = 1$ ) correspondent to an ideal diattenuator.

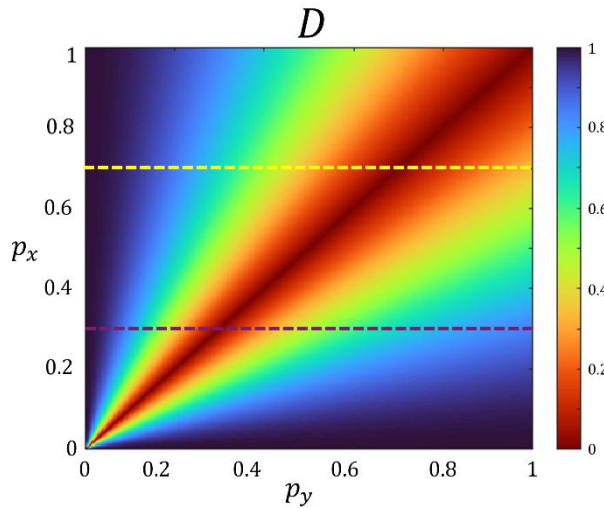


Figure 4-4 Value of diattenuation for the incoherent addition of linear diattenuators with  $\sigma_\theta = 0^\circ$ ,  $x$  and  $y$  axes correspond to  $\bar{p}_x$  and  $\bar{p}_y$  parameters, from 0 to 1.

The diagonal dark red line crossing the image in Figure 4-4 corresponds to  $D = 0$  (no dichroism is present), this situation corresponding to equal attenuation values  $\bar{p}_x = \bar{p}_y$

(generating in all the cases the identity matrix). We can relate this line with the zones in Figure 4-2 marked with the white dashed lines where the depolarization is zero ( $P_1 = P_2 = P_3 = 1$ ). That is, this represents the situation where  $D = 0$  and the system is not capable to enpolarize or depolarize. As we move far from this diagonal line ( $\bar{p}_x \neq \bar{p}_y$  situation) the diattenuation value  $D$  increases and it takes values going from 0 to 1 (see transition from dark red to orange-yellow-green-blue).

In addition, we can establish a connection between the diattenuation value of the constituent elements (associated with a pair of values  $\bar{p}_x$  and  $\bar{p}_y$  as shown in Figure 4-4) and the corresponding depolarizing response of the system, described in Figure 4-3. The yellow and purple dashed lines in Figure 4-4 correspond to the values  $\bar{p}_x = 0.7$  and  $\bar{p}_x = 0.3$ , respectively, with  $\bar{p}_y$  taking values in its full range. Following the purple dashed line, we see how the value of  $D$  increases with  $\bar{p}_y$ , reaching the maximum value of  $D = 1$  when the dashed purple line intersects with the diagonal red line (i.e.,  $\bar{p}_y = 0.3$ ; corresponding to the  $\bar{p}_x = \bar{p}_y$  case). This behavior explains the depolarization results shown in (e) and (c), where the values showing no depolarization correspond to the situation where  $D = 0$ , whereas for the situation where  $D$  approaches the maximum value of 1, the depolarization capability of samples increases, achieving IPP values different from 1. In other words, when the polarimetric feature reaches its maximum, the statistical mixture of such elementary elements has a high potential to generate depolarization.

Complementary, the yellow dashed line in Figure 4-4 corresponds to the case of  $\bar{p}_x = 0.7$ . By analyzing the behavior of  $D$ , the values equal or near 1 correspond to the zone where the range of  $\bar{p}_y$  is  $(0 - 0.3)$ ; this corresponds to the left part in the image. In this case, for values of  $\sigma_\theta$  higher than the mentioned limit, the system depolarizes anisotropically. However, as  $\bar{p}_y$  increases ( $D$  decreases) the depolarization capability of the system is lost because the system becomes less dichroic.

#### 4.1.2 Linear retarders

In this section, we inspect the case of depolarizers constituted by the incoherent addition of linear retarders. The procedure for the simulations is analogous to the previous section and the considerations for the parameters  $n$ ,  $\alpha_i$  and  $\bar{\theta}$  are the same ( $n = 1500$ ,  $\bar{\theta} = 60^\circ$  and  $\alpha_i$  equal for all terms) and the incoherent addition of linear retarders  $\hat{M}_{LRI}$  is :

$$M(\phi, \theta) = m_{00} \sum_{i=1}^n \alpha_i \hat{M}_{LRI}(\phi_i, \theta) ; \quad (4-8)$$

The results of the IPP values of the depolarizers resulting from these simulations are presented in Figure 4-5 and Figure 4-6. Figure 4-5 shows the results for  $P_1$ ,  $P_2$  and  $P_3$  indices. The  $x$  axis represents the mean value of the retardance, with values from  $0^\circ$  to  $360^\circ$  and null variance ( $\sigma_\phi = 0$ ) and the  $y$  axis represents the variance of the orientation from  $0^\circ$  to  $180^\circ$ .

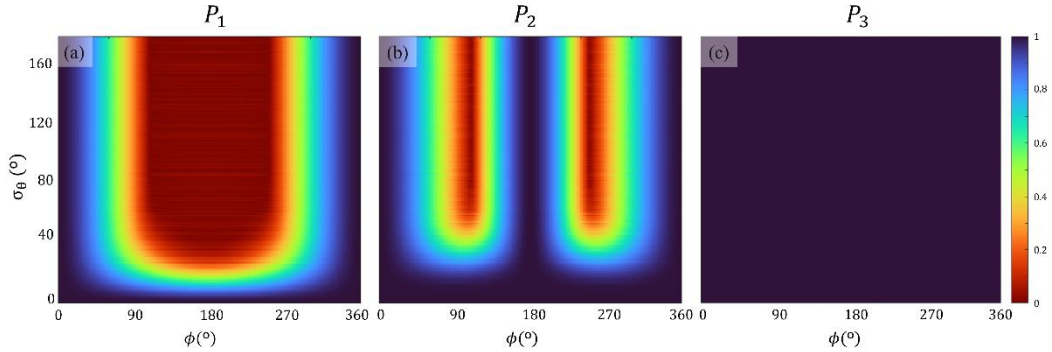


Figure 4-5 Results for the IPP of the simulated  $M$  composed by the incoherent addition of linear retarders. (a)  $P_1$ , (b)  $P_2$  and (c)  $P_3$ , where the  $x$  axis represents the value of  $\phi$  from  $0^\circ$  to  $360^\circ$ , and the  $y$  axis corresponds to  $\sigma_\theta$ , taking values from  $0^\circ$  to  $180^\circ$ .

In this case, the analysis of Figure 4-5 shows the same behavior of  $P_3$  than in the case of the diattenuators,  $P_3 = 1$  independently of the control parameters. This generalizes the previous result not only to the dichroic case but also to the birefringent one. It can be stated that, when generating dispersion from pure polarimetric elements (linear retarders or diattenuators), the behavior of  $P_3$  remains unaffected. In contrast,  $P_1$  and  $P_2$  are the channels sensitive to the statistical distribution of these constituent polarimetric elements. However, we do find differences in the results for  $P_1$  and  $P_2$ , in contrast to the depolarizers generated by diattenuators, the behavior of the two indices is clearly differentiated (see Figure 4-5 (a) and (b) for  $P_1$  and  $P_2$ , respectively). If we inspect Eq. (4-6), values of  $\bar{\phi}$  close to  $0^\circ$  and  $360^\circ$ , the Mueller matrix of the retarder becomes the identity ( $diag(1,1,1,1)$ ), behaving as a neutral polarimetric element (see yellow zones in Figure 4-5 (a) and (b);  $P_1 = P_2 = P_3 = 1$ ). Depolarizing zones correspond to values for  $40^\circ < \bar{\phi} < 320^\circ$  and orientation disorder of the retarders  $\sigma_\theta > 10^\circ$  (see Figure 4-5 (a)).  $P_1$  takes values from 0.9 to 0 and  $P_2$  from 1 to 0. In the same way as the diattenuators, depolarization is obtained for  $\sigma_\theta > 10^\circ$ , reaching values of  $P_1 < 1$ . In the case of  $P_2$  channel, values lower than 1 are obtained for a higher disorder ( $\sigma_\theta > 20^\circ$ ). In addition, there is a threshold value for  $\sigma_\theta$  above which depolarization stops increasing,  $\sigma_\theta \sim 50^\circ$  (see Figure 4-5 (b)). More in detail in Figure 4-5 (a) and (b) distributions, the index  $P_1$  shows one minimum valley, whereas  $P_2$  channel shows two (i.e.  $P_1$  distribution between  $\bar{\phi}$   $[0^\circ - 360^\circ]$  range occurs as well for the

$P_2$  channel, but in the  $\bar{\phi}$   $[0^\circ - 180^\circ]$  range, and it is doubled in the full range. For values of  $\bar{\phi}$  close to  $180^\circ$ ,  $P_1 = 0$  and  $P_2 = 1$ , this situation corresponds to a  $M = \text{diag}(1, 1, -1, -1)$ . Therefore, with the index  $P_1$  we can be able to differentiate between this case and the above-discussed scenario of  $\bar{\phi}$  near  $0^\circ$  and  $360^\circ$ . This difference between  $P_1$  and  $P_2$  is useful to distinguish between depolarizers constituted by linear retarders with different mean retardance values. For instance,  $\bar{\phi} = 90^\circ$  leads to  $P_1$  and  $P_2$  values close to zero, a value  $\bar{\phi} = 180^\circ$  to  $P_1 = 0$  and  $P_2 = 1$  and a value of  $\bar{\phi} = 0^\circ$  or  $360^\circ$  to  $P_1 = 1$  and  $P_2 = 1$ . Importantly, this diversity between  $P_1$  and  $P_2$  responses indicates that the ability to discriminate between different depolarizing systems originating from retarders using the IPP is even greater than in the dichroic case, as further discrimination is enabled by the distinct responses of such channels.

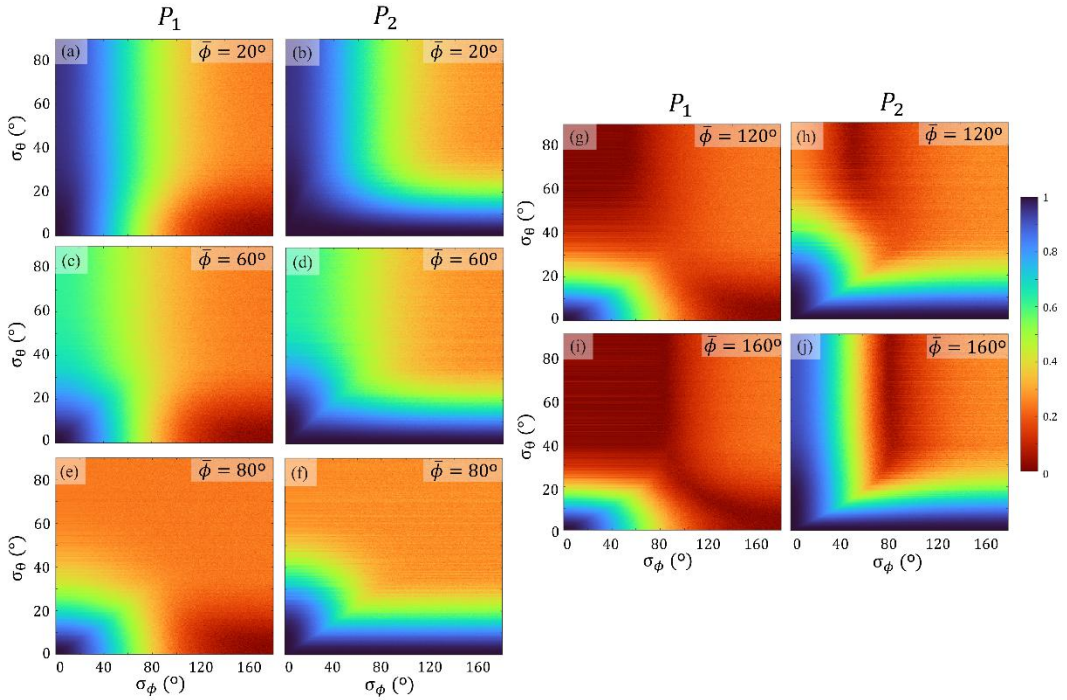


Figure 4-6 Results for the  $P_1$  (first and third columns) and  $P_2$  (second and forth columns) values of the simulated  $M$  composed by the incoherent addition of linear retarders. The  $x$  and  $y$  axes represent the variance range of the mean orientation and of the mean retardance, respectively; the mean value of the retardance variates from  $20^\circ$  to  $160^\circ$  in steps of  $40^\circ$  for each pair of IPP.

To achieve a more complete analysis, Figure 4-6 shows the dependence of the IPP in terms of the variance of the retardance ( $\sigma_\phi$ ) and the variance of the orientation ( $\sigma_\theta$ ) for different values of  $\bar{\phi}$ . The  $x$  axis represents the variance of the retardance, with values from  $0^\circ$  to  $180^\circ$  and, the  $y$  axis represents the variance of the orientation from  $0^\circ$  to  $90^\circ$ . For each of the rows in the figure the value of the retardance varies from  $0^\circ$  to  $160^\circ$ .

As for the case of linear diattenuators, when the disorder of the elements comprising the depolarizers is low (that is, low values of  $\sigma_\theta$  and  $\sigma_\phi$ ) no depolarization is present ( $P_1 = P_2 = P_3 = 1$ ; dark blue color). In all cases, depolarization is zero for  $\sigma_\theta < 10^\circ$  and  $\sigma_\phi < 10^\circ$  (see  $P_1$  images in the figure). An increase in the value of the variances is translated into larger depolarization capability, that is, lower values for  $P_1$  and  $P_2$ . Regarding the dependence of depolarization with the main value of the retardance  $\bar{\phi}$  in Figure 4-6 (a) to (j) we observe that, as the value of  $\bar{\phi}$  increases, the dark blue zone decreases, that is, a higher value of the mean retardance produces depolarization for more values of the combination  $\sigma_\theta$  and  $\sigma_\phi$ . This occurs for  $\bar{\phi} < 160^\circ$ , when the value of  $\bar{\phi}$  approaches  $180^\circ$  the value of  $P_2$  starts decreasing, we can see this behavior in the second blue zone in Figure 4-6 (b). It is reasonable to consider that certain mean retardances may have a greater or lesser capacity to induce depolarization, given that the complexity of the Mueller matrix expression for a retarder depends on this parameter. Specifically, cases with zero retardance or integer multiples of  $2\pi$  result in the identity matrix. As the retardance deviates from these special cases, the resulting Mueller matrices exhibit increasingly complex structures (with fewer zero elements). The statistical dispersion of these structures contributes to a higher depolarization capacity, which is reflected in the  $P_1$  and  $P_2$  depolarization channels.

We omit the images for the  $P_3$  channel to avoid redundancy,  $P_3$  has the same behavior for all cases as the presented in Figure 4-5 (c). The incoherent addition of linear retarders is not able to decrease  $P_3$  value.

#### 4.1.3 Addition of linear retarders and linear diattenuators

Finally, we combine the dichroic and birefringent properties, representing more complex systems. To do so, we first build a Mueller matrix ( $M_{comb,i}$ ) as the ordered product of a diattenuator ( $\hat{M}_{LDi}$ ) and a retarder ( $\hat{M}_{L Ri}$ ):

$$\hat{M}_{comb,i} = \hat{M}_{LDi}(p_{xi}, p_{yi})\hat{M}_{L Ri}(\phi). \quad (4-9)$$

To perform the simulations, we proceed similarly as in the previous subsections. In this case, we conduct the incoherent addition of  $n$  Mueller matrices,  $\hat{M}_{comb,i}$ , whose four different control parameters are: attenuations ( $\bar{p}_x, \bar{p}_y$ ), retardance ( $\bar{\phi}$ ) and the variance of the orientation ( $\sigma_\theta$ ), where the angle ( $\bar{\theta}$ ) refers here to a rotation of the whole structure  $\hat{M}_{comb,i}$ . As in the previous simulated case, the variance of the orientation follows a Gaussian distribution, and the mean orientation of the system is not considered as does not modify the depolarizing response of the system (it is arbitrarily set to  $60^\circ$ ).

Figure 4-7 shows the results of  $P_1$  and  $P_2$  parameters, we omit the  $P_3$  images because for this case it is also always equal to 1. Again,  $P_3$  is not sensitive to the depolarization induced by linear polarimetric structures, even when they are mixed. Additionally, to simplify, we use the parameter  $D$  to describe the part related to dichroism and the mean value of the total retardance ( $\bar{\phi}$ ) for the retardance properties. In the figure, each set of two images in a row represents a value of  $D$  ( $D = 0$  in Figure 4-7 (a)-(b),  $D = 0.4$  in Figure 4-7 (c)-(d),  $D = 0.6$  in Figure 4-7 (e)-(f) and  $D = 1$  in Figure 4-7 (g)-(h)); the axes of the figures represent the variance of the orientation of the system ( $y$  axis; from  $0^\circ$  to  $90^\circ$ ) and the mean retardance value ( $x$  axis; from  $0^\circ$  to  $180^\circ$ ). We observe a clear dependence of depolarization with the value of  $D$ . For low values of diattenuation ( $D \leq 0.4$ ; Figure 4-7 (a)-(d)), the dependence of the IPP with  $\sigma_\theta$  and  $\bar{\phi}$  is the same as the one shown Figure 4-7 (depolarizers generated only by birefringent elements). However, when increasing the diattenuation value, that is, the dichroic component of the systems ( $D > 0.6$ ; Figure 4-7 (g)-(h)) in the Mueller matrices, the behavior of the IPP starts to be dominated by the dichroic component. For this case,  $P_1$  and  $P_2$  have the same response (as in section 4.1.2), with a vertical shift due to the inequalities among the IPP.

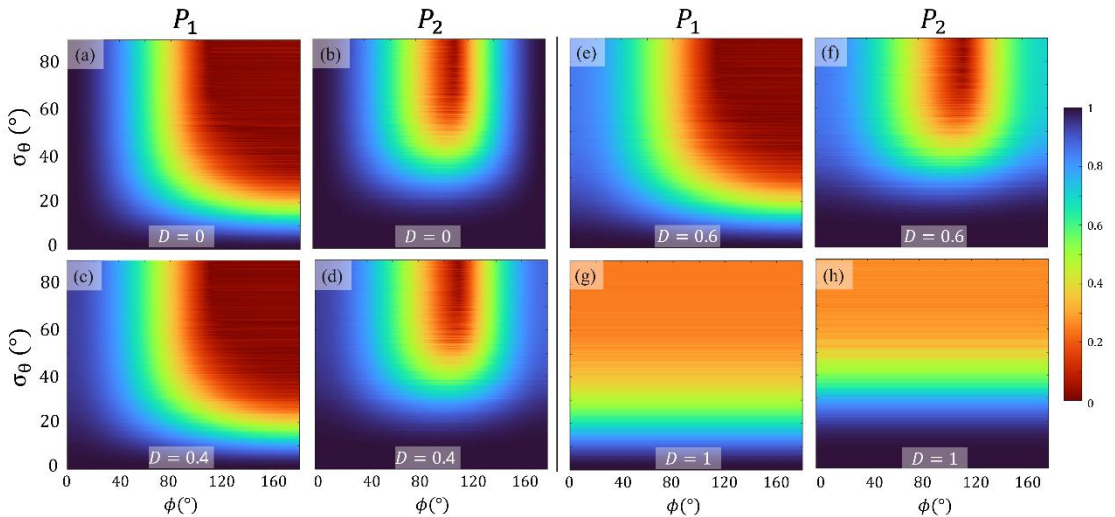


Figure 4-7 Results for the  $P_1$  and  $P_2$  values of the simulated  $M$  composed by the incoherent addition of linear retarders; each pair of images represent different values for the diattenuation: a), b)  $D = 0$ ; c), d)  $D = 0.4$ ; e), f)  $D = 0.6$ ; and g), h)  $D = 1$ . The  $x$  and  $y$  axes represent the variance range of the mean orientation and the mean retardance, respectively.

Summarizing, the simulations shown in this subsection, originated by the incoherent addition of simple polarimetric elements (retarders and diattenuators), do not modify the

value of the  $P_3$  index ( $P_3 = 1$  in all cases). However, when studying  $P_1$  and  $P_2$  parameters we observe that they have a significant dependence on the model parameters: attenuations and diattenuation ( $p_x$ ,  $p_y$  and  $D$ ), retardance and variances of retardance ( $\phi$ ) and orientation ( $\sigma_\theta, \sigma_\phi$ ). Therefore, these two indices have clear connection with physical features of depolarizing structures and can be useful to reveal underlying properties of systems and to differentiate between depolarizers based on dichroic or birefringent constituent units, even in the absence of prior information about the samples. However, in the results obtained for real samples we obtain values of  $P_3 < 1$ . This leads to a question: what mechanisms are responsible for reducing the  $P_3$  channel of the IPP if they are not the linear polarimetric elements studied in this section? In the next section we explore which are the structures or configurations that can decrease this parameter.

## 4.2 Depolarizers simulations with $P_3 < 1$

Real depolarizing systems usually have values of  $P_3$  lower than one, even achieving very low values [112,139,155]. For instance, in section 4.3 we present a table (Table 4-1) with the IPP values of different macroscopic biological samples, where the  $P_3$  values of different structures within the samples ranges between 0.1 – 0.45. Of course, these samples are composed of anisotropic elemental units; animal tissue is mainly composed of collagen fibers [156], which can be described as retarders. Also, vegetal samples are formed by dichroic units [42,157], which can be described as diattenuators.

In this section we try to find the physical mechanism that describes the depolarization behavior of real samples with  $P_3 < 1$ . In this sense, we find it interesting to study the Characteristic decomposition of  $M$  in terms of the IPP (see Eq. (2-37)). This decomposition describes the Mueller matrix of any depolarizer as the contribution of four elements where each of them is weighted by the IPP or linear combinations of them. The first term, weighted by  $P_1$ , corresponds to the pure or non-depolarizing part of the system; the second and third terms, weighted by  $P_2 - P_1$  and  $P_3 - P_2$ , respectively, are the terms representing depolarization due to 2D and 3D depolarizers. The last term, weighted by  $1 - P_3$ , corresponds to a perfect depolarizer  $diag(1,0,0,0)$ . This last term in the decomposition, the perfect depolarizer, corresponds to a system that has the capability to fully depolarize any incident SoP and, therefore, it must have some connection with the  $P_3$  value because a perfect depolarizer accomplishes  $P_3 = 0$  (and thus,  $P_1 = P_2 = 0$ ).

We realized that there must be a mechanism in the systems that generates, to a certain extent, this pure depolarizer contribution, decreasing the value of  $P_3$ . To include this

process in our models, and check if this hypothesis is valid, we add a new term in the simulated Mueller matrices inspired by the Characteristic decomposition. In this sense, the simulated systems in this section can be written as the incoherent addition of a first term describing the contribution of depolarization originated by dichroic and/or birefringent elements (as in the previous section) and a second term ( $M_{iso}$ ) representing the perfect depolarizer contribution:

$$M = m_{00}\hat{M} = \sum_i^{n'} \alpha_i(m_{00}\hat{M}_i) + \sum_j^m \beta_j(m_{00}\hat{M}_{iso}); \quad (4-10)$$

$$\alpha_i, \beta_j \geq 0; \quad \sum_i^{n'} \alpha_i + \sum_j^m \beta_j = 1,$$

where  $n' + m = n$ . In section 4.1, the simulations considered correspond to the first term of the summation ( $\sum_i^{n'} \alpha_i(m_{00}\hat{M}_i)$ ). In this section, we divide the terms in the contributions of  $\hat{M}_i$  ( $n'$ ) and  $\hat{M}_{iso}$  ( $m$ ). The second term ( $\hat{M}_{iso}$ ), is the perfect depolarizer ( $\hat{M}_{iso} = \text{diag}(1,0,0,0)$ ), so it can be written as:

$$\sum_j^m \beta_j(m_{00}\hat{M}_{iso}) = \beta m_{00}\hat{M}_{iso}, \quad (4-11)$$

$$\beta = \sum_j^m \beta_j,$$

and Eq. (4-10) can be expressed as follows:

$$M = m_{00}\hat{M} = \sum_i^{n'} \alpha_i(m_{00}\hat{M}_i) + \beta m_{00}\hat{M}_{iso}. \quad (4-12)$$

In section 4.1 we show the depolarization effect of the first term in Eq. (4-12), leading to  $P_3 = 1$  in all cases. The second term leads to  $P_3 = 0$  in all cases because as said, the IPP calculated for  $\hat{M}_{iso}$  are  $P_1 = P_2 = P_3 = 0$ . This term must be connected to isotropic processes introducing polarimetric randomness that change the properties of the polarization ellipse and its propagation direction with such a level of arbitrariness that any polarimetric signature is lost in space-time integrations, and as a consequence, any incident SoP is fully depolarized. We will refer to this depolarization, caused by such types of structures, as isotropic depolarization, in contrast to the anisotropic depolarization discussed in the previous section, which arises from polarimetric anisotropy in the



constituent elements. Let us then call the first term in Eq. (4-12) as the anisotropic depolarization term, and the second one as the isotropic depolarization term.

For the study of the depolarization response of systems comprised by the anisotropic and isotropic terms, we repeat the simulations performed in the previous section but with a new control parameter  $\beta$ , controlling the relevance of the isotropic depolarization term in the samples. For the sake of simplicity, in the following we show some representative results for each case and a more complete study of the relation between  $P_3$  and  $\beta$ .

#### 4.2.1 Simulation results

In the following, we present the simulations of systems consisting of a combination of both anisotropic and isotropic components, following Eq. (4-12).

Figure 4-8 shows the IPP values of simulated systems where the anisotropic component of the resultant  $M$  is composed by the incoherent summation of linear diattenuators. The attenuation coefficient  $\bar{p}_y$  takes values between 0 and 1,  $\sigma_\theta$  ranges from  $0^\circ$  to  $180^\circ$ ,  $\bar{p}_x$  is fixed to 0.9 for Figure 4-8 (a)-(f) and to 0.2 for Figure 4-8 (g)-(l). The value of the parameter  $\beta$  governing the isotropic component is set to  $\beta = 0.2$  for Figure 4-8 (a)-(c) and (g)-(i) and  $\beta = 0.6$  for Figure 4-8 (d)-(f) and (j)-(l).

We can compare results in Figure 4-8 with the previous simulations based on linear diattenuators (no isotropic component present) shown in Figure 4-2. The dependence of the indices  $P_1$ ,  $P_2$  and  $P_3$  with the control parameters  $\bar{p}_x$ ,  $\bar{p}_y$  and  $\sigma_\theta$  is the same as in section 4.1.1. Interestingly, although the value of  $P_3$  remains constant with respect to the control parameters of the diattenuators based structure, we observe that it is no longer always equal to 1, but its overall value now depends on  $\beta$ . Consequently, although the structure of  $P_1$  and  $P_2$  is equivalent to the case without isotropic depolarization, their range of values is reduced when  $P_3$  decreases, due to the inequality described in Eq. (2-37) ( $0 \geq P_1 \geq P_2 \geq P_3 \geq 1$ ). In particular, as the value of  $\beta$  increases, that is, as the weight of the isotropic component in the simulation increases, the value of  $P_3$  decreases. In Figure 4-8 (c) and (i), showing the  $P_3$  value for two different  $p_x$  cases (0.9 and 0.4 respectively) and with  $\beta$  set to 0.2, the depolarization variations dependence with  $p_x$  are seen in  $P_1$  and  $P_2$  channels, but  $P_3$  decreases to the same constant value of  $P_3 = 0.8$  in both cases. Importantly, note how  $P_1$  and  $P_2$  still maintains the previous dependence with the anisotropic control parameters but with the range of values decreased due to the stated reduction of the  $P_3$  value. This behavior happens until the limit where  $\beta \sim 1$  (corresponding to  $P_3 = 0$ ), where all the weight in the summation of Eq. (4-12) is due to the isotropic term and the anisotropic information is completely lost. In turn, Figure 4-7 (f) and (l) show the results for  $P_3$  with higher isotropic content,  $\beta = 0.6$ . In this case,  $P_3$  decreases to 0.4.  $P_1$

and  $P_2$  also show the same dependence with anisotropic parameters (see Figure 4-1) and a decrease in their values due to the added isotropic term.

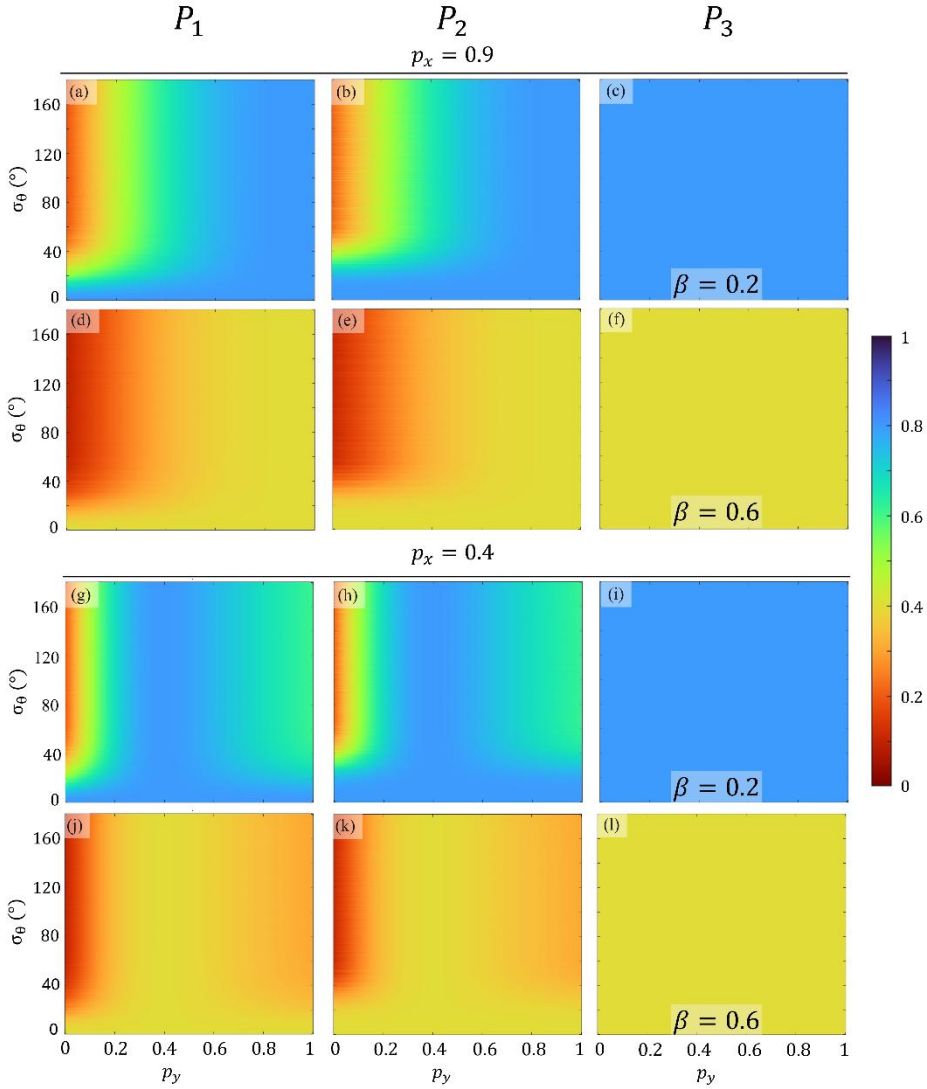


Figure 4-8 IPP results for simulated samples composed by an anisotropic (generated by the incoherent addition of diattenuators) and an isotropic part. The  $x$  and  $y$  axes correspond to  $p_y$  and the variation of orientation  $\sigma_\theta$ , respectively. The two first rows correspond to systems with a constant value of  $\bar{p}_x = 0.9$  and the second last rows to  $\bar{p}_x = 0.4$ . In both cases, the first set of IPP ((a)-(c) and (g) to (i)) represents the results for  $\beta = 0.2$  and, the in IPP images in (d) to (f) and (j) to (l) the weight of the isotropic term is  $\beta = 0.6$ .

In Figure 4-9 and Figure 4-10, we present the results for depolarizing Mueller where the anisotropic term corresponds to the incoherent addition of linear retarders. The first set of simulations, Figure 4-9 (a)-(f) correspond to the case of fixing the mean retardance  $\bar{\phi}$  and varying the standard deviation of both orientation ( $\sigma_\theta \in [0, 180]$ ) and retardance ( $\sigma_\phi \in [0, 180]$ ) angle. The weight of the isotropic term is  $\beta = 0.2$  for the first row and  $\beta = 0.6$  for the second row. We can compare these results with Figure 4-5 (a)-(b) in section 4.1.2, where the anisotropic characteristics are the same but  $\beta = 0$ . As in the previous case, the IPP dependence with the anisotropic parameters present the same structure as when no isotropic depolarization was present, the effect of the isotropic term is to decrease the IPP values in proportion to the weight of isotropic depolarization,  $\beta$ .

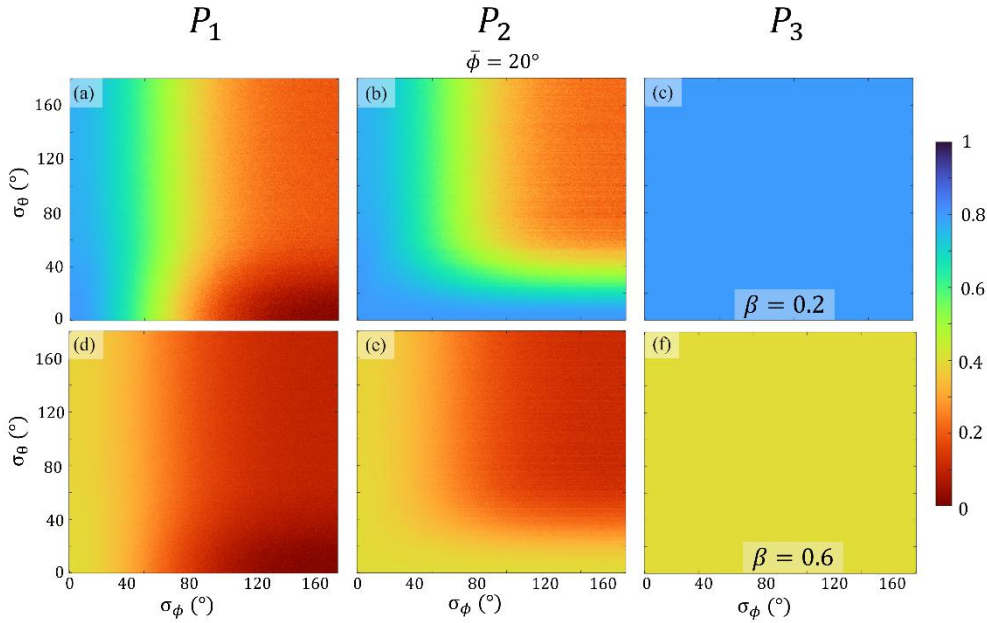


Figure 4-9 Results for the IPP values for simulated samples composed an anisotropic part (generated by the incoherent addition of linear retarders) and an isotropic part ( $diag(1,0,0,0)$ ). The  $x$  and  $y$  axes correspond to the values of variation of retardance  $\sigma_\phi$  and orientation  $\sigma_\theta$ , respectively for a constant value of retardance  $\bar{\phi} = 20^\circ$ . First row and second row correspond to  $\beta$  values of 0.2 and 0.6, respectively.

For a further analysis, in , Figure 4-9 (a)-(f), we show the results for the case of fixing  $\sigma_\phi = 0$  and varying  $\sigma_\theta$  in the range  $[0^\circ, 180^\circ]$  and the  $\bar{\phi} \in [0^\circ, 360^\circ]$ . The first and second row in this set of images correspond to  $\beta = 0.2$  and  $\beta = 0.6$ , respectively. Figure 4-6 represents the same simulation without the isotropic term ( $\beta = 0$ ). The results are in agreement to the ones described above.

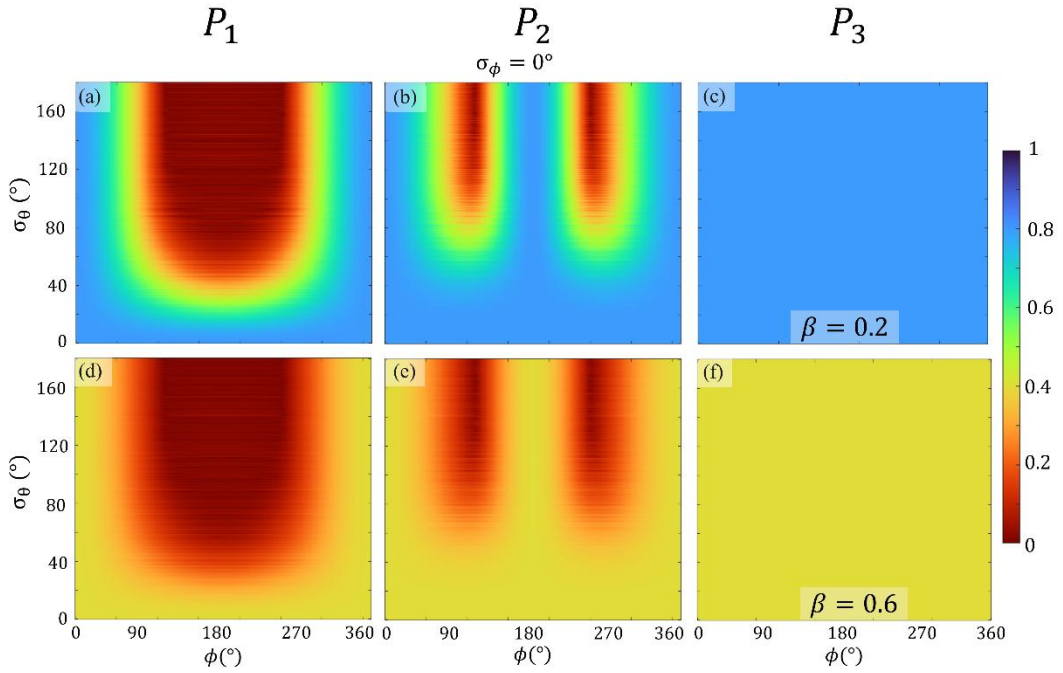


Figure 4-10 Results for the IPP values for simulated samples composed an anisotropic part (generated by the incoherent addition of retarders) and an isotropic part ( $diag(1,0,0,0)$ ). The  $x$  and  $y$  axes correspond to the values of retardance  $\bar{\phi}$  and orientation variation  $\sigma_\theta$ , respectively for a constant value of retardance variance  $\sigma_\phi = 0^\circ$ . First row and second row correspond to  $\beta$  values of 0.2 and 0.6, respectively.

Summarizing, we prove that the  $P_3$  channel of the IPP is sensitive to the contribution of the isotropic term, added to the simulations ( $\beta m_{00} \hat{M}_{iso}$ ), in depolarizing systems, whereas the  $P_2$  and  $P_1$  channels are suitable to study the anisotropic contribution, which is connected with the polarimetric features of constituent elements. Moreover, the effect of this term does not change the dependence of depolarization with the anisotropic control parameters, all the figures representing  $P_3$  for the presented examples show a homogeneous color, maintaining the independence of  $P_3$  values in the  $x$  and  $y$  axes values (and any other anisotropic related parameter). In contrast,  $P_3$  has a direct and linear dependence with  $\beta$  (see Figure 4-10).

This dependency between  $P_3$  and  $\beta$  can be obtained through the study of the Characteristic decomposition (Eq. (2-37)). Since  $\hat{M}_3 = \hat{M}_{iso}$ , by comparing Eq. (2-37) with Eq. (4-12) we can find the following relation:

$$\beta m_{00} \hat{M}_{iso} = (1 - P_3)(m_{00} \hat{M}_3) \quad (4-13)$$

and thus,  $\beta = 1 - P_3$ . This analytical result agrees with the values of  $P_3$  for the different simulations we shown in this section. Moreover, considering the relation between the weight of the anisotropic ( $\alpha_i$ ) and isotropic ( $\beta$ ) term (Eq. (4-10)) together with  $\beta = 1 - P_3$ , we obtain:

$$1 = \sum_i^{n'} \alpha_i + \beta = \sum_i^{n'} \alpha_i + (1 - P_3) \rightarrow \sum_i^{n'} \alpha_i = P_3. \quad (4-14)$$

With this, we can reformulate Eq. (4-12) and express the weight of each component in terms of  $P_3$ . To this aim, we define the following normalized Mueller matrix  $\hat{M}_A$ :

$$\sum_i^{n'} \alpha_i M_i = P_3 \hat{M}_A \rightarrow \hat{M}_A = \frac{1}{P_3} \sum_i^{n'} \alpha_i M_i. \quad (4-15)$$

Then, the equation can be written as:

$$M = P_3 m_{00} \hat{M}_A + (1 - P_3)(m_{00} \hat{M}_3), \quad (4-16)$$

where,  $\hat{M}_A$  is defined by Eq. (4-16) and  $\hat{M}_3 = \hat{M}_{iso}$ . Note that both the weights of the isotropic ( $m_{00} \hat{M}_3$ ) and anisotropic ( $m_{00} \hat{M}_A$ ) contributions in the final Mueller matrix are controlled by  $P_3$ . For  $P_3 = 1$  the isotropic term is zero (no isotropic depolarization), and thus, all the depolarization arises from anisotropic sources. In contrast, for  $P_3 = 0$  the anisotropic term is cancelled and the anisotropies of constituent elements do not contribute to depolarization. In such a case, all depolarization is due to the isotropic term, and corresponding samples behave as perfect depolarizers. In the intermediate regime  $0 < P_3 < 1$  both depolarizing origins (isotropic and anisotropic) coexist, and the predominant effect is set by the value of  $P_3$ , this is the more common scenario when measuring macroscopic biological samples. Under this scenario, we obtain an interesting and fundamental result, giving channel  $P_3$  a physical interpretation that can be very useful for easily discerning, based on polarimetric measurements, the origins of depolarization in real samples.

We also want to note that there are complex mechanisms in the sample-light interaction processes leading to isotropic depolarization. That is, isotropic depolarization can also be produced by anisotropic sources related to the samples composition, but with structures more complex than these above proposed (for instance, not restricting the elements to linear anisotropies). In some cases, the intrinsic microscopic components of a sample are able to randomize the polarization state of light transforming an incident fully polarized SoP to a fully depolarized state. However, even if this depolarization has an

anisotropic origin, the depolarization signature is the same for all the SoPs interacting with the sample. Therefore, it is still correct to classify it as isotropic depolarization because all the polarization states have the same result after interacting with the sample and thus, all the intrinsic information leading to depolarization is totally lost.

### 4.3 Experimental results

To prove the validity of the above-described simulations, in this section we provide some experiments where we mimic the simulated scenarios described in sections 4.1 and 4.2, representing anisotropic and isotropic depolarizing systems.

In the first experiment, we measured the Mueller matrix image of a radial polarizer (from Codixx). This element consists of 12 spatial sectors behaving as linear polarizers, each one of them with different orientations (see Figure 4-11 (a)). Each pixel of this element can be understood as a linear polarizer with the orientation corresponding to the spatial sector belonging to. To mimic the simulations of section 4.1.1, we select a region of interest (ROI) centered at the intersection of all the sectors (see the  $344 \times 471$  pixel white square in Figure 4-11 (a)) and containing pixels from all linear orientations present in the radial polarizer. Also, different ROIs were chosen in order to further validate the results. Then, the  $M$  of all the pixels within the ROI are added, this mimicking the incoherent addition of linear polarizers with different orientations (each one of the pixels in the ROI is equivalent to the  $M_i$  in Eq. (4-7)). This element can be considered as a diattenuator with large  $p_x$  value ( $p_x \sim 1$ ) and low  $p_y$  value ( $p_y \sim 0$ ). The orientation angle varies between 0 and  $2\pi$  through the different sectors, therefore we consider that the variation of the diattenuators angle in the ROI is  $2\pi$ .

To provide also the experimental proof for the retarders, the second experiment consists of measuring the Mueller matrix image of a liquid crystal q-plate (model WPV10-633 from Thorlabs; see Figure 4-11 (b)). This element is a patterned liquid crystal plate that can be understood as a linear retarder with a fixed retardance which depends on the illumination wavelength (ideally  $\pi$  radians for the wavelength of 633 nm) and whose neutral axes orientation changes with the spatial position, achieving orientations between 0 and  $2\pi$  [158]. In analogy as the diattenuator case, we calculate the total  $M$  by adding the Mueller matrices of all the pixels inside the ROI shown in Fig. (b) ( $344 \times 471$ ; see pink

rectangle). This result mimics the scenario discussed in sec. 4.1.2, where retarders with different orientations were added.

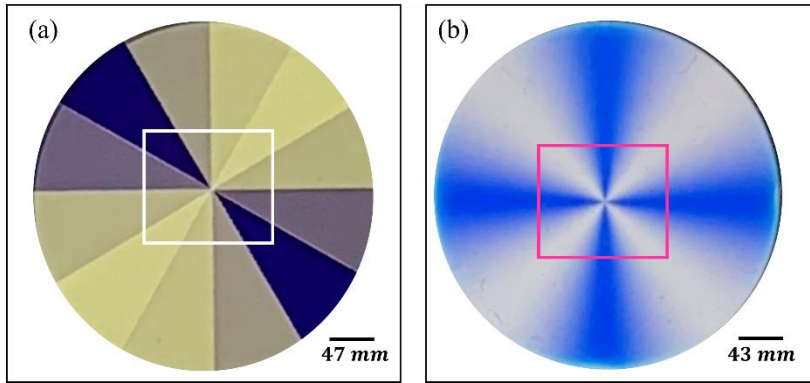


Figure 4-11 (a) Radial polarizer illuminated with linear polarization ( $45^\circ$ ), where each of the sectors indicates a different linear polarizer orientation (between 0 and  $2\pi$ ); each color in the polarizer sector represents a change in orientation of  $30^\circ$  with respect the previous sector. (b) Q-plate image; linear retarder (phase  $\pi$  for 633 nm of illumination) with different orientations, between 0 and  $2\pi$  represented by the color change in the Figure. In both cases, to see intensity variations associated with different orientations the elements are sandwiched between two crossed polarizers.

Note that the Mueller matrices resulting from the addition of the individual-pixels Mueller matrices within the select ROIs in Figure 4-11 (a) and (b) represent examples of the anisotropic depolarization samples, as they are constructed as the addition of non-depolarizing linear diattenuators or retarders with different control parameters (orientations in these cases).

For completeness, we also provide some cases of study showing isotropic depolarization. Therefore, we chose samples composed of elements producing isotropic scattering processes. The first sample is a diffuse reflector (Diffuser DG10-220-PO1, from Thorlabs) consisting of a N-BK7 substrate with a rough surface coated with a silver thin film. This roughness diffuses the light in all directions and acts as a source of isotropic depolarization. We also provide results for a second sample consisting of standard white paper. White paper is composed of sheets of a mat of random interwoven cellulose fibers with different orientations. This randomness in the paper composition makes this sample a possible source of isotropic scattering. These elements are measured with an illumination beam perpendicular to the surface of the samples, at 1500 nm for the silver diffuse reflector surface and 660 nm for the white paper. The white paper sample was measured by the Mueller polarimeter described in section 3.1, the radial polarizer and the q-plate were measured in the laboratory of Prof. Ignacio Moreno with the Mueller polarimeter described in ref. [158] and the diffuser was measured by Dra. I. Estévez in the University

of Minho (see Ref. [49] for more information of the polarimeter). In these cases, to compute the IPP values of these samples we chose a ROI centered in the image and calculated the mean value and standard deviation corresponding to each IPP. For the diffuser the ROI was  $70 \times 70$  pixels and in the case of the white paper it was a  $150 \times 150$ .

In the following table, the IPP experimental results for the four samples described above are presented:

	$P_1$	$P_2$	$P_3$
<i>Radial polarizer</i>	0.163	0.876	1
<i>Q plate</i>	0.288	0.727	1
<i>Diffuser</i>	$0.05 \pm 0.02$	$0.11 \pm 0.03$	$0.20 \pm 0.04$
<i>White paper</i>	$0.05 \pm 0.02$	$0.14 \pm 0.03$	$0.29 \pm 0.07$

Table 4-1 IPP results for the experimentally measured samples representing depolarizers comprised by anisotropic and isotropic depolarization contributions.

The first two rows of Table 4-1 show the results of the IPP for the radial polarizer and the Q-plate experiments. The IPP were calculated from the Mueller matrices of the samples measured with an illumination wavelength of 660 nm. Note that the IPP calculated from the total ROIs Mueller matrix, resulting from the incoherent addition of the  $M_s$  of the different pixels in the ROIs (see Figure 4-11), agree with the simulated results presented in sec. 4.1. In section 4.1 we analyzed anisotropic systems where the value of  $P_3$  is always equal to 1. In both cases inspected we obtain depolarization, since  $P_1$  and  $P_2$  are lower than 1, but  $P_3 = 1$  in both cases, as expected, confirming that the radial polarizer and the Q-plate based depolarizers are anisotropic depolarizers.

In Table 4-1, the last two rows correspond to the IPP results of experimental  $M_s$  obtained from the samples with isotropic depolarization contribution. As expected,  $P_3 \neq 1$  in both cases, showing the isotropic nature of the depolarization produced by these samples. The two examples show a high contribution of isotropic depolarization; the silver diffuse reflector achieves a value of  $P_3 = 0.200$  and the white paper  $P_3 = 0.294$ . The fact that  $P_3 \neq 0$  implies that the samples also have anisotropic depolarization contribution. The origin of the anisotropic depolarization must be related to the polarizing properties of the constituent elements. In the case of white paper, the cellulose fibers comprising the paper contribute to the anisotropic depolarization [42,159]. In the case of the silver diffuse



reflector, the anisotropic contribution can be due to the non-ideality of the fabrication process and some intrinsic polarimetric characteristics of the component elements. As for instance, the protection coating (silver) can present dichroic behavior. These intrinsic characteristics of the samples can explain the presence of anisotropic scattering. Note that the IPP values for the case of white paper and the diffuser reflector correspond to the mean value and standard deviation of each one of the indices in their respective selected ROIs. In the case of the radial polarizer and the q-plate, we obtain the  $M$  by means of the incoherent addition of the  $M$  in each one of the pixels. From this  $M$  we obtain only one value for each IPP, therefore this value has no deviation associated.

These results are in concordance with the discussion provided in sections 4.1 and 4.2, where we demonstrated that depolarization originated by unitary elements with polarizing features (dichroism or birefringence; related to physical anisotropies), are reflected on  $P_1$  and  $P_2$  channels, but  $P_3$  was equal to 1 in all the cases (anisotropic depolarization). To obtain response in the  $P_3$  parameter, the samples must have a contribution of isotropic depolarization, as proved with the second set of experimentally measured samples. Therefore, we prove the validity of our interpretation of the IPP parameters to characterize the polarization and depolarization response of the sample

#### 4.4 Interpretation of the results in the Purity Space and Characteristic decomposition

In section 2.3.1 we presented the Purity Space (see Figure 2-2), which is the 3D Space generated by the constraint inequalities among the IPP. This space contains the IPP of all the physically realizable depolarizers. Therefore, we find it interesting to represent the experimental results of the previous section in the IPP volume.

In section 4.1 we show the anisotropic depolarizers, comprised by incoherent addition of simple polarimetric elements such as diattenuators and retarders. We define anisotropic depolarization as depolarization due to the processes related to the polarizing properties of the constituent elements of samples. This polarization has a common characteristic in all the presented simulations, the value of the  $P_3$  parameter is independent of the constituent elements and is always equal to 1. This situation represents a particular and restricted position in the tetrahedron, the surface  $P_3 = 1$  is the top of the volume (see pink surface in Figure 4-12).

By changing the diattenuator and retarder characteristics we can achieve different values of  $P_1$  and  $P_2$ , that is, different spatial positions in the top surface of the tetrahedron ( $P_3 = 1$ ). We see that although we continuously increase the parameters responsible of

depolarization in anisotropic systems, we will never be able to reach a fully depolarizer ( $P_1 = P_2 = P_3 = 0$ ), neither any depolarizer out of the  $P_3 = 1$  plane, so a limit is imposed, where the depolarization performance (or the IPP decrease behavior) is saturated (as can be seen in Figure 4-5 for the retardance case). The specific value of the limit depends on the control parameters selected for the model, and numerically, we see that for retarder-based simulations it is around  $20^\circ$ .

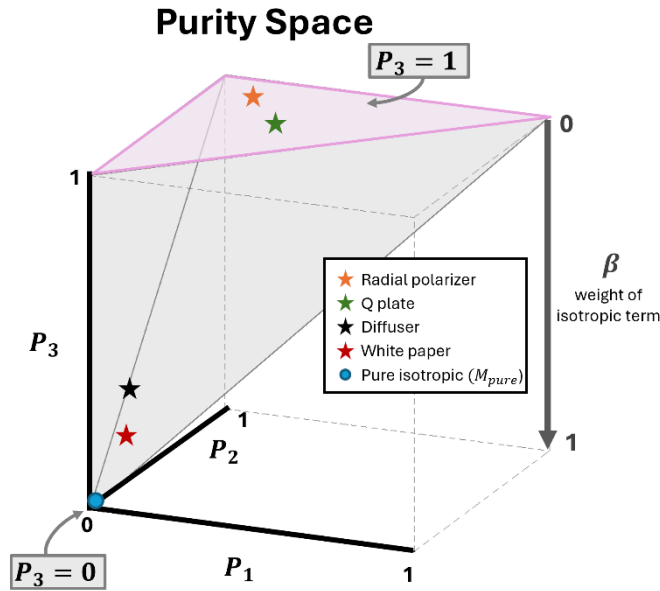


Figure 4-12 Representation of the IPP space, where all the physical realizable depolarizers are contained. The top (pink) surface represents the part of the tetrahedron where anisotropic depolarizers are located; the blue point (0,0,0) represents pure isotropic depolarizers. The stars correspond to the IPP values of the experimental samples measured. Orange, green, black and red stars correspond to the radial polarizer, q-plate, diffuser and white paper, respectively.

The points outside the top surface of the tetrahedron correspond to cases where the samples present certain isotropic depolarization content, that affects the value of  $P_3$ . Since  $P_3$  represents the height of the tetrahedron, the lower is the position of the Z axis of a depolarizer represented by a point within the tetrahedron volume, the lower is its corresponding  $P_3$  value. Samples with  $P_3 = 1$  contain only anisotropic depolarization, whereas the samples presenting only isotropic depolarization are located at the lowest point of the tetrahedron (see blue point in Figure 4-12). The rest of the volume contains samples presenting both depolarization sources. In section 4.2, we present the relation

between  $P_3$  and the weight of the isotropic depolarization term ( $\beta$ ):  $P_3 = 1 - \beta$ . That is, the  $P_3$  value decreases as  $\beta$  increases (see Figure 4-12). In this sense, the position of the points in the tetrahedron also have information of the different depolarizing sources predominance. As the points approach the isotropic depolarization point (i.e., the bottom of the volume), the more amount of isotropic depolarization they present.

The experimental results of section 4.3 are also plotted in Purity Space. The experimental anisotropic depolarizing samples (q-plate and radian polarizer) are located in the top surface of the volume ( $P_3 = 1$ ) and the samples presenting some amount of isotropic depolarization are located in positions at the lower part of the volume ( $P_3 \neq 1$ ). The orange and green stars in the top surface correspond to the radial polarizer (0.163, 0.876, 1) and the q-plate (0.288, 0.727, 1), respectively. However, the samples where some isotropic depolarization is present: the black star represents the diffuser (0.05, 0.11, 0.2) and the red star the white paper (0.05, 0.14, 0.29) are located in the lower part of the tetrahedron (see Figure 4-12).

This paves the way to the application of 3D Depolarization Spaces for sample classification according to the possible depolarization origins. For instance, in Ref. [160] further analysis of the relation between the location at the IPP Space of anisotropic depolarizers (in this case, in the top surface of the volume) and the polarimetric features of inherent elements in depolarizers were made. In addition, there are several examples using these volumes for the classification of structures within biological samples [41, 76, 111, 136]. For instance, in [140] different depolarizing spaces are inspected for the classification of different tissues within chicken samples (muscle, tendon and myotendinous junction). Also, C. Rodriguez in Ref. [41] used depolarizing spaces to discriminate different structures conforming plant samples, including the efficient classification of healthy and pathological tissue.

## Chapter 5 Depolarization Filter

Previous Chapter 4 presents a broad analysis of the relation between the IPP polarimetric parameters and different sources producing depolarization in samples, describing for the first time the isotropic and anisotropic depolarizing origins in samples. We showed how the anisotropic depolarization is originated by statistical variations of inherent polarimetric components constituting the samples, whereas isotropic depolarization is caused due to random light-matter interactions processes, which lead to a complete polarimetric information loss of any incident SoP on the sample. The study of these different sources of depolarization shed light on the idea that, while anisotropic depolarization retains relevant information about the polarimetric structures that characterize the samples, isotropic depolarization conceals such information. Therefore, implementing a mechanism that emphasizes anisotropic depolarization effects over isotropic ones in samples could hold significant potential for the characterization of depolarizing media. Recalling that, in this chapter we propose a method to filter the isotropic part and focus on the anisotropic response of the samples. By removing the isotropic depolarization content of Mueller matrices, we obtain a significant improvement in the visualization of sample structures and an increase in the contrast among different structures when inspecting polarimetric images. As will be shown in this section, polarimetric images obtained from filtered Mueller matrices surpass not only standard intensity images, but also current state-of-the-art of polarimetric imaging. It is worth noting that most of the analysis presented in this chapter corresponds to work provided in one of the articles included in this thesis [112]. In section 5.1 we present the implementation of the isotropic depolarization filter in a Mueller matrix. In addition, the effect of this filter in terms of some polarimetric observables of interest is provided in section 5.1.1 in the case of non-depolarizing metrics and 5.1.2 for the depolarizing ones. Also, it is very interesting

to study how the application of the filter affects the 3D Polarimetric Spaces (section 5.1.3). To conclude, in section 5.2 we present examples of the filter application in real biological samples both in terms of polarimetric imaging (section 5.1.2) and the Purity Space (section 5.2.2).

## 5.1 Isotropic Depolarization Filter

Real samples typically do not exhibit a purely isotropic or anisotropic depolarization response. Instead, they usually present a combination of both, showing a complex depolarization behavior that includes certain degrees of isotropic and anisotropic contributions (as a representative example, see discussion related to Table 5-1 in section 5.1.4). As previously stated, the effect of isotropic depolarization is to blur or hide information that can be obtained from the sample components and structure by means of a polarimetric analysis. As we explained in Chapter 4, isotropic depolarization completely depolarizes any incident SoP interacting with a sample. Therefore, when this kind of depolarization is present, the spatial and physical information of the sample is lost to certain extent (depending on the magnitude of the isotropic depolarization sample's response). To remove the isotropic influence from polarimetric analysis, in the following we propose the Isotropic Depolarization Filter (IDF).

To implement this filter, we start with Eq. (4-16) defined in the previous chapter:

$$M = P_3 m_{00} \hat{M}_A + (1 - P_3)(m_{00} \hat{M}_3), \quad (5-1)$$

where  $\hat{M}_A$  and  $\hat{M}_3$  encode the information related to anisotropic and isotropic depolarization, respectively. In this sense, the proposed filter consists of directly eliminating the isotropic part from  $M$ , subtracting the term  $(1 - P_3)(m_{00} \hat{M}_3)$  from the raw Mueller matrix:

$$M_a = M - (1 - P_3)(m_{00} \hat{M}_3) \quad (5-2)$$

where  $M_a$  denotes the filtered Mueller matrix. Note that the application of this filter is equivalent to impose the condition of  $P_3 = 1$  to Eq. (5-1), which corresponds to the scenario where no isotropic depolarization is present. Considering the Characteristic decomposition (Eq. (2-37)) we can identify  $M_a$  as the first three terms of such decomposition:

$$M_a = P_1(m_{00} \hat{M}_{J0}) + (P_2 - P_1)(m_{00} \hat{M}_1) - (1 - P_2)(m_{00} \hat{M}_2). \quad (5-3)$$

Therefore, the application of the isotropic depolarization filter eliminates the element in the decomposition representing isotropic depolarization ( $\hat{M}_3$ ).

As said, the filtered Mueller matrix  $M_a$  only encodes the anisotropic information of a sample. In this sense, the polarimetric observables that are traditionally computed directly from the raw Mueller Matrix can also be applied to the filtered matrix  $M_a$ . This allows us to investigate whether the removal of isotropic depolarization components enhances the contrast in the resulting observables. To do so, it is important to note that the filtered matrix  $M_a$  and the unfiltered Mueller Matrix  $M$  are identical except for the first element,  $m_{00}$ . This becomes evident when analyzing the relationship given in Eq. (5-2), if taking into account that  $\hat{M}_3 = \text{diag}(1,0,0,0)$ . Under this scenario, the relation between the elements of the Mueller matrix before ( $m_{ij}$ ) and after ( $m_{aij}$ ) applying the filter is given by  $m_{ai,j} = m_{i,j}$ , except for the case  $i = j = 0$ , which follows the relation:

$$m_{a00} = m_{00} - (1 - P_3)m_{00} = P_3m_{00}. \quad (5-4)$$

Once we have obtained in Eq. (5-4) the explicit relation between the Mueller matrix elements before and after applying the filter, the next step before obtaining the polarimetric observables is to normalize  $M_a$ . The normalization of the matrix consists of dividing all elements of the matrix by the previously obtained factor  $P_3m_{00}$ :

$$M_a = P_3m_{00} \begin{pmatrix} 1 & \frac{m_{01}}{P_3m_{00}} & \frac{m_{02}}{P_3m_{00}} & \frac{m_{03}}{P_3m_{00}} \\ \frac{m_{10}}{P_3m_{00}} & \frac{m_{11}}{P_3m_{00}} & \frac{m_{12}}{P_3m_{00}} & \frac{m_{13}}{P_3m_{00}} \\ \frac{m_{20}}{P_3m_{00}} & \frac{m_{21}}{P_3m_{00}} & \frac{m_{22}}{P_3m_{00}} & \frac{m_{23}}{P_3m_{00}} \\ \frac{m_{30}}{P_3m_{00}} & \frac{m_{31}}{P_3m_{00}} & \frac{m_{32}}{P_3m_{00}} & \frac{m_{33}}{P_3m_{00}} \end{pmatrix}. \quad (5-5)$$

After normalization, all the elements in  $M_a$  (except the first element that becomes equal to 1) are affected by the factor  $P_3m_{00}$ , this being considered as the filtering operation. Importantly, each element is divided by  $P_3$ , showing a dependence in this parameter, which, it should be recalled, determines the weight of the isotropic depolarization component in the sample. The effect of this division on the different  $M$  elements is relevant in samples presenting significant spatial variations of their polarimetric features. When studying these kinds of samples, the associated polarimetric observables depend on the spatial position, in some cases, including, the  $P_3$  parameter, that as seen, directly impact in the filtering process. Hereafter, to make explicitly this spatial dependence of the polarimetric observables, we will write them as  $f(x, y)$ , including the particular case of  $P_3(x, y)$ .

In the following, we present the effect of the Isotropic Depolarization Filter (IDF) on the different non-depolarizing and depolarizing observables of interest. In particular, the polarimetric observables correspondent to non-depolarizing channels that will be analyzed are diattenuation ( $D$ ) and polarizance ( $P$ ). The depolarizing channels correspond to the IPP ( $P_1, P_2$  and  $P_3$ ), depolarization index ( $P_\Delta$ ) and Spherical Purity index ( $P_S$ ). From now on, we will denote the filtered observables as  $X'$ . The selection of these observables was based on the most common channels used in literature when inspecting biological tissues and also, the ones leading to the best results in terms of contrast enhancement.

The study of the filter effect in the birefringence properties is not as straightforward as the cases above explained for dichroic or depolarizing metrics. For samples presenting both retardance and depolarization contribution, the obtaining of retardance observables cannot be directly calculated from the direct combination of the elements of  $M_a$ . In fact, to obtain the retardance parameters from  $M$  it is necessary to further process the data, as for instance, by applying the Lu-Chipman [131], the Arrow [132] or the Symmetric decomposition [161]. The obtention of an analytical expression for the relation between the filtered retardance observable and  $P_3(x, y)$  observable is not trivial in any of these decomposition cases, leading to intricate nonlinear dependencies between these two observables. However, as we can calculate retardance observable images from filtered experimental Mueller matrices, by following a heuristic approach, we tested the effect of the filter on resulting image contrast enhancement and structure unveiling in a wide number of biological samples through filtered retardance based images. With this, we can hypothesize that the contrast enhancement is notably lower than in observables related to dichroic and depolarization properties when inspecting biological samples. For this reason, the analysis of the effect of the filter on the retardance channel is not included in this thesis.

### 5.1.1 Non-depolarizing channels: Dichroic and Retardance properties

The main polarimetric observables related to dichroic properties of samples are the diattenuation ( $D$ ) and polarizance ( $P$ ). In section 2.2, we explain in detail how to obtain these parameters from the elements of  $M$ . In this case,  $P$  and  $D$  are obtained directly from the Mueller matrix elements without any additional transformation. In particular, the diattenuation vector corresponds to the first row of  $M$  and the polarizance vector to the first column. In Eq. (5-5), diattenuation and polarizance vectors correspond to the blue and green rectangles, respectively. The expressions for  $P$  and  $D$  (in modulus) after the application of the filter are:

$$D' = \frac{\sqrt{m_{01}^2 + m_{02}^2 + m_{03}^2}}{m_{00}P_3}, \quad P' = \frac{\sqrt{m_{10}^2 + m_{20}^2 + m_{30}^2}}{m_{00}P_3}. \quad (5-6)$$

Thus, the relation between these observables before (see Eq. (2-6)) and after the filter is clear:

$$D'(x, y) = \frac{D(x, y)}{P_3(x, y)}, \quad P'(x, y) = \frac{P(x, y)}{P_3(x, y)}. \quad (5-7)$$

The effect of the filter in the dichroic observables is the division of the original values by  $P_3(x, y)$ . This implies that, the higher is the isotropic depolarization (lower  $P_3$  value) the higher the increase in the variables can be after filtering. Of course, taking into account the spatial dependence  $(x, y)$  in polarimetric images, this filtering effect helps not only in the enhancement of contrast but also to reveal some structures hidden due to a high amount of isotropic depolarization.

Finally, note that birefringence can be a channel of interest for the study of some features of biological samples. However, for the above-mentioned we do not deepen in its study.

### 5.1.2 Depolarizing channels

As we mentioned in the introduction, the indices of polarimetric purity (IPP) are depolarizing parameters well known for their excellent performance when inspecting biological tissues. In addition, in Chapter 4, we provided a study of the relation between each one of these indices and fundamental physical characteristics of biological tissues leading to depolarization. In this context, it is very useful to inspect how the filter also affects the IPP parameters, which is the main goal of this subsection. In addition, we also study the effect on two additional depolarization metrics that are also widely used in the inspection of biological samples: the depolarization index ( $P_\Delta$ ) and the degree of spherical purity ( $P_S$ ).

To calculate the IDF effect in the IPP we recall the theoretical framework explained in Chapter 2. To obtain the IPP we need to work with the eigenvalues of the transformed matrix  $H(M)$ , therefore we need to obtain the filtered covariance matrix,  $H(M_a)$ . The elements of the covariance matrix are calculated by the linear combinations of different elements of  $M$ , and importantly, the  $m_{00}$  element is only present in the diagonal of  $H$  (see Eq. (2-21)). These will be the only elements affected by the filter, and we can obtain  $H(M_a)$  as:

$$H(M_a) = H(M) - (1 - P_3)(m_{00}\mathbb{I}), \quad (5-8)$$



where  $\mathbb{I}$  corresponds to the identity matrix ( $diag(1,1,1,1)$ ). Then, we need to calculate the eigenvalues of  $H(M_a)$ ,  $\lambda'_i$ , for the obtention of the filtered IPP. The diagonalization calculus for the filtered covariance matrix can also be related to the matrix before filtering:

$$\begin{aligned} H(M_a) - \lambda' \mathbb{I} &= 0 \rightarrow H(M) - (1 - P_3)(m_{00} \mathbb{I}) - \lambda' \mathbb{I}, \\ H(M) - (\lambda' + (1 - P_3)m_{00}) \mathbb{I} &= 0; \end{aligned} \quad (5-9)$$

$$\lambda = \lambda' - (1 - P_3)m_{00}, \quad (5-10)$$

where  $\lambda$  and  $\lambda'$  correspond to the eigenvalues of  $H(M)$  and  $H(M_a)$ , respectively. With the relation between the eigenvalues before and after the filter we can calculate the effect of the filter in the IPP. The Indices of Polarimetric Purity are defined in terms of the eigenvalues as (see section 2.2.4.1):

$$P_n = \frac{1}{trH} \sum_{k=1}^n k \Delta \lambda_k, \quad n = 1, 2, 3; \quad (5-11)$$

where  $\Delta \lambda_k = \lambda_{k-1} - \lambda_k$  and  $trH = m_{00}$ . Therefore, with these relations and the equation (5-12), the filtered IPP can be obtained as:

$$\begin{aligned} P'_n &= \frac{1}{trH(M_a)} \sum_{k=1}^n k \Delta \lambda_{ak} = \frac{1}{P_3 trH} \sum_{k=1}^n k \Delta \lambda_k = \frac{1}{P_3} P_n \\ &\downarrow \\ P'_n(x, y) &= \frac{P_n(x, y)}{P_3(x, y)}, \end{aligned} \quad (5-12)$$

where  $\Delta \lambda_{ak} = (\lambda_{k-1} - P_3) - (\lambda_k - P_3) = \lambda_{k-1} - \lambda_k = \Delta \lambda_k$ .

Therefore, we can conclude that the effect of the filter in the IPP is the same as for the dichroic variables (Eq. (5-7)); the value of the filtered indices increases by an amount given by  $1/P_3$ :

$$P'_1(x, y) = \frac{P_1(x, y)}{P_3(x, y)}, \quad P'_2(x, y) = \frac{P_2(x, y)}{P_3(x, y)}, \quad P'_3(x, y) = \frac{P_3(x, y)}{P_3(x, y)} = 1. \quad (5-13)$$

Secondly, the spherical purity index can be obtained directly from the elements of  $M$  as shown in Eq. (2-9). Therefore, in this case, by taking into account the relation between the Frobenius norm of  $m$  before and after filter,  $\|m'\|_2 = \|m\|_2/P_3$  the effect of the filter in  $P_S$  is straightforward:

$$P'_S = \frac{\|m'\|_2}{\sqrt{3}} = \frac{\|m\|_2}{P_3\sqrt{3}} \rightarrow P'_S(x, y) = \frac{P_S(x, y)}{P_3(x, y)}. \quad (5-14)$$

In the case of the depolarization index,  $P_\Delta$ , this can also be obtained from the  $M$  elements. However, since it is the index encoding the overall depolarization of the sample, it can also be calculated by means of the IPP and the CP observables. For instance, we can use the equation in terms of IPP (Eq. (2-38)):

$$P'_\Delta = \sqrt{\frac{2P_1'^2}{3} + \frac{2P_2'^2}{9} + \frac{P_3'^2}{9}} = \frac{1}{P_3} \sqrt{\frac{2P_1^2}{3} + \frac{2P_2^2}{9} + \frac{P_3^2}{9}} \rightarrow P'_\Delta(x, y) = \frac{P_\Delta(x, y)}{P_3(x, y)}. \quad (5-15)$$

Considering the results obtained in subsection 5.1.1, as well as for the depolarizing observables studied in this section (IPP,  $P_S$  and  $P_\Delta$ ), we can conclude that the effect of the IDF on depolarizing or dichroic channels is the same, responding to the general relation

$$f'(x, y) = \frac{f(x, y)}{P_3(x, y)}. \quad (5-16)$$

### 5.1.3 Dichroic and depolarizing Arrow parameters

In this subsection we want to make a special remark on the non-retardance parameters that we can extract from the Arrow decomposition. Note that these parameters ( $a_1, a_2, a_3$ ) are not encoding only depolarization or dichroic information, but a mixture of both contributions.

Then, the non-retardance parameters that we can extract from the Arrow decomposition of  $M$  are also studied. For the same reasons previously exposed in this chapter, in this case we are not interested in observables encoded in the entrance and exiting retarders) and we focus on the  $M_A(M)$  term, encoding dichroism and depolarization parameters. From Eq. (2-14) we have:

$$M'_A(M') = m_{00} \begin{pmatrix} 1 & D_A^T \\ P_A & m_A \end{pmatrix}; \quad m_A = \text{diag}(a_1, a_2, a_3). \quad (5-17)$$

In this case, the diattenuation and polarizance vectors correspond to the first row and column of  $M_A$ , respectively. The effect of the filter in each of the elements of the filtered normalized  $M_A$  is the same as the shown in Eq. (5-5):

$$M'_A(M') = P_3 m_{00} \begin{pmatrix} 1 & \frac{D_A^T}{P_3 m_{00}} \\ \frac{P_A}{P_3 m_{00}} & m'_A \end{pmatrix}; \quad m'_A = \frac{1}{P_3 m_{00}} \text{diag}(a_1, a_2, a_3). \quad (5-18)$$

Then, the effect on the dichroic observables obtained from the Arrow decomposition is equivalent to that we calculated on the complete  $M$  (see Eq. (5-7)), and filtered and non-filtered observables can be related as:

$$D'_A(x, y) = \frac{D_A(x, y)}{P_3(x, y)}, \quad P'_A(x, y) = \frac{P_A(x, y)}{P_3(x, y)}. \quad (5-19)$$

Next, we study the arrow parameters  $(a_1, a_2, a_3)$ , encoding depolarization and dichroic information. From Eq. (5-18) the effect of the filter in the arrow parameters is straightforward:

$$a'_1(x, y) = \frac{a_1(x, y)}{P_3(x, y)}, \quad a'_2(x, y) = \frac{a_2(x, y)}{P_3(x, y)}, \quad a'_3(x, y) = \frac{a_3(x, y)}{P_3(x, y)}. \quad (5-20)$$

Summarizing, in all the studied polarimetric parameters the effect of the polarimetric filter is given by the factor  $P_3(x, y)^{-1}$ . Therefore, the application of the filter is of special interest when analyzing spatial variations across the regions of interest. The effect in contrast enhancement is particularly relevant for small values of  $P_3$ , which is very common in macroscopic images of biological samples [84,139,141,155].

In the following we will also study the effect of the IDF in the 3D Polarimetric Spaces described in section 2.3, taking special attention to the space conformed by the IPP.

#### 5.1.4 Polarimetric Spaces after IDF

In sections 5.1.1 and 5.1.2 we showed the effect of the filter on different polarimetric observables. We also showed that when dealing with samples presenting significant depolarization behavior, the IDF has the potential to increase the contrast and discriminatory capability of different sections in polarimetric images. To reinforce this statement from a visual perspective, it is interesting to study the effect of the filter on the 3D polarimetric spaces described in section 2.3.

As explained before, the application of the IDF to the IPP values related to a given sample leads to the filtered IPP', which are calculated according to Eq. (5-21). As seen in such equation, the filtered  $P'_1$ ,  $P'_2$  and  $P'_3$  observables are equal to the original IPP observables but multiplied by the factor  $P_3^{-1}$ , and therefore, the  $P'_3$  observable is always equal to one. The fact that independently of the spatial heterogeneity of the  $P_3(x,y)$  image associated to a sample, its corresponding filtered observable is always transformed to 1 (i.e.,  $P'_3(x,y) = 1$ ) has a strong effect in the transformed data distribution: given a cloud of data represented in the Purity Space, corresponding to an imaged sample, when this collection of data is transformed to the filtered IPP' framework, the new collection of data will be always restricted to the top surface of the Purity Space, which corresponds to the anisotropic depolarization surface since isotropic depolarization content has been removed.

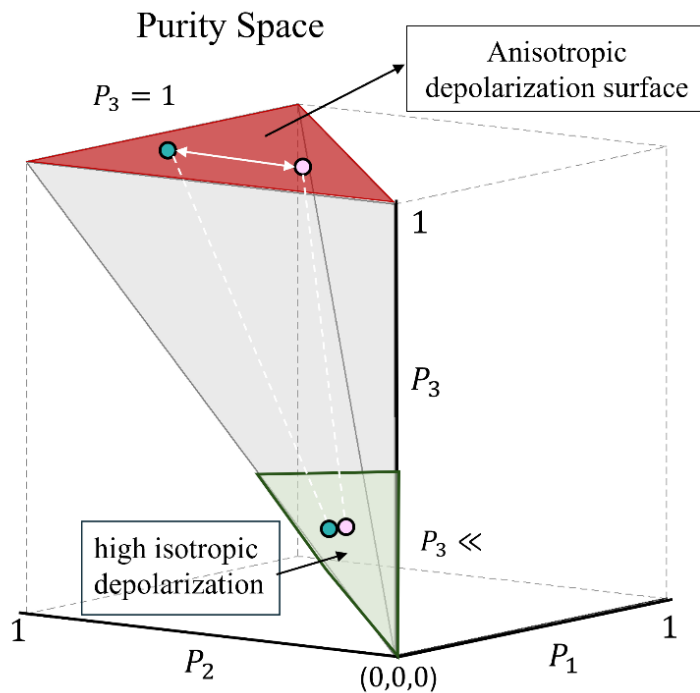


Figure 5-1 Representation of the IPP space. The red surface corresponds to the plane  $P_3 = 1$ , corresponding to the anisotropic depolarization space (no isotropic depolarization). The volume marked in green corresponds to the part of the space where samples with high amount of isotropic depolarization are located ( $P_3 \ll$ ).

Under this scenario, the effect of the filter in the IPP data makes a dimension reduction in the Purity Space; from a 3D volume (the entire IPP tetrahedron volume) before applying the filter to a 2D plane (anisotropic depolarization surface) after the filter application. Although this may seem counterproductive in terms of contrasting two structures with

different depolarizing responses —since the filter confines two data clouds distributed within a volume to a plane— it is often highly beneficial for discrimination purposes, as the anisotropic plane is the largest plane parallel to the  $z = 0$  plane, within the entire volume. In particular, when dealing with highly depolarizing samples, as is the case of numerous biological tissues, the whole image content is confined close to the point in the Purity Space (corresponding to an ideal depolarizer, see Figure 5-1). Therefore, all the information associated with different structures within the sample—despite exhibiting distinct depolarizing responses (i.e., different values for  $P_1$  and  $P_2$  metrics)—occupies a very small volume, which implies that these structures are located very close to each other or even overlap. In contrast, when this type of sample is processed using the filter, the data distribution is represented in the plane defined by  $P_3 = 1$ . In this representation, the differences associated with distinct expressions of  $P_1$  and  $P_2$  are maximized, allowing for a much clearer differentiation between the various structures.

To highlight this situation, in the following table we present some examples of the IPP values corresponding to different biological structures measured throughout this thesis:

Sample	Wavelength (nm)	$P_1$	$P_2$	$P_3$
Skin (pork)	625	0.0658	0.0976	<b>0.1313</b>
Brain <i>wm</i> (cow)	470	0.0268	0.0413	<b>0.1249</b>
Brain <i>gm</i> (cow)	470	0.1552	0.1943	<b>0.4201</b>
Epiglottis (cattle)	625	0.0718	0.2019	<b>0.2491</b>
	530	0.1307	0.2037	<b>0.3257</b>
	470	0.1541	0.2109	<b>0.3468</b>
Tong (cattle) muscle exterior	625	0.0886	0.1836	<b>0.2451</b>
	530	0.1887	0.3463	<b>0.4550</b>
	470	0.1584	0.2858	<b>0.4202</b>
Tong (cattle) muscle interior	625	0.0437	0.1292	<b>0.1971</b>
	530	0.0760	0.1290	<b>0.2222</b>
	470	0.0623	0.1134	<b>0.2434</b>
Heart (cattle) myocardium	625	0.1150	0.1790	<b>0.3200</b>

Table 5-1 IPP results for some biological samples before applying the IDF.

Results presented in Table 5-1 highlight the strong depolarization response of different biological samples. The table includes the mean values of each one of the indices of polarimetric purity in a set of biological tissues. In the last column of the table, we can inspect the values of  $P_3$ . These values range from 0.1 to 0.45, the most common ones

being around 0.1 – 0.2. To illustrate how the corresponding data is represented in the Purity Space, in Figure 5-1 we highlight a green volume corresponding to values of the IPP lower than 0.4. Therefore, we can anticipate that in such cases, the application of the IDF can be beneficial in terms of discriminatory capability, as data distribution confined in a small volume will be spread through the  $P_3 = 1$  plane. This effect is exemplified in Figure 5-1, where the blue and pink points located in the green volume represent two different structures within a hypothetical sample before applying the IDF. These points represent high depolarizing samples. When filtering the IPP values corresponding to these two points in the Purity Space, the new transformed data is relocated at the anisotropic  $P_3 = 1$  plane (red surface) and its corresponding separation is significantly increased. This situation is highlighted by the white arrow indicating the separation between the blue and pink points after the filtration process.

The effect of the filter on the Components of Purity Space (Figure 2-3) is not as direct and intuitive as in the Purity Space. In this case, the variables conforming the volume  $(P, D, P_3)$  after the filter application are once again transformed by the factor  $P_3^{-1}$  (see Eqs. (5-7) and (5-14)), but in this case, the data transformed is not confined in a plane but in a limited volume. We can estimate the possible usefulness of the filter in this space recalling the relation which provides surfaces with constant  $P_\Delta$  [143]. In this vein, in section 2.3.2 we showed that the higher the value of  $P_\Delta$ , the larger the available surface where different depolarizers with a given fixed  $P_\Delta$  can be represented in the CP Space. Therefore, recalling the relation between  $P_\Delta$  and the IPP (Eq. (2-38)), the effect of the filter is to increase the value of  $P'_\Delta$ , maximizing the surface of representation. In section 5.2.2 we show some examples of how this can be highly useful for real biological samples examination.

## 5.2 Applications of IDF to biological samples

In the following, we present some representative examples of how the application of the isotropic depolarization filter is useful for the enhanced visualization of biological tissues. We present a set of three samples from *ex-vivo* animal tissue obtained from a local slaughterhouse. In particular, two different sections from *ex-vivo* cattle heart (Figure 5-2 (a)-(b) and (e)-(f)) and a section from *ex-vivo* cattle tongue (Figure 5-2 (c)-(d); the physiological characteristics of the samples are described in detail in section 3.2). Figure 5-2 presents the non-polarimetric intensity ((a), (c) and (e)) images and the  $P_3$  ((b), (d) and (f)) images of the samples. The Mueller matrices for the three samples were obtained with the Polarimeter shown in section 3.1 and for an illumination wavelength of 625 nm.

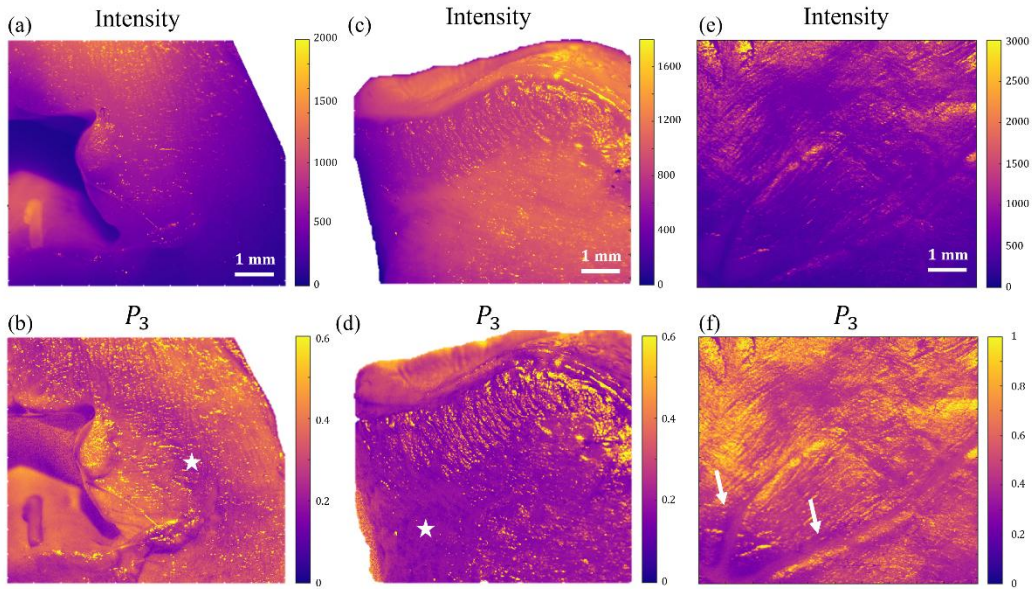


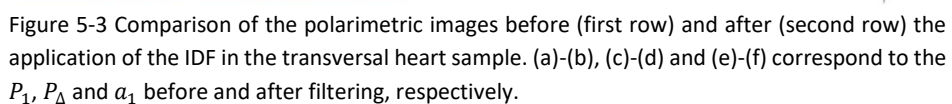
Figure 5-2 Intensity (a), (c) and (e) and  $P_3$  (b), (d) and (f) images of three different biological samples. (a)-(b), (c)-(d) and (e)-(f) correspond to transversal section of myocardium, transversal section of tongue and adventitia on epicardium with coronary artery paths, respectively.

Figure 5-2 shows how polarimetric images ( $P_3$  channel) reveal some biological structures which are invisible in the non-polarimetric intensity images. For instance, in Figure 5-2 (b) and (d), white stars indicate regions which were not visible in the correspondent intensity images (a) and (c), respectively. In Figure 5-2 (f) the white arrows indicate the same structures enhancement. Interestingly, all these marked regions, which were not detected by standard image methods, correspond to structures in the samples with different compositions and/or orientations. Thus, structural spatial variations in samples, and different compositions, alignments or other features related to the microscopic structure of the regions, lead to different depolarizing responses, thus helping to enhance the visualization of these different structures through polarimetric means. In addition, the contrast between some structures conforming the sample increases when using polarimetric methods.

Although the use of depolarizing channels such as  $P_3$  already demonstrates improved visualization of structures compared to standard intensity images, the spatial variation shown in the  $P_3$  images and the high depolarization response observed in the three samples under analysis make them excellent candidates for testing with the proposed filter. In the next section, we show the effect of the filter by comparing polarimetric observables before and after the filter application. With these results it is clear the



### 5.2.1 Filtered vs non-filtered images: application of the IDF to biological samples imaging





In this section, we present the results of applying the IDF to the three samples shown in Figure 5-2. For each one of them we select the three polarimetric observables leading to the best results when comparing the observables before and after the filter.

Figure 5-3 corresponds to the transversal section of the heart sample; Figure 5-4 shows the results of a transversal cut of tongue and Figure 5-5 an external view of the heart representing the pericardium where coronary arteries are located. In the three cases, the polarimetric images leading to the best results comparing the situation before-after filtering, correspond to metrics directly related to depolarization:  $P_1, P_\Delta$  and  $a_1$  for the transversal heart sample;  $a_1, P_1$  and  $a_3$  for the tongue sample and  $a_1, P_2$  and  $P_s$  for the pericardium heart sample.

Figure 5-3 shows the images correspondent to the transversal section of the heart sample. In the intensity image (see Figure 5-2 (a)) the sample appears as homogeneous tissue. Then, spatial differences in the image are observed when inspecting the polarimetric  $P_3$  image, correspondent to the existence of different structures and fiber organization across the sample. This dependence is also observed in Figure 5-3 for the three depolarizing channels inspected (first column). In this case Figure 5-3 (a)-(b) and (c)-(d) correspond to the depolarization parameters  $P_1$  and  $P_\Delta$  and (e)-(f) with the arrow parameter  $a_1$ , in each case, before and after filter respectively. Note that the results of the filter observables largely overcome the results obtained with conventional polarimetric images. The most interesting image to analyze is  $P'_1$  (Figure 5-3 (b)), where we can identify four different structures with larger contrast than in any other channel: subendocardium (*se*), endocardium (*e*), myocardium (*my*) and epicardium (*ep*). Interestingly, these regions correspond to different types of tissue: the myocardial tissue is composed of concentrically arranged fascicles of myocardial muscle whereas subendocardial tissue, composed of loose connective tissue and Purkinje fibers; the endocardium corresponds to a transition structure between *se* and *my* and the epicardium which corresponds to the outer wall of the heart and is composed by mesothelial cells, fat and connective tissue is also unveiled by the filter application. Therefore, the anisotropic depolarization characteristics of the tissue, highlighted after the filter application, gives a clear distinction between all the different layers comprising the sample.

In addition, in Figure 5-3 (b) and (f) we can appreciate a structure which corresponds to the endocardium (marked with white asterisks in both images). Finally, the epicardium is also unveiled by the filter application (see white dashed lines in the filtered observables (b) and (d)) and the boundaries between *my* and *ep* become clearer. That is, the application of the filter not only increases the visualization of structures that were barely visible in the

standard polarimetric images (in particular, the contrast is enhanced by an amount  $P_3^{-1}$ ) but also unveils new structures that were not previously observed.

A second example is studied in Figure 5-4, where we show the comparison between three polarimetric observables before (first column) and after (second column) the application of the IDF in the tongue sample. In this case, the observables that lead to the best results when applying the filter correspond to two of the arrow parameters ( $a_1$  and  $a_2$ ) and the  $P_1$  index.

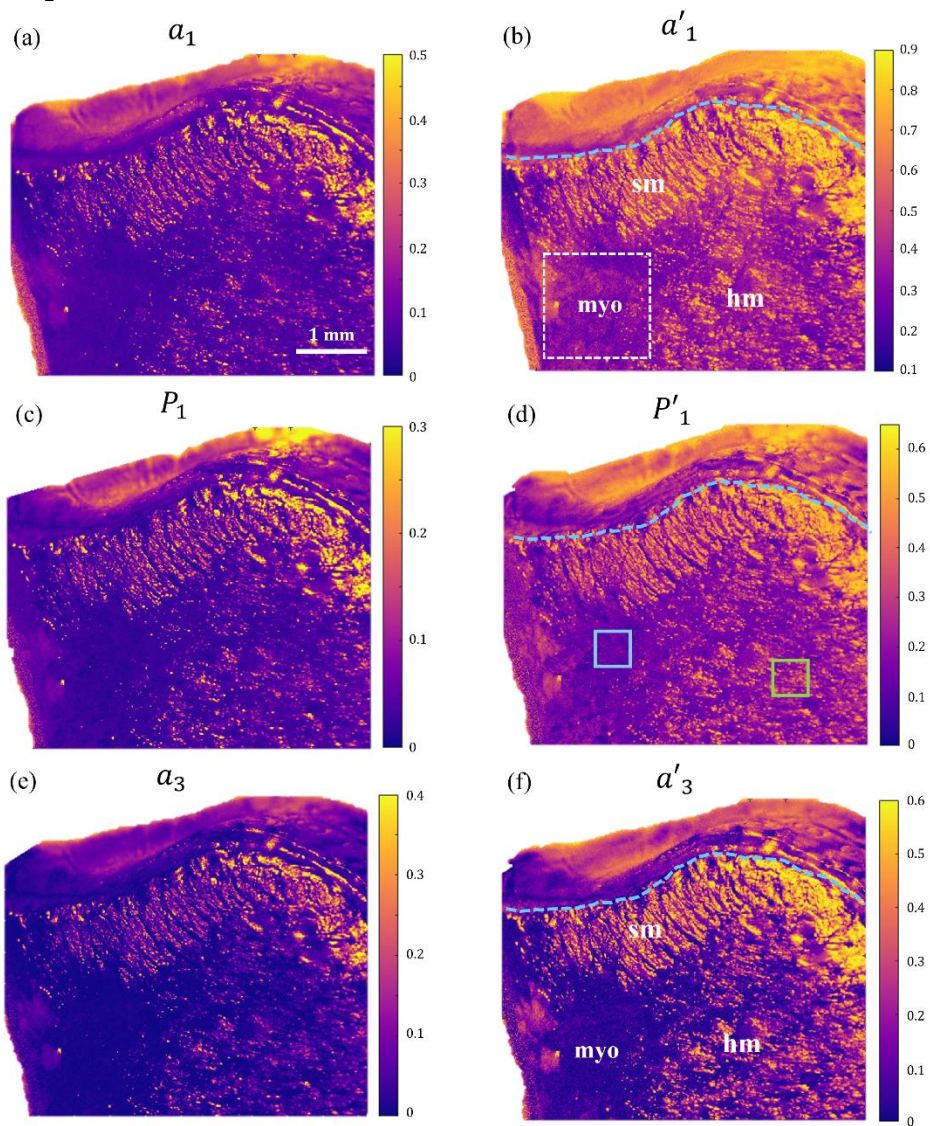


Figure 5-4 Comparison of the polarimetric images before (first row) and after (second row) the application of the IDF in a transversal section of the tongue. (a)-(b), (c)-(d) and (e)-(f) correspond to the  $a_1$ ,  $P_1$  and  $a_3$  before and after filtering, respectively.

In the conventional intensity image (see Figure 5-2 (c)), we identify two differentiated regions in the tongue (which correspond to muscles with different directionalities). When inspecting the non-filtered isotropic depolarization response,  $P_3$  image (Figure 5-2 (d)), this reveals a third new region (see white star in Figure 5-2 (d)) not detected with the standard intensity image. The region marked with the white star can be also seen in the depolarization observables of Figure 5-4 (a), (c) and (d) before filtering. In turn, when analyzing the filtered images (Figure 5-4 (b), (d) and (f)) we observe a larger contrast between different structures present in the sample, and importantly, the boundaries between them are better defined. In particular, the region marked as *sm* corresponds to styloglossus muscle, which is a longitudinal muscle, being perpendicular to the cut, whereas *hm* is the hyoglossus muscle, following a direction perpendicular to the cut. The depolarization response of these muscles depends on the directionality of the fibers comprising them. Moreover, the structure denoted as *myo* corresponds to myotendinous tissue. Although this structure has a different physiological composition than the muscle tissue, the standard intensity image was incapable to discriminate between these two tissue classes. Additionally, it is clear that in the filtered  $a'_1$  image, the contrast between the *sm*, *myo* and *hm* regions is larger compared to the images before the filter application. Note that, also in Figure 5-4 (f), these three regions are clearly differentiated by the  $a'_3$  depolarized observable. Interestingly, these three regions correspond to different physical properties of the tissue. The filtered polarimetric images, especially in the  $a'_3$  parameter in Figure 5-4 (f), show excellent results in terms of differentiating the myotendinous tissue from the muscles in the different directions (*sm* and *hm*) due to its high depolarization capability. In addition, the filter application also helps to delimit the external wall of the tongue, which corresponds to the epithelium (see blue dashed lines in Figure 5-4 (b), (d) and (f)).

The last sample we present corresponds to an external view of the heart, the pericardium of the heart with coronal arteries. In this case, the response of the sample in the intensity image (Figure 5-2 (e)) shows a tissue that seems completely homogeneous. Conversely, the  $P_3$  image reveals a distinct isotropic depolarization response across different regions of the sample. Then, when applying the filter, resulting polarimetric images (in this case  $a_1$ ,  $P_2$  and  $P_3$ ) unveil very interesting structures within the sample. For instance, in Figure 5-5 (e) the filtered polarimetric image  $P'_2$  can clearly detect the path of two of the coronary arteries and their adventitia (connective tissue, recovering the arteries walls, see white dashed lines in the figure). In addition, we can also observe differentiated structures in the region of the sample marked with a white star. This region states the presence of myocardial tissue having a different polarimetric response than the rest of the tissue. Also, the response of the walls from the coronal artery 2 has a higher depolarization

response than those from 1. This also means that we are able to infer information from the arteries directionality, the artery (1) is entering inside the tissue (towards the myocardium) whereas the other one is more superficial.

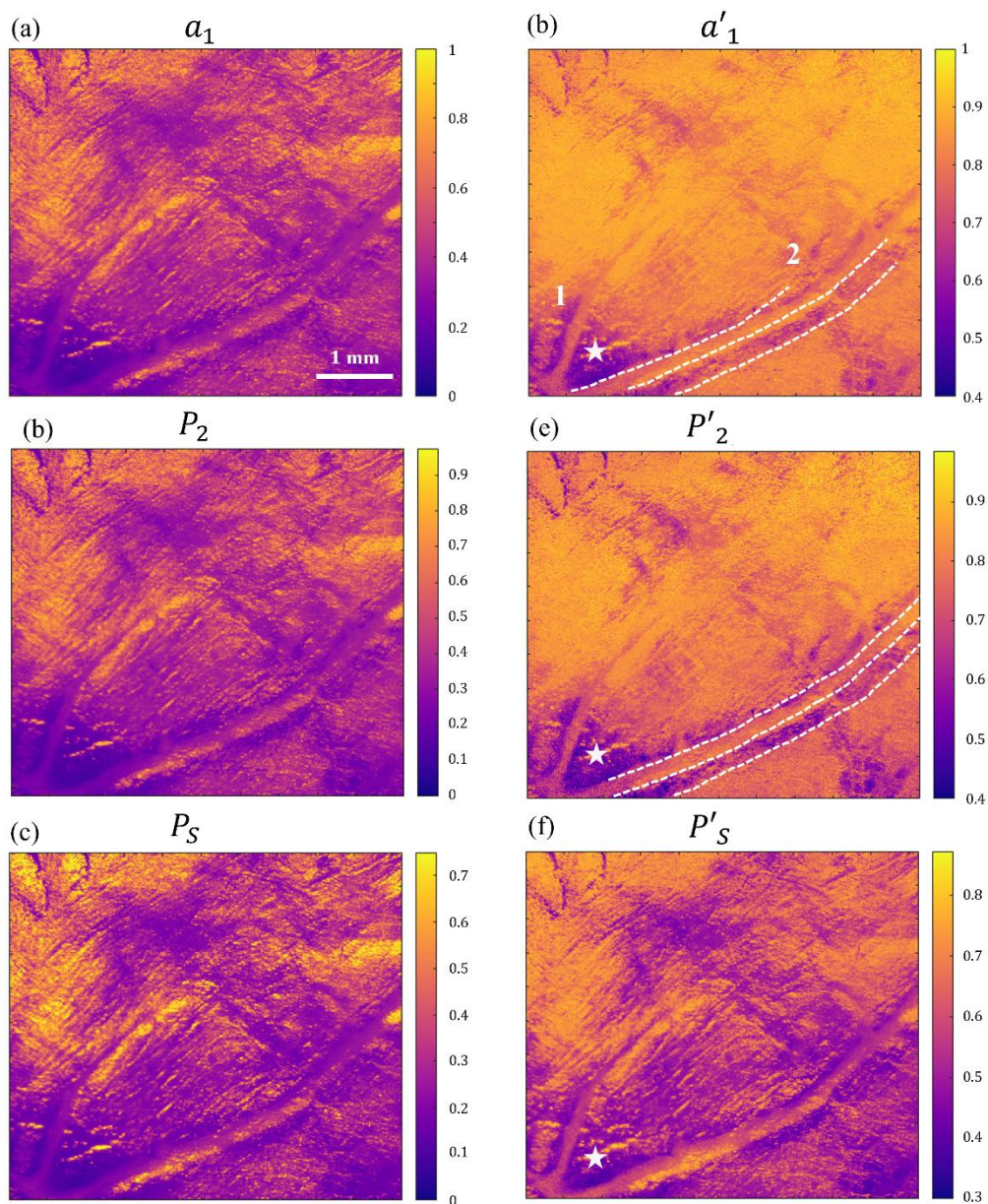


Figure 5-5 Comparison of the polarimetric images before (first row) and after (second row) the application of the IDF in the adventitia and coronal arteries sample. (a)-(b), (c)-(d) and (e)-(f) correspond to the  $a_1$ ,  $P_2$  and  $P_S$  before and after filtering, respectively.



The last sample we present corresponds to an external view of the heart, the pericardium of the heart with coronal arteries. In this case, the response of the sample in the intensity image (Figure 5-2 (e)) shows a tissue that seems completely homogeneous. Then, in the  $P_3$  image we observe a depolarization response that is slightly different in different regions of the sample. Then, when filtered, the polarimetric images (in this case  $\alpha_1$ ,  $P_2$  and  $P_S$ ) unveil very interesting structures within the sample. For instance, in Figure 5-5 (e) the filtered polarimetric image  $P'_2$  can clearly detect the path of two of the coronary arteries and their adventitia (connective tissue, recovering the arteries walls, see white dashed lines in the figure). In addition, we can observe a different depolarizing response in the region of the sample marked with a white star. This region represents the presence of myocardial tissue having a different polarimetric response than the rest of the tissue. Also, the response of the walls from the coronal artery 2 has a higher depolarization response than those from 1. This also means that we are able to infer information from the arteries directionality, the artery (1) is entering inside the tissue (towards the myocardium) whereas the other one is more superficial.

Summarizing, in this section we demonstrated how by removing the isotropic depolarization component of samples, by means of the application of the IDF, richer sample information, related to physiological information of tissues, is retrieved, this being especially relevant for highly depolarizing samples showing low  $P_3$  values, from which numerous biological tissues are particular cases. This visualization enhancement and structure revealing associated with the filter have been exemplified in diverse real biological tissues of *ex-vivo* animal origin. In this vein, the enhanced imaging results above-presented, especially those related to heart structures visualization, have great potential for the application of this technique in the medical field. In the case of the transversal section (Figure 5-3), we are able to study myocardial tissue in a more accurate way. For instance, the inspection and detection of myocardial tissue modification by means of this non-invasive technique could be applied in operating rooms. This can help with the early detection of cardiac diseases such as infarction [73]. In the case of the subendocardial external section of the heart (see Figure 5-5), the detection of coronary arteries and the adventitia walls can be crucial also for the prevention of heart diseases. The coronary arteries control the blood and oxygen supply to the heart muscle. Therefore, the detection of deformation or narrowness of the artery walls can also help to prevent serious heart problems.

### 5.2.2 IDF in Polarimetric Spaces

In the previous subsection, we showed the excellent results obtained when applying the IDF to biological samples. In this section, we want to take advantage of this performance for the classification of different structures within a sample by means of the 3D Polarimetric Spaces. In section 5.1.3, we showed the effect of the IDF both on the IPP and CP spaces. In this case, since for the selected samples the best results were obtained for the depolarization metrics, we center our study in the Purity Space. This representation gives a useful visual interpretation of the effect of IDF in terms of data discrimination.

To do so, we chose two of the biological samples analyzed in the previous section: the transversal section of the myocardium and the transversal section from the tongue. We select two regions (for the heart) and three regions (for the tongue) which present different polarimetric responses, and thus, which must represent physiologically different structures.

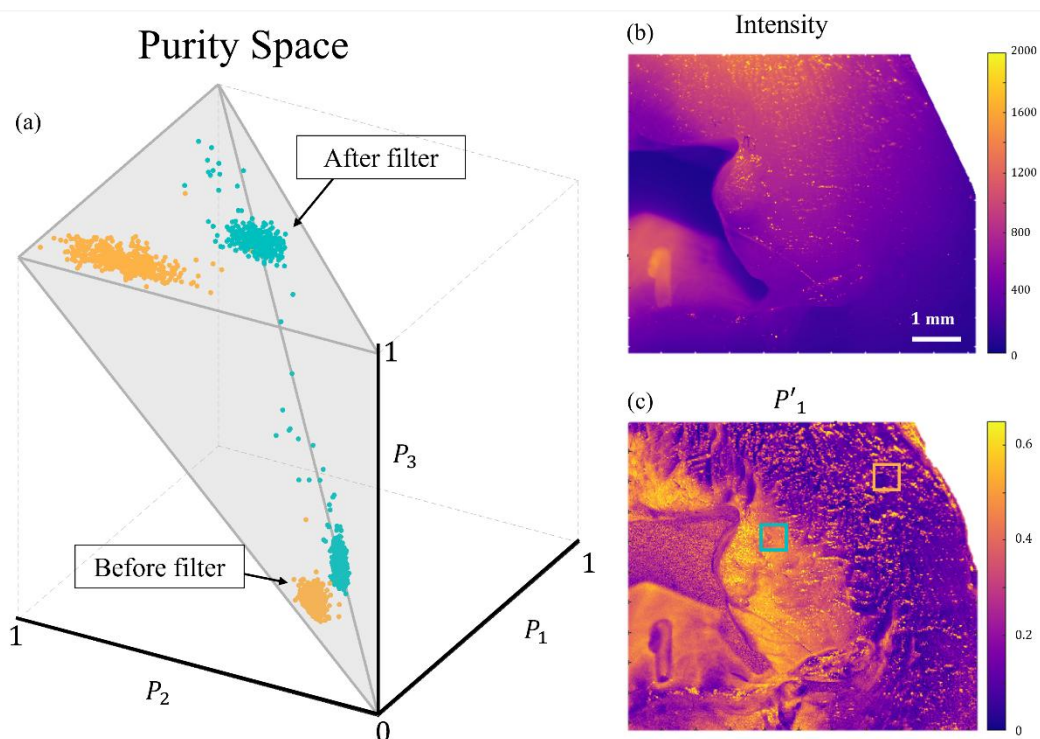


Figure 5-6 Purity Space (a), intensity (b) and filtered  $P'_1$  (c) images correspondent to the transversal section of ex-vivo cattle heart, respectively. The selected regions of the samples, represented in the Purity Figure by blue and orange points, correspond to the blue and orange squares in (c).

In Figure 5-6 we present the results for the transversal region of the heart sample. The structures that were more contrasted after the filtering correspond to myocardial (*my*) and subendocardial (*se*) tissue. Therefore, these are the zones of the sample selected to represent in the Purity Space. In particular, the blue and orange squares in Figure 5-6 (c) corresponds to the regions of interest chosen to represent the *se* and *my* structures, respectively.

In Figure 5-6 (a) we can see the effect of the filter on the Purity Space. Inside the volume, the blue and orange point clouds represent the values of the IPP in the respective regions of the sample before and after the filter applications (see the labels in the figure). As previously explained, the data clouds located at the top surface ( $P_3 = 1$ ) of the volume correspond to the values of the IPP after the application of the IDF. The values of the IPP in the regions before the filter application are located in the lower part of the tetrahedron, that is, representing the high depolarization capability of both regions of the sample, *se* and *my*, before the filtering process. Therefore in Figure 5-6 (a), although the dimensionality of the space is reduced, the potential of the filter becomes clear. The distances between the *se* and *my* heart structures (blue and orange datasets) are enlarged after the filter application, resulting in an increase in the discrimination capability between these tissue regions. In addition, the data clouds after the filter are more spread, allowing us to obtain richer and more subtle information of the structures (i.e., we capture more subtle differences between pixels within the same tissue class). This is the visual outcome that provides clearer insight into the contrast enhancement achieved by the filter described in the previous section.

As a complementary example, Figure 5-7 presents the analysis of the tongue sample within the Purity Space. In this case, we chose the three structures of the tongue explained in the previous section: the styloglossus and hyoglossus muscles and the myotendinous tissue. In Figure 5-7 (c) the green, blue and orange squares correspond to the regions selected to represent the styloglossus muscle, myotendinous tissue and hyoglossus muscle, respectively.

In this case, we observe some differences in the behavior of the data clouds if compared with the case of the heart. Note how sample data before applying the filter (see label in Figure 5-6 (a)) is almost completely mixed. Therefore, even though the volume occupied by the points in the space is larger than in the case of the heart, it is not useful to differentiate between the tissues before applying the filter.

In turn, once the data is filtered (see the top part of the figure) the region of the myotendinous tissue (blue points) is completely differentiated from the two muscle regions

(green and orange points). In the case of the muscles (green styloglossus and orange hyoglossus), the corresponding data clouds are now completely separated. Nevertheless, note how in the  $P_3 = 1$  surface of the volume, we can see some overlapping between the point clouds. This can be explained due to the very similar composition of both muscles, the main difference among them is their directionality (perpendicular to each other). In the  $P'_1$  image we can observe this effect, the two regions have a slightly different response but not as differentiated as the myotendinous tissue.

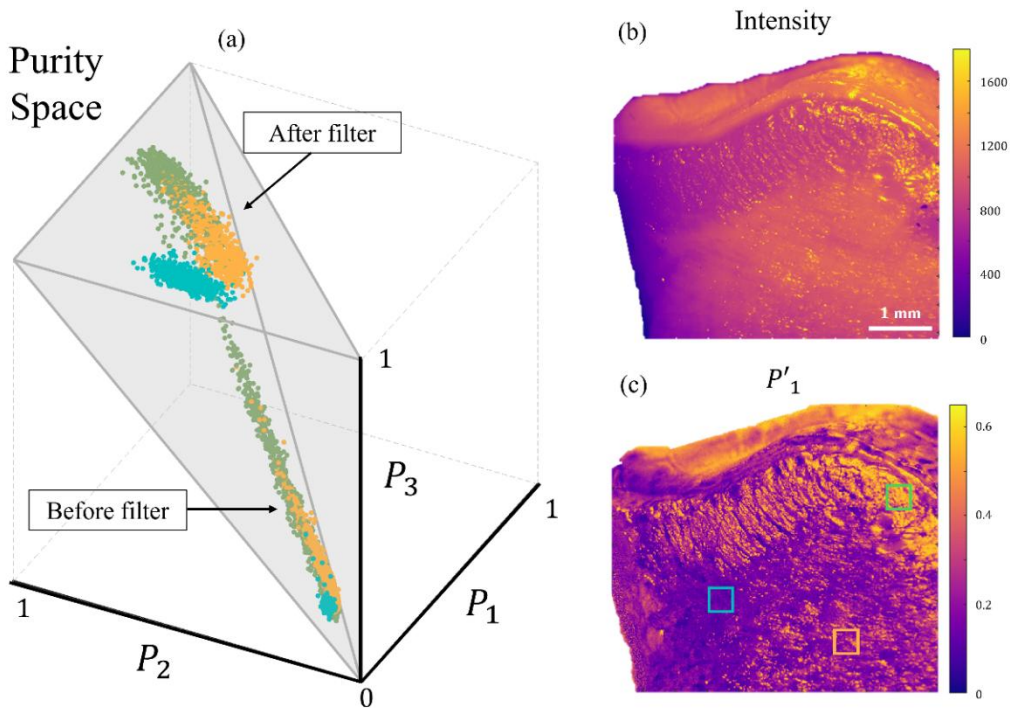


Figure 5-7 Purity Space (a), intensity (b) and filtered  $P'_1$  (c) images correspondent to the transversal cur of the tongue, respectively. The selected regions of the samples, represented in the Purity Figure by blue and orange points, correspond to the blue and orange squares in (c).

Summarizing, we have presented the performance of the IDF for the polarimetric analysis of soft biological samples. We show excellent performance of the filter for biological samples imaging when such samples present high depolarization capabilities (low values of  $P_3$ ). For the cases presented in this section as representative examples, we have obtained outstanding results, overtaking the response of conventional polarimetric methods. These results correspond not only to contrast increase and structure unveiling in the polarimetric images, but also the use of the filtered 3D Polarimetric Spaces as suitable tool for structure identification and classification purposes.



The results presented in this section highlight the interest of the filtering method for the study and characterization of biological samples, paving the way for new protocols in biomedical and clinical applications. In this section we examined the heart and tongue samples to show the good performance of the filter. In the next section we will focus on the study of different brain structures through the application of the IDF, a subject of study in which we have observed that polarimetric methods are particularly useful and hold significant potential for health-related applications.

# Chapter 6 Polarimetric tools applied to brain analysis

In the previous chapters of this thesis, we studied the relation between depolarization capabilities of a sample and the physical mechanisms behind them, defining two different depolarization processes: isotropic and anisotropic. We also take advantage of this knowledge to define an isotropic depolarization filter (IDF) that removes isotropic depolarizing content, this enhancing the anisotropic part of depolarization, which is directly related to the intrinsic properties of the sample. Importantly, we also proved the outstanding performance of the IDF in biological samples imaging through different representative examples.

In this section we apply the previously described methods for a particular case of study: the characterization of brain samples. The study of the brain is of great interest in the medical field, currently there is not a gold-standard technique to characterize certain structural features and/or pathological structures associated with brain samples. For instance, brain connectivity (white matter tracts directionality) and its functional expression is probably the present frontier in applied neuroscience, as there is no gold standard technique for pathway mapping apart from *peri-mortem* tract-tracing injections that are not ethically suitable for the study of human connectivity [162]. Techniques such as histology or ultrastructure-based methods can distinguish fiber orientation but are not useful for long range tracts [163].

As explained in the introduction, in recent years, the study of the brain by means of polarimetric techniques has yielded very interesting results. For instance, in [110,113] they use birefringence properties of brain to study white matter directionality and in [117] it is

introduced a method to implement polarimetric inspection of the brain in intraoperative neurosurgical workflows.

With this in mind, we wanted to check the suitability of the new metrics and techniques presented through this thesis in brain tissue. In particular, the polarimetric parameters obtained with the Arrow decomposition along with the IPP (see section 2.2) and the use of the Isotropic Depolarization Filter (section 5.1), among other polarimetric channels. We focus on these two studies because from a collection of different analysis they were the methods leading to the best results in terms of brain analysis. Therefore, in the following we present the study performed in brain samples from both fresh (non-fixed) *ex-vivo* animal (section 6.1) and formalin fixed human samples (section 6.2). In both cases, almost all studied metrics can notably distinguish between fiber-rich (*wm*) regions and cell-rich (*gm*) regions. In general, we have realized that these two structures have very different polarimetric responses. In addition, more interesting structures only detected by histological or other time-consuming, invasive and expensive medical procedures are detected in the filtered polarimetric channels. For instance, for the fresh animal samples, we obtain an outstanding fiber tract identification whereas for the formalin fixed human brain samples the most interesting and relevant results are obtained for the identification of the layers comprising the gray matter.

The detection or clear identification between the borders of grey matter and white matter or the layers comprising the *gm* can be very beneficial for surgery purposes. Patients with brain tumors must undergo surgery [164,165]. When doing these procedures, a clear identification of the borders of the tumors is essential to preserve all the neurological functions of the patient. In addition, the study of the *wm* fibers organization can be useful to border a tumor. The lack of organization of white matter fibers within a brain tumorous tissue can also help in the delineation and identification of these regions in the brain during surgery [116].

## 6.1 Animal Samples: Preliminary studies

In this section, we present the results obtained when polarimetrically analyzing brain tissues from *ex-vivo* animal. Polarimetric observables can provide significant distinction between cortical gray matter and subcortical white matter, as well as a clearcut boundary between fascicles within the corpus callosum, specific thalamocortical radiations and the supracallosal cingulum. In addition, it detects white matter tracts such as specific thalamocortical radiations or the U-shaped short association fibers underlying the cortex, which are probably the most elusive white matter tracts [166,167]. Some of the results

obtained with polarimetric analysis are clearly superior to any histological staining method and do not require time-consuming and destructive methods of tissue inclusion and sectioning. It is interesting to note that the two main regions of the brain (white matter and gray matter) are usually detected by the naked eye and one may think that the visual detection must be an easy and well established procedure, however, that does not always happen. In some cases, depending on the region of the brain under study the boundaries between regions can be blurred. In addition, the application of the fixation techniques changes the color of the samples. Thus, for fixed samples the differentiation is not always straightforward. That is why in some of the images we also denote these regions as *wm* and *gm*.

This section gathers the results of brain analysis from the articles of this thesis [110,112]. The samples studied in these articles correspond to (1) the coronal section taken at a crossroad between the posterior parietal lobe and the occipital lobe, approximately 2 cm from the rostral to the occipital lobe, (2) a coronal section across the occipital lobe, and (3) a coronal section across the frontal lobe.

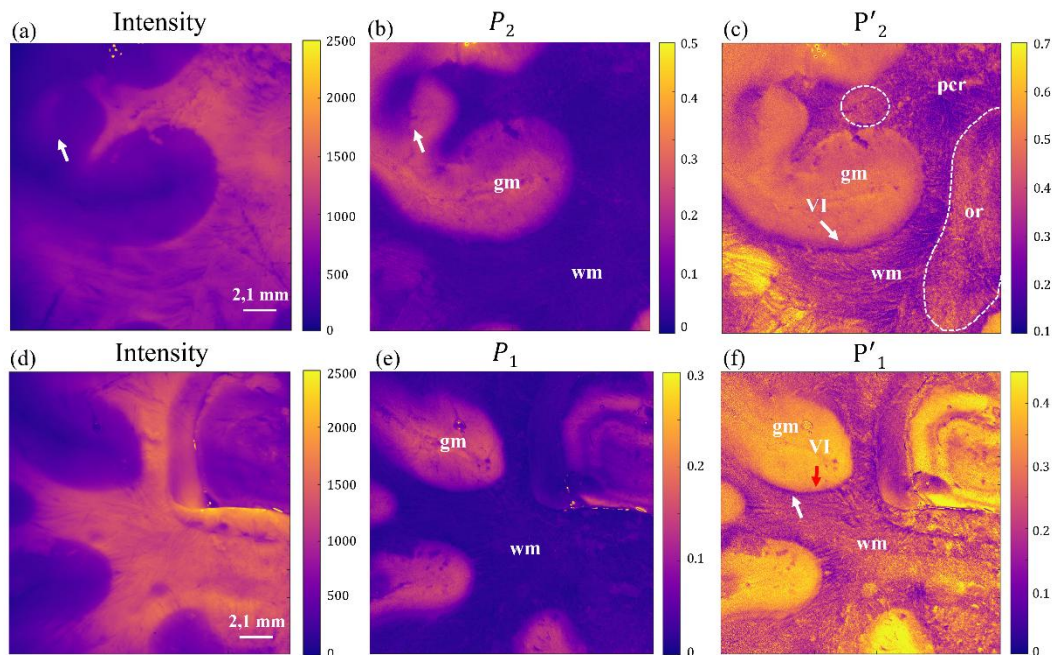


Figure 6-1 Sections of ex-vivo cow brain samples. (1) (a)-(c) coronal section taken in crossroad between the posterior parietal and occipital lobes; (2) (d)-(f) coronal section of the occipital lobe, both samples measured at 470 nm. (a) and (d) show the standard intensity images, (b) and (e) non-filtered polarimetric observables and (c) and (f) the correspondent filtered polarimetric observables.

In Figure 6-1, we provide the results for brain samples (1) (first image row) and (2) (second image row), obtained from an *ex-vivo* cow brain (see section 0 for a detailed physiological description). As in the preceding sections, in addition to the non-polarimetric intensity image, used as a reference, to prove the effect of the IDF on the polarimetric observables, we show the polarimetric observable leading to the best results (in this case, the  $P_1$  and  $P_2$  channels) both before and after the filter application. However, to avoid repetition through the analysis, in the remainder of this chapter we will present only the images corresponding to the polarimetric metrics that yield the highest contrast, regardless of whether they have been filtered or not.

In both cases, the intensity images inspected (Figure 6-1 (a) and (d)) show clear differences between *wm* and *gm* tissues. Then, polarimetric images provide clearer discrimination in some regions. For instance, in Figure 6-1 (b) the white arrow indicates a region of white matter that in the intensity image (Figure 6-1 (a)) could be misclassified as *gm*. In addition, the filtered depolarization channels (Figure 6-1 (c) and (d)) also provide a better delimitation of *wm* and *gm* than the standard intensity image and the non-filtered channels.

Importantly, note how structures that were veiled in the standard intensity and non-filtered images can be observed in the filtered images. In Figure 6-1 (d), we can identify fiber tracts of the subcortical *wm* classified according to their directionality. This allows tracing the borders between different types of radiation. The longitudinal (at this level) parietal radiations of the corona radiata (*pcr* in the figure), optical radiations (transversal, or in the figure; framed with the white dashed lines in the figure) and specific fascicles probably corresponding to the dorsal visual processing pathway (for example, white dashed ellipse in the upper part of the figure). For sample 2 (second row in Figure 6-1), the white arrow in the  $P'_1$  figure indicates the presence of short-range U-shaped fibers within *wm*. It is very important to note that these short-range fibers are the most elusive fiber tracts. To conclude, some rich information about the *gm* is provided by  $P'_1$  and  $P'_2$  channels. In both figures ((c) and (f)), the layer VI can be delimited because of its particular depolarization response. In both figures, this layer can be identified due to the higher depolarization response compared to the *wm* and the rest of the *gm*.

The next sample to study is the coronal section shown in Figure 6-2. In this case, addition to  $P'_1$  and  $P'_2$  images, we also obtained impressive imaging results for the filtered diattenuation parameter ( $D'$ ). This result agrees with recent studies [62], showing the interest of diattenuation measurements to reveal information related to white matter fiber

tracts directionality among other brain structure properties. Therefore, this filtered channel can also be of interest for polarimetric white matter inspection.

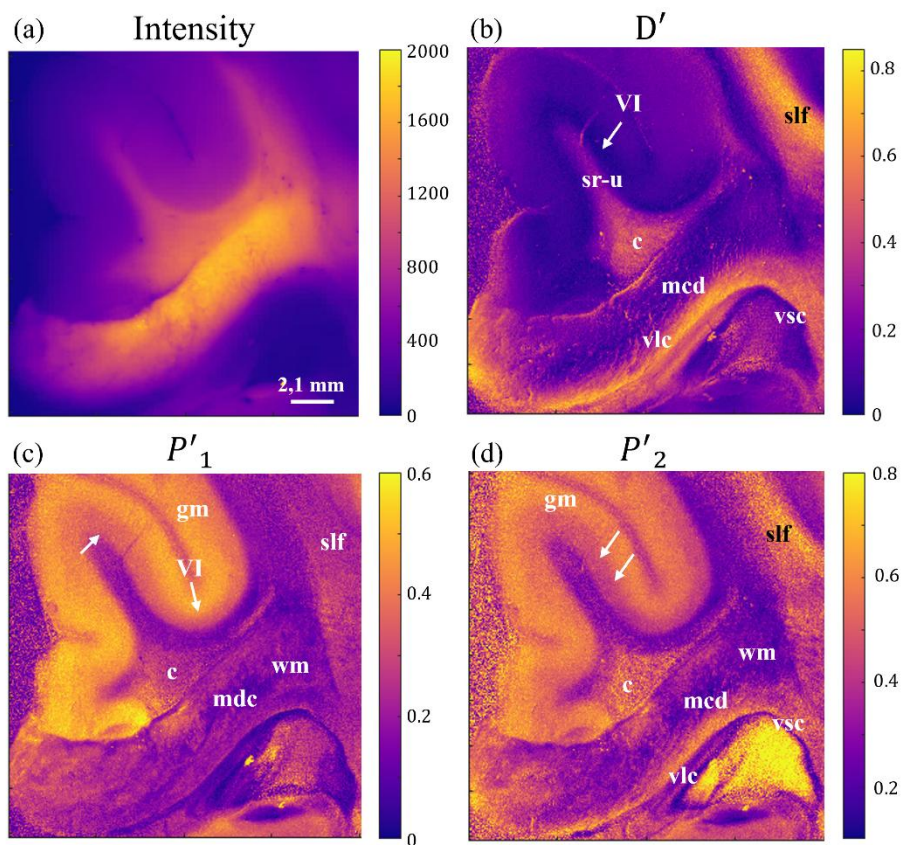


Figure 6-2 (3) Section taken from the coronal section of ex-vivo cattle brain measured at 470 nm of illumination wavelength. (a) is the standard intensity images and (b)-(d) the filtered polarimetric channels revealing the best results:  $D'$ ,  $P'_1$  and  $P'_2$ .

The filtered diattenuation channel ( $D'$ ) provides a visualization of brain structures significantly improved when compared with the intensity image. The polarimetric inspection of this sample leads to an outstanding identification of *wm* tracts both subcortical and within the corpus callosum. Interestingly, tracts following different planes of the section (i.e., coronal, or vertical) correspond to the medio-dorsal callosal fibers (*mdc*; long-range interhemispheric U-shaped fibers) and the short range U-shaped fibers (noted as *sr-u*) and tracts, either rostro-caudal (superior longitudinal fasciculus (*slf*) and cingulum (*c*)) or medio-lateral: ventro-lateral (left-right) callosal fibers (*vlc*) and ventro-striatal callosal fibers (*vsc*) [168].

The filtered depolarization images (Figure 6-2 (c) and (d)) also show outstanding results in the identification of fiber tracts in white matter. In  $P'_1$  channel the tracts *slf*, *c* and *mcd* can be identified. In addition to that, the layer VI of *wm* shows a different depolarization response than the rest of the tissue, making it easy to delineate this region in the upper part of the figure. In the case of  $P'_2$ , the same tracts than in the filtered diattenuation image are detected, and also the layer VI can be identified.

Above-stated results demonstrate how the application of the filter in brain samples provide excellent results for structure detection and visualization, both in white and gray matter regions. Filtered images provide information about the directionality of the fibers in the *wm*: such as fibers connecting both regions of the brain (*mdc*), fibers with different directionalities (coronal, rostro-caudal or medio-lateral); excellent discrimination between *gm* and *wm* and even the detection of some features in the *gm* region as the detection of layer VI.

In the medical field, the study of white matter presents a high complexity. Traditional anatomical methods for white matter tractography are rather destructive, as they require cycles of freezing and thawing [169] and the dissection procedure is relatively rough. In addition, histological and immunohistochemical methods (e.g. silver-based stains, Klüver-Barrera, MCOLL or FluoroMyelin™) cannot adequately discriminate between fascicles within the white matter [170]. Finally, Water-Diffusion Magnetic Resonance Imaging technology, which provided a great leap forward to white matter tractography (diffusion in the direction of the fibers is faster than in the perpendicular one), lacks a comparable histological standard; therefore, there is still no consensus on tract definition and inter- and intra-user reproducibility is still lagging behind [171]. Also, MRI technology is expensive, and the correct interpretation of diffusion images requires the careful selection of anatomical regions of interests that require (as long as automated methods are able to reach a fair degree of reproducibility) specifically trained morphologists [171,172].

## 6.2 Human Samples: Polarimetric parcellation of the human prosencephalon

The excellent results shown for fresh animal samples analyzed in the previous section pave the way for the inspection of human brain tissues. The structures of animal and human brain tissue are, of course, different since the connections and functionalities of human brain are more complex. Besides, fresh human tissues are not readily available for research for obvious ethical reasons and, as previously mentioned, fixation may alter tissue

properties. However, in this section we demonstrate that the polarimetric techniques applied to human samples are as outstanding as in the animal brain case.

The samples used in this study were two *post-mortem* female human brains from the Universidad de la Laguna. These two brains were preserved in a formalin solution. The anatomical description of each section is provided in section 0. From each one of the two brains, we selected different tissue blocks and then, we also selected different regions of interest within them. Each one of the sections of the brain selected for measurement, were kept in a histological cassette and preserved in formol until the measuring. In addition, after the measurement process, the samples were preserved again in formol to perform a histological analysis. This second analysis allows us to compare the results obtained by means of polarimetry and the standard histological processes and identify the structures detected macroscopically by polarimetric means. Note that before conducting the polarimetric measurements, we make sure that the formalin was completely removed from the samples. To do so, we washed the samples for 30 minutes under running water just before performing the polarimetric measurement.

The samples were measured for four different wavelengths (470 nm, 530 nm, 590 nm and 625 nm). The results for the intermediate values (530 nm and 590 nm) were redundant with the information obtained by the extremal wavelengths at the visible range (470 nm and 625 nm). Thus, in the following analysis the results presented are only for these two cases. The results obtained in blue give more information about the more superficial layers of the samples, whereas with the red wavelength the information obtained is also due to more inner layers. Of course, the penetration capability of visible light in biological tissues is very superficial, however, the complexity of the brain structure leads to differences in the results obtained with the two extremal wavelengths in the visible range.

The results obtained for the fixed human samples are more focused on the detection of layers within the *gm* as well as other structures of the brain other than *wm*. The detection of cortical layers can be very beneficial in brain tumor operations because the unwanted or unneeded modification of *gm* leads to catastrophic consequences in the patient. At this moment, the technique used to localize the functions of specific areas in the cortex is a type of electrocorticography called cortical stimulation mapping. This technique is invasive and involves pacing electrodes directly onto the exposed brain. It is used in clinical and therapeutic applications including pre-surgical mapping [173].

This subsection aims to study the effect of the filtered polarimetric observables in *ex-vivo* formalin fixed human brain. To this aim, all the polarimetric observables related to the physical properties of the samples introduced in section 2.2 were analyzed, both before



and after the IDF application. At this stage, a medical doctor helps in the selection of different sections of medical interest within the samples. These sections are shown and anatomically explained in section 0. For a further anatomical description and to prove the results obtained by means of polarimetry, we also provide in this section a comparison of the polarimetric results with the histology of each of the samples.

In the previous subsection we analyzed both the directionality of white matter fiber and some features of the gray matter composition. The animal samples were measured fresh, without any fixation method. Therefore, that makes the study of the fibers easiest than in the formalin fixed human brain samples. The effect of formalin is to reduce the water content of the samples to preserve them in time. One of the main components of soft biological tissues is water, therefore the elimination of the water will make structural changes in the sample. There are some studies showing that this effect is not critical when polarimetrically inspecting brain samples [116].

Figure 6-3 shows the comparison between the intensity image (a) and three filtered polarimetric images (b), (c) and (d) obtained for two different wavelengths ( $a'_3$  for 470 nm and 625 nm and  $P'_2$ ). In Figure 6-3 (b) and (d) we can clearly see the boundaries between white and gray matter. This is due to the strong difference in the response they show in anisotropic depolarization; the yellowish color of *wm* corresponds to low depolarization response, while the purple color shown by *gm*, corresponds to higher depolarization response. It is important to note that the depolarization response depends not only on the nature of the tissue (*gm* or *wm*) but also on the spatial distribution of the tissue. That is, depending on the studied region or the direction of the cut performed to obtain the brain section. This is more noticeable for the *wm*, where due to its intrinsically complicated arrangement and directionality. For instance, when the cutting plane is perpendicular to the fibers, they tend to produce less depolarization than in the parallel case.

In addition to the *wm/gm* discrimination, Figure 6-3 (b) and (c), both showing the  $a'_3$  channel but for 625 nm and 470 nm, respectively, provide richer information within the gray matter region. As previously explained, the gray matter of brain is comprised by six neocortical layers with different cell composition and density. These layers are noted by roman numerals from I to VI, the layer VI being the closer layer to *wm*. In the  $a'_3$  images, the different depolarization responses of each layer allows to differentiate among them and delimit the region they occupy. In Figure 6-3 (b) the black arrow indicates the location of layer VI, having a strong depolarization behavior (purple color,  $a'_3$  close to zero). In the same image, we can observe a layer composition, however in Figure 6-3 (c) the contrast between them is higher and the layers I, II/III, IV and V are detected.

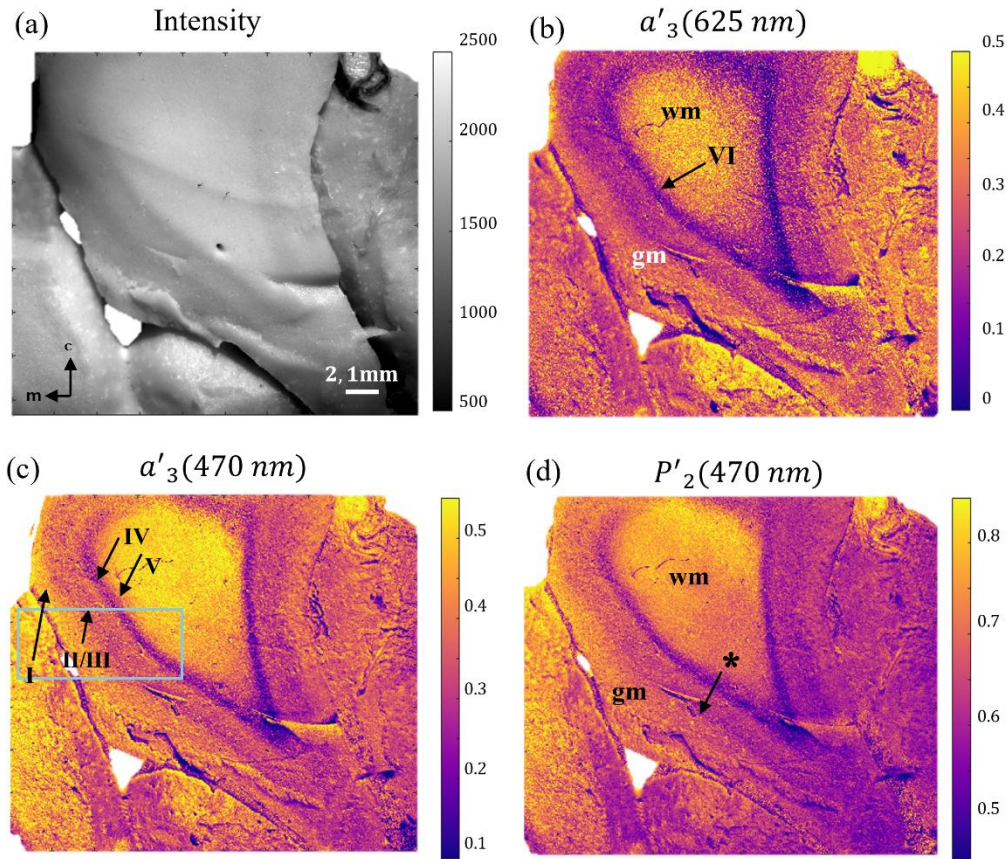


Figure 6-3 Section selected from the coronal section of sample ULLA251 cut through AP+2, corresponding to the middle frontal gyrus, correspondent to sample 12 in section 3.2. (a) Shows the histochemical staining of this section with the Nissl technique; (b) is the standard intensity image and (b)-(d) show the filtered metrics showing the best results. C and m correspond to coronal and medial, respective.

Finally, the leptomeningeal tissue of both the cerebral surface and the Virchow-Robin spaces (see [174]) are highly depolarizing and can be spotted in Figure 6-3 (d), marked with black asterisks. The relevance of the Virchow-Robin spaces has only recently been fully understood, as they are an essential component of the glymphatic system, a brain-wide fluid clearance network responsible for the exchange between cerebrospinal fluid and interstitial water that, among many other functions, removes metabolic waste [175,176].

After the polarimetric measurements the samples were preserved to perform the histochemical staining process and analysis. Figure 6-4 shows the comparison of the Nissil and myelin histological section analyzed (a) and the corresponding macroscopic section (b), marked in Figure 6-3 with the blue rectangle.

In Figure 6-4 (a) we can appreciate the structural differences between the six layers, from the outer layer (I) and the inner layer (VI). As explained in section 0 and depicted in Figure 3-6 in the histological image, we can clearly see the pyramidal cells comprising layer V, the lower density of cells in layer I and the subtle differences among the rest of the layer. In Figure 6-4 (b) we show how the location of the layers is detected at macroscopic level in the filtered polarimetric images. The black lines in the right of the image indicate the regions corresponding to layers I, II-III, IV, V and VI. The different composition of the layers is translated in a different polarimetric response, in particular to different depolarization capability. Thanks to the application of the IDF in the depolarization metrics, the identification of the layers becomes easier. In this sense, we propose this technique as a highly useful and interesting tool for the study of regions of the brain (in this case *gm* layers).

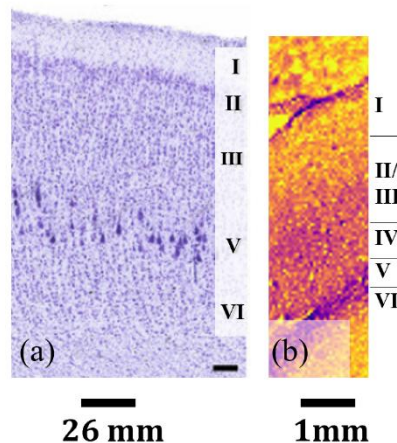


Figure 6-4 (a) Histochemical staining of the section of sample 12 marked with a blue rectangle in Figure 6-3, the macroscopic (and not stained) section of the sample is shown in (b).

In the next examples we show more structures that are detected by histochemical processes (or other time consuming and destructive techniques) identified thanks to anisotropic depolarization parameters. This paves the way for the application of these techniques in *in-vivo* brain operations and as a quick alternative in the analysis of *ex-vivo* histological samples.

Figure 6-5 shows the results for the second region selected of the sample ULLA251, this region corresponds to sample 32 (see section 0). In the same way as before, in the image we present the standard intensity image of the sample (Figure 6-5 (a)) with the three polarimetric channels providing the best results. In this case, one of the metrics presented

correspond to a combination of non-filtered parameters. In particular, Figure 6-5 (b) is the result of the combination of two indices from the IPP before filter  $P_3 - P_2$  for an illumination wavelength of 625 nm. This result is very interesting because this combination corresponds to the weight of one of the matrices in the Characteristic decomposition (see Eq. (2-37)). Figure 6-5 (c) and (d) are the filtered depolarization parameters  $P'_2$  and  $a'_3$ , measured in blue (470 nm).

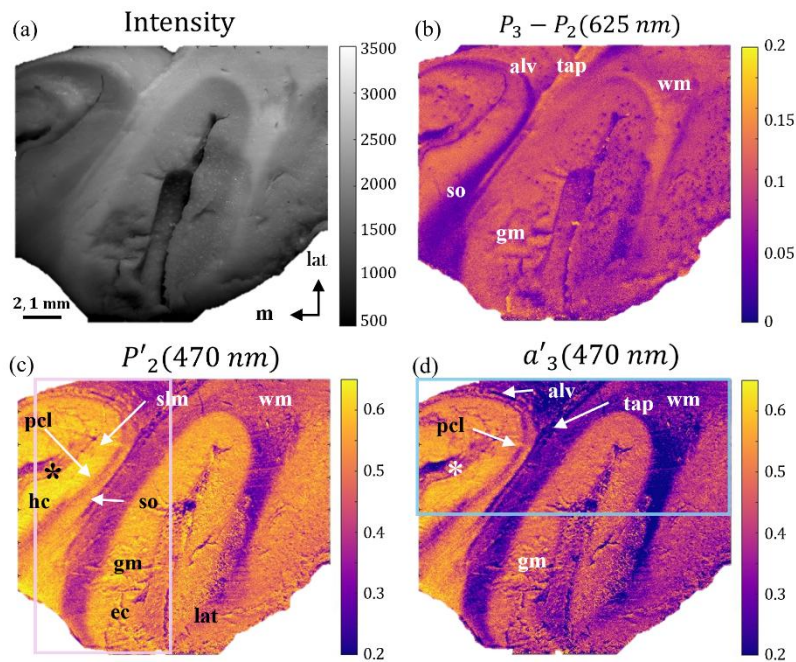


Figure 6-5 Section selected from the coronal section of sample ULLA251 cut through AP+2, corresponding to the middle temporal lobe, centered in the parahippocampal gyrus, correspondent to the sample 32 in section 3.2. (a) Intensity image, (b)-(d) filtered and non-filtered polarimetric channels showing the best results ( $P_3 - P_2$ ,  $P'_2$  and  $a'_3$ ). Lat and c indicate lateral and coronal directions.

In this case discrimination between *wm* and *gm* is obtained for  $P'_2$  and  $a'_3$  (see Figure 6-5 (c) and (d), respectively). In addition, these figures allow the delineation of several structures of interest in the brain different from the *gm* layers. In particular, Figure 6-5 (c) unveils the pyramidal cell layer (*pcl*) in its entire length both in the *subiculum* (*Sb*) and *cornu ammonis* (*CA1*). Other structures, such as the extrinsic mesotemporal connections through the alveus (*al*) and tapetum (*tap*, commissural connections) that share orientation regarding the cutting plane, share polarimetric features are detected in Figure 6-5 (d). In addition, Figure 6-5 (b) provides a clear segmentation of the stratum oriens (*so*). Finally,



the leptomeningeal-rich region of the hippocampal fissure (asterisk in Figure 6-5 (c) and (d)) can also be detected.

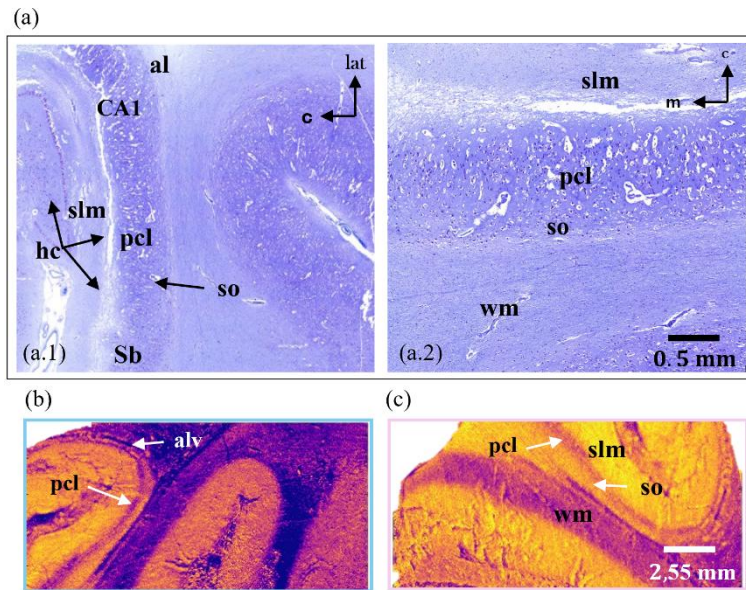


Figure 6-6 (a) Histochemical staining of the section of sample 32, (a.1) corresponds to the section marked with the blue rectangle in Figure 6-5 and (a.2) to the pink square in Figure 6-5. (b) and (c) correspond to the regions marked with the blue and pink squares, respectively.

For a deep study of the results, a histochemical analysis of the regions marked with the pink and blue rectangles in Figure 6-5 (c) and (d), respectively, is provided in Figure 6-6 (a). In addition, we provide enlarged regions of the macroscopic polarimetric images in Figure 6-6 (b) and (c). In the histological images we can clearly see all the structures comprising this region of the brain. In Figure 6-6 (a.1), from left to right, we can discern the three layers comprising the hippocampus: a cell-rich pyramidal cell layer (*pcl*) in the subiculum -*Sb*- and cornu ammonis -*CA1*-, and the stratum *lacunosum moleculare* (*slm*) and the stratum oriens (*so*) both cell-poor regions. Then, the *hc* is coated laterally by the alvelus (*alv*), a white matter tract.

Figure 6-6 (a.2) shows the coronal-medial perspective where the structures (from bottom to top) correspond to a white matter region, followed by *so*, *pcl* and *slm*. We can compare the results provided by the histological image with the structures obtained through  $P'_2$  channel in Figure 6-6 (c). In the image, each of these regions give a particular depolarization response and thus, we can delimit not only *wm* but also the stratum oriens, the *pcl* and the *slm*. Interestingly, the two cell poor regions (*so* and *slm*) that are cell poor

regions have a lower depolarization response whereas the *pcl* being a cell rich region presents higher depolarization response.

In turn, Figure 6-7 shows the results for samples 11 and 31 from the frontal lobe section of ULLA621. In this case, all the polarimetric images correspond to a measurement wavelength of 625 nm.

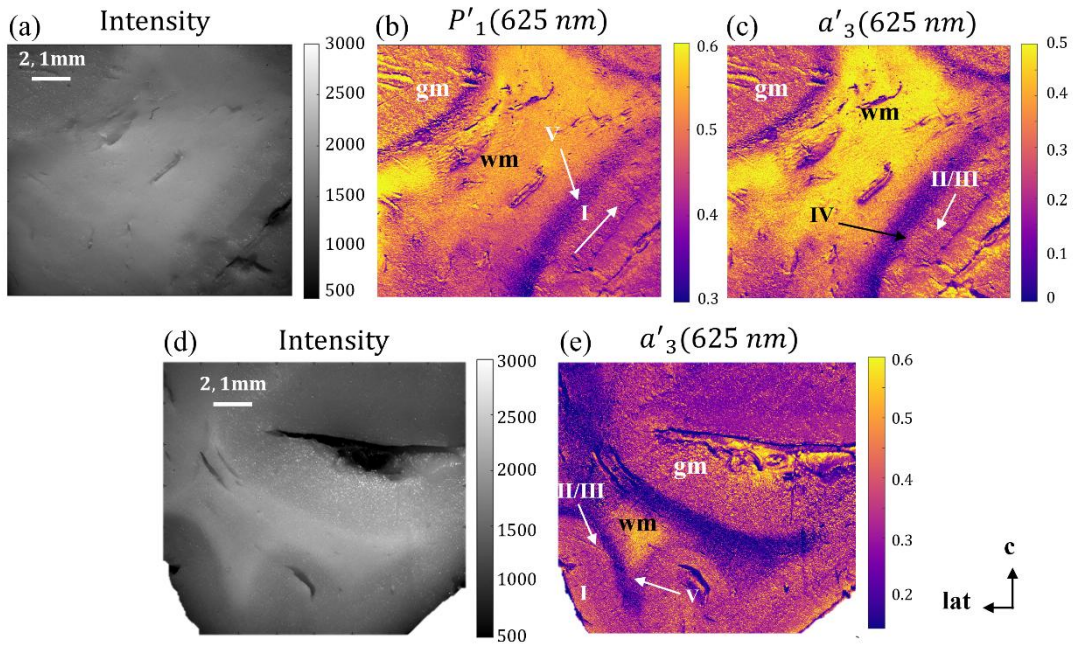


Figure 6-7 Sections obtained from the frontal lobe of ULLA621. (a) and (d) show the intensity images of samples 11 and 31, respectively and (b), (c) and (e) correspond to the best filtered polarimetric channels for both samples.

The depolarization response of the paracentral gyrus shows contrast enough to discriminate between layers (I to V) in both regions (see marks in Figure 6-7 (b) and (e)). In particular, the delineation of layer V is very prominent in Figure 6-7 (b) for sample 11 and in Figure 6-7 (e) for sample 31, being the most depolarizing structure (darker color). Layer I also presents a different polarimetric response than the tissue surrounding, in this case the cell composition of this layer makes it less depolarizing (see white diagonal arrow in Figure 6-7 (d) and (e) for sample 11 and I in Figure 6-7 (e) for sample 31). Continuing with the layer detection, the  $a'_3$  parameter in both cases is able to reveal more structural levels of gray matter. In (e), layers I, IV and II/III are detected (see black and white arrow, respectively). In the case of (e), the layers identified are I, II/III and V. Finally, all metrics are useful to trace the limit between white and grey matter.

Figure 6-8 (a) provides the results of the histological staining provided by the medical doctor. In this case, we cannot do the direct identification of the histological images with the polarimetric ones. The brain samples were approximately 2 cm thick, and the section taken for the histological inspection cannot, by definition, belong to the cutting surface of the paraffin block in which the brain sample is embedded. Therefore, any histological analysis corresponds to a slice of the sample which was in a deeper region than the surface measured with the polarimeter. However, the comparison between the structures in Figure 6-7 is still consistent.

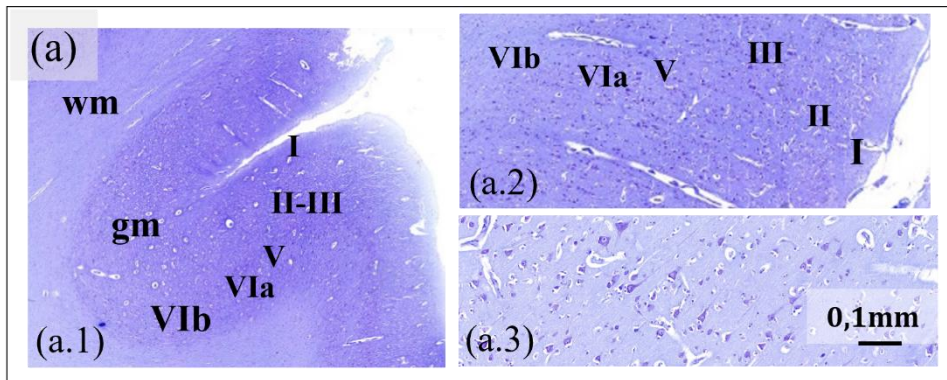


Figure 6-8 (a) Histochemical staining of the section of sample 31, (a.1) corresponds to the back section of the sample, (a.2) and (a.3) zoomed regions of (a.1).

In Figure 6-8 (a.1) we can see a section of the part of the sample where the regions under study are located and the correspondent structures. The distinction between the *gm* and *wm* is clear, the location of the different layers of *gm* are also marked. To make the distinction between them clearer, Fig. (a.2) provides a zoomed image marked by the pathologist indicating the location of the layers (I, II, III, V, VIa and VIb). Finally, Figure 6-8 (a.3) provides a zoomed image of region identified as layer V.

Finally, the region of the brain presented in Figure 6-9 corresponds to the prosencephalon, which is the most forward region of the brain and controls body temperature, reproductive functions, eating, sleeping, and the display of emotions. In this region, we can differentiate many tissues with the aid of the depolarization filtered metrics (again,  $P'_1$  and  $a'_3$  in this case).



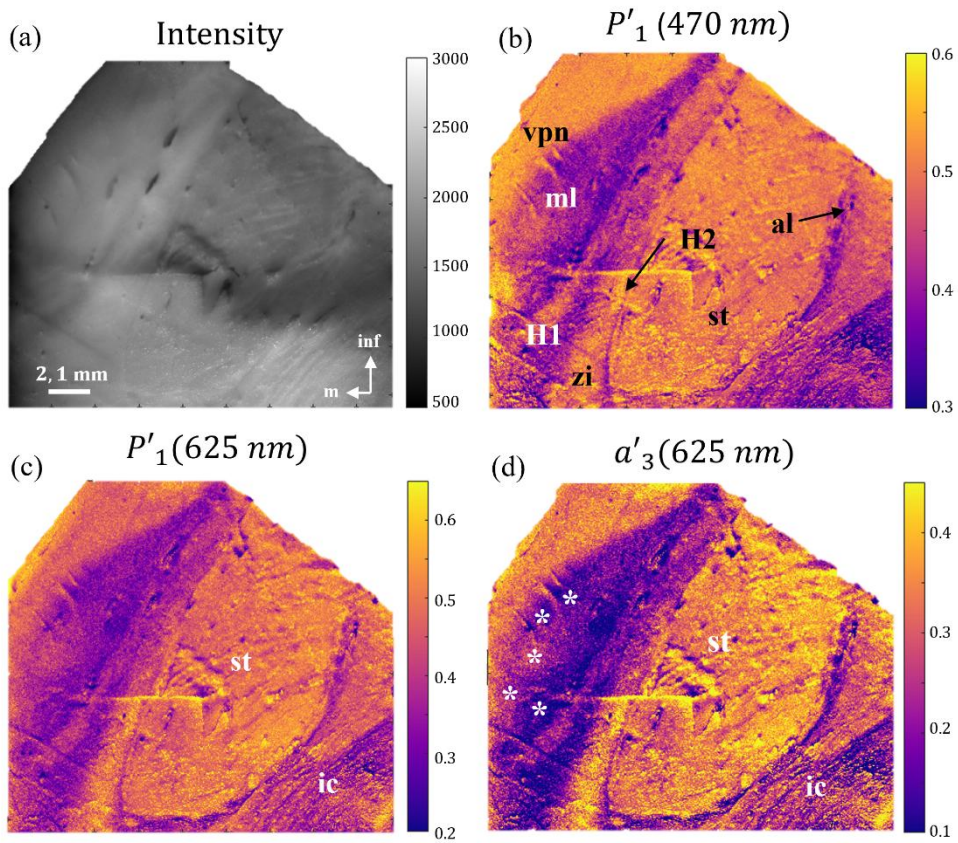


Figure 6-9 Section obtained from the frontal lobe of ULLA621 corresponding to a deep region of the human prosencephalon, this sample corresponds to the section 22 described in 0.(a) shows the intensity image and (b)-(d) the best filtered polarimetric channels ( $P'_1$  and  $a'_3$ ).

This section is mainly composed by the internal capsule (*ic*), separating the stratum (*str*) and the thalamus (*t*). The thalamus is segregated into different nuclei by the internal medullary lamina (*iml*), being highlighted the predominantly somatosensorial ventral posterior nuclei (*vpn*), which receives the medial lemniscus (*ml*). The ventral posterior thalamus is separated from the subthalamic nucleus (*st*) through a complicated area that includes Forel fields H1 and H2 and the zona incerta (*zi*). Forel field H2 is, in turn, formed by the ansa lenticularis (*al*) that surrounds the subthalamic nucleus. In the three figures correspondent to  $P'_1$  and  $a'_3$  observables (Figure 6-9 (b)-(d)) the internal capsule and the stratum are clearly identified. In addition,  $P'_1$  channel in blue (Figure 6-9 (b)) provides an excellent identification of all the aforementioned regions, highlighting among other features the borders of the H1 field and the zona incerta. Main descending (*ic*) and



ascending tracts (*ml*) are readily identifiable, being the heterogeneity of the *ic* justified by the gradual change of curvature that this tract suffers between the prosencephalon and the mesencephalon. In addition, in Figure 6-9 (d) the medial lemniscus is identifiable as it reaches the *vpn* and spreads into different smaller bundles directed to different subnuclei (asterisks). In this case, neither Nissl nor Luxol Fast-Blue staining would allow such a clearcut distinction of bundles in the area, as Nissl does not stain white matter and Luxol Fast Blue is not able to discriminate minor or poorly myelinated tracts, and is also unable to classify tracts according to the directionality of their fibers.

Summarizing, in this section we have shown the utility of the techniques introduced in this thesis for the study and identification of structures in brain samples. From the study of white matter directionality in fresh animal samples to the identification of many structures within gray and white matter. In particular, in most of the samples the application of the IDF allows the identification of the layers (I to VI) of *gm*, important regions such as the hippocampus, the thalamus or the Virchow-Robin spaces. Importantly, we also show the comparison between the filtered polarimetric and the histological images, showing the excellent performance of the IDF channels for brain structure identification.

Interestingly, the results presented in this section are clearly superior to any histological staining method and do not require time-consuming and destructive methods of tissue inclusion and sectioning. Also, signal (Mueller-matrix derived values) seems to be directly related to the orientation of the fiber bundles. This offers alternative applications that are far beyond the field of basic neuroscience or even brain pathology, as provide the basis for in-vivo tract tracing in neurosurgical theaters [177].

## Chapter 7 Conclusions

### 7.1 Summary and conclusions

The following subsections summarize the main conclusions from each chapter of this thesis. Mathematical formalism

In Chapter 2, we introduce the mathematical framework used to describe polarization light-matter interactions. We review the Mueller-Stokes formalism that allows us to mathematically deal with both the polarimetric state of light, by the Stokes vector, and the polarimetric properties of matter, through the Mueller matrix.

To further describe the polarimetric features of samples, we need to perform a deep analysis of the Mueller matrix. The physical characteristics of the samples related to polarization that can be extracted from  $M$  are dichroism, depolarization and birefringence. To obtain polarimetric observables from  $M$  relating to these three different polarimetric features, there exist a number of different methods processing the information of  $M$ , as it is the case of Mueller matrix decompositions. In this sense, the main decompositions used in this manuscript are:

- 1) The block form, that allows obtaining dichroic and depolarization metrics from  $M$ ;
- 2) The Arrow decomposition, that separates any Mueller matrix in a multiplication of three simpler  $M$  (an entrance retarder, the arrow form of  $M$  encoding dichroic and depolarizing properties, and an exit retarder) from which we can obtain several parameters related to the three polarimetric properties;
- 3) The Spectral and the Characteristic decompositions of  $M$ , which are particularly suitable for the study of depolarization properties.

We mainly focus on the depolarization-related parameters, including the Indices of Polarimetric Purity (IPP), which are specially suitable for the visualization of biological samples, and the physical meaning of the terms comprising the Characteristic decomposition of  $M$ , which provide us with fundamental knowledge that allow implementing new polarimetric tools for application in biological imaging.

Finally, in this chapter, we also describe the concept of 3D polarimetric spaces built from combinations of some of the previously mentioned polarimetric parameters. For its

usefulness in the studies conducted in this thesis, we focus on two main spaces: the Purity Space and the Components of Purity Space. The first one consists of the three IPP ( $P_1$ ,  $P_2$  and  $P_3$ ). In the case of the Components of Purity Space, the generator observables are the diattenuation, the polarizance and the spherical purity. Both spaces arise as efficient tools to represent and visualize different types of depolarizers.

### 7.1.1 Materials and methods

In the materials and methods chapter, we describe the complete image Mueller matrix polarimeter used in this thesis to obtain the experimental  $M$  of studied biological samples. Moreover, this chapter also includes a detailed description of the biological samples measured and characterized throughout the manuscript, which include sections of soft tissues such as heart, tongue and brain animal samples and brain human samples. We select to focus on the analysis of soft tissues as they are especially sensible to benefit from the methods proposed in this thesis.

The description of the Mueller matrix polarimeter includes details about its main optical components. Some relevant characteristics of the set-up are the capability to measure at different wavelengths in the visible range (470 nm, 490 nm, 530 nm and 625 nm) or at different angular measuring configurations. Note that the multi-wavelength illumination capability is useful for the biological sample inspection, since the penetration depth is wavelength dependent.

We also provide a brief description of the mathematical theory behind the operation principle of the complete Mueller image polarimeter, as well as the calibration procedure and the obtention of the experimental Mueller matrices. We want to highlight that all the experimental  $M$  of samples presented in this thesis were obtained in the reflection configuration because they are bulky tissues which are opaque in the visible range.

### 7.1.2 Discovering anisotropic and isotropic depolarization sources

Recently, the Indices of Polarimetric Purity have proved to be ideal metrics to study the depolarization characteristics of media. In Chapter 4, we present a deep analysis of the physical interpretation of IPP by conducting a collection of simulations mimicking the behavior of different classes of depolarizers. In particular, we construct depolarizing systems via the incoherent addition of simpler polarimetric elements, in accordance with

the Parallel decomposition of a Mueller matrix. This decomposition states that any depolarizing  $M$  can be described as an incoherent sum of pure Mueller matrices.

The elements used for the addition of pure matrices (leading to the simulated depolarizers) are pure diattenuators, pure retarders or combinations of both with different polarimetric properties and orientations. The aim of these studies is to relate the characteristics of the simulations with their effect on the IPP behavior. This helps to connect the magnitudes of the IPP with different scattering sources in light-matter interaction processes. The control parameters in the simulations are related to the diattenuation, retardance, orientation of each one of the elements and the statistical variation from this orientation. To better approach our simulations to the behavior of real biological samples, we add an extra control parameter: the orientation of each element is modeled as a Gaussian distribution defined by a mean value and a standard deviation. In addition, in the case of depolarizers based on retarders, we also perform further simulations by adding these characteristics to the mean retardance of each element. Interestingly, this is a key parameter in the study of the depolarization response of the samples. We find that there is a threshold from which the depolarization behavior starts appearing in samples. Therefore, one of the main conclusions of this chapter is that a certain degree of structural disorganization is necessary to produce depolarization. Complementarily, we also find a superior limit: from certain threshold, adding larger dispersion on the control parameters does not introduce further depolarization capability on simulated depolarizers.

Furthermore, the simulations also reveal an interesting relationship between the IPP and the control parameters within our simulations. Specifically, the  $P_1$  and  $P_2$  index values depend on the above-mentioned physical control parameters. However, the  $P_3$  parameter remains fixed as 1 independently of the different cases of simulated depolarizers.

The above-stated results lead to an interesting consideration. In the case of biological samples, we usually obtain values of  $P_3$  ranging from 0 to 1. Therefore, to obtain depolarization response in the  $P_3$  parameter, we need to add an extra term in the simulations. We prove this term corresponds to an ideal (or isotropic) depolarizer whose weight in the summation is directly related to the value of  $P_3$ . In fact, as more weight this term has, the more affected is the value of  $P_3$ .

IPP based simulated results show that we can differentiate between two different depolarization sources, named as anisotropic and isotropic depolarization sources. To get into specifics, the indices  $P_1$  and  $P_2$  are related to the intrinsic polarimetric properties of samples, giving measure of the anisotropic depolarization content. The simulation results

show that this kind of depolarization originates by the interaction of light with anisotropic basic elements (diattenuators and retarders) with different physical properties and orientations. The degree of polarization of light exiting from samples presenting anisotropic depolarization is dependent on the input state of polarization. In turn, we find that  $P_3$  is related to the other type of depolarization; named isotropic depolarization. In this case, the effect of the isotropic depolarization in light matter interaction is independent of the input state of light, being any incident polarization state fully depolarized. These systems can be related to a wide range of physical processes related to diffuse reflections and multiple scattering processes where the polarimetric fingerprint is lost.

Note that these results allow us to link depolarization measures at macroscopic scale with microscopic properties of samples. In addition, by inspecting the Characteristic decomposition of  $M$ , we can identify the contribution of each one of its terms as non-depolarizing ( $\hat{M}_{J0}$ ), anisotropic depolarizing ( $\hat{M}_1$  and  $\hat{M}_2$ ) and isotropic depolarizing ( $\hat{M}_3$ ) terms. To conclude, we also provide some simple and representative experimental cases of study, to validate the simulated results.

### 7.1.3 Isotropic Depolarization Filter (IDF)

In Chapter 5, we present a digital filter that separates the two depolarization contributions identified in the previous chapter: isotropic and anisotropic depolarization. As previously said, isotropic depolarization is associated with multiple scattering processes, and it can be interpreted as white noise. In contrast, anisotropic depolarization contains valuable information about the physical microscopic constituents of matter leading to depolarization. Since isotropic depolarization acts as a veil, hiding the anisotropic information contained in the samples (which is correlated with the main physical features as dichroism and/or birefringence), separating these two components enables removing the isotropic content, which is highly beneficial in terms of tissue imaging.

To implement this filter in the experimental Mueller matrices, we use the Characteristic decomposition. In this decomposition, the isotropic depolarization is encoded in the last term  $(1 - P_3)\hat{M}_3$ ; where  $\hat{M}_3 = \text{diag}(1,0,0,0)$  is the  $M$  of a perfect depolarizer and  $(1 - P_3)$  is the weight of the isotropic depolarization. The remaining terms of the decomposition are related to anisotropic depolarization and pure non-depolarizing contributions. Therefore, the isotropic depolarization filter consists of removing the last term of the decomposition  $((1 - P_3)\hat{M}_3)$  and conducting the polarimetric inspection directly on the filtered matrix, noted as  $M'$ .

We analyze the effect of this filter on several polarimetric observables, particularly those related to dichroism and depolarization. In these cases, the effect of the filter is to multiply the observables by a factor  $1/P_3$ . Note that for image applications, this effect can be different for different regions within an image. That is, when we analyze a sample including two separated structures, leading to different magnitudes of  $P_3$ , this spatial dependence of  $P_3(x, y)$ , results in a contrast enhancement between structures as well as in structure unveiling in some samples. In addition to the spatial dependence of  $P_3$ , the filter is especially effective when also presents low values of  $P_3$  (i.e. high isotropic depolarization). These two conditions are common in soft biological samples.

In addition to that, we also analyze the effect of the filter in the framework of 3D Polarimetric Spaces described in the mathematical formalism chapter. This analysis is very useful for a visual interpretation of the filter. In the Purity Space, where the vertical axis corresponds to  $P_3$ , the effect of the IDF is clear. Once a Mueller matrix image is filtered, all the points represented within the volume are transferred to the top surface of the volume ( $P_3 = 1$ ; anisotropic surface). As this is the plane parallel to the  $P_3 = 0$  plane with larger area, data distributions correspondent to different structures are largely separated when transferred to this top plane. This situation leads to better identification and visualization of biological structures. Then, in the case of the Components of Purity Space, the filter application is related to an increase in the Depolarization Index ( $P_\Delta$  is proportional to  $P_3$ ). An augmentation in the  $P_\Delta$  parameter after the filter application is related to an increase in the region where data is located, leading to equivalent results than in the IPP space case.

To validate the filter, different soft tissues of animal origin have been analyzed, including heart and tongue samples. These samples contain regions with different structural features, some of which are not detected with standard intensity images or even by conventional polarimetric based imaging methods. Once applying the filter, we observe not only a significant contrast enhancement among the different structures but also unveils some structures that could only be detected by the filtered polarimetric observables. For instance, for the transversal section of the cattle heart sample, important anatomical structures, such as the myocardium, endocardium, subendocardium and epicardium, become clearly distinguishable. While the conventional intensity image suggests a homogeneous tissue and the standard polarimetric image reveals some structures, the filtered polarimetric observable provides richer visualization of internal structures.

The above-highlighted results demonstrate the potential of the isotropic depolarization filter as a powerful tool for biomedical imaging. It offers a simpler, non-invasive and potentially more cost-effective alternative to conventional imaging techniques. Both the filtered polarimetric channels and the use of the filtered 3D Polarimetric Spaces can be very

useful in several medical scenarios. For example, in the study of cardiac pathologies or the recognition of different structures of interest within the samples.

Finally, although the aim of this thesis is to apply polarimetric techniques in the analysis of biological samples, we would like to note that the proposed methods are general and could be useful for a wide range of applications if the conditions for the effective application of the IDF are fulfilled.

#### **7.1.4 Polarimetric tools applied to brain analysis**

Chapter 6 is meant to apply all the techniques and metrics developed throughout this thesis to the polarimetric study of the brain. In previous chapters of this thesis, we show the usefulness of the filtered polarimetric observables for biological samples inspection. Therefore, in this chapter, we study both animal and human brain samples by means of filtered polarimetric channels, mostly studying the depolarization properties of the tissues comprising the samples studied.

Moreover, it is worth noting that we have presented a very simple filtering method for improved visualization of sample features, which can be experimentally implemented using a macroscopic and non-destructive technique. The results presented in this work highlight the interest of the filtering method for the study and characterization of biological samples, paving the way for new protocols in biomedical and clinical applications.

Returning to the specific case of brain samples, brain tissue is primarily composed of two different structures: gray matter, characterized by a cell-like structure, and white matter, composed of fiber-like tracts. Filtered polarimetric observables, especially those related to depolarization and dichroism, are able to detect features within these regions that are, some of them, very hard to detect by other means. For instance, the detection of white matter tracts, such as specific thalamocortical radiations or the U-shaped short association fibers underlying the cortex, are efficiently visualized after the IDF application. This is a relevant contribution if considering that these kind of fibers are probably the most elusive white matter tracts. The layers comprising gray matter are also detected and delimited by the filtered channels. Also, interesting structures such as the thalamus or the Virchow-Robin spaces are detected.

In many cases, the results obtained through polarimetric analysis surpass those of traditionally histological staining methods, without time consuming and destructive procedures, such as tissue embedding. The ability to detect cortical layers is of particular interest in neurosurgical context, where unwanted or unneeded modification of gray matter leads to catastrophic consequences in the patient. At this moment, the technique

used to localize the functions of specific areas in the cortex is a type of electrocorticography called cortical stimulation mapping. This technique is invasive and involves placing electrodes directly onto the exposed brain. It is used in clinical and therapeutic applications including pre-surgical mapping.

Summarizing, the application of filtered polarimetric observables to brain tissue analysis demonstrates the significant potential of this technique for structural characterization and clinical use. The results not only validate the effectiveness of the proposed methods but also highlight their superiority over existing polarimetric and medical imaging techniques.

## 7.2 Proposal for future research

- Analyze and isolate every component of the Characteristic decomposition of the Mueller matrix. This can help to relate physical mechanism behind the 2D and 3D Mueller matrices with diattenuator and birefringence properties as well as to develop new filtering approaches.
- Deduce the analytical relation between the Arrow parameters ( $a_1$ ,  $a_2$  and  $a_3$ ) and the Indices of Polarimetric Purity. This could lead to a common basis of analysis samples even using these two different observable families.
- Extend the IDF studies to different brain conditions, including aging or pathologies such as cancer or Alzheimer. Create a wide database of human brain samples to do statistically significant analysis of the filtered results for structure detections and pathologies recognition.
- Application of these techniques in *in-vivo* situations or as aid in medical studies as a part of clinical solutions. Develop a specific device for brain studies combining our polarimetric-based methods with another optical techniques for specific and strategic clinical applications.





# Bibliography

1. A. H.-P. Ho, D. Kim, and M. G. Somekh, eds., *Handbook of Photonics for Biomedical Engineering*, SpringerLink Bücher (Springer, 2017).
2. A. R. Kherlopian, T. Song, Q. Duan, M. A. Neimark, M. J. Po, J. K. Gohagan, and A. F. Laine, "A review of imaging techniques for systems biology," *BMC Syst. Biol.* **2**, 74 (2008).
3. B. W. Pogue, "Perspective on the optics of medical imaging," *J. Biomed. Opt.* **28**, (2023).
4. X. Luo, K. Mori, and T. M. Peters, "Advanced Endoscopic Navigation: Surgical Big Data, Methodology, and Applications," *Annu. Rev. Biomed. Eng.* **20**, 221–251 (2018).
5. S. A. Antoniou, G. A. Antoniou, C. Koutras, and A. I. Antoniou, "Endoscopy and laparoscopy: a historical aspect of medical terminology," *Surg. Endosc.* **26**, 3650–3654 (2012).
6. G. R. Baran, M. F. Kiani, and S. P. Samuel, *Healthcare and Biomedical Technology in the 21st Century: An Introduction for Non-Science Majors* (Springer New York, 2014).
7. Y. Baashar, G. Alkaws, W. N. Wan Ahmad, M. A. Alomari, H. Alhussian, and S. K. Tiong, "Towards Wearable Augmented Reality in Healthcare: A Comparative Survey and Analysis of Head-Mounted Displays," *Int. J. Environ. Res. Public. Health* **20**, 3940 (2023).
8. F. H. Mustafa and M. S. Jaafar, "Comparison of wavelength-dependent penetration depths of lasers in different types of skin in photodynamic therapy," *Indian J. Phys.* **87**, 203–209 (2013).
9. Y. Shimojo, T. Nishimura, H. Hazama, T. Ozawa, and K. Awazu, "Measurement of absorption and reduced scattering coefficients in Asian human epidermis, dermis, and subcutaneous fat tissues in the 400- to 1100-nm wavelength range for optical penetration depth and energy deposition analysis," *J. Biomed. Opt.* **25**, 1 (2020).
10. Lt. P. Aggarwal and F. A. Papay, "Applications of Multispectral and Hyperspectral Imaging in Dermatology," *Exp. Dermatol.* exd.14624 (2022).
11. H. Akbari, L. V. Halig, D. M. Schuster, A. Osunkoya, V. Master, P. T. Nieh, G. Z. Chen, and B. Fei, "Hyperspectral imaging and quantitative analysis for prostate cancer detection," *J. Biomed. Opt.* **17**, 0760051 (2012).
12. A. Spreinat, G. Selvaggio, L. Erpenbeck, and S. Kruss, "Multispectral near infrared absorption imaging for histology of skin cancer," *J. Biophotonics* **13**, e201960080 (2020).

13. S. L. Jacques, "Origins of Tissue Optical Properties in the UVA, Visible, and NIR Regions," in *Advances in Optical Imaging and Photon Migration* (Optica Publishing Group, 1996), p. OPC364.
14. R. F. Spaide, J. G. Fujimoto, N. K. Waheed, S. R. Sadda, and G. Staurengi, "Optical coherence tomography angiography," *Prog. Retin. Eye Res.* **64**, 1–55 (2018).
15. B. Baumann, "Polarization Sensitive Optical Coherence Tomography: A Review of Technology and Applications," *Appl. Sci.* **7**, 474 (2017).
16. D. R. Lally, J. S. Heier, C. Bauman, A. J. Witkin, S. Maler, C. P. Shah, E. Reichel, N. K. Waheed, I. Bussel, A. Rogers, and J. S. Duker, "Expanded spectral domain-OCT findings in the early detection of hydroxychloroquine retinopathy and changes following drug cessation," *Int. J. Retina Vitre.* **2**, 18 (2016).
17. D. Restrepo, J. M. Quion, F. Do Carmo Novaes, I. D. Azevedo Costa, C. Vasquez, A. N. Bautista, E. Quiminiano, P. A. Lim, R. Mwavu, L. A. Celi, and L. F. Nakayama, "Ophthalmology Optical Coherence Tomography Databases for Artificial Intelligence Algorithm: A Review," *Semin. Ophthalmol.* **39**, 193–200 (2024).
18. M. Campagnolo, M. Puthenparampil, A. Emmi, L. Weis, E. Basili, V. Mauceri, A. Miscioscia, M. Carecchio, A. Guerra, V. Misenti, C. Fogliano, P. Gallo, and A. Antonini, "Optical coherence tomography reveals retinal structural abnormalities in  $\alpha$ -synucleinopathies: insights from the Padua-CESNE cohort," *J. Neural Transm.* **132**, 1013–1022 (2025).
19. C. Rosendahl, *Dermatoscopy and Skin Cancer, Updated Edition: A Handbook for Hunters of Skin Cancer and Melanoma* (Scion Publishing, 2023).
20. A. Golaraei, L. Kontenis, R. Cisek, D. Tokarz, S. J. Done, B. C. Wilson, and V. Barzda, "Changes of collagen ultrastructure in breast cancer tissue determined by second-harmonic generation double Stokes-Mueller polarimetric microscopy," *Biomed. Opt. Express* **7**, 4054 (2016).
21. R. Huang, Z. Lin, Y. Liu, X. Wu, and K. Yuan, "A "hand-held" polarimeter for on-site chiral drug measurement and chemical reaction monitoring," *Anal. Bioanal. Chem.* **417**, 1055–1065 (2025).
22. S. Jo, I. Estévez, A. Lizana, J. Campos, and A. Mihi, "Enhanced Circularly Polarized Lasing in Nanocellulose-Silica Composites," *Adv. Opt. Mater.* **13**, 2500212 (2025).
23. M. Gioti, "Spectroscopic Ellipsometry Studies on Solution-Processed OLED Devices: Optical Properties and Interfacial Layers," *Materials* **15**, 9077 (2022).
24. Q. Chen, M. Ge, C. Geng, J. Zhang, L. Gao, Z. Huang, S. Wang, Y. Feng, X. Yue, S. M. H. Qaid, X. Fu, M. Wang, Y. Jiang, and M. Yuan, "Manipulating perovskite structural asymmetry for high-performing self-powered full-stokes polarimetry," *Sci. Adv.* **11**, eads6123 (2025).
25. V. Pérez-Díez, I. Martí-Vidal, E. Albentosa-Ruiz, J. González-García, F. Jaron, T. Savolainen, M. H. Xu, and R. Bachiller, "Towards an astronomical use of new-generation geodetic observations: I. From the correlator to full-polarization images," *Astron. Astrophys.* **688**, A151 (2024).
26. J. S. Tyo, D. L. Goldstein, D. B. Chenault, and J. A. Shaw, "Review of passive imaging polarimetry for remote sensing applications," *Appl. Opt.* **45**, 5453 (2006).
27. E. Zubko, M. Zheltobryukhov, E. Chornaya, K. A. Shmirko, V. V. Lisitsa, A. N. Pavlov, A. Kochergin, G. Kornienko, and G. Videen, "Characterizing atmospheric aerosols using polarimetry and shadow hiding," *Front. Remote Sens.* **4**, (2024).
28. F. Xu, O. Dubovik, P.-W. Zhai, D. J. Diner, O. V. Kalashnikova, F. C. Seidel, P. Litvinov, A. Bovchaliuk, M. J. Garay, G. van Harten, and A. B. Davis, "Joint retrieval of aerosol and water-leaving radiance from multispectral, multiangular and polarimetric measurements over ocean," *Atmospheric Meas. Tech.* **9**, 2877–2907 (2016).

29. Q. Liu, S. Wu, B. Liu, J. Liu, K. Zhang, G. Dai, J. Tang, and G. Chen, "Shipborne variable-FOV, dual-wavelength, polarized ocean lidar: design and measurements in the Western Pacific," *Opt. Express* **30**, 8927 (2022).
30. J. S. Schlosser, S. Stamnes, S. P. Burton, B. Cairns, E. Crosbie, B. V. Diedenhoven, G. Diskin, S. Dimitrovic, R. Ferrare, J. W. Hair, C. A. Hostetler, Y. Hu, X. Liu, R. H. Moore, T. Shingler, M. A. Shook, K. L. Thornhill, E. Winstead, L. Ziemba, and A. Sorooshian, "Polarimeter + Lidar-Derived Aerosol Particle Number Concentration," *Front. Remote Sens.* **3**, (2022).
31. M. J. Behrenfeld, Y. Hu, R. T. O'Malley, E. S. Boss, C. A. Hostetler, D. A. Siegel, J. L. Sarmiento, J. Schulien, J. W. Hair, X. Lu, S. Rodier, and A. J. Scarino, "Annual boom-bust cycles of polar phytoplankton biomass revealed by space-based lidar," *Nat. Geosci.* **10**, 118–122 (2017).
32. M. J. Behrenfeld, P. Gaube, A. D. Penna, R. T. O'Malley, W. J. Burt, Y. Hu, P. S. Bontempi, D. K. Steinberg, E. S. Boss, D. A. Siegel, C. A. Hostetler, P. D. Tortell, and S. C. Doney, "Global satellite-observed daily vertical migrations of ocean animals," *Nature* **576**, 257–261 (2019).
33. S. Tan and R. M. Narayanan, "Design and performance of a multiwavelength airborne polarimetric lidar for vegetation remote sensing," *Appl. Opt.* **43**, 2360 (2004).
34. G. David, B. Thomas, T. Nousiainen, A. Miffre, and P. Rairoux, "Retrieving simulated volcanic, desert dust and sea-salt particle properties from two/three-component particle mixtures using UV-VIS polarization lidar and T matrix," *Atmospheric Chem. Phys.* **13**, 6757–6776 (2013).
35. J. P. Brown, R. G. Roberts, D. C. Card, C. L. Saludez, and C. K. Keyser, "Hybrid passive polarimetric imager and lidar combination for material classification," *Opt. Eng.* **59**, 1 (2020).
36. G. G. Politano and C. Versace, "Spectroscopic Ellipsometry: Advancements, Applications and Future Prospects in Optical Characterization," *Spectrosc. J.* **1**, 163–181 (2023).
37. S. Bairagi, C.-L. Hsiao, R. Magnusson, J. Birch, J. P. Chu, F.-G. Tarntair, R.-H. Horng, and K. Järrendahl, "Zinc gallate ( $\text{ZnGa}_2\text{O}_4$ ) epitaxial thin films: determination of optical properties and bandgap estimation using spectroscopic ellipsometry," *Opt. Mater. Express* **12**, 3284 (2022).
38. E. Márquez, E. Blanco, M. García-Gurrea, M. C. Puerta, M. D. de la Vega, M. Ballester, J. M. Manuel, M. I. Rodríguez-Tapiador, and S. M. Fernández, "Optical Properties of Reactive RF Magnetron Sputtered Polycrystalline  $\text{Cu}_3\text{N}$  Thin Films Determined by UV/Visible/NIR Spectroscopic Ellipsometry: An Eco-Friendly Solar Light Absorber," *Coatings* **13**, 1148 (2023).
39. G. G. Politano and C. Versace, "Variable-Angle Spectroscopic Ellipsometry of Graphene-Based Films," *Coatings* **11**, 462 (2021).
40. C. H. L. Patty, D. A. Luo, F. Snik, F. Ariese, W. J. Buma, I. L. ten Kate, R. J. M. van Spanning, W. B. Sparks, T. A. Germer, G. Garab, and M. W. Kudenov, "Imaging linear and circular polarization features in leaves with complete Mueller matrix polarimetry," *Biochim. Biophys. Acta BBA - Gen. Subj.* **1862**, 1350–1363 (2018).
41. C. Rodríguez, E. Garcia-Caurel, T. Garnatje, M. S. i Ribas, J. Luque, J. Campos, and A. Lizana, "Polarimetric observables for the enhanced visualization of plant diseases," *Sci. Rep.* **12**, 14743 (2022).
42. B. A. Bugami, Y. Su, C. Rodríguez, A. Lizana, J. Campos, M. Durfort, R. Ossikovski, and E. Garcia-Caurel, "Characterization of vine, *Vitis vinifera*, leaves by Mueller polarimetric microscopy," *Thin Solid Films* **764**, 139594 (2023).

43. A. V. Eeckhout, E. Garcia-Caurel, T. Garnatje, J. C. Escalera, M. Durfort, J. Vidal, J. J. Gil, J. Campos, and A. Lizana, "Polarimetric imaging microscopy for advanced inspection of vegetal tissues," *Sci. Rep.* **11**, 3913 (2021).
44. Z. Zhuo, H. Wang, R. Liao, and H. Ma, "Machine Learning Powered Microalgae Classification by Use of Polarized Light Scattering Data," *Appl. Sci.* **12**, 3422 (2022).
45. I. Shtein, Y. Shelef, Z. Marom, E. Zelinger, A. Schwartz, Z. A. Popper, B. Bar-On, and S. Harpaz-Saad, "Stomatal cell wall composition: distinctive structural patterns associated with different phylogenetic groups," *Ann. Bot.* **119**, 1021–1033 (2017).
46. V. Bischoff, S. Nita, L. Neumetzler, D. Schindelasch, A. Urbain, R. Eshed, S. Persson, D. Delmer, and W.-R. Scheible, "*TRICHOME BIREFRINGENCE* and Its Homolog *AT5G01360* Encode Plant-Specific DUF231 Proteins Required for Cellulose Biosynthesis in Arabidopsis," *Plant Physiol.* **153**, 590–602 (2010).
47. M. W. Kudenov, D. Krafft, C. G. Scarboro, C. J. Doherty, and P. Balint-Kurti, "Hybrid spatial–temporal Mueller matrix imaging spectropolarimeter for high throughput plant phenotyping," *Appl. Opt.* **62**, 2078 (2023).
48. Z. Zhu, X. Li, J. Zhai, and H. Hu, "PODB: A learning-based polarimetric object detection benchmark for road scenes in adverse weather conditions," *Inf. Fusion* **108**, 102385 (2024).
49. I. Estévez, F. Oliveira, P. Braga-Fernandes, M. Oliveira, L. Rebouta, and M. I. Vasilevskiy, "Urban objects classification using Mueller matrix polarimetry and machine learning," *Opt. Express* **30**, 28385 (2022).
50. Y. Dong, J. Wan, X. Wang, J.-H. Xue, J. Zou, H. He, P. Li, A. Hou, and H. Ma, "A Polarization-Imaging-Based Machine Learning Framework for Quantitative Pathological Diagnosis of Cervical Precancerous Lesions," *IEEE Trans. Med. Imaging* **40**, 3728–3738 (2021).
51. T. Marvdashti, L. Duan, S. Z. Aasi, J. Y. Tang, and A. K. E. Bowden, "Classification of basal cell carcinoma in human skin using machine learning and quantitative features captured by polarization sensitive optical coherence tomography," *Biomed. Opt. Express* **7**, 3721 (2016).
52. D. Ivanov, V. Dremine, T. Genova, A. Bykov, T. Novikova, R. Ossikovski, and I. Meglinski, "Polarization-Based Histopathology Classification of Ex Vivo Colon Samples Supported by Machine Learning," *Front. Phys.* **9**, (2022).
53. X. Liu, Y. Sun, W. Gu, J. Sun, Y. Wang, and L. Li, "Discrimination and quantification of scar tissue by Mueller matrix imaging with machine learning," *J. Innov. Opt. Health Sci.* **16**, (2023).
54. X. Fang, Q. Luo, B. Zhou, C. Li, and L. Tian, "Research Progress of Automated Visual Surface Defect Detection for Industrial Metal Planar Materials," *Sensors* **20**, 5136 (2020).
55. A. Z. Kechiche, O. Aubreton, A. Mathieu, A. Mannucci, and C. Stolz, "Polarimetric imaging method for surface quality evaluation of a liquid metal pool obtained during welding," *Opt. Eng.* **59**, (2020).
56. J. Agagliate, R. Foster, A. Ibrahim, and A. Gilerson, "A neural network approach to the estimation of in-water attenuation to absorption ratios from PACE mission measurements," *Front. Remote Sens.* **4**, (2023).
57. M. Gao, K. Knobelspiesse, B. A. Franz, P.-W. Zhai, V. Martins, S. P. Burton, B. Cairns, R. Ferrare, M. A. Fenn, O. Hasekamp, Y. Hu, A. Ibrahim, A. M. Sayer, P. J. Werdell, and X. Xu, "Adaptive Data Screening for Multi-Angle Polarimetric Aerosol and Ocean Color Remote Sensing Accelerated by Deep Learning," *Front. Remote Sens.* **2**, (2021).

58. B. Yang, P.-Y. Lee, Y. Hua, B. Brazile, S. Waxman, F. Ji, Z. Zhu, and I. A. Sigal, "Instant polarized light microscopy for imaging collagen microarchitecture and dynamics," *J. Biophotonics* **14**, (2021).
59. F. Fanjul-Vélez, N. Ortega-Quijano, and J. L. Arce-Diego, "Polarimetry group theory analysis in biological tissue phantoms by Mueller coherency matrix," *Opt. Commun.* **283**, 4525–4530 (2010).
60. N. Ghosh and I. A. Vitkin, "Tissue polarimetry: concepts, challenges, applications, and outlook," *J. Biomed. Opt.* **16**, 110801 (2011).
61. C. Rodríguez, I. Estévez, E. González-Arnay, J. Campos, and A. Lizana, "Optimizing the classification of biological tissues using machine learning models based on polarized data," *J. Biophotonics* **16**, (2023).
62. M. Menzel, M. Axer, K. Amunts, H. D. Raedt, and K. Michielsen, "Diattenuation Imaging reveals different brain tissue properties," *Sci. Rep.* **9**, 1939 (2019).
63. M. Sun, H. He, N. Zeng, E. Du, Y. Guo, S. Liu, J. Wu, Y. He, and H. Ma, "Characterizing the microstructures of biological tissues using Mueller matrix and transformed polarization parameters," *Biomed. Opt. Express* **5**, 4223 (2014).
64. O. Sieryi, Y. Ushenko, V. Ushenko, O. Dubolazov, A. V. Syvokorovskaya, O. Vanchulyak, A. G. Ushenko, M. Gorsky, Y. Tomka, A. Bykov, W. Yan, and I. Meglinski, "Optical anisotropy composition of benign and malignant prostate tissues revealed by Mueller-matrix imaging," *Biomed. Opt. Express* **13**, 6019 (2022).
65. J. Chue-Sang and N. Holness, "Use of Mueller matrix colposcopy in the characterization of cervical collagen anisotropy," *J. Biomed. Opt.* **23**, 1 (2018).
66. I. Pardo, S. Bian, J. Gomis-Brescó, E. Pascual, A. Canillas, S. Bosch, and O. Arteaga, "Wide-field Mueller matrix polarimetry for spectral characterization of basic biological tissues: Muscle, fat, connective tissue, and skin," *J. Biophotonics* **17**, (2024).
67. Y. Dong, J. Qi, H. He, C. He, S. Liu, J. Wu, D. S. Elson, and H. Ma, "Quantitatively characterizing the microstructural features of breast ductal carcinoma tissues in different progression stages by Mueller matrix microscope," *Biomed. Opt. Express* **8**, 3643 (2017).
68. Y. Wang, H. He, J. Chang, C. He, S. Liu, M. Li, N. Zeng, J. Wu, and H. Ma, "Mueller matrix microscope: a quantitative tool to facilitate detections and fibrosis scorings of liver cirrhosis and cancer tissues," *J. Biomed. Opt.* **21**, 071112 (2016).
69. A. G. Clark and D. M. Vignjevic, "Modes of cancer cell invasion and the role of the microenvironment," *Curr. Opin. Cell Biol.* **36**, 13–22 (2015).
70. A. Keikhosravi, Y. Liu, C. Drifka, K. M. Woo, A. Verma, R. Oldenbourg, and K. W. Eliceiri, "Quantification of collagen organization in histopathology samples using liquid crystal based polarization microscopy," *Biomed. Opt. Express* **8**, 4243 (2017).
71. S. Sugiyama, Y.-J. Hong, D. Kasaragod, S. Makita, S. Uematsu, Y. Ikuno, M. Miura, and Y. Yasuno, "Birefringence imaging of posterior eye by multi-functional Jones matrix optical coherence tomography," *Biomed. Opt. Express* **6**, 4951 (2015).
72. A. W. Dixon, A. J. Taberner, M. P. Nash, and P. M. F. Nielsen, "Quantifying optical anisotropy in soft tissue membranes using Mueller matrix imaging," *J. Biomed. Opt.* **26**, (2021).
73. M. F. G. Wood, N. Ghosh, M. A. Wallenburg, S.-H. Li, R. D. Weisel, B. C. Wilson, R.-K. Li, and I. A. Vitkin, "Polarization birefringence measurements for characterizing the myocardium, including healthy, infarcted, and stem-cell-regenerated tissues," *J. Biomed. Opt.* **15**, 047009 (2010).

74. A. Pierangelo, A. Benali, M.-R. Antonelli, T. Novikova, P. Validire, B. Gayet, and A. D. Martino, "Ex-vivo characterization of human colon cancer by Mueller polarimetric imaging," *Opt. Express* **19**, 1582 (2011).
75. E. Du, H. He, N. Zeng, M. Sun, Y. Guo, J. Wu, S. Liu, and H. Ma, "Mueller matrix polarimetry for differentiating characteristic features of cancerous tissues," *J. Biomed. Opt.* **19**, 076013 (2014).
76. D. Ivanov, V. Dremine, E. Borisova, A. Bykov, T. Novikova, I. Meglinski, and R. Ossikovski, "Polarization and depolarization metrics as optical markers in support to histopathology of ex vivo colon tissue," *Biomed. Opt. Express* **12**, 4560 (2021).
77. M. Kupinski, M. Boffety, F. Goudail, R. Ossikovski, A. Pierangelo, J. Rehbinder, J. Vizet, and T. Novikova, "Polarimetric measurement utility for pre-cancer detection from uterine cervix specimens," *Biomed. Opt. Express* **9**, 5691 (2018).
78. B. Nirmal, "Dermatoscopy: Physics and principles," *Indian J. Dermatopathol. Diagn. Dermatol.* **4**, 27 (2017).
79. R. Oldenbourg, "Polarized Light Microscopy: Principles and Practice," *Cold Spring Harb. Protoc.* **2013**, pdb.top078600 (2013).
80. N. Mazumder, Y. V. Kistenev, E. Borisova, and S. P. K, eds., *Optical Polarimetric Modalities for Biomedical Research* (Springer International Publishing, 2023).
81. L. Van Manen, J. Dijkstra, C. Boccara, E. Benoit, A. L. Vahrmeijer, M. J. Gora, and J. S. D. Mieog, "The clinical usefulness of optical coherence tomography during cancer interventions," *J. Cancer Res. Clin. Oncol.* **144**, 1967–1990 (2018).
82. J. M. Bueno, "Polarimetry in the human eye using an imaging linear polariscope," *J. Opt. Pure Appl. Opt.* **4**, 311 (2002).
83. J. M. Bueno and F. Vargas-Martín, "Measurements of the corneal birefringence with a liquid-crystal imaging polariscope," *Appl. Opt.* **41**, 116 (2002).
84. V. M. Alonso, G. Anichini, J. Qi, K. O'Neill, O. M. Conde, and D. S. Elson, "PoLambRimetry: a multispectral polarimetric atlas of lamb brain," *J. Biomed. Opt.* **29**, (2024).
85. N. Ortega-Quijano, T. Marvdashti, and A. K. Ellerbee Bowden, "Enhanced depolarization contrast in polarization-sensitive optical coherence tomography," *Opt. Lett.* **41**, 2350 (2016).
86. J. Vizet, S. Manhas, J. Tran, P. Validire, A. Benali, E. Garcia-Caurel, A. Pierangelo, A. D. Martino, and D. Pagnoux, "Optical fiber-based full Mueller polarimeter for endoscopic imaging using a two-wavelength simultaneous measurement method," *J. Biomed. Opt.* **21**, 071106 (2016).
87. S. Forward, A. Gribble, S. Alali, A. A. Lindenmaier, and I. A. Vitkin, "Flexible polarimetric probe for  $3 \times 3$  Mueller matrix measurements of biological tissue," *Sci. Rep.* **7**, 11958 (2017).
88. Y. Fu, Z. Huang, H. He, H. Ma, and J. Wu, "Flexible  $3 \times 3$  Mueller Matrix Endoscope Prototype for Cancer Detection," *IEEE Trans. Instrum. Meas.* **67**, 1700–1712 (2018).
89. J. Qi, T. Tatla, E. Nissanka-Jayasuriya, A. Y. Yuan, D. Stoyanov, and D. S. Elson, "Surgical polarimetric endoscopy for the detection of laryngeal cancer," *Nat. Biomed. Eng.* **7**, 971–985 (2023).
90. J. Bonaventura, K. Morara, R. Carlson, C. Comrie, N. Daigle, E. Hutchinson, and T. W. Sawyer, "Backscattering Mueller Matrix polarimetry on whole brain specimens shows promise for minimally invasive mapping of microstructural orientation features," *Front. Photonics* **3**, (2022).
91. T. Novikova, J. Rehbinder, S. Deby, H. Haddad, J. Vizet, A. Pierangelo, P. Validire, A. Benali, B. Gayet, B. Teig, A. Nazac, B. Drévillon, F. Moreau, and A. De Martino,

- "Multi-spectral Mueller Matrix Imaging Polarimetry for Studies of Human Tissues," in *Biomedical Optics 2016* (OSA, 2016), p. TTh3B.2.
92. Y. Zhang, S. Y. C. Lee, Y. Zhang, D. Furst, J. Fitzgerald, and A. Ozcan, "Wide-field imaging of birefringent synovial fluid crystals using lens-free polarized microscopy for gout diagnosis," *Sci. Rep.* **6**, 28793 (2016).
  93. A. Keikhosravi, M. Shribak, M. W. Conklin, Y. Liu, B. Li, A. Loeffler, R. M. Levenson, and K. W. Eliceiri, "Real-time polarization microscopy of fibrillar collagen in histopathology," *Sci. Rep.* **11**, 19063 (2021).
  94. J. Wang, Y. He, Y. Wu, P. Tang, Y. Wang, and Z. Tang, "Cytomembrane visualization using Stokes parameter confocal microscopy," *Appl. Opt.* **60**, 5081 (2021).
  95. D. S. Gareau, J. Lagowski, V. M. Rossi, J. A. Viator, G. Merlino, M. Kulesz-Martin, and S. L. Jacques, "Imaging Melanoma in a Murine Model Using Reflectance-Mode Confocal Scanning Laser Microscopy and Polarized Light Imaging," *J. Investig. Dermatol. Symp. Proc.* **10**, 164–169 (2005).
  96. A. Aghigh, S. Bancelin, M. Rivard, M. Pinsard, H. Ibrahim, and F. Légaré, "Second harmonic generation microscopy: a powerful tool for bio-imaging," *Biophys. Rev.* **15**, 43–70 (2023).
  97. J. Moon, S. Kang, Y.-C. Cho, J. H. Hong, D.-J. Shin, S.-H. Gong, S.-C. Yoon, and W. Choi, "Second-harmonic generation microscopy with synthetic aperture and computational adaptive optics," *Optica* **11**, 128 (2024).
  98. K. Tilbury and P. J. Campagnola, "Applications of Second-Harmonic Generation Imaging Microscopy in Ovarian and Breast Cancer," *Perspect. Med. Chem.* **7**, PMC.S13214 (2015).
  99. G. Latour, I. Gusachenko, L. Kowalczyk, I. Lamarre, and M.-C. Schanne-Klein, "In vivo structural imaging of the cornea by polarization-resolved second harmonic microscopy," *Biomed. Opt. Express* **3**, 1 (2012).
  100. A. N. Yaroslavsky, X. Feng, A. Muzikansky, and M. R. Hamblin, "Fluorescence Polarization of Methylene Blue as a Quantitative Marker of Breast Cancer at the Cellular Level," *Sci. Rep.* **9**, 940 (2019).
  101. M. Dubreuil, P. Babilotte, L. Martin, D. Sevrain, S. Rivet, Y. Le Grand, G. Le Brun, B. Turlin, and B. Le Jeune, "Mueller matrix polarimetry for improved liver fibrosis diagnosis," *Opt. Lett.* **37**, 1061 (2012).
  102. A. L. Gratiet, A. Mohebi, F. Callegari, P. Bianchini, and A. Diaspro, "Review on Complete Mueller Matrix Optical Scanning Microscopy Imaging," *Appl. Sci.* **11**, 1632 (2021).
  103. A. Le Gratiet, M. Dubreuil, S. Rivet, and Y. Le Grand, "Scanning Mueller polarimetric microscopy," *Opt. Lett.* **41**, 4336 (2016).
  104. M. Gonzalez, K. A. Montejo, K. Krupp, V. Srinivas, E. DeHoog, P. Madhivanan, and J. C. Ramella-Roman, "Design and implementation of a portable colposcope Mueller matrix polarimeter," *J. Biomed. Opt.* **25**, (2020).
  105. J. Vizet, J. Rehbinder, S. Deby, S. Roussel, A. Nazac, R. Soufan, C. Genestie, C. Haie-Meder, H. Fernandez, F. Moreau, and A. Pierangelo, "In vivo imaging of uterine cervix with a Mueller polarimetric colposcope," *Sci. Rep.* **7**, 2471 (2017).
  106. R. D. Fields, "White matter in learning, cognition and psychiatric disorders," *Trends Neurosci.* **31**, 361–370 (2008).
  107. M. Wawrzyniak, H. R. Schneider, J. Klingbeil, A. Stockert, G. Hartwigsen, C. Weiller, and D. Saur, "Resolution of diaschisis contributes to early recovery from post-stroke aphasia," *NeuroImage* **251**, 119001 (2022).
  108. K. Anand and V. Dhikav, "Hippocampus in health and disease: An overview," *Ann. Indian Acad. Neurol.* **15**, 239 (2012).



109. E. A. Genina, A. N. Bashkatov, D. K. Tuchina, P. A. Dyachenko (Timoshina), N. Navolokin, A. Shirokov, A. Khorovodov, A. Terskov, M. Klimova, A. Mamedova, I. Blokhina, I. Agranovich, E. Zinchenko, O. V. Semyachkina-Glushkovskaya, and V. V. Tuchin, "Optical properties of brain tissues at the different stages of glioma development in rats: pilot study," *Biomed. Opt. Express* **10**, 5182 (2019).
110. J. J. Gil, I. S. José, M. Canabal-Carbia, I. Estévez, E. González-Arnay, J. Luque, T. Garnatje, J. Campos, and A. Lizana, "Polarimetric Images of Biological Tissues Based on the Arrow Decomposition of Mueller Matrices," *Photonics* **10**, 669 (2023).
111. O. Rodríguez-Núñez, P. Schucht, E. Hewer, T. Novikova, and A. Pierangelo, "Polarimetric visualization of healthy brain fiber tracts under adverse conditions: ex vivo studies," *Biomed. Opt. Express* **12**, 6674 (2021).
112. M. Canabal-Carbia, I. Estévez, E. González-Arnay, I. Montes-Gonzalez, J. J. Gil, A. Barrera, E. García-Caurel, R. Ossikovski, I. Moreno, J. Campos, and A. Lizana, "Revealing hidden bioimaging information by isotropic depolarization filtering," *Opt. Laser Technol.* **188**, 112956 (2025).
113. F. Auf Der Heiden, M. Axer, K. Amunts, and M. Menzel, "Scattering polarimetry enables correlative nerve fiber imaging and multimodal analysis," *Sci. Rep.* **15**, 18493 (2025).
114. C. Guan, N. Zeng, and H. He, "Review of polarization-based technology for biomedical applications," *J. Innov. Opt. Health Sci.* **18**, 2430002 (2025).
115. P. Schucht, H. R. Lee, M. H. Mezouar, E. Hewer, A. Raabe, M. Murek, I. Zubak, J. Goldberg, E. Kovari, A. Pierangelo, and T. Novikova, "Wide-Field Mueller Polarimetry of Brain Tissue Sections for Visualization of White Matter Fiber Tracts," (2020).
116. R. Gros, O. Rodríguez-Núñez, L. Felger, S. Moriconi, R. McKinley, A. Pierangelo, T. Novikova, E. Vassella, P. Schucht, E. Hewer, and T. Maragkou, "Effects of formalin fixation on polarimetric properties of brain tissue: fresh or fixed?," *Neurophotonics* **10**, (2023).
117. S. Moriconi, O. Rodríguez-Núñez, É. Gros, L. A. Felger, T. Maragkou, E. Hewer, A. Pierangelo, T. Novikova, P. Schucht, and R. McKinley, "Near-real-time Mueller polarimetric image processing for neurosurgical intervention," *Int. J. Comput. Assist. Radiol. Surg.* **19**, 1033–1043 (2024).
118. M. Canabal-Carbia, I. Estévez, E. Nabadda, E. Garcia-Caurel, J. J. Gil, R. Ossikovski, A. Márquez, I. Moreno, J. Campos, and A. Lizana, "Connecting the microscopic depolarizing origin of samples with macroscopic measures of the Indices of Polarimetric Purity," *Opt. Lasers Eng.* **172**, 107830 (2024).
119. R. C. Jones, "A New Calculus for the Treatment of Optical Systems I Description and Discussion of the Calculus," *J. Opt. Soc. Am.* **31**, 488 (1941).
120. D. W. Berreman, "Optics in Stratified and Anisotropic Media: 4x4-Matrix Formulation," *J. Opt. Soc. Am.* **62**, 502 (1972).
121. H. Mueller, "The foundation of optics," *J. Opt. Soc. Am.* **38**, (1948).
122. G. Stokes, "On the composition and resolution of streams of polarised light from different sources," *Trans. Camb. Philos. Soc.* **9**, (1852).
123. D. H. Goldstein, *Polarized Light* (CRC Press, 2017).
124. J. J. Gil and R. Ossikovski, *Polarized Light and the Mueller Matrix Approach* (CRC Press, 2022).
125. H. Poincare, *Theorie Mathematique de La Lumiere*, XII. (Gauthier-Villars, 1892).
126. Z.-F. Xing, "On the Deterministic and Non-deterministic Mueller Matrix," *J. Mod. Opt.* **39**, 461–484 (1992).
127. J. J. Gil, "Polarimetric characterization of light and media," *Eur. Phys. J. Appl. Phys.* **40**, 1–47 (2007).

128. J. J. Gil and E. Bernabeu, "Depolarization and Polarization Indices of an Optical System," *Opt. Acta Int. J. Opt.* **33**, 185–189 (1986).
129. J. J. Gil, "Components of purity of a Mueller matrix," *J. Opt. Soc. Am. A* **28**, 1578 (2011).
130. J. J. Gil, I. S. José, and R. Ossikovski, "Serial–parallel decompositions of Mueller matrices," *J. Opt. Soc. Am. A* **30**, 32 (2013).
131. S.-Y. Lu and R. A. Chipman, "Interpretation of Mueller matrices based on polar decomposition," *J. Opt. Soc. Am. A* **13**, 1106 (1996).
132. J. J. Gil, "Transmittance constraints in serial decompositions of depolarizing Mueller matrices: the arrow form of a Mueller matrix," *J. Opt. Soc. Am. A* **30**, 701 (2013).
133. N. Ghosh, M. F. G. Wood, and I. A. Vitkin, "Mueller matrix decomposition for extraction of individual polarization parameters from complex turbid media exhibiting multiple scattering, optical activity, and linear birefringence," *J. Biomed. Opt.* **13**, 044036 (2008).
134. S. Cloude, "Group theory and polarisation algebra," *Optik* **75**, 26–36 (1986).
135. I. S. José and J. J. Gil, "Invariant indices of polarimetric purity," *Opt. Commun.* **284**, 38–47 (2011).
136. R. Ossikovski and J. Vizet, "Eigenvalue-based depolarization metric spaces for Mueller matrices," *J. Opt. Soc. Am. A* **36**, 1173 (2019).
137. R. A. Chipman, "Depolarization index and the average degree of polarization," *Appl. Opt.* **44**, 2490 (2005).
138. A. V. Eeckhout, A. Lizana, E. Garcia-Caurel, J. J. Gil, R. Ossikovski, and J. Campos, "Synthesis and characterization of depolarizing samples based on the indices of polarimetric purity," *Opt. Lett.* **42**, 4155 (2017).
139. M. Canabal-Carbia, A. V. Eeckhout, C. Rodríguez, E. González-Arnay, I. Estévez, J. J. Gil, E. García-Caurel, R. Ossikovski, J. Campos, and A. Lizana, "Depolarizing metrics in the biomedical field: Vision enhancement and classification of biological tissues," *J. Innov. Opt. Health Sci.* (2023).
140. A. V. Eeckhout, E. Garcia-Caurel, R. Ossikovski, A. Lizana, C. Rodríguez, E. González-Arnay, and J. Campos, "Depolarization metric spaces for biological tissues classification," *J. Biophotonics* **13**, (2020).
141. A. V. Eeckhout, A. Lizana, E. Garcia-Caurel, J. J. Gil, A. Sansa, C. Rodríguez, I. Estévez, E. González, J. C. Escalera, I. Moreno, and J. Campos, "Polarimetric imaging of biological tissues based on the indices of polarimetric purity," *J. Biophotonics* **11**, e201700189 (2018).
142. A. V. Eeckhout, J. J. Gil, E. Garcia-Caurel, J. G. Romero, R. Ossikovski, I. S. José, I. Moreno, J. Campos, and A. Lizana, "Unraveling the physical information of depolarizers," *Opt. Express* **29**, 38811 (2021).
143. A. V. Eeckhout, "Polarimetric methods for the image enhancement in biological applications," PhD Thesis, Universitat Autònoma de Barcelona (2021).
144. A. Peinado, A. Lizana, J. Vidal, C. Iemmi, and J. Campos, "Optimization and performance criteria of a Stokes polarimeter based on two variable retarders," *Opt. Express* **18**, 9815 (2010).
145. A. Peinado, "Analysis, optimization and implementation of a variable retardance based polarimeter," PhD Thesis, Universitat Autònoma de Barcelona (2014).
146. K. M. Twietmeyer and R. A. Chipman, "Optimization of Mueller matrix polarimeters in the presence of error sources," *Opt. Express* **16**, 11589 (2008).
147. D. S. Sabatke, M. R. Descour, E. L. Dereniak, W. C. Sweatt, S. A. Kemme, and G. S. Phipps, "Optimization of retardance for a complete Stokes polarimeter," *Opt. Lett.* **25**, 802 (2000).

148. D. S. Sabatke, A. M. Locke, M. R. Descour, W. C. Sweatt, J. P. Garcia, E. L. Dereniak, S. A. Kemme, and G. S. Phipps, "Figures of merit for complete Stokes polarimeter optimization," in D. B. Chenault, M. J. Duggin, W. G. Egan, and D. H. Goldstein, eds. (2000), pp. 75–81.
149. A. Goldstein, B. P. Covington, N. Mahabadi, and F. B. Mesfin, *Neuroanatomy, Corpus Callosum* (2025).
150. R. Nieuwenhuys, J. Voogd, and C. van Huijzen, *The Human Central Nervous System* (Springer Berlin Heidelberg, 2008).
151. P. Rubio-Garrido, F. Pérez-de-Manzo, C. Porrero, M. J. Galazo, and F. Clascá, "Thalamic Input to Distal Apical Dendrites in Neocortical Layer 1 Is Massive and Highly Convergent," *Cereb. Cortex* **19**, 2380–2395 (2009).
152. J. K. Kushner, P. B. Hoffman, C. R. Brzezinski, M. N. Svalina, B. R. O'Neill, T. C. Hankinson, C. C. Wilkinson, M. H. Handler, S. M. Baca, M. M. Huntsman, and A. L. Alexander, "Characterizing the Diversity of Layer 2/3 Human Neocortical Neurons in Pediatric Epilepsy," *eneuro* **12**, ENEURO.0247-24.2025 (2025).
153. M. Catani, F. Dell'Acqua, F. Vergani, F. Malik, H. Hodge, P. Roy, R. Valabregue, and M. T. de Schotten, "Short frontal lobe connections of the human brain," *Cortex* **48**, 273–291 (2012).
154. M. Ouyang, H. Kang, J. A. Detre, T. P. L. Roberts, and H. Huang, "Short-range connections in the developmental connectome during typical and atypical brain maturation," *Neurosci. Biobehav. Rev.* **83**, 109–122 (2017).
155. C. Rodríguez, A. V. Eeckhout, E. Garcia-Caurel, A. Lizana, and J. Campos, "Automatic pseudo-coloring approaches to improve visual perception and contrast in polarimetric images of biological tissues," *Sci. Rep.* **12**, 18479 (2022).
156. L. V. Wang, G. L. Coté, and S. L. Jacques, "Special Section Guest Editorial," *J. Biomed. Opt.* **7**, 278 (2002).
157. J. Breton, M. Michel-Villaz, and G. Paillotin, "Orientation of pigments and structural proteins in the photosynthetic membrane of spinach chloroplasts: A linear dichroism study," *Biochim. Biophys. Acta BBA - Bioenerg.* **314**, 42–56 (1973).
158. G. López-Morales, M. Sánchez-López, Á. Lizana, I. Moreno, and J. Campos, "Mueller Matrix Polarimetric Imaging Analysis of Optical Components for the Generation of Cylindrical Vector Beams," *Crystals* **10**, 1155 (2020).
159. B. A. Palevitz and P. K. Hepler, "Cellulose microfibril orientation and cell shaping in developing guard cells of *Allium*: The role of microtubules and ion accumulation," *Planta* **132**, 71–93 (1976).
160. D. Li, I. Montes, M. Canabal-Carbia, I. Estévez, O. Lopez-Coronado, Z. Guo, J. Campos, and Á. Lizana, "Enhanced characterization of depolarizing samples using indices of polarization purity and polarizance–reflection–transformation spaces," *Adv. Photonics Nexus* **4**, (2025).
161. R. Ossikovski, "Analysis of depolarizing Mueller matrices through a symmetric decomposition," *J. Opt. Soc. Am. A* **26**, 1109 (2009).
162. C. J. Charvet, "Mapping human brain pathways: challenges and opportunities in the integration of scales," *Brain. Behav. Evol.* (2023).
163. A. Agrawal, J. P. Kapfhammer, A. Kress, H. Wichers, A. Deep, W. Feindel, V. K. H. Sonntag, R. F. Spetzler, and M. C. Preul, "Josef Klingler's Models of White Matter Tracts: Influences on Neuroanatomy, Neurosurgery, and Neuroimaging," *Neurosurgery* **69**, 238–254 (2011).
164. A. S. Jakola, A. J. Skjalsvik, K. S. Myrmel, K. Sjøvik, G. Unsgård, S. H. Torp, K. Aaberg, T. Berg, H. Y. Dai, K. Johnsen, R. Kloster, and O. Solheim, "Surgical resection versus watchful waiting in low-grade gliomas," *Ann. Oncol.* **28**, 1942–1948 (2017).







165. I. E. McCutcheon and M. C. Preul, "Historical Perspective on Surgery and Survival with Glioblastoma: How Far Have We Come?," *World Neurosurg.* **149**, 148–168 (2021).
166. T. Zhang, H. Chen, L. Guo, K. Li, L. Li, S. Zhang, D. Shen, X. Hu, and T. Liu, "Characterization of U-shape streamline fibers: Methods and applications," *Med. Image Anal.* **18**, 795–807 (2014).
167. T. Xue, F. Zhang, C. Zhang, Y. Chen, Y. Song, A. J. Golby, N. Makris, Y. Rathi, W. Cai, and L. J. O'Donnell, "Superficial white matter analysis: An efficient point-cloud-based deep learning framework with supervised contrastive learning for consistent tractography parcellation across populations and dMRI acquisitions," *Med. Image Anal.* **85**, 102759 (2023).
168. E. Mandonnet, S. Sarubbo, and L. Petit, "The Nomenclature of Human White Matter Association Pathways: Proposal for a Systematic Taxonomic Anatomical Classification," *Front. Neuroanat.* **12**, (2018).
169. T. A. Dziedzic, A. Balasa, M. P. Jeżewski, Ł. Michałowski, and A. Marchel, "White matter dissection with the Klingler technique: a literature review," *Brain Struct. Funct.* **226**, 13–47 (2021).
170. Ó. D. García-García, V. Carriel, and J. Chato-Astrain, "Myelin histology: a key tool in nervous system research.," *Neural Regen. Res.* **19**, 277–281 (2024).
171. A. Joshi, H. Li, N. A. Parikh, and L. He, "A systematic review of automated methods to perform white matter tract segmentation," *Front. Neurosci.* **18**, (2024).
172. Y. Zhang, J. Zhang, K. Oishi, A. V. Faria, H. Jiang, X. Li, K. Akhter, P. Rosa-Neto, G. B. Pike, A. Evans, A. W. Toga, R. Woods, J. C. Mazziotta, M. I. Miller, P. C. M. van Zijl, and S. Mori, "Atlas-guided tract reconstruction for automated and comprehensive examination of the white matter anatomy," *NeuroImage* **52**, 1289–1301 (2010).
173. J. K. W. Gerritsen, M. L. D. Broekman, S. D. Vleeschouwer, P. Schucht, B. V. Nahed, M. S. Berger, and A. J. P. E. Vincent, "Safe surgery for glioblastoma: Recent advances and modern challenges," *Neuro-Oncol. Pract.* **9**, 364–379 (2022).
174. M. M. Esiri and D. Gay, "Immunological and neuropathological significance of the Virchow-Robin space," *J. Neurol. Sci.* **100**, 3–8 (1990).
175. D. Zagzag, M. Esencay, O. Mendez, H. Yee, I. Smirnova, Y. Huang, L. Chiriboga, E. Lukyanov, M. Liu, and E. W. Newcomb, "Hypoxia- and Vascular Endothelial Growth Factor-Induced Stromal Cell-Derived Factor-1 $\alpha$ /CXCR4 Expression in Glioblastomas," *Am. J. Pathol.* **173**, 545–560 (2008).
176. N. A. Jessen, A. S. F. Munk, I. Lundgaard, and M. Nedergaard, "The Glymphatic System: A Beginner's Guide," *Neurochem. Res.* **40**, 2583–2599 (2015).
177. D. C. Vanderweyen, G. Theaud, J. Sidhu, F. Rheault, S. Sarubbo, M. Descoteaux, and D. Fortin, "The role of diffusion tractography in refining glial tumor resection," *Brain Struct. Funct.* **225**, 1413–1436 (2020).



## **Papers of this doctoral thesis**

## Article

# Polarimetric Images of Biological Tissues Based on the Arrow Decomposition of Mueller Matrices

José J. Gil <sup>1,\*</sup> , Ignacio San José <sup>2</sup> , Mónica Canabal-Carbia <sup>3</sup> , Irene Estévez <sup>3</sup> , Emilio González-Arnav <sup>4</sup>,  
Jordi Luque <sup>5</sup> , Teresa Garnatje <sup>6</sup>, Juan Campos <sup>3</sup> and Angel Lizana <sup>3</sup> 

- <sup>1</sup> Departamento de Física Aplicada, Universidad de Zaragoza, Pedro Cerbuna 12, 50009 Zaragoza, Spain
  - <sup>2</sup> Instituto Aragonés de Estadística, Gobierno de Aragón, Bernardino Ramazzini 5, 50015 Zaragoza, Spain
  - <sup>3</sup> Grup d'Òptica, Departament de Física, Universitat Autònoma de Barcelona, 08193 Bellaterra, Spain
  - <sup>4</sup> Servicio de Anatomía Humana, Departamento de Ciencias Médicas Básicas, Universidad de la Laguna, 38200 Santa Cruz de Tenerife, Spain
  - <sup>5</sup> Institute of Agrifood Research and Technology (IRTA), 08348 Cabrils, Spain
  - <sup>6</sup> Botanical Institute of Barcelona (IBB, CISC-ICUB), 08038 Barcelona, Spain
- \* Correspondence: ppgil@unizar.es

**Abstract:** Polarimetric techniques are widely used in a vast number of applications such as remote sensing, material characterization, astronomy and biological tissue inspection. In this last scenario, different polarimetric observables have proved their potential for enhancing imaging visualization. In this work we use a set of polarimetric observables derived from the arrow decomposition of the Mueller matrix for the first time: enpolarizing, retarding and depolarizing descriptors. In particular, the mean intensity coefficient and the three indices of polarimetric purity, the absolute values and Poincaré orientations of diattenuation, polarizance, entrance retardance and exit retardance vectors are considered. Results show images with enhanced visualization or even revealing invisible structures when compared to standard intensity images. In particular, thanks to these metrics, we improve the visualization of the necrotic areas of a *Vitis rupestris* leaf. In the case of animal samples, boundaries between different fascicles inside a tendon of an ex vivo chicken sample are revealed, as is the directionality of fiber tracts of the subcortical white matter in an ex vivo cow brain. The experimental results show the potential for biophotonics imaging and how polarimetric techniques could be useful for biomedical and botanical applications.

**Keywords:** Mueller matrix; polarimetry; diattenuation; polarizance; depolarization; biophotonics



**Citation:** Gil, J.J.; San José, I.; Canabal-Carbia, M.; Estévez, I.; González-Arnav, E.; Luque, J.; Garnatje, T.; Campos, J.; Lizana, A. Polarimetric Images of Biological Tissues Based on the Arrow Decomposition of Mueller Matrices. *Photonics* **2023**, *10*, 669. <https://doi.org/10.3390/photonics10060669>

Received: 29 April 2023

Revised: 24 May 2023

Accepted: 1 June 2023

Published: 8 June 2023



**Copyright:** © 2023 by the authors. Licensee MDPI, Basel, Switzerland. This article is an open access article distributed under the terms and conditions of the Creative Commons Attribution (CC BY) license (<https://creativecommons.org/licenses/by/4.0/>).

## 1. Introduction

Mueller polarimetry constitutes a powerful tool to generate images of a material sample based on the spatial variation of polarization descriptors derived from the corresponding point-to-point Mueller matrices (**M**). Even though the sixteen elements of a given Mueller matrix can be used to build their respective images, each of those elements are related in an intricate manner to the polarimetric properties of the sample at the particular point under consideration. Consequently, the identification of appropriate sets of physical parameters representing, in a separate manner, the fundamental (phenomenological) polarimetric properties of the sample at each point, appears a key aspect to optimize the contrast in imaging polarimetry, while the said properties can be monitored and represented.

From this point of view, in the specialized literature, there is a wide number of polarimetric observables derived from **M** that allow a physical interpretation of some characteristics of samples [1–6]. In particular, one can mention properties such as [2]:

- diattenuation and polarizance vectors, which can be obtained from the first row and column of **M**, respectively [7,8];

- depolarization, which can be globally characterized by means of the depolarization index (or degree of polarimetric purity) [7], the polarization entropy [9], the depolarization power [8], the first and second Lorentz depolarization indices [10], the overall purity index [11], etc., while the detailed information on depolarization can be characterized by the indices of polarimetric purity [12,13];
- retardance, whose characterization for general Mueller matrices requires a criterion to define both the entrance and exit retardance vectors.

A number of these observables have also proved their suitability in terms of biological tissue imaging and characterization [14–19]. This is because most biological samples show spatially heterogeneous polarimetric responses depending on the particular tissues they are composed of. In this sense, some works provide the relation of some physiological characteristics of tissues to polarimetric signals. For instance, Danijela et al., in the work [20], relate the anisotropy in collagen fibers by connecting them to birefringent values, to different cancer stages in tumors of epithelial origin.

Additionally, in references [21,22], the anisotropy levels and the orientation disorder are directly related to heart pathologies such as infarction. Therefore, in these cases, both the birefringent and depolarizing properties can help to differentiate between these different (healthy and pathological) kinds of tissue.

Moreover, structures such as collagen, with a high presence in animal tissue, and cellulose, present in vegetal tissue, are highly birefringent structures [23–25]. Depolarizing responses are also related to multiple scattering due to the high presence of scattering centers in tissues [26,27]. Dichroism carries information about the absorption of light in tissue structures depending on the polarization of light. In the case of plant samples, this helps in the detection of the organization and concentration of chloroplasts and related organelles in plant species [28]. In [29], the authors provide a list of animal and human samples where different tissue regions and pathologies were inspected by means of imaging polarimetry.

As a consequence of the above, in the last few years, the use of polarimetric imaging has been broadly used in the field of biomedicine [14,30–40] and plant studies [41–46], for instance, to study heart capillary structures in myocardium tissue [14,36], the visualization of brain fiber tracks [47,48], the presence of raphides in plants [42], classification of different kinds of tissue [31,36], cancerous tissues inspection in cancerous prostate [30,49], colon [32,33], skin [50], and plant pathologies [15], among others [51–55].

As previously discussed, a particular spatial physiological modification is connected to a specific polarimetric change. Note that if these different responses are produced in different spatial regions of the sample, we will obtain better visualization (enhanced contrast) through polarimetric imaging. In this framework, this work focuses on studying the suitability of a different set of observables, derived from the so-called arrow decomposition of Mueller matrices [56], in biological applications. To this aim, the Mueller matrix of a given sample at a given point is entered into the arrow decomposition, which allows for the decoupling of sixteen meaningful and significant independent polarimetric properties. Note that other well-known serial decompositions of Mueller matrices do not provide such a decoupling; in particular, the Lu–Chipman decomposition [8] contains a depolarizer that also involves both polarizance and retardance [57], while the normal form decomposition contains equivalent diattenuators whose diattenuation and polarizance do not match those of the sample as a whole [58]. Furthermore, the indices of polarimetric purity [12] (describing the depolarizing properties of the material sample) of the depolarizers associated with both indicated approaches are in general different from those of the original Mueller matrix [2].

In this work, the arrow decomposition approach is applied to the obtainment of sets of sixteen images for a series of biological tissue samples (two of animal origin, and one of vegetal origin), leading to improved contrast with respect to other conventional approaches. The results obtained are discussed and analyzed from both a physical and a physiological point of view.



The contents of this communication are organized as follows. Section 2 contains a summary of the concepts and notations that are necessary to formulate and analyze the new polarimetric imaging approach. Section 3 is devoted to describing a set of polarimetric observables derived from the arrow decomposition. Afterwards, in Section 4, materials and methods are provided. In Section 5, we show the polarimetric images of three different biological samples (*Vitis rupestris* leaf, tendinous tissue from a chicken leg and a coronal section of a cow brain), and they are compared to standard intensity images to highlight the visualization improvement associated with arrow-decomposition-based observables. Finally, Section 6 provides the main conclusions of the work.

## 2. Theoretical Background

Linear polarimetric interactions are characterized by means of their corresponding Mueller matrices, which encompass all the measurable information regarding the changes of the Stokes parameters of the polarized light probe for each given interaction condition (angle of incidence and spectral profile of light, angle of observation, spot-size of the sample, measurement time, etc.).

Let us consider the transformation of polarized light by the action of a linear medium (under fixed interaction conditions). It can always be formulated as  $\mathbf{s}' = \mathbf{M}\mathbf{s}$  where  $\mathbf{s}$  and  $\mathbf{s}'$  are the Stokes vectors that represent the states of polarization of the incident and emerging light beams, respectively, while  $\mathbf{M}$  is the Mueller matrix associated with this kind of interaction and can always be expressed as [8,59,60].

$$\mathbf{M} = m_{00}\hat{\mathbf{M}}, \quad \hat{\mathbf{M}} \equiv \begin{pmatrix} 1 & \mathbf{D}^T \\ \mathbf{P} & \mathbf{m} \end{pmatrix},$$

$$\mathbf{m} \equiv \frac{1}{m_{00}} \begin{pmatrix} m_{11} & m_{12} & m_{13} \\ m_{21} & m_{22} & m_{23} \\ m_{31} & m_{32} & m_{33} \end{pmatrix}, \quad (1)$$

$$\mathbf{D} \equiv \frac{(m_{01}, m_{02}, m_{03})^T}{m_{00}}, \quad \mathbf{P} \equiv \frac{(m_{10}, m_{20}, m_{30})^T}{m_{00}},$$

where  $m_{ij}$  ( $i, j = 0, 1, 2, 3$ ) are the elements of  $\mathbf{M}$ ; the superscript  $T$  indicates transpose matrix;  $m_{00}$  is the mean intensity coefficient (MIC), i.e., the ratio between the intensity of the emerging light and the intensity of incident unpolarized light;  $\mathbf{D}$  and  $\mathbf{P}$  are the diattenuation and polarizance vectors, with absolute values  $D$  (diattenuation) and  $P$  (polarizance); and  $\mathbf{m}$  is the normalized  $3 \times 3$  submatrix associated with  $\mathbf{M}$ .

Leaving aside systems exhibiting magneto-optic effects, given a Mueller matrix  $\mathbf{M}$ , the Mueller matrix that represents the same linear interaction as  $\mathbf{M}$ , but with the incident and emergent directions of the propagation of the electromagnetic wave interchanged, is given by [2,61,62]

$$\mathbf{M}^r = \text{diag}(1, 1, -1, 1) \mathbf{M}^T \text{diag}(1, 1, -1, 1). \quad (2)$$

Consequently, the diattenuation (polarizance) of  $\mathbf{M}^r$  coincides with the polarizance (diattenuation) of  $\mathbf{M}$ , showing that  $D$  and  $P$  share a common essential nature related to the ability of the medium to enpolarize (increase the degree of polarization) unpolarized light incoming in either forward or reverse directions [2]. Since magneto-optic effects only affect the sign of certain elements of  $\mathbf{M}$ , this does not affect  $D$ ,  $P$  and other quantities considered below (when applied to the reverse Mueller matrix), which are defined from the square averages of some Mueller matrix elements.

Since  $0 \leq D \leq 1$  and  $0 \leq P \leq 1$ , vectors  $\mathbf{D}$  and  $\mathbf{P}$  can be represented in the Poincaré sphere; in fact, they are closely linked to the Stokes vectors  $\mathbf{M}\hat{\mathbf{s}}_u$  and  $\mathbf{M}^T\hat{\mathbf{s}}_u$ ,  $\hat{\mathbf{s}}_u = (1, 0, 0, 0)^T$ , representing input unpolarized light and parameterized as follows:

$$\begin{aligned} \mathbf{D} &= \frac{1}{m_{00}} \begin{pmatrix} m_{01} \\ m_{02} \\ m_{03} \end{pmatrix} \equiv D \begin{pmatrix} \cos 2\varphi_D \cos 2\chi_D \\ \sin 2\varphi_D \cos 2\chi_D \\ \sin 2\chi_D \end{pmatrix}, \quad [0 \leq \varphi_D < \pi, -\pi/4 \leq \chi_D \leq \pi/4] \\ \mathbf{P} &= \frac{1}{m_{00}} \begin{pmatrix} m_{10} \\ m_{20} \\ m_{30} \end{pmatrix} \equiv P \begin{pmatrix} \cos 2\varphi_P \cos 2\chi_P \\ \sin 2\varphi_P \cos 2\chi_P \\ \sin 2\chi_P \end{pmatrix}, \quad [0 \leq \varphi_P < \pi, -\pi/4 \leq \chi_P \leq \pi/4] \end{aligned} \quad (3)$$

Regarding the ability of  $\mathbf{M}$  to preserve the degree of polarization (DOP) of totally polarized incident light, a proper measure is given by the *degree of polarimetric purity* of  $\mathbf{M}$  (also called *depolarization index*) [7],  $P_\Delta$ , which can be expressed as

$$P_\Delta = \sqrt{\frac{D^2 + P^2 + 3P_S^2}{3}}, \quad (4)$$

where  $P_S$  is the *polarimetric dimension index* (also called the *degree of spherical purity*), defined as [2,63]

$$P_S \equiv \frac{\|\mathbf{m}\|_2}{\sqrt{3}} \left[ \|\mathbf{m}\|_2 \equiv \frac{1}{m_{00}} \sqrt{\sum_{k,l=1}^3 m_{kl}^2} \right], \quad (5)$$

with  $\|\mathbf{m}\|_2$  being the Frobenius norm of  $\mathbf{m}$ .

While the set  $D$ ,  $P$  and  $P_S$  of components of purity (hereafter CP) contain complete information on the qualitative sources of polarimetric purity (see Equation (4)), the quantitative information of the structure of polarimetric randomness is provided by the set of indices of polarimetric purity (IPP) [12], defined as

$$\begin{aligned} P_1 &\equiv \hat{\lambda}_0 - \hat{\lambda}_1, \quad P_2 \equiv \hat{\lambda}_0 + \hat{\lambda}_1 - 2\hat{\lambda}_2, \quad P_3 \equiv \hat{\lambda}_0 + \hat{\lambda}_1 + \hat{\lambda}_2 - 3\hat{\lambda}_3, \\ &[\hat{\lambda}_0 \geq \hat{\lambda}_1 \geq \hat{\lambda}_2 \geq \hat{\lambda}_3, \quad \hat{\lambda}_0 + \hat{\lambda}_1 + \hat{\lambda}_2 + \hat{\lambda}_3 = 1], \end{aligned} \quad (6)$$

where  $\hat{\lambda}_i$  ( $i = 0, 1, 2, 3$ ) are the trace-normalized eigenvalues (in decreasing order) of the coherency matrix  $\mathbf{C}$  associated with  $\mathbf{M}$ . The values of the IPP satisfy the nested inequalities  $0 \leq P_1 \leq P_2 \leq P_3 \leq 1$  and the following weighted square average of them equals the degree of polarimetric purity [12]:

$$P_\Delta = \frac{1}{3} \sqrt{6P_1^2 + 2P_2^2 + P_3^2} \quad (7)$$

Equations (4) and (7) show the single connection between the CP and the IPP via  $P_\Delta$ . Parameters  $m_{00}$ ,  $D$ ,  $P$ ,  $P_S$ ,  $P_1$ ,  $P_2$ ,  $P_3$  and  $P_\Delta$  take their achievable values in the interval  $[0, 1]$ . A detailed description of the properties and relations among these parameters can be found in [2]. In particular, it is remarkable that all of them are invariant under dual retarder transformations [64], that is to say, transformations of the form  $\mathbf{M}_{R2}\mathbf{M}\mathbf{M}_{R1}$ , with  $\mathbf{M}_{R1}$  and  $\mathbf{M}_{R2}$  being Mueller matrices of the respective retarders, which have the generic form [2]

$$\mathbf{M}_R \equiv \begin{pmatrix} 1 & \mathbf{0}^T \\ \mathbf{0} & \mathbf{m}_R \end{pmatrix}, \quad [\mathbf{m}_R = \mathbf{m}_R^T, \quad \det \mathbf{m}_R = +1] \quad (8)$$

and can be parameterized in terms of the azimuth  $\varphi_R$  and the ellipticity  $\chi_R$  of the fast eigenstate, together with the retardance  $\Delta$  of the retarder. Thus,  $\mathbf{M}_R$  is fully determined by its associated Poincaré retardance vector, defined as [2]

$$(\mathbf{M}_R \neq \mathbf{M}_R^T) \quad \bar{\mathbf{R}} = \frac{\Delta}{2\pi \sin \Delta} \begin{pmatrix} m_{R23} - m_{R32} \\ m_{R31} - m_{R13} \\ m_{R12} - m_{R21} \end{pmatrix} \equiv R \begin{pmatrix} \cos 2\varphi_R \cos 2\chi_R \\ \sin 2\varphi_R \cos 2\chi_R \\ \sin 2\chi_R \end{pmatrix} \quad \begin{bmatrix} 0 < \Delta_R < \pi, & 0 < R \leq 1 \\ 0 \leq \varphi_R < \pi \\ -\pi/4 \leq \chi_R \leq \pi/4 \end{bmatrix}. \quad (9)$$

Hereafter, we will use the following generic parameterization of a Stokes vector  $\mathbf{X}$  (akin to that used for the diattenuation, polarizance, Poincaré entrance retardance and Poincaré exit retardance vectors):

$$\mathbf{X} \equiv \begin{pmatrix} x_1 \\ x_2 \\ x_3 \end{pmatrix} \equiv X \begin{pmatrix} \cos 2\varphi_X \cos 2\chi_X \\ \sin 2\varphi_X \cos 2\chi_X \\ \sin 2\chi_X \end{pmatrix}, \quad [0 \leq \varphi_X < \pi, -\pi/4 \leq \chi_X \leq \pi/4]. \quad (10)$$

From the previous equation, the absolute value and angular parameters (Poincaré azimuth and ellipticity) can be calculated using

$$\begin{aligned} X &= \sqrt{x_1^2 + x_2^2 + x_3^2}, \\ \varphi_X &= \frac{1}{2} \arctan \frac{x_2}{x_1}, \quad \text{sgn} \varphi_X = \text{sgn} x_2, \\ \chi_X &= \frac{1}{2} \arcsin x_3, \quad \text{sgn} \chi_X = \text{sgn} x_3. \end{aligned} \quad (11)$$

### 3. Arrow-Form-Inspired Parameterization of the Information Contained in a Mueller Matrix

Let us consider the following modified singular value decomposition of the  $3 \times 3$  submatrix  $\mathbf{m}$  of  $\mathbf{M}$  [56]

$$\mathbf{m} = \mathbf{m}_{RO} \mathbf{m}_A \mathbf{m}_{RI} \quad \left[ \begin{array}{l} \mathbf{m}_{RI}^{-1} = \mathbf{m}_{RI}^T \quad \det \mathbf{m}_{RI} = +1 \quad (i = I, O) \\ \mathbf{m}_A \equiv \text{diag}(a_1, a_2, \varepsilon a_3) \quad \varepsilon \equiv \det \mathbf{m} / |\det \mathbf{m}| \end{array} \right] \quad (12)$$

where the nonnegative parameters  $(a_1, a_2, a_3)$  are the singular values of  $\mathbf{m}$ , so that the following orthogonal Mueller matrices (representing respective retarders) can be defined as

$$\mathbf{M}_{RI} = \begin{pmatrix} 1 & \mathbf{0}^T \\ \mathbf{0} & \mathbf{m}_{RI} \end{pmatrix} \quad (i = I, O) \quad (13)$$

The arrow form  $\mathbf{M}_A(\mathbf{M})$  associated with a given  $\mathbf{M}$  is then defined as

$$\begin{aligned} \mathbf{M}_A(\mathbf{M}) &\equiv \mathbf{M}_{RO}^T \mathbf{M} \mathbf{M}_{RI}^T = m_{00} \begin{pmatrix} 1 & \mathbf{D}_A^T \\ \mathbf{P}_A & \mathbf{m}_A \end{pmatrix} \\ \left[ \begin{array}{l} \mathbf{m}_A \equiv \mathbf{m}_{RO}^T \mathbf{m} \mathbf{m}_{RI}^T = \text{diag}(a_1, a_2, \varepsilon a_3) \\ a_1 \geq a_2 \geq a_3 \geq 0 \quad \varepsilon \equiv \det \mathbf{m} / |\det \mathbf{m}| \\ \mathbf{D}_A = \mathbf{m}_{RI} \mathbf{D} \quad \mathbf{P}_A = \mathbf{m}_{RO}^T \mathbf{P} \end{array} \right] \end{aligned} \quad (14)$$

and the corresponding *arrow decomposition* of  $\mathbf{M}$  is [56] (see Figure 1)

$$\mathbf{M} = \mathbf{M}_{RO} \mathbf{M}_A \mathbf{M}_{RI} \quad (15)$$

Note that, to avoid ambiguity in the definition of  $\mathbf{M}_A(\mathbf{M})$ , the retarders  $\mathbf{M}_{RI}$  and  $\mathbf{M}_{RO}$  have been chosen so as to satisfy  $a_1 \geq a_2 \geq a_3$  (with,  $1 \geq a_1 \geq a_2 \geq a_3 \geq 0$ ) with  $\text{sgn} \varepsilon a_3 = \text{sgn} \det \mathbf{m}$  ( $\text{sgn} x$  standing for the sign of  $x$ ), thus ensuring that  $\det \mathbf{M}_{RI} = \det \mathbf{M}_{RO} = +1$ , as required for  $\mathbf{M}_{RI}$  and  $\mathbf{M}_{RO}$  to represent Mueller matrices of retarders.

The diattenuation and polarizance vectors of  $\mathbf{M}$  are recovered from those of  $\mathbf{M}_A$  through the respective rotations in the Poincaré sphere representation  $\mathbf{D} = \mathbf{m}_{RI}^T \mathbf{D}_A$  and  $\mathbf{P} = \mathbf{m}_{RO} \mathbf{P}_A$  (thus preserving the respective absolute values  $|\mathbf{D}_A| = |\mathbf{D}| = D$ ,  $|\mathbf{P}_A| = |\mathbf{P}| = P$ ), which are directly determined from the *entrance* and *exit retarders*  $\mathbf{M}_{RI}$  and  $\mathbf{M}_{RO}$  of  $\mathbf{M}$ .

The arrow decomposition of  $\mathbf{M}$  shows that  $\mathbf{M}$  can be interpreted through the serial combination of the entrance retarder  $\mathbf{M}_{RI}$  of  $\mathbf{M}$ , the arrow form  $\mathbf{M}_A$  of  $\mathbf{M}$  and the exit retarder  $\mathbf{M}_{RO}$  of  $\mathbf{M}$ . Consequently, the physical information held by  $\mathbf{M}$  can be parameterized through the following set of sixteen independent parameters [64,65]:

- the three parameters  $(\varphi_I, \chi_I, R_I)$  determining the entrance retarder;
- the three parameters  $(\varphi_O, \chi_O, R_O)$  determining the exit retarder;

- the MIC  $m_{00}$  of  $\mathbf{M}$  (which coincides with that of  $\mathbf{M}_A$ );
- the three parameters  $(\varphi_D, \chi_D, D)$  determining the diattenuation vector  $\mathbf{D}$  of  $\mathbf{M}$ , or, alternatively, the three parameters  $(\varphi_{DA}, \chi_{DA}, D)$  determining the diattenuation vector  $\mathbf{D}_A = \mathbf{m}_{RI} \mathbf{D}$  of  $\mathbf{M}_A$ ;
- the three parameters  $(\varphi_P, \chi_P, P)$  determining the polarizance vector  $\mathbf{P}$  of  $\mathbf{M}$ , or, alternatively, the three parameters  $(\varphi_{PA}, \chi_{PA}, P)$  determining the polarizance vector  $\mathbf{P}_A = \mathbf{m}_{RO}^T \mathbf{D}$  of  $\mathbf{M}_A$ ;
- the three indices of polarimetric purity  $P_1, P_2, P_3$  of  $\mathbf{M}$  (which coincide with those of  $\mathbf{M}_A$ ).

It should be noted that, due to the simple links between the diattenuation vectors  $\mathbf{D}$  and  $\mathbf{D}_A$  and between the polarizance vectors  $\mathbf{P}$  and  $\mathbf{P}_A$ , and since the polarimetric images generated from their respective parameters only depend on their variations, for imaging purposes the use of  $\mathbf{D}$  ( $\mathbf{P}$ ) is entirely equivalent to that of  $\mathbf{D}_A$  ( $\mathbf{P}_A$ ).

Therefore, the Mueller polarimetry described in further sections and applied to a set of biological tissues, leads to sixteen images (in general independent) for each sample, one for each of the sixteen parameters described above.

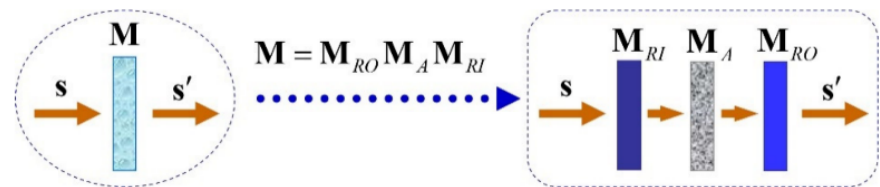


**Figure 1.** Arrow decomposition of a Mueller matrix. For any incident polarization state, with Stokes vector  $\mathbf{S}$ , the effect of any given Mueller matrix  $\mathbf{M}$  is equivalent to that of a serial combination of an entrance retarder  $\mathbf{M}_{RI}$ , the arrow form  $\mathbf{M}_A$  associated with  $\mathbf{M}$  and an exit retarder  $\mathbf{M}_{RO}$ .

## 4. Materials and Methods

### 4.1. Experimental Setup Description: Complete Image Mueller Matrix Polarimeter

In this section, we describe the experimental setup used to obtain the experimental Mueller matrix images of the biological samples inspected in this work.

The polarimeter employed to obtain the experimental  $\mathbf{M}$  of the analyzed samples is a complete imaging Mueller polarimeter. The polarimeter comprises two main parts: the Polarization State Generator (PSG) and the Polarization State Analyzer (PSA). The PSG and the PSA are composed of the respective series of optical elements (see Figure 2a) and devices, which allow to generate and analyze, respectively, any state of fully polarized light. In the case of the PSG, for being able to generate any state of polarization, it is comprised by a linear polarizer oriented at  $0^\circ$  with respect to the laboratory vertical and two Parallel Aligned Liquid Crystals (PA-LC) retarders oriented at  $45^\circ$  and  $0^\circ$  respectively. The PSA is comprised of the same optical elements as the PSG but located in inverse order (Figure 2a). To obtain the Mueller matrix images of the samples, a CCD camera is placed after the PSA to capture the intensity of the sample correspondent to each pixel. In addition, the PSG is illuminated with a light source which can work at different wavelengths in the visible spectrum (625 nm, 530 nm and 470 nm) allowing us to inspect different characteristics of samples. In particular, larger wavelengths polarimetrically interact with deeper tissues and shorter wavelengths mostly interacts with superficial tissues [66,67]. To reduce the spectrum of the different wavelengths of the LED source and to prevent artificial depolarization originated by the PA-LC's performance dependence on said parameter, 10 nm filters for blue and green illumination are used. Note that, for an accurate experimental determination of the Mueller matrix of the samples, it is important to control external light sources, so that the only light source interacting with the sample is that present in the PSG. For this reason, experimental measurements of the Mueller matrix have been conducted in dark conditions in the laboratory.



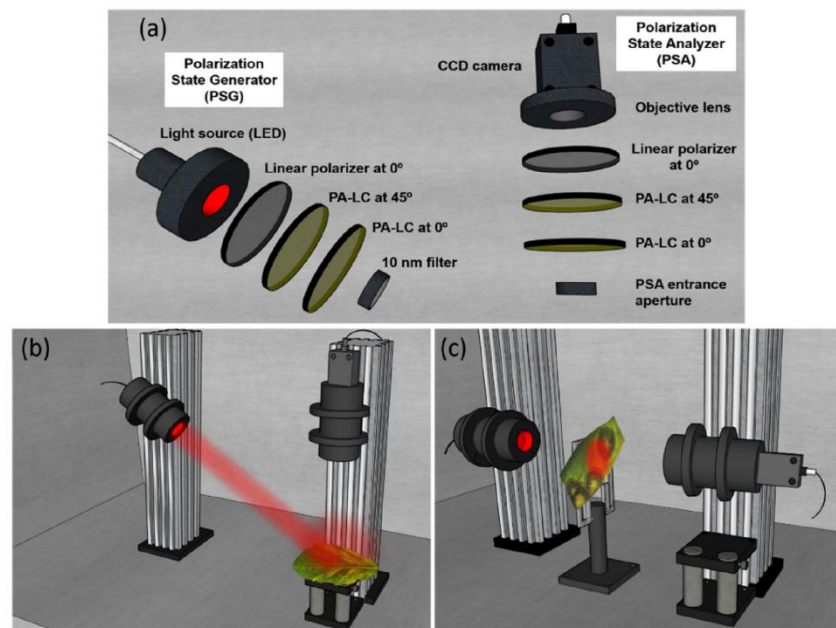


**Figure 2.** Three-dimensional representation of (a) the PSG and PSA optical components; the complete image Mueller polarimeter configurations used in this work; (b) reflection configuration; and (c) transmission configuration. Image reproduced from Ref. [15].

The PSG and the PSA systems are set into two mobile arms, where their respective angles can be adjusted to achieve different measuring configurations, as defined by an angular-based variable Polarimeter. This capability allows us to measure samples at two measuring configurations: transmission and reflection.

To measure samples in the reflection configuration (see Figure 2b), the PSG is located at  $34^\circ$  with respect to the laboratory vertical and the PSA is at  $0^\circ$  with respect to the laboratory vertical, thus avoiding ballistic reflection (scattered light is measured). If the samples are thin enough, they are also measured in the transmission configuration (see Figure 2c), where the two arms (PSG and PSA) are located in the laboratory horizontal, one facing the other. This is the case for vegetal samples such as, for example, leaves. In turn, in the case of animal samples, due to the sample thickness and characteristics, we only use the above-mentioned reflection configuration. Last but not least, we want to note that we use the polarimeter in optimized conditions in order to minimize the noise amplification from intensity measures to the final experimental  $M$ . This has been done in terms of condition numbers and equally weighted variance metrics, by using the six based polarizing basis described in [68]. In this sense, the polarimeter provides an accuracy of 2% in the measurements [69].

In this section, we also provide the detailed characteristics of the employed setup. The illumination is provided by a Thorlabs LED source (LED4D211, operated by DC4104 drivers distributed by Thorlabs) complemented with 10 nm dielectric bandwidth filters FB530-10 and FB470-10 for green and blue wavelengths, respectively, from Thorlabs. The linear polarizers are a Glam-Thompson prism-based CASIX and a dichroic sheet polarizer from Meadowlark Optics in the case of the PSG and the PSA, respectively. The four PA-LC retarders are Variable Retarders with Temperature Control (LVR-200-400-700-1LTSC distributed by Meadowlark Optics). Finally, imaging is performed by means of a 35 mm focal length Edmund Optics TECHSPEC<sup>®</sup> high resolution objective followed by an Allied Vision Manta G-504B CCD camera, with 5 Megapixel GigE Vision and Sony ICX655 CCD sensor,  $2452(H) \times 2056(V)$  resolution, and cell size of  $3.45 \mu\text{m} \times 3.45 \mu\text{m}$ , so that a spatial resolution of  $22 \mu\text{m}$  is achieved.

#### 4.2. Sample Description and Preparation

In this subsection, we provide the physiological description of the animal and vegetal samples inspected in this work as well as the preparation procedure for the measures. The different structural components of tissue are directly related to their polarimetric response. Therefore, different structures can generate different values in the polarimetric observables. For instance, birefringent properties leading to retardance in biological samples can be produced by the organization of some fibers such as collagen and elastin [24]. To allow us to interpret the results when inspecting the polarimetric observables of the different samples, here we provide a brief physiological analysis of the different animal and plant structures inspected.

The plant sample is a pathological grapevine (*Vitis rupestris* Scheele) leaf. It was obtained from a collaboration with the Botanical Institute of Barcelona and the Institute of Agrifood Research and Technology. The leaf sample showed symptoms of black rot disease. Black rot of grapes is caused by the Ascomycete *Guignardia bidwellii* (Ellis) Viala and Ravaz (Botryosphaerales). *Guignardia bidwellii* is a hemibiotrophic endoparasite that affects all growing green vine parts [70]; i.e., mainly occurring on leaves and additionally including leaf petioles, flowers and bunch peduncles and pedicels, shoots and tendrils [71]. On shoots, petioles, and pedicels, spots appear as small, darkened depressions. Lesions appear one or two weeks after infection on the infected plant part. The spots are roughly round or slightly segmented, some millimeters in size, initially brown-reddish and darkening with age.

During the biotrophic stage of *G. bidwellii*, soon after infection, hyphae grow mainly between the leaf cuticle and the walls of the palisade parenchyma. They form a dense, two-dimensional mycelium with no visible disease symptoms occurring during this latent incubation period, which may extend to up to 12 days [72,73]. When a later transition to necrotrophic stage occurs, mycelium of *G. bidwellii* expands and colonizes all leaf tissues (including epidermis, mesophyll and vascular bundles), thus leading to an overall necrosis of the infected plant part. Leaf samples used in this study were all showing necrotic lesions corresponding to the necrotrophic stage, and latent lesions (i.e., the biotrophic stage) were neither observed nor analyzed.

Production of secondary metabolites including guignardic acid, phenguignardic acid, alaguignardic acid, (6S,9R)-vomifoliol, several guignardianones (A–F), and several guignarenones (A–D) have been reported to date to be produced by different *Guignardia* species, which have been potentially demonstrated to show phytotoxic effects on plant cells [71]. Specifically, only (6S,9R)-vomifoliol and guignarenones (A–D) are known to be produced by *G. bidwellii* [74]. However, their phytotoxic action is disputed and their role in the development of grapevine black rot has not yet been confirmed [71].

The animal samples correspond to an ex vivo chicken tendon and a biopsy from an ex vivo cow brain. They were obtained from a local slaughterhouse and no laboratory animals were used for the experiments; previous treatment and commercial use of the animal tissue were in accordance with Spanish legislation. The samples were stored at  $-16^{\circ}\text{C}$  after the acquisition and until the measurements.

Tendons are composed of parallel fascicles of collagen following the same directionality as the corresponding muscle. Both tendinous and its surrounding tissue (fascia and areolar fatty tissue corresponding to paratenon) are of mesodermal origin, while the tendon is composed of densely packed directional bundles of type I collagen. This organization creates a striated structure.

The brain sample corresponds to a coronal section taken in the crossroad between the posterior parietal lobe and the occipital lobe of a cow, approximately 2 cm from the rostral to the occipital pole. This section is composed of cortical grey matter (GM), which is a layered cell-rich structure, and subcortical white matter (WM), which is sparsely cellular and composed of bundles of nerve fibers that connect the cortex with other cortical areas or with subcortical structures (at this level, mainly thalamus).

As previously stated, the plant sample was measured in the transmission configuration whereas for the animal samples, the reflection configuration was employed. All the samples

were measured at the three available wavelengths in the polarimeter. For simplicity, here we only present the results providing the best structure visualization of the polarimetric observables (corresponding to 470 nm).

## 5. Application of the Mueller Matrix Parameterization to Polarimetric Imaging of Biological Tissues

In this section, we show the comparison between the standard intensity images of the studied samples (grapevine, tendon and brain; see Section 4) and some of the selected polarimetric observables' images ( $R_I$ ,  $\varphi_D$  and  $\varphi_I$ ; see Section 3). To highlight the potential of this set of observables calculated for each one of the studied samples, we provide the best observables-based images results in terms of tissue visualization in this section. Note that common biological samples present different polarimetric features and specific observables will focus on a particular characteristic inspecting such features. This limits the situation of retrieving all possible biological structures at the same time with a single polarimetric channel and, thus, multiple observables should be considered for a complete analysis of the sample under inspection. In turn, the sixteen arrow-decomposition-derived observables discussed in this work present a set of metrics studying the main polarimetric characteristics of samples (retardance, diattenuation and depolarization). In the following examples, from all calculated metrics (see Section 2), we choose to present the channels providing the best visualization of particular biological structures of interest.

On the one hand, in Figure 3, we show the results for the grapevine sample. In particular, we compare the intensity image (Figure 3a) of the plant sample and the polarimetric image correspondent to the entrance retardance parameter ( $R_I$ ) (Figure 3b,c). We clearly observe the visualization enhancement between different structures of the plant associated with the polarimetric channel  $R_I$  when comparing Figure 3a,b. To benefit from the visual improvement related to colormaps, an image based on the entrance retardance parameter ( $R_I$ ) is represented in Figure 3c in a different colormap than the grayscale in Figure 3b. For the following discussion, we will compare images (a) and (c).

In Figure 3c, we see how some structures almost invisible to the standard intensity image (Figure 3a) are clearly observable. For instance, in Figure 3c, we observe how different structures present in the leaf have different polarimetric responses—in this case in the entrance retardance value, which is translated in a different value of  $R_I$ . For instance, the pathological areas of the plant (see yellow arrows) present different retardance values than the rest of the healthy leaf lamina. That is, the structural changes produced in these necrotic areas of the leaf (see description in Section 4) produce a very different entrance retardance,  $R_I$ , behavior which allows us to have a great contrast between the not infected part of the plant and the necrotic stage of the pathology. Moreover, we also can differentiate the vascular structure of the plant, especially the highlighted primary veins (see yellow dashed rectangles). Note how the stated visualization improvement can be of interest for characterization as well as the pathological analysis of plants.

On the other hand, in Figures 4 and 5, we show the results for the two studied animal samples. In the same way as with the plant sample, the polarimetric-observables-based images (both in grayscale and optimized colormap) are compared with the intensity image as a reference for each case.

In Figure 4, we see the images correspondent to the tendon sample. Figure 4a shows the standard intensity image of a tendon which is partially enveloped by fascia and areolar fatty tissue (indicated by the symbol \* in the figure). In the polarimetric image (Figure 4c), which in these cases corresponds with the azimuth of the diattenuation ( $\varphi_D$ ) observable, we are able to see structures almost not visible in the intensity channel (Figure 4a). In Figure 4b,c, we can appreciate a larger contrast between the fascia covering the right part of the tendon, where the different folds composing this structure have different azimuth values (see white rectangle in Figure 4). Moreover, the polarimetric channel  $\varphi_D$  also reveals a structure in the left part of the samples. These structures (see red arrows), hidden in the intensity image, are the boundaries between different fascicles inside the same tendon.



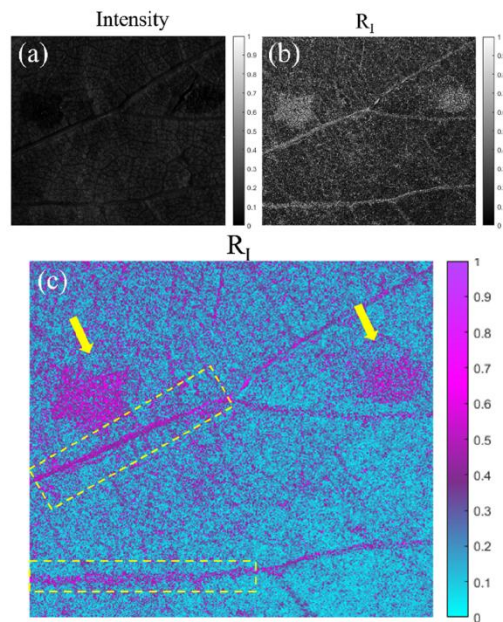


**Figure 3.** Images of the pathological grapevine sample for the 470 nm illumination wavelength. (a) Intensity image; (b,c) images of the  $R_I$  polarimetric channel with different colormaps (indicated on the right of the image). The yellow arrows indicate the necrotic lesions of the leaf and, the yellow dashed rectangles indicate some of the primary veins in the leaf.

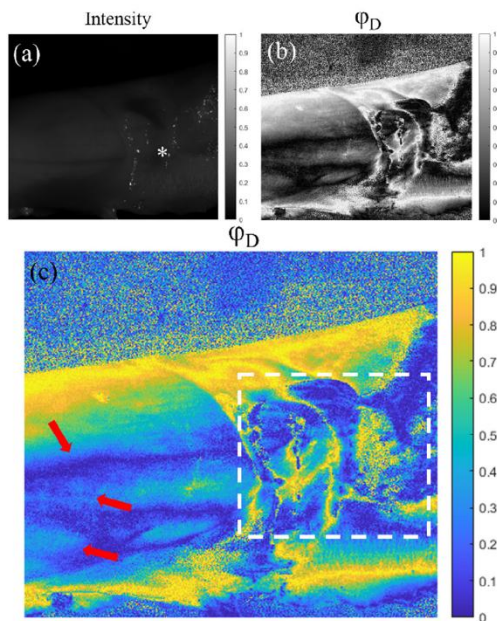


**Figure 4.** Images of the tendon sample for the 470 nm illumination wavelength. (a) Intensity image, (b,c) azimuth of the diattenuation,  $\varphi_D$ , images with different colormaps (indicated on the right of each image). The tendon is partially (\*) enveloped by fascia and areolar fatty tissue corresponding to paratenon. Red arrows in (c) indicate boundaries between different fascicles inside the same tendon.



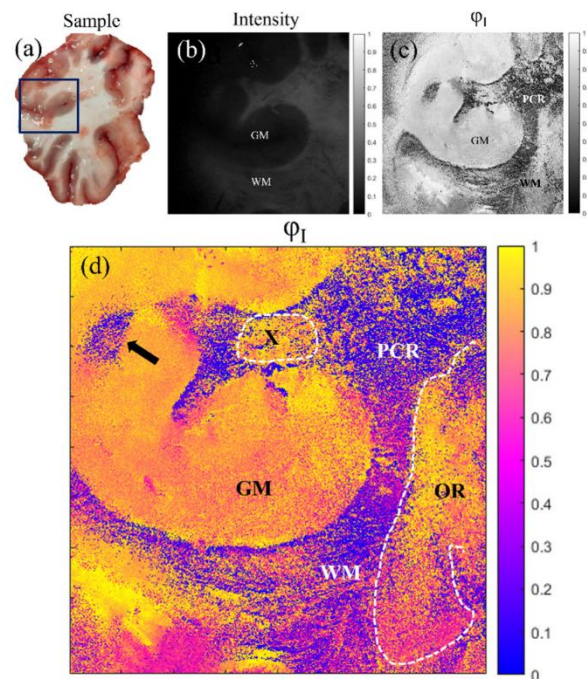


**Figure 5.** Images of a coronal section of a cow brain sample for the 470 nm illumination wavelength. The sample corresponds to a section taken in the crossroad between the posterior parietal and occipital lobes with cortical grey matter (GM) and subcortical white matter (WM) fibers correspondent to different types of radiation; parietal radiations of the *corona radiata* (PCR) and optical radiations (OR). (a) Macroscopic plain view of the full cut of the sample, (b) intensity image, (c,d) entrance retarder azimuth images,  $\varphi_I$ , with different colormaps (indicated on the right of each image).

In this example, we show how the features of the directionality of fibers of a similar nature (collagen and elastic) may be useful to distinguish tissues with roughly similar compositions (tendon vs. peritenon; tendon strongly directional vs. peritenon looser and non-directional) but different organizations that are not readily identifiable at plain view. Although the direct application of that is not near in the future, it might be useful in the analysis of musculoskeletal diseases that imply long-term changes in motor strategies and, therefore, in the balance of mechanical forces that determine the organization of collagen-rich tissues [75,76].

Finally, in Figure 5, we provide the results for a coronal section of a cow brain (see a photograph of the sample in Figure 5a). Once again, the comparison is set between the standard intensity image (Figure 5b) and the best results for polarimetric images (azimuth of the entrance retarder,  $\varphi_I$ ; Figure 5c,d). In this vein, in Figure 5a,b, we can see two different structures in the brain: gray matter (GM) and white matter (WM); which present different compositions and functions in the brain. However, in the polarimetric images (Figure 5c,d), we are able to distinguish information about the sample structure which is not visible in the intensity channel. Firstly, the boundaries of the WM and the GM are better observed in the  $\varphi_I$  image, where we can see a region of WM (see black arrow in Figure 5d) clearly contrasted (note that this WM region is not distinguished in the intensity image and can be misclassified as GM). Importantly, other interesting structures are revealed in the  $\varphi_I$  image. In particular, in Figure 5d we can identify fiber tracts of the subcortical WM classified according to their directionality. This allows tracing the borders between the longitudinal (at this level) parietal radiations of the *corona radiata* (PCR in the figure), optical radiations (transversal, OR in the figure; framed with white dashed lines in

the right of the figure) and specific fascicles probably corresponding to the dorsal visual processing pathway (for example, X in the figure; framed with white dashed lines).

Note that WM is composed of bundles of nerve fibers whose directionality is not identifiable macroscopically or with routine histochemistry, while specific techniques are time consuming or not easily reproducible. However, as we are sensible to different directionalities of the fibers composing the WM through the entrance retarder azimuth,  $\varphi_I$ , this channel leads to the high contrast of these structures. Therefore, with this channel, we are capable of detecting information about the directionality of the fibers by means of macroscopic and nondestructive measures of the sample.

Brain connectivity and its functional expression is probably the present frontier of applied neuroscience, as there is no gold-standard technique for pathway mapping apart from peri-mortem tract-tracing injections that are not ethically suitable for the study of human connectivity [77]. Histology or ultrastructure-based methods can distinguish fiber orientation but are not useful for tracing long range tracts, which are only revealed by specific techniques of microdissection [78] where resolution in smaller areas is lost. In vivo diffusion magnetic resonance tractography is a widely used method that, however, lacks (by design) histological counterchecks and is unable to resolve crossing tracts, as well as providing amputated images in areas such as the corticospinal tract where terminations are unambiguous (see Ref. [77] for a review on the matter). There are two methodological studies that provide acceptable anatomical resolution after the ex vivo analysis of the directionality of white matter tracts in large specimens: optical coherence tomography [79] and Mueller matrix polarimetry [80]. Both studies demonstrate the ability to classify large tracts that are known to have different orientations (internal capsule, cerebral peduncles, fimbria, medial lemniscus, optic tract, see also Ref. [81]) and to resolve the limits between gray and white matter. Our approach is similar to that described by Felger et al. in Ref. [81] but shows a better resolution of tracts within the white matter.

## 6. Conclusions

In this work, we analyzed the suitability of a particular set of polarimetric observables in the framework of biological imaging, which are derived from the arrow decomposition of a Mueller matrix of a given sample: (1) the mean intensity coefficient ( $m_{00}$ ) of  $\mathbf{M}_A$  of the measured Mueller matrix; (2) six angles (azimuth, ellipticity and retardance) determining the entrance and exit retarders ( $\varphi_I, \chi_I, R_I, \varphi_O, \chi_O, R_O$ ), respectively; (3) three parameters (azimuth, ellipticity and diattenuation) determining the diattenuation vector ( $\varphi_D, \chi_D, D$ ); (4) three parameters (azimuth, ellipticity and polarizance) determining the polarizance vector ( $\varphi_P, \chi_P, P$ ); and (5) the three indices of polarimetric purity ( $P_1, P_2, P_3$ ). These conform to a polarimetric space of sixteen polarimetric properties which are reviewed in Section 2.

These sixteen metrics have been applied to test the suitability for the visualization enhancement of biological tissues. To experimentally determine such properties, we have measured the experimental Mueller matrix of the samples, thanks to a complete imaging polarimeter. In particular, the samples under study have been: (1) a vegetal sample, i.e., *Vitis rupestris* leaf; (2) an animal ex vivo sample, i.e., a chicken tendon; and (3) an animal ex vivo sample, i.e., a cow brain. The description of the samples as well as of the image polarimeter is provided in Section 3.

In Section 4, we have proved the potential of the methods by analyzing the experimental results for the above stated samples. In the case of the *Vitis rupestris* leaf, the entrance retardance parameter ( $R_I$ ) leads to the best visualization results, allowing for a clear visualization of the necrotic areas of the leaf. For the case of tendinous tissue, the best visualization is provided by the azimuth of the diattenuation ( $\varphi_D$ ), revealing the dichroic nature of the tissue and allowing for detecting the boundaries between different fascicles inside the same tendon. Finally, for the coronal section of the brain, the azimuth of the entrance retardance ( $\varphi_I$ ) was selected, with this channel revealing fiber tracts of the subcortical white matter classified according to their directionality.



The improved results in terms of structure visualization pave the way for new applications in the fields of biomedical and botanical areas. We think they offer new possibilities for the early detection of some pathologies or for fundamental physiological studies. Importantly, we want to highlight that with this technique we are able to clearly observe some structures, as is the case for different bundles within the subcortical white matter of the brain, which are difficult to describe both *in vivo* and *postmortem* and require time-consuming and not easily reproducible methods, such as microinjections or specific, highly destructive techniques for dissection. Importantly, the methods provided are non-invasive and could be applied in real time applications, being in numerous cases less expensive than other existing alternatives. Last but not least, these polarimetric methods can be combined with other well-known optical techniques [82–84] to help the early detection of pathologies. In this sense, structures showing retardance features seem to be ideal to be analyzed through the arrow metrics, as can be the case of tissues consisting of collagen (muscle, tendon, myotendinous junction, skin, brain and associated pathologies).

To summarize, we have demonstrated the excellent potential of these metrics to not only enhance the contrast between different relevant structures in biological samples (both of animal and vegetal origin) but also to show structures that are hidden by using basic imaging systems. These are very promising results in biological applications such as plant pathology detection or animal tissue recognition. Nevertheless, further research would be required to compare the utility of such metrics with other well-known polarimetric observables in order to find the best suited polarimetric observables in terms of sample visualization (including human studies), but further studies point out in the direction that suitability will strongly depend on specific samples.

**Author Contributions:** J.J.G. and I.S.J. methodology; M.C.-C. and I.E. writing—original draft preparation and data acquisition; I.S.J. data curation; E.G.-A. data analysis in animal tissue; T.G. and J.L. data analysis in vegetal tissue; J.C. hardware construction; A.L. supervision and writing—review; J.C. and A.L. funding acquisition. All authors have read and agreed to the published version of the manuscript.

**Funding:** This research was funded by Ministerio de Ciencia e Innovación and Fondos FEDER (PID2021-126509OB-C21 and PDC2022-133332-C21), Generalitat de Catalunya (2021SGR00138) and Beatriu de Pinós Fellowship (2021-BP-00206).

**Informed Consent Statement:** Not applicable.

**Data Availability Statement:** Not applicable.

**Conflicts of Interest:** The authors declare no conflict of interest.

## References

- Goldstein, D.H. *Polarized Light, Revised and Expanded*; CRC Press: Boca Raton, FL, USA, 2003; ISBN 9780203911587.
- Gil, J.J.; Ossikovski, R. *Polarized Light and the Mueller Matrix Approach*; CRC Press: New York, NY, USA, 2022; ISBN 9780367815578.
- Chipman, R.A. Polarimetry. In *Handbook of Optics II*; McGraw-Hill: New York, NY, USA, 1995; Chapter 22.
- Sheppard, C.J.R.; Bendandi, A.; Le Gratiet, A.; Diaspro, A. Eigenvectors of Polarization Coherency Matrices. *J. Opt. Soc. Am. A* **2020**, *37*, 1143. [[CrossRef](#)] [[PubMed](#)]
- Ignatenko, D.N.; Shkirin, A.V.; Lobachevsky, Y.P.; Gudkov, S.V. Applications of Mueller Matrix Polarimetry to Biological and Agricultural Diagnostics: A Review. *Appl. Sci.* **2022**, *12*, 5258. [[CrossRef](#)]
- Li, J.; Liao, R.; Guan, C.; Wang, H.; Zhuo, Z.; Zeng, Y.; Ma, H. Particulate Mueller Matrix Polarimetry. *Opt. Laser. Technol.* **2023**, *158*, 108780. [[CrossRef](#)]
- Gil, J.J.; Bernabeu, E. Depolarization and Polarization Indices of an Optical System. *Opt. Acta Int. J. Opt.* **1986**, *33*, 185–189. [[CrossRef](#)]
- Lu, S.-Y.; Chipman, R.A. Interpretation of Mueller Matrices Based on Polar Decomposition. *J. Opt. Soc. Am. A* **1996**, *13*, 1106. [[CrossRef](#)]
- Cloude, S. Group Theory and Polarisation Algebra. *Optik* **1986**, *75*, 26–36.
- Ossikovski, R. Alternative Depolarization Criteria for Mueller Matrices. *J. Opt. Soc. Am. A* **2010**, *27*, 808. [[CrossRef](#)]
- Tariq, A.; Li, P.; Chen, D.; Lv, D.; Ma, H. Physically Realizable Space for the Purity-Depolarization Plane for Polarized Light Scattering Media. *Phys. Rev. Lett.* **2017**, *119*, 033202. [[CrossRef](#)]

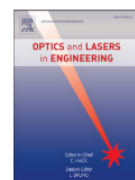
12. San José, I.; Gil, J.J. Invariant Indices of Polarimetric Purity: Generalized Indices of Purity for  $n \times n$  Covariance Matrices. *Opt. Commun.* **2011**, *284*, 38–47. [\[CrossRef\]](#)
13. Ossikovski, R.; Vizet, J. Eigenvalue-Based Depolarization Metric Spaces for Mueller Matrices. *J. Opt. Soc. Am. A* **2019**, *36*, 1173. [\[CrossRef\]](#)
14. Van Eeckhout, A.; Lizana, A.; Garcia-Caurel, E.; Gil, J.J.; Sansa, A.; Rodríguez, C.; Estévez, I.; González, E.; Escalera, J.C.; Moreno, I.; et al. Polarimetric Imaging of Biological Tissues Based on the Indices of Polarimetric Purity. *J. Biophotonics* **2018**, *11*, e201700189. [\[CrossRef\]](#) [\[PubMed\]](#)
15. Rodríguez, C.; Garcia-Caurel, E.; Garnatje, T.; Serra i Ribas, M.; Luque, J.; Campos, J.; Lizana, A. Polarimetric Observables for the Enhanced Visualization of Plant Diseases. *Sci. Rep.* **2022**, *12*, 14743. [\[CrossRef\]](#) [\[PubMed\]](#)
16. Khan, S.; Qadir, M.; Khalid, A.; Ashraf, S.; Ahmad, I. Characterization of Cervical Tissue Using Mueller Matrix Polarimetry. *Lasers Med. Sci.* **2023**, *38*, 46. [\[CrossRef\]](#) [\[PubMed\]](#)
17. Ahmad, I.; Gribble, A.; Ikram, M.; Pop, M.; Vitkin, A. Polarimetric Assessment of Healthy and Radiofrequency Ablated Porcine Myocardial Tissue. *J. Biophotonics* **2016**, *9*, 750–759. [\[CrossRef\]](#)
18. Canabal-Carbia, M.; Rodríguez, C.; Estévez, I.; Van Eeckhout, A.; González-Arnay, E.; García-Caurel, E.; Garnatje, T.; Lizana, A.; Campos, J. Enhancing Biological Tissue Structures Visualization through Polarimetric Parameters. In Proceedings of the SPIE 1238205, San Francisco, CA, USA, 28 January–2 February 2023; p. 16. [\[CrossRef\]](#)
19. Borovkova, M.; Trifonyuk, L.; Ushenko, V.; Dubolazov, O.; Vanchulyak, O.; Bodnar, G.; Ushenko, Y.; Olar, O.; Ushenko, O.; Sakhnovskiy, M.; et al. Mueller-Matrix-Based Polarization Imaging and Quantitative Assessment of Optically Anisotropic Polycrystalline Networks. *PLoS ONE* **2019**, *14*, e0214494. [\[CrossRef\]](#)
20. Clark, A.G.; Vignjevic, D.M. Modes of Cancer Cell Invasion and the Role of the Microenvironment. *Curr. Opin. Cell Biol.* **2015**, *36*, 13–22. [\[CrossRef\]](#)
21. Wood, M.F.G.; Ghosh, N.; Wallenburg, M.A.; Li, S.-H.; Weisel, R.D.; Wilson, B.C.; Li, R.-K.; Vitkin, I.A. Polarization Birefringence Measurements for Characterizing the Myocardium, Including Healthy, Infarcted, and Stem-Cell-Regenerated Tissues. *J. Biomed. Opt.* **2010**, *15*, 047009. [\[CrossRef\]](#)
22. Hogan, B.T.; Ushenko, V.A.; Syvokorovskaya, A.-V.; Dubolazov, A.V.; Vanchulyak, O.Y.; Ushenko, A.G.; Ushenko, Y.A.; Gorsky, M.P.; Tomka, Y.; Kuznetsov, S.L.; et al. 3D Mueller Matrix Reconstruction of the Optical Anisotropy Parameters of Myocardial Histopathology Tissue Samples. *Front. Phys.* **2021**, *9*, 737866. [\[CrossRef\]](#)
23. Palevitz, B.A.; Hepler, P.K. Cellulose Microfibril Orientation and Cell Shaping in Developing Guard Cells of Allium: The Role of Microtubules and Ion Accumulation. *Planta* **1976**, *132*, 71–93. [\[CrossRef\]](#)
24. Wang, L.V.; Coté, G.L.; Jacques, S.L. Special Section Guest Editorial. *J. Biomed. Opt.* **2002**, *7*, 278. [\[CrossRef\]](#)
25. Peyvaste, M.; Dubolazov, A.; Popow, A.; Ushenko, A.; Ushenko, Y.; Meglinski, I. Two-point Stokes vector diagnostic approach for characterization of optically anisotropic biological tissues. *J. Phys. D Appl. Phys.* **2020**, *53*, 395401. [\[CrossRef\]](#)
26. Ghosh, N.; Vitkin, I.A. Tissue Polarimetry: Concepts, Challenges, Applications, and Outlook. *J. Biomed. Opt.* **2011**, *16*, 110801. [\[CrossRef\]](#) [\[PubMed\]](#)
27. Borovkova, M.; Peyvaste, M.; Dubolazov, O.; Ushenko, Y.; Ushenko, V.; Bykov, A.; Deby, S.; Rehbindler, J.; Novikova, T.; Meglinski, I. Complementary Analysis of Mueller-Matrix Images of Optically Anisotropic Highly Scattering Biological Tissues. *J. Eur. Opt. Soc.-Rapid Publ.* **2018**, *14*, 20. [\[CrossRef\]](#)
28. Shtein, I.; Shelef, Y.; Marom, Z.; Zelinger, E.; Schwartz, A.; Popper, Z.A.; Bar-On, B.; Harpaz-Saad, S. Stomatal Cell Wall Composition: Distinctive Structural Patterns Associated with Different Phylogenetic Groups. *Ann. Bot.* **2017**, *119*, 1021–1033. [\[CrossRef\]](#) [\[PubMed\]](#)
29. Ali, Z.; Mahmood, T.; Shahzad, A.; Iqbal, M.; Ahmad, I. Assessment of Tissue Pathology Using Optical Polarimetry. *Lasers Med. Sci.* **2022**, *37*, 1907–1919. [\[CrossRef\]](#) [\[PubMed\]](#)
30. Badiéyan, S.; Ameri, A.; Razzaghi, M.R.; Rafii-Tabar, H.; Sasanpour, P. Mueller Matrix Imaging of Prostate Bulk Tissues; Polarization Parameters as a Discriminating Benchmark. *Photodiagnosis Photodyn. Ther.* **2019**, *26*, 90–96. [\[CrossRef\]](#) [\[PubMed\]](#)
31. Van Eeckhout, A.; Garcia-Caurel, E.; Ossikovski, R.; Lizana, A.; Rodríguez, C.; González-Arnay, E.; Campos, J. Depolarization Metric Spaces for Biological Tissues Classification. *J. Biophotonics* **2020**, *13*, e202000083. [\[CrossRef\]](#)
32. Ivanov, D.; Dremine, V.; Borisova, E.; Bykov, A.; Novikova, T.; Meglinski, I.; Ossikovski, R. Polarization and Depolarization Metrics as Optical Markers in Support to Histopathology of Ex Vivo Colon Tissue. *Biomed. Opt. Express* **2021**, *12*, 4560. [\[CrossRef\]](#)
33. Pierangelo, A.; Benali, A.; Antonelli, M.-R.; Novikova, T.; Validire, P.; Gayet, B.; De Martino, A. Ex-Vivo Characterization of Human Colon Cancer by Mueller Polarimetric Imaging. *Opt. Express* **2011**, *19*, 1582. [\[CrossRef\]](#)
34. Rodríguez, C.; Van Eeckhout, A.; Ferrer, L.; Garcia-Caurel, E.; González-Arnay, E.; Campos, J.; Lizana, A. Polarimetric Data-Based Model for Tissue Recognition. *Biomed. Opt. Express* **2021**, *12*, 4852. [\[CrossRef\]](#)
35. Wan, J.; Dong, Y.; Xue, J.-H.; Lin, L.; Du, S.; Dong, J.; Yao, Y.; Li, C.; Ma, H. Polarization-Based Probabilistic Discriminative Model for Quantitative Characterization of Cancer Cells. *Biomed. Opt. Express* **2022**, *13*, 3339. [\[CrossRef\]](#) [\[PubMed\]](#)
36. Canabal-Carbia, M.; Van Eeckhout, A.; Rodríguez, C.; González-Arnay, E.; Estévez, I.; Gil, J.J.; Garcia-Caurel, E.; Ossikovski, R.; Campos, J.; Lizana, A. Depolarizing Metrics in the Biomedical Field: Vision Enhancement and Classification of Biological Tissues. *J. Innov. Opt. Health Sci.* **2023**, *2330004*, 1–17. [\[CrossRef\]](#)
37. Chue-Sang, J.; Holness, N. Use of Mueller Matrix Colposcopy in the Characterization of Cervical Collagen Anisotropy. *J. Biomed. Opt.* **2018**, *23*, 1. [\[CrossRef\]](#) [\[PubMed\]](#)



38. Sprenger, J.; Murray, C.; Lad, J.; Jones, B.; Thomas, G.; Nofech-Mozes, S.; Khorasani, M.; Vitkin, A. Toward a Quantitative Method for Estimating Tumour-Stroma Ratio in Breast Cancer Using Polarized Light Microscopy. *Biomed. Opt. Express* **2021**, *12*, 3241. [\[CrossRef\]](#)
39. Ramella-Roman, J.C.; Saytashev, I.; Piccini, M. A Review of Polarization-Based Imaging Technologies for Clinical and Preclinical Applications. *J. Opt.* **2020**, *22*, 123001. [\[CrossRef\]](#)
40. Trifonyuk, L.; Sdobnov, A.; Baranowski, W.; Ushenko, V.; Olar, O.; Dubolazov, A.; Pidkamin, L.; Sidor, M.; Vanchuliak, O.; Motrich, A.; et al. Differential Mueller Matrix Imaging of Partially Depolarizing Optically Anisotropic Biological Tissues. *Lasers Med. Sci.* **2020**, *35*, 877–891. [\[CrossRef\]](#)
41. Van Eeckhout, A.; Garcia-Caurel, E.; Garnatje, T.; Escalera, J.C.; Durfort, M.; Vidal, J.; Gil, J.J.; Campos, J.; Lizana, A. Polarimetric Imaging Microscopy for Advanced Inspection of Vegetal Tissues. *Sci. Rep.* **2021**, *11*, 3913. [\[CrossRef\]](#)
42. Van Eeckhout, A.; Garcia-Caurel, E.; Garnatje, T.; Durfort, M.; Escalera, J.C.; Vidal, J.; Gil, J.J.; Campos, J.; Lizana, A. Depolarizing Metrics for Plant Samples Imaging. *PLoS ONE* **2019**, *14*, e0213909. [\[CrossRef\]](#)
43. Savenkov, S.N.; Muttiah, R.S.; Oberemok, E.A.; Priezhev, A.V.; Kolomiets, I.S.; Klimov, A.S. Measurement and Interpretation of Mueller Matrices of Barley Leaves. *Quantum Elec.* **2020**, *50*, 55–60. [\[CrossRef\]](#)
44. Al Bugami, B.; Su, Y.; Rodríguez, C.; Lizana, A.; Campos, J.; Durfort, M.; Ossikovski, R.; Garcia-Caurel, E. Characterization of Vine, Vitis Vinifera, Leaves by Mueller Polarimetric Microscopy. *Thin Solid Films* **2023**, *764*, 139594. [\[CrossRef\]](#)
45. Rodríguez, C.; Van Eeckhout, A.; Garcia-Caurel, E.; Lizana, A.; Campos, J. Automatic Pseudo-Coloring Approaches to Improve Visual Perception and Contrast in Polarimetric Images of Biological Tissues. *Sci. Rep.* **2022**, *12*, 18479. [\[CrossRef\]](#) [\[PubMed\]](#)
46. Patty, C.H.L.; Luo, D.A.; Snik, F.; Ariese, F.; Buma, W.J.; ten Kate, I.L.; van Spanning, R.J.M.; Sparks, W.B.; Germer, T.A.; Garab, G.; et al. Imaging Linear and Circular Polarization Features in Leaves with Complete Mueller Matrix Polarimetry. *Biochim. Biophys. Acta (BBA) Gen. Subj.* **2018**, *1862*, 1350–1363. [\[CrossRef\]](#) [\[PubMed\]](#)
47. Rodríguez-Núñez, O.; Schucht, P.; Hewer, E.; Novikova, T.; Pierangelo, A. Polarimetric Visualization of Healthy Brain Fiber Tracts under Adverse Conditions: Ex Vivo Studies. *Biomed. Opt. Express* **2021**, *12*, 6674. [\[CrossRef\]](#) [\[PubMed\]](#)
48. Schucht, P.; Lee, H.R.; Mezouar, H.M.; Hewer, E.; Raabe, A.; Murek, M.; Zubak, I.; Goldberg, J.; Kovari, E.; Pierangelo, A.; et al. Visualization of White Matter Fiber Tracts of Brain Tissue Sections With Wide-Field Imaging Mueller Polarimetry. *IEEE Trans. Med. Imaging* **2020**, *39*, 4376–4382. [\[CrossRef\]](#)
49. Ushenko, V.A.; Hogan, B.T.; Dubolazov, A.; Piavchenko, G.; Kuznetsov, S.L.; Ushenko, A.G.; Ushenko, Y.O.; Gorsky, M.; Bykov, A.; Meglinski, I. 3D Mueller Matrix Mapping of Layered Distributions of Depolarisation Degree for Analysis of Prostate Adenoma and Carcinoma Diffuse Tissues. *Sci. Rep.* **2021**, *11*, 5162. [\[CrossRef\]](#)
50. Ahmad, I.; Khaliq, A.; Iqbal, M.; Khan, S. Mueller Matrix Polarimetry for Characterization of Skin Tissue Samples: A Review. *Photodiagnosis Photodyn. Ther.* **2020**, *30*, 101708. [\[CrossRef\]](#)
51. Du, E.; He, H.; Zeng, N.; Sun, M.; Guo, Y.; Wu, J.; Liu, S.; Ma, H. Mueller Matrix Polarimetry for Differentiating Characteristic Features of Cancerous Tissues. *J. Biomed. Opt.* **2014**, *19*, 076013. [\[CrossRef\]](#)
52. Kupinski, M.; Boffety, M.; Goudail, F.; Ossikovski, R.; Pierangelo, A.; Rehbindler, J.; Vizet, J.; Novikova, T. Polarimetric Measurement Utility for Pre-Cancer Detection from Uterine Cervix Specimens. *Biomed. Opt. Express* **2018**, *9*, 5691. [\[CrossRef\]](#)
53. Van Eeckhout, A.; González, E.; Escalera, J.C.; Moreno, I.; Campos, J.; Zhang, H.; Ossikovski, R.; Lizana, A.; Garcia-Caurel, E.; Gil, J.J.; et al. Indices of Polarimetric Purity to Enhance the Image Quality in Biophotonics Applications. In Proceedings of the SPIE 10685, Strasbourg, France, 22–26 April 2018; p. 9. [\[CrossRef\]](#)
54. Ushenko, V.; Sdobnov, A.; Syvokorovskaya, A.; Dubolazov, A.; Vanchulyak, O.; Ushenko, A.; Ushenko, Y.; Gorsky, M.; Sidor, M.; Bykov, A.; et al. 3D Mueller-Matrix Diffusive Tomography of Polycrystalline Blood Films for Cancer Diagnosis. *Photonics* **2018**, *5*, 54. [\[CrossRef\]](#)
55. Ushenko, V.A.; Hogan, B.T.; Dubolazov, A.; Grechina, A.V.; Boronikhina, T.V.; Gorsky, M.; Ushenko, A.G.; Ushenko, Y.O.; Bykov, A.; Meglinski, I. Embossed Topographic Depolarisation Maps of Biological Tissues with Different Morphological Structures. *Sci. Rep.* **2021**, *11*, 3871. [\[CrossRef\]](#)
56. Gil, J.J. Transmittance Constraints in Serial Decompositions of Depolarizing Mueller Matrices: The Arrow Form of a Mueller Matrix. *J. Opt. Soc. Am. A* **2013**, *30*, 701–707. [\[CrossRef\]](#)
57. Gil, J.J.; San José, I. Reduced Form of a Mueller Matrix. *J. Mod. Opt.* **2016**, *63*, 1579–1583. [\[CrossRef\]](#)
58. Ossikovski, R. Analysis of Depolarizing Mueller Matrices through a Symmetric Decomposition. *J. Opt. Soc. Am. A* **2009**, *26*, 1109. [\[CrossRef\]](#) [\[PubMed\]](#)
59. Xing, Z.-F. On the Deterministic and Non-Deterministic Mueller Matrix. *J. Mod. Opt.* **1992**, *39*, 461–484. [\[CrossRef\]](#)
60. Robson, B.A. *The Theory of Polarization Phenomena*; Clarendon Press: Oxford, UK, 1975.
61. Sekera, Z. Scattering Matrices and Reciprocity Relationships for Various Representations of the State of Polarization. *J. Opt. Soc. Am.* **1966**, *56*, 1732. [\[CrossRef\]](#)
62. Schönhofer, A.; Kuball, H.-G. Symmetry Properties of the Mueller Matrix. *Chem. Phys.* **1987**, *115*, 159–167. [\[CrossRef\]](#)
63. Gil, J.J. Components of Purity of a Mueller Matrix. *J. Opt. Soc. Am. A* **2011**, *28*, 1578. [\[CrossRef\]](#)
64. Gil, J.J. Invariant Quantities of a Mueller Matrix under Rotation and Retarder Transformations. *J. Opt. Soc. Am. A* **2016**, *33*, 52–58. [\[CrossRef\]](#)
65. Gil, J.J. Physical Quantities Involved in a Mueller Matrix. In Proceedings of the SPIE 9853, Baltimore Chenault, MD, USA, 17–21 April 2016; p. 985302. [\[CrossRef\]](#)

66. Jacquemoud, S.; Ustin, S. *Leaf Optical Properties*; Cambridge University Press: Cambridge, UK, 2019; ISBN 9781108686457.
67. Mustafa, F.H.; Jaafar, M.S. Comparison of Wavelength-Dependent Penetration Depths of Lasers in Different Types of Skin in Photodynamic Therapy. *Indian J. Phys.* **2013**, *87*, 203–209. [[CrossRef](#)]
68. Peinado, A.; Lizana, A.; Vidal, J.; Iemmi, C.; Campos, J. Optimization and Performance Criteria of a Stokes Polarimeter Based on Two Variable Retarders. *Opt. Express* **2010**, *18*, 9815. [[CrossRef](#)]
69. Peinado, A. *Analysis, Optimization and Implementation of a Variable Retardance Based Polarimeter*; Universitat Autònoma de Barcelona: Barcelona, Spain, 2014.
70. De Silva, N.; Lumyong, S.; Hyde, K.D.; Bulgakov, T.; Philips, A.J.L.; Yan, J. Mycosphere Essays 9: Defining Biotrophs and Hemibiotrophs. *Mycosphere* **2016**, *7*, 545–559. [[CrossRef](#)]
71. Szabó, M.; Csikász-Krizsics, A.; Dula, T.; Farkas, E.; Roznik, D.; Kozma, P.; Deák, T. Black Rot of Grapes (*Guignardia bidwellii*)—A Comprehensive Overview. *Horticulturae* **2023**, *9*, 130. [[CrossRef](#)]
72. Ullrich, C.I.; Kleespies, R.G.; Enders, M.; Koch, E. Biology of the Black Rot Pathogen, *Guignardia bidwellii*, Its Development in Susceptible Leaves of Grapevine *Vitis Vinifera*. *J. Kulturpflanzen* **2009**, *61*, 82–90.
73. Kuo, K.; Hoch, H.C. The Parasitic Relationship between *Phyllosticta Ampeliciida* and *Vitis Vinifera*. *Mycologia* **1996**, *88*, 626–634. [[CrossRef](#)]
74. Sommart, U.; Rukachaisirikul, V.; Trisuwan, K.; Tadpetch, K.; Phongpaichit, S.; Preedanon, S.; Sakayaroj, J. Tricycloalternarene Derivatives from the Endophytic Fungus *Guignardia Bidwellii* PSU-G11. *Phytochem. Lett.* **2012**, *5*, 139–143. [[CrossRef](#)]
75. Rosin, N.L.; Agabalyan, N.; Olsen, K.; Martufi, G.; Gabriel, V.; Biernaskie, J.; Di Martino, E.S. Collagen Structural Alterations Contribute to Stiffening of Tissue after Split-Thickness Skin Grafting. *Wound Repair Regen.* **2016**, *24*, 263–274. [[CrossRef](#)]
76. Chen, P.; Wang, A.; Haynes, W.; Landao-Bassonga, E.; Lee, C.; Ruan, R.; Breidahl, W.; Shiroud Heidari, B.; Mitchell, C.A.; Zheng, M. A Bio-Inductive Collagen Scaffold That Supports Human Primary Tendon-Derived Cell Growth for Rotator Cuff Repair. *J. Orthop. Transl.* **2021**, *31*, 91–101. [[CrossRef](#)]
77. Charvet, C.J. Mapping Human Brain Pathways: Challenges and Opportunities in the Integration of Scales. *Brain Behav. Evol.* [[CrossRef](#)]
78. Agrawal, A.; Kapfhammer, J.P.; Kress, A.; Wichers, H.; Deep, A.; Feindel, W.; Sonntag, V.K.H.; Spetzler, R.F.; Preul, M.C. Josef Klingler’s Models of White Matter Tracts: Influences on Neuroanatomy, Neurosurgery, and Neuroimaging. *Neurosurgery* **2011**, *69*, 238–254. [[CrossRef](#)]
79. Wang, H.; Black, A.J.; Zhu, J.; Stigen, T.W.; Al-Qaisi, M.K.; Netoff, T.I.; Abosch, A.; Akkin, T. Reconstructing Micrometer-Scale Fiber Pathways in the Brain: Multi-Contrast Optical Coherence Tomography Based Tractography. *Neuroimage* **2011**, *58*, 984–992. [[CrossRef](#)]
80. Felger, L.; Rodríguez-Núñez, O.; Gros, R.; Maragkou, T.; McKinley, R.; Moriconi, S.; Murek, M.; Zubak, I.; Novikova, T.; Pierangelo, A.; et al. Robustness of the Wide-Field Imaging Mueller Polarimetry for Brain Tissue Differentiation and White Matter Fiber Tract Identification in a Surgery-like Environment: An Ex Vivo Study. *Biomed. Opt. Express* **2023**, *14*, 2400. [[CrossRef](#)]
81. Mandonnet, E.; Sarubbo, S.; Petit, L. The Nomenclature of Human White Matter Association Pathways: Proposal for a Systematic Taxonomic Anatomical Classification. *Front. Neuroanat.* **2018**, *12*, 94. [[CrossRef](#)] [[PubMed](#)]
82. Helmchen, F.; Denk, W. Deep Tissue Two-Photon Microscopy. *Nat. Methods* **2005**, *2*, 932–940. [[CrossRef](#)] [[PubMed](#)]
83. Arano-Martinez, J.A.; Martínez-González, C.L.; Salazar, M.I.; Torres-Torres, C. A Framework for Biosensors Assisted by Multiphoton Effects and Machine Learning. *Biosensors* **2022**, *12*, 710. [[CrossRef](#)] [[PubMed](#)]
84. Raja, H.; Akram, M.U.; Hassan, T.; Ramzan, A.; Aziz, A.; Raja, H. Glaucoma Detection Using Optical Coherence Tomography Images: A Systematic Review of Clinical and Automated Studies. *IETE J. Res.* **2022**, 1–21. [[CrossRef](#)]

**Disclaimer/Publisher’s Note:** The statements, opinions and data contained in all publications are solely those of the individual author(s) and contributor(s) and not of MDPI and/or the editor(s). MDPI and/or the editor(s) disclaim responsibility for any injury to people or property resulting from any ideas, methods, instructions or products referred to in the content.



# Connecting the microscopic depolarizing origin of samples with macroscopic measures of the Indices of Polarimetric Purity

Mónica Canabal-Carbia<sup>a,\*</sup>, Irene Estévez<sup>a</sup>, Esther Nabadda<sup>b</sup>, Enrique Garcia-Caurel<sup>c</sup>, J.J. Gil<sup>d</sup>, Razvigor Ossikovski<sup>c</sup>, Andrés Márquez<sup>e,f</sup>, Ignacio Moreno<sup>b,g</sup>, Juan Campos<sup>a</sup>, Angel Lizana<sup>a</sup>

<sup>a</sup> Grup d'Òptica, Departament de Física, Universitat Autònoma de Barcelona, Bellaterra 08193, Spain

<sup>b</sup> Instituto de Bioingeniería, Universidad Miguel Hernández de Elche, Elche 03202, Spain

<sup>c</sup> LPICM, CNRS, Ecole Polytechnique, Institut Polytechnique de Paris, Palaiseau 91120, France

<sup>d</sup> Departamento de Física Aplicada, Universidad de Zaragoza, Pedro Cerbuna 12, Zaragoza 50009, Spain

<sup>e</sup> Departamento de Física, Ing. de Sistemas y T. Señal, Universidad de Alicante, Alicante 03080, Spain

<sup>f</sup> I.U. Física Aplicada a las Ciencias y las Tecnologías, Universidad de Alicante, Alicante 03080, Spain

<sup>g</sup> Departamento de Ciencias de Materiales, Óptica y Tecnología Electrónica, Universidad Miguel Hernández, Elche 03202, Spain

## ARTICLE INFO

### Keywords:

Mueller matrices  
Indices of Polarimetric Purity  
Depolarizers  
Biophotonics  
Polarization

## ABSTRACT

In this work we show how a specific set of three depolarizing observables, the Indices of Polarimetric Purity (IPP),  $P_1$ ,  $P_2$  and  $P_3$ , are ideal metrics to study the depolarization characteristic of media. We simulate different depolarizing scenarios, based on different depolarizing origins, and we study the corresponding IPP values. The simulations are based on the incoherent addition of multiple elemental polarizing elements, as ideal polarizers and/or retarders with different specific characteristics (orientation, retardance, transmittance, etc.). Further depolarizing scenarios are also studied by including the effect of ideal depolarizers. We show for the first time how by analyzing depolarizing systems through IPP we unravel two different depolarizing origins: isotropic and anisotropic depolarization, with meaningful physical interpretation. The former, isotropic depolarization is related to pure scattering processes, and mainly connected with  $P_3$  observable. The later, anisotropic depolarization is originated by microscopic constituent elements showing polarimetric anisotropy (dichroic and/or birefringent elements with different characteristics) and anisotropic scattering produced by these elements, and mainly described by  $P_1$  and  $P_2$  observables. Both effects can be simultaneously observed in real samples and give us information of the processes that give rise to depolarization in light-matter interactions. The simulated results are experimentally validated by analyzing the depolarizing behavior, in terms of IPP, of diverse real samples with easy physical interpretation, and direct connection with simulations. The present study could be of interest in multiple scenarios, to further understand the depolarizing response of samples, and it can be of special interest for the study of biological tissues and pathologies, as they present important depolarizing behavior.

## 1. Introduction

Polarimetry encompasses a collection of optical techniques devoted to analyzing one main characteristic of transversal waves, the polarization, or the polarimetric property of samples, through light-matter interactions. Nowadays, polarimetry is useful in a wide range of applications, as in astronomy [1], remote sensing [2], material characterization and quality control [3,4], food analysis [5], botanical applications [6], biomedicine [7], among other.

In the case of biological samples, polarized light may be modified in different ways when interacting with different organic structures, this

being of interest in terms of contrast enhancement between different structures in the samples. These differences in the exiting polarization after interacting with different tissues are related to the specific polarimetric characteristics of tissues, as the birefringence, dichroism, or depolarization. Typically, birefringence and dichroism are two polarimetric responses well-studied in biological samples, as it is common to find that constituent elements of tissues present some significant behavior in terms of birefringence or dichroism. For instance, in Ref. [8] the birefringent properties of a sample help to differentiate between healthy and cancerous tissue, in Ref. [9] elastic and collagen fibers in a rabbit aortic wall are characterized by its retardance, and in Ref. [10]

\* Corresponding author.

E-mail address: [monica.canabal@uab.cat](mailto:monica.canabal@uab.cat) (M. Canabal-Carbia).

<https://doi.org/10.1016/j.optlaseng.2023.107830>

Received 29 May 2023; Received in revised form 5 September 2023; Accepted 6 September 2023

Available online 20 September 2023

0143-8166/© 2023 The Authors. Published by Elsevier Ltd. This is an open access article under the CC BY license (<http://creativecommons.org/licenses/by/4.0/>).



diattenuation allows to distinguish between brain regions with different tissue properties.

Depolarization is a measure of the sample capability to depolarize an incident fully polarized light beam. Traditionally, in terms of image contrast, depolarization was seen as a non-desired magnitude, which was tried to be minimized to exploit the other polarimetric properties. However, in the last decades, it has been revealed that depolarization channel itself provides large intrinsic information of samples (as for instance, organization, size, density of structures, etc.), as well as it is very relevant in terms of structures visualization enhancement. In this sense, depolarizing channels have been reported as useful to detect cancer stages in different human and animal tissues as *ex-vivo* human colon and skin [11,12] colon cancer, skin carcinoma, pathology detection in vegetal tissue [13] and, tissue recognition [14].

An ideal framework to study depolarizing properties of samples is the Mueller–Stokes (M-S) formalism. In this sense, the Mueller matrix of a sample, can be experimentally determined from intensity measurements. Different observables that can be deduced from the coefficients of the Mueller matrix allow to study the depolarizing properties of samples [15–17]. Among these different approaches, in this work we use the Indices of Polarimetric Purity (IPP) [18–20] as reference metrics to study the depolarization. The IPP comprises a set of three observables, the  $P_1$ ,  $P_2$  and  $P_3$ , channels, that can be derived from the eigenvalues of the covariance matrix [20] (a transformation of the Mueller matrix), and they are connected to the polarimetric randomness structure of the sample that they represent [21–23]. The IPP are an ideal framework to study the depolarizing properties of biological samples, as they have already proved their interest for the image enhancement and discrimination of biological structures [6,13,24,25] as well as to construct recognition models for the guided detection of biological structures [14].

In this work we take advantage of the IPP as a metrics to study the depolarization origin. For this purpose, we construct different depolarizers through the incoherent summation of different basic elements (pure diattenuators, pure retarders and perfect depolarizers), with different properties and orientations. The resulting simulated scenarios, studied in terms of IPP, allow us to understand the inherent constituents within samples with regards to their macroscopic depolarizing response. In this sense, the proposed simulations allow us to differentiate between different kind of depolarizers, arising two main depolarizing mechanisms: (1) depolarizers whose depolarizing response does not depend on the input state of polarization; and (2) depolarizers whose depolarizing response depends on the input polarization. Importantly, we demonstrate how those depolarizing vias can be quantified by using the IPP framework. In addition, the proposed simulated environments are experimentally validated with simple samples with well-defined polarization properties that reproduce phantom experiments.

The presented study allows us to connect inherent physical properties of samples with measurable depolarization data and it provides new analytical tools for a better understanding of depolarizing mechanisms in biological samples, and therefore, to their inherent structures.

## 2. Indices of Polarimetric Purity (IPP) as a framework to study depolarizing behavior of samples

In this section we provide the fundamentals necessary to construct the models given in further Section 3, which will help us to study different depolarizing scenarios.

In particular, we focus on the IPP to provide fundamental information about the origin of depolarization. The choice of the IPP is not arbitrary since they provide further information than other well-known depolarizing observables (as the Degree of Polarization or the Depolarizing index [27]) as well as because their interest for the enhanced visualization of tissues has already been demonstrated [13]. To study the IPP parameters we construct our simulations and experiments based on the M-S formalism [28,29]. In this formalism, the state of polarization

of the light is described by the Stokes vector ( $S$ ), whereas the polarimetric properties of samples are described by Mueller matrices ( $M$ ) [17, 28–32].

In the following, we briefly review the calculation of the IPP. These three magnitudes arise naturally when applying the spectral theorem [33] on polarimetric systems. The IPP constitute a set of three real magnitudes, named  $P_1$ ,  $P_2$  and  $P_3$ , defined as combinations of the covariance matrix  $H$  (associated with  $M$ ) eigenvalues ( $\lambda_i$ ) [17,20,33]:

$$\begin{aligned} P_1 &\equiv \frac{\lambda_0 - \lambda_1}{TrH}, \\ P_2 &\equiv \frac{\lambda_0 + \lambda_1 - 2\lambda_2}{TrH}, \\ P_3 &\equiv \frac{\lambda_0 + \lambda_1 + \lambda_2 - 3\lambda_3}{TrH}, \end{aligned} \quad (1)$$

where, the values are restricted between 0 and 1, and follow the relation:

$$0 \leq P_1 \leq P_2 \leq P_3 \leq 1, (i = 1, 2, 3) \quad (2)$$

Pure or non-depolarizing systems are characterized by  $P_1=P_2=P_3=1$ , while for totally or ideal depolarizers  $P_1=P_2=P_3=0$ .

Importantly, the characteristic decomposition of the Mueller matrix can be expressed in terms of the IPP as [19,20]:

$$\begin{aligned} M &= P_1(m_{00}\hat{M}_{J0}) + (P_2 - P_1)(m_{00}\hat{M}_1) + (P_3 - P_2)(m_{00}\hat{M}_2) \\ &\quad + (1 - P_3)(m_{00}\hat{M}_3) \end{aligned} \quad (3)$$

where,  $P_1$  is the weight of the nondepolarizing component  $\hat{M}_{J0}$ ,  $P_2-P_1$  is the portion of the medium that behaves as a 2D depolarizer (represented by  $\hat{M}_1$ ),  $P_3-P_2$  summarizes the part of the medium that behaves as a 3D depolarizer (represented by  $\hat{M}_2$ ),  $1-P_3$  is the portion of the medium behaving as a perfect depolarizer where  $\hat{M}_3=diag(1,0,0,0)$  and the circumflex in  $M$  denotes the normalized matrix in each case [17,19,30].

Note how Eq. (3) becomes very interesting because it allows us connecting the weights of the different terms of the characteristic decomposition, which are physically interpretable, with combinations of IPP, which can be experimentally obtained.

## 3. Depolarizing systems with $P_3=1$

Depolarizing behavior of samples can be understood as their ability to introduce polarimetric randomness to an input polarized light beam. When an expanded beam illuminates a sample, light-matter interactions are produced which result in heterogeneous modifications of the polarization spatial distribution of light. Those polarization spatial distributions are incoherently added at the detectors of polarimeters, leading to depolarization measurements. The physical origin behind the depolarizing response of a sample is multiple, but it is always connected to the inherent constituents of the sample, and how they modify polarization through light-matter interactions. In this work, we provide different cases of study which lead to depolarization, and they are very easy to interpret. The cases will be studied in terms of their Indices of Polarimetric Purity (IPP) values, because, as we will show, the IPP allow us to catalog different kinds of depolarizers as a function of the inherent processes that give rise to the depolarization.

To do so, we will model different depolarizer scenarios in which depolarization takes place, consisting of basic physical elements, this leading to a very simple interpretation of the depolarizing processes behind them. In particular, in this section we present two different simulations of depolarizers that are based on the simplest polarimetric elements: linear retarders and linear diattenuators. As it will be shown, these two scenarios lead to the particular value of  $P_3=1$ , whereas  $P_1$  and  $P_2$  are different from case to case. In Section 1.3 of the supplementary document, we also include the simulation where the Mueller matrix is constructed by the combination of linear diattenuators and retarders. The behavior of these  $M$  is similar to the ones presented in the main text,



and  $P_3=1$  for all the cases.

The models presented in the following are implemented in a way that is in adequacy with the premises of the parallel decomposition [17]. The latter decomposition states that, any depolarizing  $M$  can be described as an incoherent sum of Mueller matrices  $M_i$  [18,19,21,33,34]

$$M = m_{00}\hat{M} = m_{00} \sum_i \alpha_i \hat{M}_i; \alpha_i \geq 0; \sum_{i=1}^n \alpha_i = 1 \quad (4)$$

In this section, we conduct the simulations based on the incoherent addition of  $n$  Mueller matrices of pure polarimetric elements (linear diattenuators and linear retarders; with different values and orientations). These simulations pretend to mimic the macroscopic response of complex systems including dichroism, birefringence, or both.

### 3.1. Depolarizers originated by the incoherent addition of linear diattenuators

The first case of study consists of the simulation of depolarizers constituted by the incoherent addition of linear diattenuators. The Mueller matrix of a  $x$ - $y$  aligned linear diattenuator  $M_{LD}$  can be written as [28]:

$$M_{LD}(p_x, p_y) = \frac{1}{2} \begin{pmatrix} p_x^2 + p_y^2 & p_x^2 - p_y^2 & 0 & 0 \\ p_x^2 - p_y^2 & p_x^2 + p_y^2 & 0 & 0 \\ 0 & 0 & 2p_x p_y & 0 \\ 0 & 0 & 0 & 2p_x p_y \end{pmatrix}; 0 \leq p_x, p_y \leq 1, \quad (5)$$

here  $p_x$  and  $p_y$  are the amplitude attenuation coefficients for the  $x$  and  $y$  components, respectively. To make the simulation more realistic, we will consider diattenuators oriented at different angles. To do so, we have to take into account the Mueller matrix of a rotator [28], where  $\theta$  is the angle of the rotator. Therefore, the Mueller matrix of each linear diattenuator rotated to an angle  $\theta$  can be obtained as [28]:

$$M(p_x, p_y, \theta) = M_{rot}(-\theta) M_{LD} M_{rot}(\theta). \quad (6)$$

Under this scenario, by applying the summation in Eq. (4) to Mueller matrices with the structure given in Eq. (6), we achieve a model with different control parameters: the number  $n$  of Mueller matrices in the summation, the amplitude coefficients ( $p_x$  and  $p_y$ ) and the orientation angle ( $\theta$ ) for each Mueller matrix.

Therefore, we need a criterion to choose the way to assign different values to the parameters in each diattenuator within the summation. These values could be set arbitrarily, for instance, by generating random numbers, but to simulate a situation closer to real samples, such as the distribution of collagen fibers in a tendon or cellulose in the vascular tube of a leaf, we restrict the domain of variation. We consider a group of dichroic optical elements, with a privileged direction, with deviations from this direction. To do that, the values for the control parameters in each of the  $n$  matrices in the summation are assigned by  $\bar{X} + \delta$ , where  $\bar{X}$  is the mean value parameter and  $\delta$  is a random variable that follows a Gaussian distribution with a null mean and a given variance ( $\sigma$ ). The mean values for the amplitude coefficients  $p_x, p_y$  are bounded within the range (0, 1) and the mean orientation of the diattenuators within the range (0, 180°).

Afterwards, for the sake of interpretation (to limit the space of simulations), we chose to fix in all the simulations the value of the amplitude coefficient in the  $x$  direction  $p_x$  to a constant value. Regarding the number of elements in the incoherent addition, we set  $n = 1500$ , this number being a trade-off between a large number of elements (to mimic real processes of light-matter interaction) and a reasonable computation time.

Once we have set the values for  $p_x$  and  $n$ , our remaining control parameters are  $p_y$  and  $\theta$ . For each value of  $p_x$ , we conduct a collection of simulations by taking a given value of  $p_y$  and changing the values of  $p_y$

from 0 to 1 with steps of 0.003 and with a null variance ( $\sigma_{py}=0$ ), and values of  $\theta$  with a given mean value (we choose  $\theta=60^\circ$  and a variance ( $\sigma_\theta$ ) taking values from  $0^\circ$  to  $180^\circ$  with steps of  $0.6^\circ$ . This lead to a  $300 \times 300 = 90,000$  simulations, each one leading to a Mueller matrix of a composed depolarizer. In order to study the depolarizing properties of the resulting 90,000 depolarizers, the IPP (i.e.,  $P_1, P_2$  and  $P_3$  channels) values are calculated according to formulation given in Section 2.

The results obtained for  $P_1, P_2$  and  $P_3$  are presented in Fig. 1. The  $x$  axis provides the  $p_y$  parameter, whereas the  $y$  axis shows the values for the variance of  $\theta$ , the  $\sigma_\theta$  parameter. Therefore, the resulting images include the IPP values for the 90,000 simulations, each pixel of the image corresponding to a particular ( $p_y, \sigma_\theta$  combination). The values for the IPP are coded in a color scale ranging from the minimum value (0 value, in blue) to the maximum value (1 value, in yellow), as provided by the colorbar. In addition, different rows in Fig. 1 provide the IPP simulations for two different values of  $p_x$  (0.8 and 0.2). We have also computed the simulations for different values of  $p_x$ , these results are presented in Section 1 of the supplementary material.

In Fig. 1(a)–(f) we observe the behavior of different depolarizers based on incoherent addition of linear diattenuators with different characteristics of ( $p_x, p_y$ , and  $\sigma_\theta$ ). Regarding the orientation angle mean value for the constituent diattenuators,  $\sigma_\theta$ , this parameter is set as  $60^\circ$  for all simulations in Fig. 1. The choice of such angle was arbitrary as we have observed that simulations are independent of this parameter. In fact, the orientation angle does not affect the polarimetric characteristics of the resulting depolarizers since it can be understood as a rotation of the system, and thus, the enpolarizing and depolarizing properties of the simulated samples should be conserved.

Regarding data in Fig. 1(a)–(f), the first result we observe is that, independently of the model parameters ( $p_x, p_y$ , and  $\sigma_\theta$ ), the  $P_3$  parameter always equals 1. Therefore, we cannot modify the  $P_3$  value with this combination of diattenuators and the consequent depolarizers are always restricted to the top of the tetrahedron of the Purity Space [35]. As a consequence of this, we cannot achieve an ideal depolarizer ( $diag(1, 0, 0, 0)$ ) by simply varying the parameter values in the diattenuation model. Indeed, the  $P_3 = 1$  plane does not contain the ideal depolarizer, and thus all the points on such a plane necessarily exhibit depolarizations strictly lower than the maximum one that is, depolarization cannot be continuously increased to the ideal depolarizer value.

Secondly, we note that the values of  $P_1$  and  $P_2$  channels are modified with different values of  $p_x, p_y$ , and  $\sigma_\theta$ , and thus, the depolarizing response of resulting depolarizers strongly depend on these parameters. As  $P_3$  is always equal to 1, this implies that different depolarizers (different pixels in images in Fig. 1(a)–(f)) correspond to different spatial positions at the plane  $P_3=1$  in the Purity Space [35]. Therefore, the channels  $P_1$  and  $P_2$  are suitable tools to differentiate between different depolarizers originated by dichroic structures. Importantly, note the close similarity in the responses of  $P_1$  and  $P_2$  images. In fact, they present identical behavior for a fixed value of  $p_x$  (different rows), but  $P_2$  presents a vertical shift upwards as  $p_x$  increases (from bottom to upper row). This situation can be explained by taking into account the inequality shown in Eq. (2), which forces  $P_2$  to have larger (or equal) values than  $P_1$ . In turn, we also observe that larger  $\sigma_\theta$  values (vertical axis) lead to smaller values for  $P_1$  and  $P_2$ . In fact, for  $\sigma_\theta = 0$  we obtain  $P_1=P_2=P_3=1$  (yellow color) in all the cases, and  $P_1$  and  $P_2$  tend to decrease their values as  $\sigma_\theta$  increase. This situation implies that the larger the loss of organization for the constituent units (diattenuators) (i.e.,  $\sigma_\theta$  increase), the larger the depolarizing capability of the system (i.e.,  $P_1$  and  $P_2$  decrease). Note that this behavior is observed until a certain limit value for  $\sigma_\theta$ , that depends on the  $p_x$  value (different rows) but in general it occurs around  $\sigma_\theta = 40^\circ$  both for  $P_1$  and  $P_2$  metrics. This implies that even increasing the disorder of polarizing units constituting samples, there is a certain limit from which depolarizing response of samples is not modified anymore. The existence of this limit can also be discussed in an intuitive and visual way in terms of the Purity Space, as presented in the Supplementary material

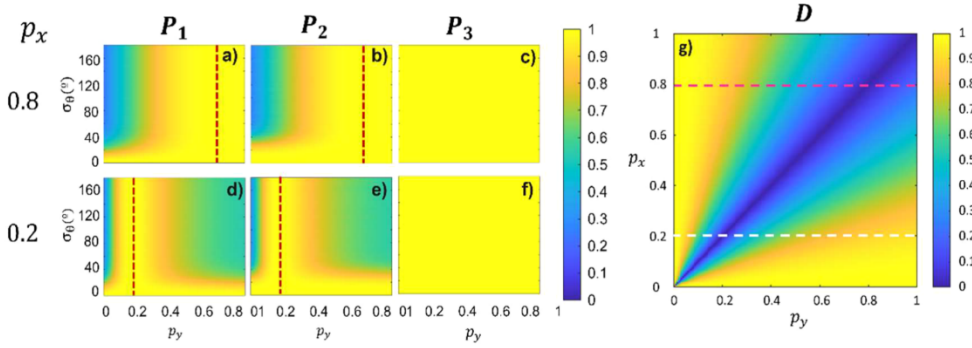


**Fig. 1.** (a)–(f) IPP values for simulated samples composed by incoherent additions of linear diattenuators. The x axis represents the mean values of  $p_y$  and, the y axis the values for  $\sigma_\theta$ . The value of  $p_x$  is set as a constant for each image, with values of 0.8 and 0.2, respectively for the two different rows. The value of the mean orientation angle  $\theta$  is set as  $60^\circ$  for all cases. (g)  $D$  value for the incoherent addition of linear diattenuators with  $\sigma_\theta = 0$ , the x and y axis represent the  $p_x$  and  $p_y$  parameters, defined in the range 0 to 1.

### (Section 5).

This set of simulations can also be studied in terms of the diattenuation  $D$  observable, representing the dependence of the sample transmittance with the state of polarization of the incident light. The diattenuation  $D$  can be calculated as the absolute value of the diattenuation vector, which can be written in terms of the first row Mueller matrix elements in the following way [28]:

$$D = \frac{1}{m_{00}}(m_{01}, m_{02}, m_{03})^T. \quad (7)$$

If we substitute in Eq. (7) the elements of the Mueller matrix correspondent to a general diattenuator (Eq. (5)), the absolute value of the diattenuation vector,  $D$ , can be expressed as [17]:

$$D = \frac{|p_x^2 - p_y^2|}{p_x^2 + p_y^2}. \quad (8)$$

Note that the diattenuation parameter  $D$  is a significant feature of diattenuators, taking values of  $D = 1$  for an ideal diattenuator, and values of  $D = 0$  for a medium with no diattenuation.

Taking the definition of  $D$  in mind, and back again to Fig. 1(a)–(f), we find a non-depolarizing zone (yellow color) when  $p_x = p_y$  (indicated with a red dotted line in each image). According to Fig. 1(g) this situation corresponds to values of  $D = 0$  (see positive diagonal in blue), and therefore, non polarimetric elements (thus without the capability of enpolarize and depolarize). This condition leads to simulations based on the incoherent addition of media represented by the identity matrix, and as a consequence, without the potential of implementing depolarizers (see red dotted line in Fig. 1(a)–(f)). However, for  $p_x \neq p_y$ , the units of the incoherent addition present certain diattenuation (i.e.,  $D \neq 0$ ) (see Fig. 1(g)), which leads to systems with certain depolarizing response. This depolarization response directly depends on the organization disorder ( $\sigma_\theta$ ) (see vertical axis in Fig. 1(a)–(g)).

The dependence of the IPP with the  $p_x$  and  $p_y$  values is easily understood by studying Fig. 1(g). The pink and the white dashed lines in the figure, indicate the  $D$  value for  $p_x = 0.8$  and  $p_x = 0.2$ , respectively, with  $p_y$  taking values from 0 to 1. Following the dashed white line in Fig. 1(p), the value of  $D$  is maximum for  $p_y = 0$  and start to decrease as  $p_y$  increases, reaching the minimum for  $p_y = 0.2$  (i.e.,  $p_x = p_y$ ). As  $p_y$  increases, the value of  $D$  increases as well, reaching the  $D = 1$  value. This behavior explains the depolarization results obtained from Fig. 1(d) and (e), where  $P_1 = P_2 = 1$  (non depolarizing scenarios) correspond to values of  $D$  equal or very close to zero (i.e., corresponding to the blue diagonal in Fig. 1(g)), whereas for the situations where  $D$  reaches its maximum of high values, the depolarization capability of the samples increase, achieving values of  $P_2$  and  $P_1$  different from 1. The pink line indicates the case for  $p_x = 0.8$ . If we study the  $D$  behavior through this line, we can see that  $D$  is

equal to 1 (or near) when the values of  $p_y$  are in the range (0,0.3). This corresponds with the left zone of the images where  $p_y$  is in the mentioned range and, we can see that in this case, for  $\sigma_\theta$  values higher than the limit, the system depolarizes anisotropically. However, as  $p_y$  increases ( $D$  decreases) the depolarizing capability of the system is lost because the system becomes less dichroic.

Results shown in Fig. 1(g) corresponds with the case of  $\sigma_\theta = 0$ . We have also tested other values for the standard deviation of the mean orientation of the diattenuators and results and discussion are provided in the supplementary Material. The main conclusions are that the general structure shown in Fig. 1(g) is maintained, but the diattenuation values decrease with  $\sigma_\theta$ , reaching a limit scenario, where diattenuation is equal to 0 for  $\sigma_\theta \geq 40^\circ$ . This result has sense because as larger the deviation of  $\theta$ , as larger the depolarizing capability of the depolarizer consisting of dichroic unitary elements.

Summarizing, in this subsection we have mimicked multiple depolarizers consisting of dichroic microscopic elements. As expected, incoherent addition of isotropic (in terms of dichroism) units (i.e.,  $p_x = p_y$  scenario), lead to non-depolarizing samples (i.e.,  $P_1 = P_2 = P_3 = 1$ ). In turn, in the case of anisotropic elements ( $p_x \neq p_y$ ), the resulting systems become depolarizers, and their depolarization capability increases for larger diattenuation  $D$  values (which depends on the  $p_x$  and  $p_y$  relation) of the constituent diattenuators, as well as with the units orientation disorder  $\sigma_\theta$ . Importantly, the value of  $P_3$  is independent of all the model parameters, and it maintains a constant value of  $P_3 = 1$  for all the simulations, and therefore, all depolarizers consisting of collections of linear diattenuators are placed into a specific plane of the Purity Space [35].

### 3.2. Depolarizers originated by the incoherent addition of linear retarders

The second study considers depolarizers consisting of microscopic unit elements presenting linear retardance. We proceed in analogy to the previous study corresponding to diattenuation, building in this case models consisting in the incoherent sum of sets of retarders as a function of their retardation and orientation. In Ref. [36] it is shown how the incoherent addition of linear retarders can also be performed analytically. We show the Mueller matrix for a linear retarder oriented at  $0^\circ$  [28]:

$$M_{LR} = \begin{pmatrix} 1 & 0 & 0 & 0 \\ 0 & 1 & 0 & 0 \\ 0 & 0 & \cos\phi & \sin\phi \\ 0 & 0 & -\sin\phi & \cos\phi \end{pmatrix}; 0 \leq \phi \leq \pi, \quad (9)$$

where,  $\phi$  is the phase shift introduced to the orthogonal components of the incident light field. As in the previous case, to make simulations more realistic, we consider an ensemble of retarders oriented at different



angles, according to the relation  $M = M_{\text{rot}}(-\theta)M_{\text{LR}}M_{\text{rot}}(\theta)$ . For the incoherent sum of Mueller matrices of retarders, we consider a mean orientation ( $\bar{\theta}$ ) for the retarders with a standard deviation ( $\sigma_{\theta}$ ) following a probabilistic Gaussian distribution. In addition, we vary the retardance value  $\phi$  from  $0^\circ$  to  $360^\circ$  and with a null variance. As in the previous case, the obtained simulations (which are functions of  $\phi$  and  $\sigma_{\theta}$ ) are interpreted in terms of the  $P_1$ ,  $P_2$ ,  $P_3$  metrics.

In Fig. 2 we present the three IPP metrics corresponding to the simulations with linear retarders. The x axis represents the mean values of retardance  $\phi$ , taking values from  $0^\circ$  to  $360^\circ$ , whereas the y axis represents the variance range from the mean orientation value,  $\sigma_{\theta}$ , which can take values from  $0^\circ$  to  $180^\circ$ . For each of the possible values of  $\phi$  we build the  $M$  corresponding to the incoherent sum of  $n = 1500$  Mueller matrices where each of them has a value of orientation with a variance given by a Gaussian distribution. This process is repeated for the possible values of  $\phi$  and  $\sigma_{\theta}$ , both can take 300 different values within their respective ranges, this leads to  $300 \times 300$  (90,000) Mueller matrices representing different depolarizers based on retarders. Afterwards, we calculate the IPP values of these matrices according to the calculus given Section 2. As in the previous case, depolarization response of the simulated systems is independent of the mean orientation of the retarders, as system rotations do not represent changes in its physical properties. Therefore, the mean orientation of the unit retarders is arbitrarily set to  $\bar{\theta} = 60^\circ$  in conducted simulations.

In Fig. 2 the values of  $P_1$  and  $P_2$  vary from 0 to 1 depending on the combination of ( $\sigma_{\theta}$ ,  $\phi$ ), whereas  $P_3$  is always 1. Therefore, as it happened in the case of systems consisting of dichroic elements, systems based on linear retarders are not able to decrease the value for  $P_3$ . In terms of Purity Space, different depolarizers consisting of linear retarders are distributed as well within the plane  $P_3=1$ . As already discussed in the diattenuation section, due to this restriction of  $P_3=1$  in the retardance case we cannot achieve an ideal depolarizer ( $\text{diag}(1,0,0,0)$ ) by simply varying the parameter values in the retardance model, as it is not contained in such a plane.

Unlike the previous case, where  $P_1$  and  $P_2$  showed a very similar behavior (just modified by a vertical shift), in the case of linear retarder based systems, the  $P_1$  shows one minimum valley instead of the two shown by the  $P_2$  channel (i.e. the  $P_1$  distribution between  $\phi$   $[0-360^\circ]$  range occurs as well for the  $P_2$  channel, but in the  $\phi$   $[0-180^\circ]$  range, and it is doubled in the  $\phi$   $[0-360^\circ]$  range). Obviously, according to inequality shown in Eq. (2), the vertical shift in  $P_2$  with respect  $P_1$  is also present. In detail, for retardances  $\phi$  lower than  $40^\circ$  and higher than  $320^\circ$  the simulated samples become non depolarizing (yellow color) independently of the  $\sigma_{\theta}$  value, having  $P_1=P_2=P_3=1$ . This is because for values of retardance  $\phi$  close to  $0^\circ$  and  $360^\circ$ , Eq. (9) becomes the identity, and therefore, the resulting systems loss their depolarizing capability. Interestingly, as we go far from such values, retardance behavior becomes significant and the resulting systems become depolarizers (going gradually from yellow to blue in Fig. 2(a) and (b)). In particular, depolarizing behavior of systems is achieved for values of  $\phi$  in the range

( $40^\circ-320^\circ$ ). Within this scenario, the orientation disorder of the retarders units (given by the parameter  $\sigma_{\theta}$ ) becomes significant, and depolarization is observed for  $\sigma_{\theta}$  values larger than  $20^\circ$ :  $P_1$  taking values from 0.9 to 0 and  $P_2$  from 1 to 0.

In analogy to diattenuators, it seems that there is a limit value of  $\sigma_{\theta}$ , above which depolarization does not increase. For the case of retarders, such limit value is around  $20^\circ$  (see more details in Section 5 of the supplementary text).

Note that, for values of  $\phi$  close to  $180^\circ$ ,  $P_1$  becomes 0 and  $P_2$  is equal to 1. In this case, the Eq. (9) becomes  $\text{diag}(1,1,-1,-1)$ , and therefore, only  $P_1$  is able to differentiate between this case and the above-discussed identity matrix scenario ( $\phi=0^\circ$  or  $360^\circ$ ). Accordingly, this difference between  $P_1$  and  $P_2$  can be useful to distinguish between different depolarizers consisting of linear retarders with different retardance  $\phi$  values. For example, a retardance value of  $\phi=90^\circ$  leads to  $P_1$  and  $P_2$  values close to zero, a value of  $\phi=180^\circ$  to  $P_1=0$  and  $P_2=1$  and a value of  $\phi=0^\circ$  or  $360^\circ$  to  $P_1=1$  and  $P_2=1$ .

Finally, as a complementary material, in the supplementary text (Fig. S3) we provide the results for further simulated scenarios for the linear retarders case, for instance by adding a variance  $\sigma_{\phi}$  (based on a Gaussian probability) to the mean retardance  $\bar{\phi}$ . Note that even though different simulations lead to different values for  $P_1$  and  $P_2$  channels, in all the cases, the value of  $P_3$  remains always constant to  $P_3=1$ .

Summarizing, the simulations shown in this subsection further reinforces the idea that depolarizing systems originated by diattenuators or linear retarders microscopic units, are always placed at the top plane ( $P_3=1$  plane) of the tetrahedron of the Purity space. We also observe that  $P_1$  and  $P_2$  parameters strongly depend on the model parameters: attenuations ( $p_x$ ,  $p_y$ ), retardance ( $\phi$ ) and the variance of the orientation ( $\sigma_{\theta}$ ), as well as the diattenuation  $D$ . These two metrics can be useful to reveal underlying properties of the systems, as if their main constituents are based on diattenuators, linear retarders, or a mix of them. Therefore, they can be used to discriminate between depolarizers based on different linear retarders configurations, or even to differentiate between depolarizers based on dichroic or on linear retarder constituent elements. Under this scenario, a question arises. Which kind of structures are able to decrease the  $P_3$  parameter? This situation is explored in the following section.

#### 4. Depolarizing systems with $P_3 < 1$

In practical situations, it is common to find depolarizing systems (both organic and inorganic) with values of  $P_3$  smaller than one, even achieving very low values (close to zero). For instance, in plant and animal tissue we can find  $P_3$  values ranging from 0 to 1 in different structures [24,37]. Note that some of these samples indeed consist of anisotropic elementary components (for instance, animal tissues are mainly based on collagen fibers [38], which can be described by retarders, or vegetal samples are rich in dichroic units [39,40], which can be described by diattenuators).

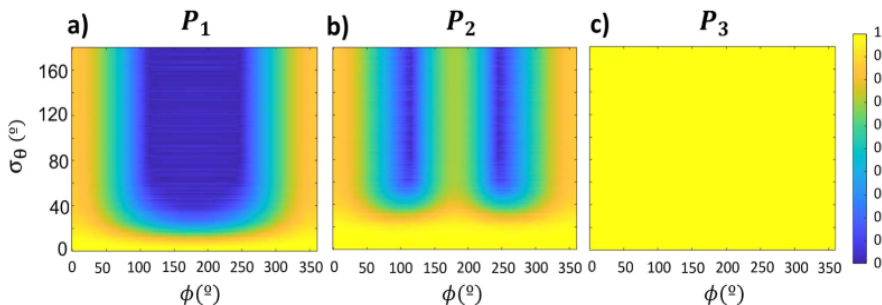


Fig. 2. IPP values for simulated samples composed by linear retarders; (a)  $P_1$ , (b)  $P_2$  and, (c)  $P_3$ , where x axis represents the mean values of  $\phi$  simulated and, the y axis the variance range values from the from the mean orientation  $\bar{\theta} = 60^\circ$ .

Recalling the results of previous Section 3, we realize that anisotropic constituent elements in samples cannot explain why all those real samples led to values of  $P_3 < 1$ , and therefore, it may exist another depolarizing mechanism to be considered.

Under this scenario, this section focuses on finding a physical mechanism able to describe the depolarizing behavior of real samples with  $P_3 < 1$ . We want to note that there are different mechanisms leading to  $P_3 < 1$ , but we only focus on those that seem more adequate to explain the depolarizing behavior of most real samples. Some uncommon exotic mechanisms leading to  $P_3 < 1$  (some of them even not representing physical systems) are provided in Section 2.1 of the supplementary document.

In this section we introduce a new group of simulations that lead to  $P_3 < 1$ . As in previous Section 3, they consist of an incoherent addition of a number of  $M$  representing basic systems (linear retarders and diattenuators), but now, we add an extra term in the summation, this being the Mueller matrix of a perfect depolarizer with a certain weight ( $\beta$ ).

The addition of this term in the simulations is inspired on the characteristic decomposition. As can be seen in Eq. (3), this decomposition describes a general matrix  $M$  as the addition of four terms, where each one of them is weighted by a linear combination of the IPP. The first term carries the fully polarized contribution of the system. The second and third terms, represent the depolarizing contribution of 2D and 3D systems [17]. Finally, the last term depends on a perfect depolarizing medium ( $\text{diag}(1,0,0,0)$ ), which completely depolarizes any incident polarization state of light independently of its initial polarization state. Interestingly, the IPP corresponding to a perfect depolarizer are  $P_1 = P_2 = P_3 = 0$ , and thus, such systems have the capability of decreasing the  $P_3$  channel [41].

For these reasons, we realize that the addition of a perfect depolarizer contribution to the simulations described in previous Section 3 may lead to a decrease of the  $P_3$  value. Therefore, in the new set of simulations, we add an additional term representing a perfect depolarizing Mueller matrix with a certain weight that can be controlled. In particular, this new system can be written as the incoherent addition of a first term describing the contribution to depolarization originated by anisotropic (linear retarders, diattenuators) constituent elements (and obtained as described in Eq. (4)), with a second term,  $M_{\text{iso}}$ , representing the perfect depolarizing or isotropic contribution. The resulting  $M$  can be written as follows:

$$M = m_{00}\hat{M} = \sum_i^n \alpha_i(m_{00}\hat{M}_i) + \sum_j^m \beta_j(m_{00}\hat{M}_{\text{iso}}); \quad (10)$$

$$\alpha_i, \beta_j \geq 0; \sum_{i=1}^n \alpha_i + \sum_{j=1}^m \beta_j = 1,$$

where,  $n' + m = n$ . Note that as in Section 3,  $n$  gives the total number of terms in the summation (we set  $n = 1500$  once again). Since the  $M_{\text{iso}}$  is the Mueller matrix of a perfect depolarizer ( $\text{diag}(1,0,0,0)$ ) the second term can be written as:

$$\sum_j^m \beta_j(m_{00}\hat{M}_{\text{iso}}) = \beta m_{00}\hat{M}_{\text{iso}}, \quad (11)$$

where,  $\beta = \sum_j^m \beta_j$ . Therefore, the Eq. (10) can be expressed as:

$$M = m_{00}\hat{M} = \sum_i^n \alpha_i(m_{00}\hat{M}_i) + \beta m_{00}\hat{M}_{\text{iso}}. \quad (12)$$

The first term,  $\sum_i^n \alpha_i(m_{00}\hat{M}_i)$ , represents the effects of depolarizing systems already described in Section 3, that is, depolarizing systems originated by component elements showing retardance or dichroism, and leading to  $P_3 = 1$ . In turn, the new added term,  $\beta m_{00}\hat{M}_{\text{iso}}$ , corresponds to depolarizing systems that fully depolarize light, independently of the input state of polarization of the illumination, and leading to  $P_3 = 0$ . In

addition, as discussed before, the depolarization introduced by the  $\beta m_{00}\hat{M}_{\text{iso}}$  term cannot relate to systems based on anisotropic constituent elements (retarders, diattenuators, mix of them etc.) and thus, it must be connected with isotropic processes introducing polarimetric randomness, as it is the case of isotropic scattering. For this reason, from now on, let us call the first term of Eq. (12) as the anisotropic depolarization term, and the second term as the isotropic depolarization term.

The relation between  $P_3$  and the new added term in the simulation is studied by a set of simulations. By following such Eq. (12), as in previous Section 3, we have access to different control parameters (orientations, retardances, absorption coefficients, deviations, etc.) involved in the anisotropic term, but now, we also control the isotropic component relevance through the weight of the parameter  $\beta$ . We conducted a full space of simulations by repeating the cases analyzed in previous Section 3, but now, by adding the effect of the isotropic term. For the sake of simplicity, in the following we only show and discuss simulations corresponding to a particular case, the incoherent addition of linear diattenuators (Section 3.1) but generalized by the isotropic term. Further simulations results (retarders, combination of linear diattenuators and retarders, etc.) generalized with the isotropic term, can be found in the supplementary text (see Fig. S6), but main conclusions are analogous for all these cases.

Simulated results corresponding to the case of linear diattenuator systems (anisotropic term) incoherently added with the isotropic term are shown in Fig. 3. Results are given in terms of the  $P_3$  metric,  $P_1$  and  $P_2$  have the same dependence with the anisotropic term parameters as in the previous section. As the value of  $\beta$  increases (i.e.  $P_3$  decreases), the value of  $P_1$  and  $P_2$  also decrease (see Eq. (2)) but maintaining the dependence with the anisotropic parameters. To implement the corresponding simulations, the control parameters associated to the anisotropic term were set as: absorption coefficient in the  $x$  direction,  $p_x$ , set to 1, mean orientation of linear diattenuators,  $\bar{\theta}$ , set to  $60^\circ$ , absorption coefficient in the  $y$  direction,  $p_y$ , taking values from 0 to 1 (values of  $x$  axis) and, orientation deviation from mean value,  $\sigma_\theta$ , taking values from  $0^\circ$  to  $180^\circ$  (values of  $y$  axis). In addition, from Fig. 3(a) to (e) the weight of the isotropic term,  $\beta$  (see Eq.(12)), increases in steps of 0.2 from  $\beta = 0$  to  $\beta = 1$ .

In Fig. 3 we see that, as expected, the  $P_3$  metric does not depend on the control parameters of the anisotropic term, i.e., all the images in Fig. 3 show a homogeneous color (i.e., present the same value for  $P_3$ ), because  $P_3$  values are independent of  $x$  and  $y$  axes values. This situation occurs independently of the anisotropic term control parameters chosen for  $x$  and  $y$  axes and the elements conforming this term (see Sections 2.2 and 6 of the supplementary material). Unlike this, the values of the isotropic weight,  $\beta$ , control the values of the  $P_3$  Purity parameter (see Fig. 3(a)–(c)). In particular, as larger the  $\beta$  value as shorter the  $P_3$  (note the colorbar in Fig. 3). For the sake of clarity, we also provide Fig. 3(d) where we directly represent the relation between  $\beta$  and  $P_3$ , where we note an inverse linear relation between these two parameters. We want to note that the values for the  $p_x$  and  $\sigma_\theta$  selected for the simulations are arbitrary and we could set other values within the range of the parameters:  $p_x$  [0,1] and  $\sigma_\theta$  [0,180]. Nevertheless, the main conclusions would remain the same. According to Eq. (12), results in Fig. 3(d) have been obtained from a Mueller matrix composed by an anisotropic part (incoherent addition of diattenuators) and the isotropic part ( $\text{diag}(1,0,0,0)$ ). To cover all the possible range of  $P_3$  values, we conduct simulations with  $\beta$  from 0 to 1. This situation confirms that the amount of isotropic scattering in samples is described by the  $P_3$  metric and is directly related to the weight of the isotropic term in Eq. (12). Moreover, since  $\hat{M}_3 = \hat{M}_{\text{iso}}$ , by comparing Eq. (12) with the characteristic decomposition (Eq. (3)) we can find the following relation:

$$\beta m_{00}\hat{M}_{\text{iso}} = (1 - P_3)(m_{00}\hat{M}_3) \quad (13)$$

and thus,  $\beta = 1 - P_3$  (note that this result is in agreement with previous Fig. 3(d)). In this way, we find the relation between the weight of the



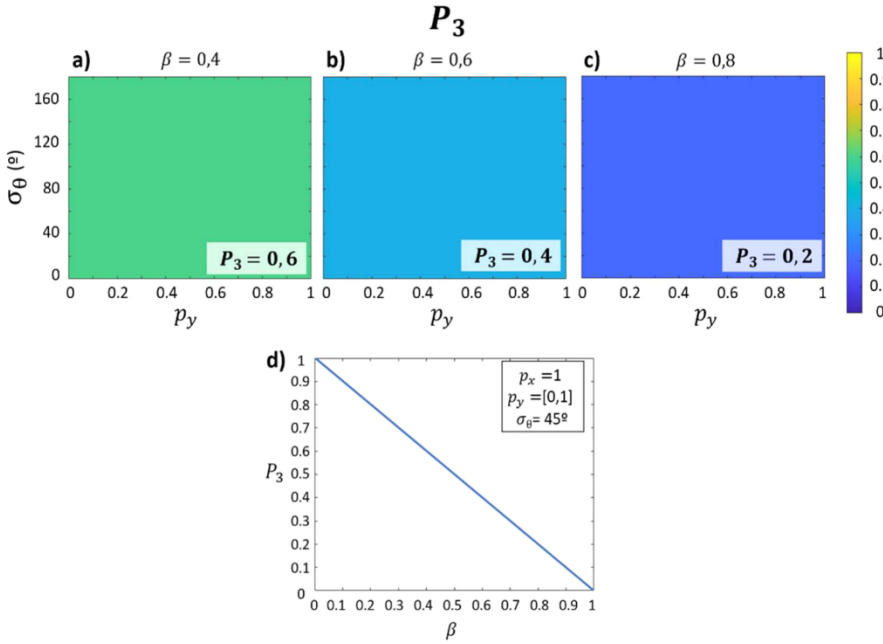


**Fig. 3.**  $P_3$  values for the simulated samples composed by the incoherent addition of linear diattenuators and a pure depolarizing component with different weights:  $\beta=0.4$  (a),  $\beta=0.6$  (b) and  $\beta=0.8$  (c). The x axis represents the mean value of  $p_y$  (where  $p_x=1$ ) and the y axis the variance range values of the orientation ( $\sigma_\theta$ ) from  $0^\circ$  to  $180^\circ$ . (d) Relation between  $\beta$  and  $P_3$  obtained from a Mueller matrix with isotropic and anisotropic component, the weight of each component is given by the  $\beta$  value and the parameters that control the anisotropic term are set as  $p_x=1$ ,  $\sigma_\theta=45^\circ$  and  $p_y$  varies in the range  $[0,1]$ .

isotropic contribution,  $\beta$ , with  $P_3$ . Moreover, considering the relation between  $\alpha_i$  and  $\beta$  weights in Eq. (10), together with  $\beta=1-P_3$ , we obtain:

$$1 = \sum_{i=1}^n \alpha_i + \beta = \sum_{i=1}^n \alpha_i + (1-P_3) \rightarrow \sum_{i=1}^n \alpha_i = P_3. \quad (14)$$

By taking into account these results, we can reformulate the weights of the two terms in Eq. (12) just as a function of  $P_3$ . To this aim, we define a normalized Mueller matrix  $\hat{M}_A$  in the following way:

$$\sum_{i=1}^n \alpha_i M_i = P_3 \hat{M}_A \rightarrow \hat{M}_A = \frac{1}{P_3} \sum_{i=1}^n \alpha_i M_i. \quad (15)$$

This relation allows us to re-write Eq. (12) as:

$$M = P_3 m_{00} \hat{M}_A + (1-P_3)(m_{00} \hat{M}_3), \quad (16)$$

where,  $\hat{M}_A$  is defined by Eq. (15) and  $\hat{M}_3 = \hat{M}_{iso}$ . Note that considering the equivalence of Eqs. (16) and (12), the first term,  $m_{00} \hat{M}_A$ , is the anisotropic term; and the second term,  $m_{00} \hat{M}_3$ , is the isotropic term, and their significance in the incoherent addition is controlled by the Purity term  $P_3$ .

Under this scenario, we can say that  $P_3$  controls the depolarizing origin of samples. When  $P_3=1$  the isotropic term is zero (no isotropic depolarization is present), and thus, all the depolarization behavior of samples is given by the anisotropic term, hence, depolarization is originated by the intrinsic polarimetric anisotropies of the sample. In contrast, for  $P_3=0$ , the anisotropic term is cancelled and polarimetric anisotropies of constituent elements do not contribute to the depolarizing behavior. In such a case, all depolarization is due to the isotropic term, and corresponding samples behave as perfect depolarizers, originated by processes such as isotropic scattering. In the regime  $0 < P_3 < 1$  both depolarizing origins (isotropic and anisotropic) coexist, and the predominant effect is set by the value of  $P_3$ .

In addition, recalling the discussion provided in Section 3, the Purity terms  $P_1$  and  $P_2$  complement the information of  $P_3$ , as they are able to provide further information about intrinsic characteristics of depolarizing samples based on anisotropic component elements (anisotropic term). In particular, they can estimate if anisotropic depolarization is

related to constituent elements showing retardance and/or dichroism and anisotropic scattering produced by these elements. Therefore, the larger the value of  $P_3$ , the more relevant become  $P_1$  and  $P_2$  metrics. In this vein, is interesting to note the particular case where  $P_3=P_2=P_1$ . In this case, if we study the terms in the characteristic decomposition Eq. (3) the two terms corresponding to the  $M$  representing the anisotropic information of the sample disappear. Therefore, this particular case represents a sample where the depolarization is due only to isotropic processes and the parts of the sample representing  $M_A$  only contribute to the non-depolarizing term.

Summarizing, in this section we have demonstrated that the depolarizing response of samples can be categorized in two subgroups: (1) those originated by isotropic processes; and (2) those originated by anisotropic processes. These two origins can be produced simultaneously in samples, but their significance can be studied in terms of the Indices of Polarimetric Purity ( $P_1$ ,  $P_2$  and  $P_3$  metrics). On the one hand, the  $P_3$  metric gives a measure of the presence of depolarization behavior originated by isotropic processes. On the other hand, by considering results provided in Section 3, the metrics  $P_1$  and  $P_2$  complete this information by describing characteristics of anisotropic origin of depolarization (as dichroism, retardance, or a mixture of them). Moreover, the difference between the IPP ( $P_2-P_1$  and  $P_3-P_2$ ) gives information about the amount of anisotropic depolarization: more difference between the IPP implies more anisotropic depolarization, representing only isotropic depolarization processes when such difference is zero (i.e.,  $P_1=P_2=P_3$  case). More insight in this topic can be obtained by studying how a particular depolarizer depolarizes the fully polarized states of polarization at the surface of the Poincaré Sphere and study this situation in terms of IPP [17,42]. A brief discussion in this regard is also provided in Supplementary material.

Note that this is a fundamental result providing which phenomenon originates and/or dominates sample depolarization. In this vein, the association of physical mechanisms leading to depolarization with particular values of IPP provides further description, categorization, and recognition of depolarizing systems, these being very common in both biologic and synthetic materials [6,13,23–25,43,44]. More importantly, this intrinsic microscopic information of samples can be obtained from very feasible macroscopic measurements (measure of Mueller matrix

image).

## 5. Experimental results

In this section we present simple experiments based on basic polarimetric elements to validate the simulations and conclusions described in Sections 3 and 4. To do so, we obtain the experimental Mueller matrix resulting from the incoherent addition of experimental Mueller matrices of representative polarimetric elements. From these obtained  $M_i$ , we can calculate the corresponding IPP values and compare them with the results corresponding to the stated simulations. On the one hand, in Section 5.1 we present two experimental scenarios corresponding to the  $P_3=1$  case (one of them based on dichroic systems and the other based on retarders), and thus, representing anisotropic depolarizing systems to be compared with simulations in Section 3. On the other hand, in Section 5.2, the experimental  $M$  of different scattering media are measured to mimic the  $P_3 < 1$  scenario, i.e., the isotropic depolarizing performance of systems, and thus, to be compared with simulations in Section 4. To measure the experimental  $M$  of the samples of interest, we use an image Mueller polarimeter [45] described in Section 3 of the supplementary document. In this way, we can compare the experimental and simulated values of the IPP in each case analyzed.

### 5.1. Experimental results for the $P_3 = 1$ case

In this section we mimic simulated scenarios described in Section 3, representing anisotropic depolarizing systems.

In the first experiment, we measured the Mueller matrix image of a radial polarizer (from Codixx), which consists of an element including 12 different spatial sectors presenting each a linear polarizer with a different orientation (see Fig. 4(a)). Under this scenario, each pixel of the  $M$  image can be understood as a linear polarizer whose orientation is that of the corresponding spatial sector. Afterwards, we set a Region Of Interest (ROI) centered at the intersection of all the sectors (see blue square in Fig. 4(a)), which include  $344 \times 471$  pixels, including all the 12 linear polarizer orientations. Finally, the Mueller matrices of all the pixels within this ROI are added, this mimicking the incoherent addition of linear polarizers with different orientations simulated in 3.1 (i.e., the  $M$  of each pixel is one of the  $M_i$  in Eq. (4)). This element can be considered as a diattenuator with large  $p_x$  value (we can consider it almost as 1) and low  $p_y$  value (we can consider it almost as zero). The orientation angle varies between 0 and  $2\pi$  through the different sectors. The region selected for the calculations is centered and includes all the polarizer sectors, having therefore a  $2\pi$  variation of the orientation angle.

The second experiment consist of measuring the Mueller matrix of a

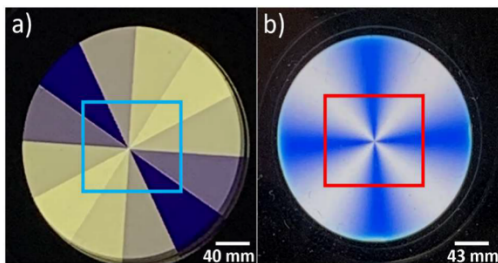


Fig. 4. (a) Radial polarizer illuminated with linear polarization ( $45^\circ$ ), where each of the sectors indicates a different linear polarizer orientation (between 0 and  $2\pi$ ); each color in the polarizer sector represents a change in orientation of  $30^\circ$  with respect the previous sector. (b) Q-plate image; linear retarder (phase  $\pi$  for 633 nm of illumination) with different orientations, between 0 and  $2\pi$  represented by the color change in the Figure. In both cases, to see intensity variations associated with different orientations the elements are sandwiched between two crossed polarizers.

liquid crystal q-plate (model WPV10-633 from Thorlabs). This element is a patterned liquid crystal plate that can be understood as a linear retarder with a fixed retardance which depends on the illuminating wavelength (ideally of  $\pi$  radians for the wavelength of 633 nm) and whose neutral axes orientation changes with the spatial position, achieving orientations between 0 and  $2\pi$  [45] (see Fig. 4(b)). Once again, the  $M$  image is calculated, and all the Mueller matrices for the pixels within a ROI with  $344 \times 471$  pixels (see red rectangle in Fig. 4(b)) are added. Note that this process mimics the scenario discussed in Section 3.2, where different linear retarders with different orientations are incoherently added. Once again, the Mueller matrices within a set ROI (see Fig. 4) are added to construct the incoherent addition of different linear retarders. Therefore, with the q-plate case, by adding the Mueller matrices of the different ROI pixels, we are obtaining the  $M_i$  terms in the incoherent addition of a linear retarder with different orientations.

In Table 1 we present the IPP results for the above-stated radial polarizer and q-plate experiments. The results provided correspond to the Mueller matrices obtained with illumination at 660 nm wavelength. The samples were measured at different wavelengths giving results in agreement (with the simulated samples) with the presented here. Note that by computing the IPP of the  $M$  obtained by performing the incoherent addition of the pixels in both the radial polarizer and the q-plate we obtain values in agreement with the simulations in Section 3, where anisotropic depolarizing ( $P_3=1$ ) systems were analyzed. In both cases, we obtain depolarizing systems, since  $P_1$  and  $P_2$  have values lower than one. However, as expected, the value of  $P_3$  is one for both samples. These results are consistent with the discussion provided in Section 3, where we demonstrated that depolarization originated by unitary elements with polarizing features (dichroism or birefringence; related to physical anisotropies), are reflected on  $P_1$  and  $P_2$  channels, but  $P_3$  was equal to 1 in all the cases (anisotropic depolarization). Moreover, we can consider the radial polarizer as a diattenuator with high  $p_x$  and low  $p_y$  values, leading to low values for  $P_1$  and high values for  $P_2$ . For the q-plate, since the retardance is almost  $180^\circ$  for the illumination wavelength, we also expect a low value for the  $P_1$  parameter and a high value for  $P_2$ . In addition, we want to note that we chose different regions (in size and position) for the calculations, where different regions can imply different orientation variations. These results were in accordance with the presented here, also obtaining values of  $P_3$  equal to 1. In turn, as discussed in Section 4, scattering processes lead to isotropic depolarization, and a signature in  $P_3$  channel with values lower than 1. This situation is experimentally validated in the following subsection.

### 5.2. Experimental results for the $P_3 < 1$ case

In this section we provide experimental evidence of the  $P_3 < 1$  case, i.e., samples showing isotropic depolarization. These experimental scenarios are based on isotropic scattering processes and validate the simulations performed in Section 4. To this aim, we chose samples composed by elements producing isotropic scattering processes, and thus, that present some contribution of the  $M = \text{diag}(1, 0, 0, 0)$  type.

The first sample is a diffuse reflector (Diffuser DG10-220-P01, from Thorlabs) consisting in a N-BK7 substrate with a rough surface coated with a silver thin film. This roughness diffuses light in all directions and acts as a source with a high degree of isotropic depolarization, as we will show next. For the second sample we chose standard white paper, which is composed by sheets of a mat of random

Table 1

IPP results of the experimentally measured samples representing the incoherent addition of linear polarizers with different orientations and the incoherent addition of linear retarders with different orientations.

	$P_1$	$P_2$	$P_3$
Radial polarizer	0.163	0.876	1
Q plate	0.288	0.727	1



interwoven cellulose fibers with different orientations. This randomness in the paper composition makes it another possible source of isotropic scattering.

In Table 2 we present the resulting IPP from the experimental Mueller matrix images corresponding to the above-mentioned samples. The results correspond to the  $M$  obtained with an illumination beam perpendicular to the surface of the samples, at 1500 nm for the silver diffuse reflector surface and 660 nm for the white paper, and they were measured by the Mueller matrix polarimeter described in the supplementary information. In this case, to compute the IPP values of these samples we chose a ROI centered in the image and calculate the mean value and standard deviation corresponding to each IPP. For the diffuser the ROI was  $70 \times 70$  pixels and in the case of the white paper it was a  $150 \times 150$ -pixel ROI.

As expected, the value of  $P_3$  is different from one in both cases, showing the isotropic nature of the depolarization produced by these samples. Therefore, the composition of the samples makes isotropic scattering the predominant process in their light interaction. In the case of the silver diffuse reflector the value achieved for  $P_3$  is 0.200 and, 0.294 for the white paper. Recalling the inequality related to IPP (see Eq. (2)), values for  $P_1$  and  $P_2$  are restricted to be equal or lower than 0.200 and, 0.294, for the two samples respectively. However, due to the fact that  $P_3$  is not exactly equal to zero, still there is some non-zero values for  $P_1$  and  $P_2$ . This situation shows that even though isotropic depolarization is the predominant depolarizing mechanism in these samples, still there is some anisotropic depolarization present. The origin of these anisotropic depolarization must be related with the polarizing properties of the constituent elements. In the case of the white paper, this anisotropic scattering is due to the retardance properties present in the cellulose fibers [39,46]. For the silver diffuse reflector, it can be due to the non ideality of the fabrication process and some intrinsic polarimetric characteristic of the component elements. As for instance, the protection coating (silver) can present dichroic behavior. These intrinsic characteristics of the samples can explain the presence of anisotropic scattering.

Moreover, if we inspect the differences between the IPP values we find that these values are different to zero, that is it ( $P_1 - P_2$ ) and ( $P_2 - P_3$ ) achieve values larger than zero for both samples. Taking into account the expression of the characteristic decomposition (Eq. (3)) we can see that the weight of all the terms is different from zero. These weights represent the amount of anisotropic scattering present in the sample (being zero for the case of  $P_3 = P_2 = P_1$ ). These results are in concordance with conclusions of Section 4.

In conclusion, with these experimental results we show the concordance of our study of the IPP by means of the simulations of the previous sections. With the experimental results obtained by the measurement of the Mueller matrix of different polarimetric elements we prove the validity of our interpretation of the IPP parameters to characterize the polarization and depolarization response of the sample.

## 6. Conclusions

In this manuscript we provided the usefulness of the Indices of Polarimetric Purity (IPP) to study depolarizing samples. Previous studies have already shown that the IPP are ideal metrics to be used for the enhanced visualization of structures, as in the case of biological samples. In this manuscript, we focused on the physical interpretation of the IPP, which, in turn, gives physical information about the samples themselves,

and in particular, about the intrinsic mechanisms giving rise to depolarization. In this sense, we propose for the first time the concept of isotropic and anisotropic depolarization, as distinct depolarizing origins that can take place simultaneously or separately in samples, and their connection with IPP values. This thorough information of the physical origin of depolarizers is directly obtained from IPP values associated to samples and can be applied in multiple scenarios when dealing with depolarizing samples.

The study is based on a series of simulations in Sections 3 and 4 that help to connect the magnitudes of IPP with different scattering sources in light-matter interaction processes. The simulations are based on the incoherent addition of Mueller matrices representing elemental polarimetric samples and give rise to different simulated depolarizers. The physical interpretation of results was also conducted in terms of the characteristic decomposition, which decompose a general Mueller matrix as the addition of four different Mueller matrices (with clear physical interpretation) whose weights are given by combinations of IPP.

Results show that the index  $P_3$  is related with isotropic depolarization, where input light is fully depolarized independently of its polarization. These systems represent samples associated with scattering processes, which may be originated by a wide range of physical processes based on diffuse reflections. In fact, isotropic depolarization is a multiple scattering process where the polarimetric signature is lost (independently of the input polarization, the exiting beam is fully depolarized). This process only connects with the  $P_3$  value.

In turn, we also show that  $P_1$  and  $P_2$  metrics give measure of the anisotropic depolarization processes. Simulations provide that this depolarization is originated by light-matter interactions with anisotropic basic elements (dichroic and/or birefringent) with different orientations or physical magnitudes (transmittances, retardance, etc.). Anisotropic depolarizing media differently affects an input light beam as a function of their state of polarization. Simulations have been experimentally validated by conducting different simple experiments where different polarimetric samples, mimicking the simulated scenarios, were measured and analyzed in terms of IPP. Furthermore, by inspecting the characteristic decomposition (Eq. (3)) and the results of our work we can relate the  $P_1$  and  $P_2$  changes with the polarimetric component units of a sample which are encoded in the  $M_{J0}$ ,  $M_1$  and  $M_2$  matrices of the stated characteristic decomposition. Note that these three matrices have physical interpretation as stated in the description of above-presented Eq. (3).

In conclusion, by studying the IPP magnitudes associated to a sample, we reveal the physical origins that give rise to depolarization: scattering processes, anisotropic elements or a mix of them. Note that provided results are of crucial importance because they allow us to link depolarization measures at macroscopic scale, with microscopic properties of samples, and with a non-invasive and non-destructive technique (polarimetry).

The present manuscript can be useful for a wide range of applications, where depolarizing samples are involved. In this sense, we put special focus on applications in biophotonics, as organic (vegetal and animal) tissues strongly depolarize incident light. In this regard, different authors have analyzed biological tissues in terms of the IPP. For instance, in Ref. [13] we can see how by means of the IPP channels unwrap new information which was hidden by using other polarimetric channels in different biological samples such as the nutritive channels in an ex-vivo rabbit leg and capillaries of the papillary muscles of an ex-vivo lamb heart. Also, the different IPP response of samples is highly useful for biological tissue discrimination [25,26], which can be different structures (Ref. [26]) or discrimination between healthy or pathological tissue (Ref. [25]). In all these cases, the information given by IPP relate to methods and discussions presented in the current manuscript.

Therefore, the use of IPP as a tool to study tissues could give relevant information of the interaction of incident light with inherent polarimetric elements in tissues (for instance, different types of collagen,

**Table 2**

Mean values and standard deviation of the samples comprised by an isotropic and anisotropic term.

	$\bar{P}_1 \pm \sigma_{P1}$	$\bar{P}_2 \pm \sigma_{P2}$	$\bar{P}_3 \pm \sigma_{P3}$
Silver diffuse reflector	0.05 $\pm$ 0.02	0.11 $\pm$ 0.03	0.20 $\pm$ 0.04
White paper	0.05 $\pm$ 0.02	0.14 $\pm$ 0.04	0.29 $\pm$ 0.07

identified as birefringent elements, or different structures in vegetal samples, identified as dichroic [38]). Under this scenario, for each studied sample, we can evaluate the relevance of diffuse reflections and/or polarizing elements in final depolarizing measures, or more importantly, the spatial depolarizing heterogeneity in such samples, this being applicable to the study of pathological tissues (which modifies internal polarizing properties, organization, etc.).

### CRediT authorship contribution statement

**Mónica Canabal-Carbia:** Writing – original draft, Formal analysis, Software, Conceptualization, Data curation. **Irene Estévez:** Writing – review & editing, Conceptualization. **Esther Nabadda:** Validation, Investigation. **Enrique García-Caurel:** Writing – review & editing, Conceptualization. **J.J. Gil:** Writing – review & editing, Conceptualization. **Razvigor Ossikovski:** Writing – review & editing. **Andrés Márquez:** Writing – review & editing. **Ignacio Moreno:** Writing – review & editing, Validation, Investigation. **Juan Campos:** Project administration, Funding acquisition, Writing – review & editing, Conceptualization, Supervision. **Angel Lizana:** Writing – review & editing, Conceptualization, Project administration, Funding acquisition, Supervision.

### Declaration of Competing Interest

The authors declare the following financial interests/personal relationships which may be considered as potential competing interests:

Monica Canabal-Carbia reports financial support was provided by Spain Ministry of Science and Innovation (PID2021-560 126509OB-C21 and PDC2022-133332-C21). Juan Campos reports financial support was provided by Spain Ministry of Science and Innovation (PID2021-560 126509OB-C21 and PDC2022-133332-C21). Angel Lizana reports financial support was provided by Spain Ministry of Science and Innovation (PID2021-560 126509OB-C21 and PDC2022-133332-C21). Irene Estevez reports financial support was provided by Government of Catalonia (Beatriu de Pinos, 2021-BP-00206). Ignacio Moreno reports financial support was provided by Spain Ministry of Science and Innovation (PID2021-126509OB-C22). Andres Marquez reports financial support was provided by Government of Valencia. Andres Marquez reports financial support was provided by Spain Ministry of Science and Innovation (PID2021-123124OB-I00). Esther Nabadda reports financial support was provided by Government of Valencia. Mónica Canabal-Carbia, Angel Lizana and Juan Campos reports financial support was provided by the Generalitat de Catalunya (2021SGR00138).

### Data availability

Data will be made available on request.

### Acknowledgments

The authors acknowledge the financial support of Ministerio de Ciencia e Innovación and Fondos FEDER (PID2021-126509OB-C21 and PDC2022-133332-C21) and support of Generalitat de Catalunya (2021SGR00138).

IM acknowledge the financial support of Ministerio de Ciencia e Innovación and Fondos FEDER (PID2021-126509OB-C22) AM acknowledges support from project PROMETEO/2021/006 (Generalitat Valenciana, Spain) and PID2021-123124OB-I00 (Ministerio de Ciencia e Innovación, Spain).

EN acknowledges a grant from Generalitat Valenciana, Santiago Grisolia Program (ref. GRISOLIAP/2020/004).

IE acknowledges financial support from a Beatriu de Pinós Fellowship (2021-BP-00206).

### Supplementary materials

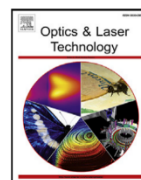
Supplementary material associated with this article can be found, in the online version, at doi:10.1016/j.optlaseng.2023.107830.

### References

- [1] Honda M, Tazaki R, Murakawa K, Terada H, Kudo T, Hattori T, et al. Subaru/IRCS L-band spectro-polarimetry of the HD 142527 disk scattered light. *Publ Astron Soc Jpn* 2022;74:851–6. <https://doi.org/10.1093/pasj/psac041>.
- [2] Asgarimehr M, Hoseini M, Semmling M, Ramatschi M, Camps A, Nahavandchi H, et al. Remote sensing of precipitation using reflected GNSS signals: response analysis of polarimetric observations. *IEEE Trans Geosci Remote Sens* 2022;60: 1–12. <https://doi.org/10.1109/TGRS.2021.3062492>.
- [3] Richter S, Rebarz M, Herrfurth O, Espinoza S, Schmidt-Grund R, Andreasson J. Broadband femtosecond spectroscopic ellipsometry. *Rev Sci Instrum* 2021;92: 033104. <https://doi.org/10.1063/5.0027219>.
- [4] Mahmoud NA-E. Analytical study of precision optical glass surface and its effect on some polarimetric parameters. *J Surf Eng Mater Adv Technol* 2022;12:14–21. <https://doi.org/10.4236/jsemat.2022.121002>.
- [5] Shkirin AV, Ignatenko DN, Chirikov SN, Bunkin NF, Astashev ME, Gudkov SV. Analysis of fat and protein content in milk using laser polarimetric scatterometry. *Agriculture* 2021;11:1028. <https://doi.org/10.3390/agriculture11111028>.
- [6] Van Eeckhout A, García-Caurel E, Garnatje T, Durfort M, Escalera JC, Vidal J, et al. Depolarizing metrics for plant samples imaging. *PLOS One* 2019;14:e0213909. <https://doi.org/10.1371/journal.pone.0213909>.
- [7] Rehinder J, Vizet J, Park J, Ossikovski R, Vanel J-C, Nazac A, et al. Depolarization imaging for fast and non-invasive monitoring of cervical microstructure remodeling *in vivo* during pregnancy. *Sci Rep* 2022;12:12321. <https://doi.org/10.1038/s41598-022-15852-w>.
- [8] He C, He H, Chang J, Dong Y, Liu S, Zeng N, et al. Characterizing microstructures of cancerous tissues using multispectral transformed Mueller matrix polarization parameters. *Biomed Opt Express* 2015;6:2934. <https://doi.org/10.1364/BOE.6.002934>.
- [9] Dubreuil M, Tissier F, Rivet S, Le GY. Linear diattenuation imaging of biological tissues with near infrared Mueller scanning microscopy. *Biomed Opt Express* 2021; 12:41. <https://doi.org/10.1364/BOE.408354>.
- [10] Menzel M, Axer M, Amunts K, De Raedt H, Michelsen K. Diattenuation imaging reveals different brain tissue properties. *Sci Rep* 1939;9. <https://doi.org/10.1038/s41598-019-38506-w>. 2019.
- [11] Pierangelo A, Benali A, Antonelli M-R, Novikova T, Validire P, Gayet B, et al. Ex-vivo characterization of human colon cancer by Mueller polarimetric imaging. *Opt Express* 2011;19:1582. <https://doi.org/10.1364/OE.19.001582>.
- [12] Du E, He H, Zeng N, Sun M, Guo Y, Wu J, et al. Mueller matrix polarimetry for differentiating characteristic features of cancerous tissues. *J Biomed Opt* 2014;19: 076013. <https://doi.org/10.1117/1.JBO.19.7.076013>.
- [13] Van Eeckhout A, Lizana A, García-Caurel E, Gil JJ, Sansa A, Rodríguez C, et al. Polarimetric imaging of biological tissues based on the indices of polarimetric purity. *J Biophotonics* 2018;11:e201700189. <https://doi.org/10.1002/jbio.201700189>.
- [14] Rodríguez C, Van Eeckhout A, Ferrer L, García-Caurel E, González-Arney E, Campos J, et al. Polarimetric data-based model for tissue recognition. *Biomed Opt Express* 2021;12:4852. <https://doi.org/10.1364/BOE.426387>.
- [15] Van Eeckhout A, García-Caurel E, Ossikovski R, Lizana A, Rodríguez C, González-Arney E, et al. Depolarization metric spaces for biological tissues classification. *J Biophotonics* 2020;13. <https://doi.org/10.1002/jbio.202000083>.
- [16] Ossikovski R, Vizet J. Eigenvalue-based depolarization metric spaces for Mueller matrices. *J Opt Soc Am A* 2019;36:1173. <https://doi.org/10.1364/JOSAA.36.001173>.
- [17] Gil JJ, Ossikovski R. Polarized light and the Mueller matrix approach. CRC Press; 2022. <https://doi.org/10.1201/9780367815578>. New York.
- [18] Van Eeckhout A, Gil JJ, García-Caurel E, Romero JG, Ossikovski R, José IS, et al. Unraveling the physical information of depolarizers. *Opt Express* 2021;29:38811. <https://doi.org/10.1364/OE.438673>.
- [19] Gil JJ. Polarimetric characterization of light and media: physical quantities involved in polarimetric phenomena. *Eur Phys J Appl Phys* 2007;40:1–47.
- [20] San José I, Gil JJ. Invariant indices of polarimetric purity: generalized indices of purity for  $n \times n$  covariance matrices. *Opt Commun* 2011;284:38–47. <https://doi.org/10.1016/j.optcom.2010.08.077>.
- [21] Van Eeckhout A, Lizana A, García-Caurel E, Gil JJ, Ossikovski R, Campos J. Synthesis and characterization of depolarizing samples based on the indices of polarimetric purity. *Opt Lett* 2017;42:4155. <https://doi.org/10.1364/OL.42.004155>.
- [22] Wang P, Li D, Wang X, Guo K, Sun Y, Gao J, et al. Analyzing polarization transmission characteristics in foggy environments based on the indices of polarimetric purity. *IEEE Access* 2020;8:227703–9. <https://doi.org/10.1109/ACCESS.2020.3045993>.
- [23] Li X, Zhang L, Qi P, Zhu Z, Xu J, Liu T, et al. Are indices of polarimetric purity excellent metrics for object identification in scattering media? *Remote Sens* 2022; 14:4148. <https://doi.org/10.3390/rs14174148> (Basel).
- [24] Rodríguez C, Van Eeckhout A, García-Caurel E, Lizana A, Campos J. Automatic pseudo-coloring approaches to improve visual perception and contrast in polarimetric images of biological tissues. *Sci Rep* 2022;12:18479. <https://doi.org/10.1038/s41598-022-23330-6>.



- [25] Ivanov D, Dremín V, Borisova E, Bykov A, Novikova T, Meglinski I, et al. Polarization and depolarization metrics as optical markers in support to histopathology of ex vivo colon tissue. *Biomed Opt Express* 2021;12:4560. <https://doi.org/10.1364/BOE.426713>.
- [26] Rodríguez C, Estévez I, González-Arnav E, Campos J, Lizana A. Optimizing the classification of biological tissues using machine learning models based on polarized data. *J Biophotonics* 2023;16. <https://doi.org/10.1002/jbio.202200308>.
- [27] Gil JJ, Bernabeu E. Depolarization and polarization indices of an optical system. *Opt Acta Int J Opt* 1986;33:185–9. <https://doi.org/10.1080/713821924>.
- [28] Goldstein DH. Polarized light. CRC Press; 2017. <https://doi.org/10.1201/b10436>.
- [29] Chipman R.A. Polarimetry. Chapter 22 in handbook of optics II 1995.
- [30] Gil JJ. Structure of polarimetric purity of a Mueller matrix and sources of depolarization. *Opt Commun* 2016;368:165–73. <https://doi.org/10.1016/j.optcom.2016.01.092>.
- [31] Ossikovski R, Gil JJ. Basic properties and classification of Mueller matrices derived from their statistical definition. *J Opt Soc Am A* 2017;34:1727. <https://doi.org/10.1364/JOSAA.34.001727>.
- [32] Gil JJ, San José I. Information structure and general characterization of Mueller matrices. *J Opt Soc Am A* 2022;39:314. <https://doi.org/10.1364/JOSAA.448255>.
- [33] Cloude S. Group theory and polarisation algebra. *Optik* 1986;75:26–36 (Stuttg).
- [34] Gil JJ, José IS. Arbitrary decomposition of a Mueller matrix. *Opt Lett* 2019;44:5715. <https://doi.org/10.1364/OL.44.005715>.
- [35] Gil JJ. Components of purity of a three-dimensional polarization state. *J Opt Soc Am A* 2016;33:40. <https://doi.org/10.1364/JOSAA.33.000040>.
- [36] Ossikovski R, Arteaga O, García-Caurel E, Hingerl K. Model for the depolarizing retarder in Mueller matrix polarimetry. *J Opt Soc Am A* 2022;39:873. <https://doi.org/10.1364/JOSAA.451106>.
- [37] Canabal-Carbia M, Van Eeckhout A, Rodríguez C, González-Arnav E, Estévez I, Gil JJ, et al. Depolarizing metrics in the biomedical field: vision enhancement and classification of biological tissues. *J Innov Opt Health Sci* 2023. <https://doi.org/10.1142/S1793545823300045>.
- [38] Wang LV, Coté GL, Jacques SL. Special section guest editorial. *J Biomed Opt* 2002;7:278. <https://doi.org/10.1117/1.1489434>.
- [39] Al BB, Y Su, Rodríguez C, Lizana A, Campos J, Durfort M, et al. Characterization of vine, *Vitis vinifera*, leaves by Mueller polarimetric microscopy. *Thin Solid Films* 2023;764:139594. <https://doi.org/10.1016/j.tsf.2022.139594>.
- [40] Breton J, Michel-Villaz M, Paillotin G. Orientation of pigments and structural proteins in the photosynthetic membrane of spinach chloroplasts: a linear dichroism study. *Biochimica et Biophysica Acta (BBA) - Bioenerg* 1973;314:42–56. [https://doi.org/10.1016/0005-2728\(73\)90062-5](https://doi.org/10.1016/0005-2728(73)90062-5).
- [41] Gil JJ. On optimal filtering of measured Mueller matrices. *Appl Opt* 2016;55:5449. <https://doi.org/10.1364/AO.55.005449>.
- [42] Van Eeckhout A. Polarimetric methods for the image enhancement in biological applications. *Universitat Autònoma de Barcelona*; 2017.
- [43] Shen F, Zhang M, Guo K, Zhou H, Peng Z, Cui Y, et al. The depolarization performances of scattering systems based on the Indices of Polarimetric Purity (IPPs). *Opt Express* 2019;27:28337. <https://doi.org/10.1364/OE.27.028337>.
- [44] Li D, Guo K, Sun Y, Bi X, Gao J, Guo Z. Depolarization characteristics of different reflective interfaces indicated by Indices of Polarimetric Purity (IPPs). *Sensors* 2021;21:1221. <https://doi.org/10.3390/s21041221>.
- [45] López-Morales G, Sánchez-López M, Lizana A, Moreno I, Campos J. Mueller matrix polarimetric imaging analysis of optical components for the generation of cylindrical vector beams. *Crystals* 2020;10:1155. <https://doi.org/10.3390/cryst10121155> (Basel).
- [46] Palevitz BA, Hepler PK. Cellulose microfibril orientation and cell shaping in developing guard cells of *Allium*: the role of microtubules and ion accumulation. *Planta* 1976;132:71–93. <https://doi.org/10.1007/BF00390333>.



## Full length article

# Revealing hidden bioimaging information by isotropic depolarization filtering

Mónica Canabal-Carbia<sup>a,\*,</sup>, Irene Estévez<sup>a</sup>, Emilio González-Arnay<sup>b</sup>, Ivan Montes-Gonzalez<sup>a</sup>, Jose J. Gil<sup>c</sup>, Anrau Barrera<sup>a</sup>, Enrique García-Caurel<sup>d</sup>, Razvigor Ossikovski<sup>d</sup>, Ignacio Moreno<sup>e,f</sup>, Juan Campos<sup>a</sup>, Angel Lizana<sup>a</sup>

<sup>a</sup> Grup d'Òptica, Dept. de Física, Universitat Autònoma de Barcelona, Bellaterra, 08193, Spain

<sup>b</sup> Servicio de Anatomía Humana, Dept. de Ciencias Médicas Básicas, Universidad de la Laguna, Santa Cruz de Tenerife, 38200, Spain

<sup>c</sup> Universidad de Zaragoza, Pedro Cerbuna 12, Zaragoza, 50009, Spain

<sup>d</sup> LPICM, CNRS, Ecole Polytechnique, Institut Polytechnique de Paris, Palaiseau, 91120, Spain

<sup>e</sup> Instituto de Bioingeniería, Universidad Miguel Hernández de Elche, Elche, 03202, Spain

<sup>f</sup> Dept. de Ciencia de Materiales, Óptica y Tecnología Electrónica, Universidad Miguel Hernández, Elche, 03202, Spain

## ARTICLE INFO

## Keywords:

Polarimetry

Depolarization

Indices of polarimetric purity

Biomedicine

Imaging

## ABSTRACT

We propose an imaging method to enhance and reveal structures within samples by using a polarization-based filter. This filter removes the isotropic content while amplifying the anisotropic component of depolarization. Whereas isotropic depolarization leads to a complete loss of polarimetric information, the anisotropic one is connected with intrinsic characteristics of samples. The filter has the capability to diminish the isotropic depolarization of samples, revealing their inherent information. As representative cases, we analyze the effect of the filter in heart and brain sections of animal origin. Results highlight the outstanding performance of the filter. In heart, myocardial and subendocardial structures are better visualized, whereas in the brain, fiber tracts are identified. These prove the significance of this filter in the medical field, paving the way to the early detection of pathologies. The methodologies here presented could be applied in a wide range of applications, providing a significant advance in polarization imaging where high isotropic depolarization response is present, this being a common scenario in nature.

## 1. Introduction

Polarimetric based methods are a powerful tool in a wide number of applications, as for instance in astronomy [1], remote sensing [2], environment [3], automated guided vehicles [4], botanical applications [5,6], biomedical applications [7,8], among others. In the case of biomedical applications, polarimetric imaging and polarimetric based sample recognition are nowadays being used to study diverse human pathologies [8–10]. There are three main polarimetric properties that could be useful when studying samples: dichroism, retardance and depolarization. Depending on the nature and polarimetric features of the tissue to be inspected, one of these properties, or several, can store information about the sample after light–matter interactions. If the tissue presents a spatially heterogeneous polarimetric response, image contrast between structures can be highly improved through polarimetric methods [11–15], this being of interest for imaging applications [12–15], as well as for tissues or pathologies automatic recognition [16,17]. Let us review the interest of these three main

properties of materials in biomedical applications. Biological tissues are collagen rich structures, and collagen fibers are birefringent materials so retardance has arisen as an interesting tool to investigate different samples and pathologies, both through macroscopic or microscopic polarimetric techniques [18–23]. In this sense, collagen density and fibrillar collagen orientation determine, respectively, the magnitude, orientation and alignment of birefringence in biological tissues. Therefore, the amount, distribution, fiber orientation and alignment of fibrillar collagen are important factors underlying the properties of tissues, playing an important role in many diseases. For instance, the connection between collagen organization and birefringent properties has been used for the detection and progression study of different types of cancer [24,25]. Also nerve fibers and some proteins have an important birefringent response [26]. In addition, although the depolarization feature of samples was initially understood as a characteristic with little value in biomedical applications (it was regarded as noise to be minimized by some users), recent works have demonstrated

\* Corresponding author.

E-mail address: [monica.canabal@uab.cat](mailto:monica.canabal@uab.cat) (M. Canabal-Carbia).

<https://doi.org/10.1016/j.optlastec.2025.112956>

Received 24 July 2024; Received in revised form 31 March 2025; Accepted 8 April 2025

Available online 23 April 2025

0030-3992/© 2025 The Authors. Published by Elsevier Ltd. This is an open access article under the CC BY license (<http://creativecommons.org/licenses/by/4.0/>).

that depolarizing channel encodes rich information of samples, as it is related with inherent features, as constituent units disorder, density, physical characteristics, etc. In this vein, due to the stronger scattering effects and organization changes on most tissues related to pathological processes, depolarization is a key method for the study and characterization of diverse human pathologies [8,9,27–29]. For instance, changes in cellular concentration of tissues related to pre-cancer to cancer progression can be studied by means of depolarization variations [29]; also the variation of anisotropy levels and orientation disorder are directly related to heart pathologies such as infarction [27], cancer stages in different tissues as *ex-vivo* human colon, skin, cervix and laryngeal cancer [9,28,29]. Therefore, anisotropic properties of samples can be related to different pathological stages. In this regard, the use of depolarizing metrics derived from the experimental Mueller matrix of the studied samples have demonstrated their interest in such applications. In turn, although observables related to samples dichroism, as diattenuation or polarizance [30], are not commonly used in terms of biomedical samples imaging, due to the weak dichroic response of biological tissues [31], they have demonstrated to be helpful for tissues classification [16,32] and, in the case of diattenuation this polarimetric feature has recently demonstrated its good performance in the study of brain tractography [33]. Moreover, they have proved a high interest for the study of plant samples, helping in the detection of chloroplasts and related organelles in plant species [34].

In this context, we recently published a study showing that depolarizing properties of samples can have two main origins: isotropic and anisotropic depolarization [35]. In this scenario, biological samples may exhibit anisotropic depolarization, isotropic depolarization, or a mixture of both [33].

In this work, we show that in those samples where isotropic depolarization is a predominant effect, the anisotropic depolarization part may be present but hidden, this contribution being much more valuable in terms of image visualization and contrast enhancement. The discussion is conducted considering some metrics suitable for the description of depolarizing samples, which have already demonstrated their interest regarding tissue imaging: the indices of polarimetric purity (IPP) [8,11,12,14]. Once this idea is set, we use this concept to implement an imaging filter with a clear physical interpretation and very simple implementation. Such filter is based on removing the influence of one the IPP in the response of the sample. The interest of this new filter is tested on different biological samples, showing outstanding results in terms of sample visualization, and improving actual state-of-the-art.

Finally, we want to note that the methods provided in this work are general and could be useful not only in biomedical applications, as motivated in this work, but in all those applications where polarization methods have already proved their interest in imaging or classification applications, as those stated at the beginning of this introduction.

The present manuscript is organized as follows. In Section 2, we present a brief summary of the isotropic and anisotropic depolarization concepts, the mathematical background related to the filter implementation in the Mueller matrix and the impact on some polarimetric observables after the isotropic filtering. Section 3 provides the description of the two biological samples (transverse section of an *ex-vivo* lamb heart and a coronal section across the frontal lobe of an *ex-vivo* cattle brain sample) inspected in this work as well as their interest in the biomedical field (Section 3.1). The experimental results of the samples once the filter has been applied are shown in Sections 3.2 and 3.3. To conclude, in Section 4 we provide the main conclusions of the work.

## 2. Isotropic depolarization filter (IDF): Mathematical background

In this section, we present the mathematical background detailing a new tool for image processing based on polarization with high potential for vision applications, being specially suitable in samples showing depolarization, which is applicable to a large number of real scenarios. Specifically, we present a new concept for image polarimetric filtering

which is applied to the experimental Mueller matrix images of samples, and exploits the fact that depolarizing samples may present isotropic and/or anisotropic depolarization.

As discussed in Ref. [35], depolarization associated with a given uniformity in polarimetric properties is called anisotropic depolarization, while isotropic depolarization is caused by other effects that randomize the polarization state of light, such multiple scattering, but are unrelated to the polarimetric properties of the sample.

In real samples, both isotropic and anisotropic depolarization usually occur simultaneously. The effect of isotropic depolarization is to reduce the contrast of images because it affects all elements of the Mueller matrix ( $M$ ) in the same way. On the other hand, anisotropic depolarization affects the elements of  $M$  differently and can therefore contribute to the improvement of the contrast in polarimetric images. Therefore, anisotropic depolarization seems to be more interesting for practical applications in polarimetric imaging than isotropic depolarization, and it is therefore interesting to find a way to separate their respective effects. In the following, we propose a method to filter out the isotropic content of the depolarization, which leads to a significant improvement in the visualization of sample structures, surpassing not only standard intensity images, but also current state-of-the-art polarimetric images.

To implement the polarimetric filter, we use the characteristic decomposition of  $M$  [36] in terms of the indices of polarimetric purity (IPP) observables [37], because the IPP represent a suitable framework to separate isotropic and anisotropic depolarizing origins. Moreover, the characteristic decomposition has a clear physical interpretation that allows the filter to be implemented in an intuitive and simple way, which is useful in practical applications. In addition, this decomposition can also be useful for filtering polarimetric noise [38].

In the following we review the concept of isotropic and anisotropic depolarization in the context of characteristic decomposition (Section 2.1), and then we describe the filtering method and derive some observables of interest (Section 2.2).

### 2.1. Isotropic and anisotropic depolarization content derived from the characteristic decomposition of the mueller matrix

The characteristic decomposition allows to write the  $M$  of any depolarizer as the incoherent addition of different Mueller matrices. In fact, it separates  $M$  as the contribution of four different matrices with physical interpretation (describing polarizing or depolarizing properties), and each one of these terms is weighted by one of the IPP or a linear combination of them. In particular, it can be expressed as follows [36,37]:

$$M = P_1(m_{00}\hat{M}_{J0}) + (P_2 - P_1)(m_{00}\hat{M}_1) + (P_3 - P_2)(m_{00}\hat{M}_2) + (1 - P_3)(m_{00}\hat{M}_3), \quad (1)$$

where  $m_{00}$  is an scalar value representing the mean intensity coefficient and the circumflex in the different matrices  $\hat{M}_i$  ( $i = J0, 1, 2$  and  $3$ ) denotes the normalized matrix.

Each one of the four matrices appearing in the incoherent addition in Eq. (1) has a particular physical meaning:  $\hat{M}_{J0}$  represents the nondepolarizing features of  $M$ ,  $\hat{M}_1$  represents the portion of the medium that behaves as a 2D depolarizer,  $\hat{M}_2$  represents the part of the medium that behaves as a 3D depolarizer and the term  $\hat{M}_3$  gives the portion of the medium behaving as a perfect depolarizer [36,39,40]. For further interpretation, recall that a 2D depolarizer is a system that can be written as the incoherent addition of two specific pure Mueller matrices derived from  $M$ , whereas a 3D depolarizer is a system that can be written as the incoherent addition of three specific pure Mueller matrices derived from  $M$ , and a perfect depolarizer is a system that when a light beam interacts with it, regardless of its state of polarization, always transforms the incident polarization state into a



fully unpolarized state (perfect depolarizers can be represented by the Mueller matrix  $M_{\text{perfect depolarizer}} = \text{diag}(1, 0, 0, 0)$ ).

Note that this additive scheme of interpretable elements give us valuable information about the polarimetric contributions leading to the final particular system represented by  $M$ . Importantly to our study, note that the significance (the weight) of each term in Eq. (1) is provided by a linear combination of the IPP parameters ( $P_1$ ,  $P_2$ ,  $P_3$ ,  $P_2 - P_1$ ,  $P_3 - P_2$  and  $1 - P_3$ , respectively). Recall here that IPP are three polarimetric observables,  $P_1$ ,  $P_2$  and  $P_3$ , with values between 0 and 1, which are derived from the covariance matrix associated with a given  $M$ , and which provide quantitative information on the polarimetric randomness of the system [35,37]. Therefore, the particular IPP combinations above-stated can be understood as metrics quantifying different polarimetric origins existing in a given sample.

Stated the interest of IPP for an in-depth knowledge of depolarizing samples, in a previous work (Ref. [35]) we further studied the interpretation of IPP observables, by analyzing a collection of depolarizers consisting of the incoherent addition of easily interpretable devices (diattenuators and retarders), and inspecting the associated IPP values. We demonstrated that  $P_1$  and  $P_2$  were connected with anisotropic depolarization (originated by polarimetric anisotropy), and  $P_3$  was connected with isotropic depolarization (perfect depolarizers). It was shown that depolarizing systems fully governed by anisotropic processes were characterized by  $P_3 = 1$ , regardless of the values of  $P_1$  and  $P_2$ . Moreover, when  $P_3 < 1$  means that a given amount of isotropic depolarization was present. The limiting case of a fully unpolarizing sample occurs when  $P_3 = 0$ . Readers interested in further evidence and discussion related to the connection of  $P_1$  and  $P_2$  with anisotropic depolarization, and  $P_3$  with isotropic depolarization are addressed to Ref. [35].

In this framework, it is interesting to analyze how the characteristic decomposition changes when we consider systems with only anisotropic depolarization (i.e., with zero isotropic depolarization content) for which  $P_3 = 1$ . Therefore, by imposing such a condition in Eq. (1), the last term of the characteristic decomposition (corresponding to the contribution of the perfect depolarizer) becomes zero. Therefore, for this particular case Eq. (1) can be rewritten as [35]:

$$M_{P_3=1} = M_a = P_1(m_{00}\hat{M}_{J0}) + (P_2 - P_1)(m_{00}\hat{M}_1) + (1 - P_2)(m_{00}\hat{M}_2), \quad (2)$$

where  $M_a$  denotes depolarizing systems without isotropic depolarization.

On the other hand, the last term of Eq. (1) represents isotropic depolarization. In fact, by taking into account the weight of this last term in Eq. (1), i.e.  $1 - P_3$ , it can be shown that the value of  $P_3$  measures the proportion of anisotropic depolarization in a sample  $M$  [35]. For instance, the condition  $P_3 = 1$  is satisfied when no isotropic depolarization is presented in the sample and  $P_3 = 0$  when depolarization is fully isotropic. Moreover, due to the inequalities governing IPP, if  $P_3 = 0$ , the other IPP must be also zero,  $P_1 = P_2 = 0$  (see Eq. (S4) of the Supplementary document). As a consequence, the characteristic decomposition of a system that only presents isotropic depolarization processes is written as [35]:

$$M_{P_3=0} = M_{iso} = m_{00}\hat{M}_3, \quad (3)$$

where  $M_{iso}$  denotes depolarizing systems fully governed by isotropic depolarization and represented by perfect depolarizers. Note that, in the equation describing isotropic depolarization processes the information is codified in only one term ( $m_{00}\hat{M}_3$ ), whereas the anisotropic depolarization is described by three different terms (see Eq. (2)).

A general system that may present both isotropic and anisotropic depolarization can be written as follows [35]:

$$M = P_3 m_{00}\hat{M}_a + (1 - P_3)(m_{00}\hat{M}_{iso}), \quad (4)$$

where  $M$  is divided in the anisotropic ( $\hat{M}_a$ ) and isotropic ( $\hat{M}_{iso}$ ) depolarizing contributions.

From Eq. (4) we clearly realize that the  $P_3$  metric associated to a Mueller matrix determines the portion of isotropic and anisotropic depolarization features in the samples. Note also that, as a consequence of the inequality relation of IPP ( $P_1 \leq P_2 \leq P_3$ ), if isotropic features of samples are predominant,  $P_3$  takes small values, and thus, the valuable information of anisotropic depolarization, which is connected with physical properties of samples (through channels  $P_1$  and  $P_2$  and other related polarimetric observables [39]) is mostly masked. This situation can be intuitively interpreted using the graphical representation of Purity Space [41] (see sec. 3.1 of the Sup. doc.).

At this point, the following questions arise: (a) could it be possible to remove the influence of isotropic depolarization of a sample in order to highlight more physical properties of samples? and (b) if this is possible, would this be a powerful tool for image visualization of structures after removing isotropic depolarization? The main goal of this manuscript is to answer these questions and to prove, that: (a) it is very easy to isolate isotropic depolarizing features of a Mueller matrix (let us call it isotropic depolarization filtering) by using decomposition in Eq. (4); and (b) the application of this filter paves the way for a new dimension of image processing based on polarimetric data. In the next subsection, the theoretical fundamentals of the proposed filter are described in detail. In turn, to highlight the potential of the method for practical applications, some experimental results and examples are provided in Section 3.

## 2.2. Isotropic depolarization filter

The filter we propose consists in eliminating the isotropic  $((1 - P_3)(m_{00}\hat{M}_3))$  term from  $M$ . The filtered Mueller matrix  $M_a$  is implemented as follows:

$$M_a = M - (1 - P_3)(m_{00}\hat{M}_3) = \quad (5)$$

$$P_1(m_{00}\hat{M}_{J0}) + (P_2 - P_1)(m_{00}\hat{M}_1) + (1 - P_2)(m_{00}\hat{M}_2).$$

In this way, we isolate the anisotropic information in the new filtered matrix  $M_a$ , which corresponds to the anisotropic terms of the characteristic decomposition. In other words, we subtract the last term in Eq. (2) to the Mueller matrix  $M$ , to get  $M_a$ .

Once the anisotropic information is isolated, we can study how this filtering affects the polarimetric observables that can be calculated from  $M_a$  (and how they compare with the same observables derived from  $M$ ). To do so, we can write the filtered matrix elements (those of  $M_a$ ) in terms of the elements before the filtering. As the  $\hat{M}_3$  matrix has the diagonal form  $\text{diag}(1, 0, 0, 0)$ , it is straightforward to see that  $m_{00}$  is the only element in  $M$  affected by the filter:

$$m_{a00} = m_{00} - (1 - P_3)m_{00} = P_3 m_{00}. \quad (6)$$

The rest of the elements of the filtered matrix (before normalization) are not affected by these operation, that is  $m_{ai,j} = m_{i,j}$  for all elements except for  $i = j = 0$  (Eq. (6)). To obtain the different polarimetric observables from  $M$ , it is necessary to normalize the matrix (divide every element of the matrix by  $m_{00}P_3$ ). The normalized form of  $M_a$  in terms of the elements before the filter, can be expressed as (the filtered polarimetric parameters are noted with the superindex  $'$ ):

$$M_a = m_{00}P_3 \begin{pmatrix} 1 & \frac{m_{01}}{m_{00}P_3} & \frac{m_{02}}{m_{00}P_3} & \frac{m_{03}}{m_{00}P_3} \\ \frac{m_{10}}{m_{00}P_3} & \frac{m_{11}}{m_{00}P_3} & \frac{m_{12}}{m_{00}P_3} & \frac{m_{13}}{m_{00}P_3} \\ \frac{m_{20}}{m_{00}P_3} & \frac{m_{21}}{m_{00}P_3} & \frac{m_{22}}{m_{00}P_3} & \frac{m_{23}}{m_{00}P_3} \\ \frac{m_{30}}{m_{00}P_3} & \frac{m_{31}}{m_{00}P_3} & \frac{m_{32}}{m_{00}P_3} & \frac{m_{33}}{m_{00}P_3} \end{pmatrix} \quad (7)$$

$P'$

From Eq. (7) we see that, since the  $m_{00}$  element of the filtered matrix  $M_a$  was affected by the IDF, the new normalized elements of the

matrix are also affected. In particular, all the elements in the matrix have a dependency on  $P_3$ . The interest of filtering the isotropic part of the depolarization is particularly evident when it comes to image non-homogeneous samples which show a given spatial variation of their respective polarimetric properties across the imaged area. In this way, the value of  $P_3$  will vary across the sample and therefore affect the observed value of the polarimetric properties differently. For instance, when we obtain the Mueller matrix image of a sample, we compute the value of each polarimetric characteristic pixel by pixel. Hereafter, we will explicitly write this point-to-point dependence of the polarimetric observables,  $P_3(x, y)$ .

Once the filtered matrix is obtained, we recalculated the polarimetric observables from this matrix in order to analyze the effect of subtracting the isotropic depolarization on them. For more detailed calculations, see sec. 2 of the Supplementary document.

### 2.2.1. Non-depolarizing channels: Dichroic and retardance properties

In this subsection, we discuss the contrast improvement related to non-depolarizing observables (i.e., dichroic and retardance-based properties) by using the proposed  $P_3$  based filter. Regarding to the sample characteristics related to dichroism, we mainly focus on diattenuation ( $D$ ) and polarizance ( $P$ ). These metrics can be obtained directly from the  $M$  elements, as shown in Eq. (7). The relationship between the parameters before and after the filter can also be extracted directly from Eq. (7).

$$D'(x, y) = \frac{D(x, y)}{P_3(x, y)}, \quad P'(x, y) = \frac{P(x, y)}{P_3(x, y)}. \quad (8)$$

From Eq. (8) we see that filtering  $P$  and  $D$  means dividing the original values of these observables by  $P_3$ . When the isotropic depolarization is high, the values of  $P_3$  are low, and therefore filtering the isotropic component will imply a significant contrast enhancement in  $P$  and  $D$ . In Section 3 we show how this effect help not only to the contrast enhancement but also to reveal some structures hidden due to a high amount of isotropic depolarization.

The filtered retardance ( $R'$ ) cannot be obtained directly from the elements of  $M_a$ . To obtain the retardance observables from a Mueller matrix, we need to further processing the data, as for instance, by applying Mueller decompositions, as the Lu-Chipman, the Arrow or the Symmetric decompositions [39]. The calculations from which those methods are based are not straightforward, so to obtain an analytical expression for the filter effect on  $R'$  is not trivial and it is out of the scope of this manuscript. However, considering a heuristic approach based on the study of the filter effect in retardance images corresponding to a wide range of tested samples, we hypothesize that the contrast enhancement is notably lower than in observables related to dichroic and depolarization properties and that such filter effect can be considered negligible for the retardance case.

### 2.2.2. Depolarizing channels

Different sets of depolarization related parameters can be deduced from  $M$ . It has been demonstrated that the IPP give the best performance and provide fundamental information about the origin of depolarization in biological tissues [35]. In addition to IPP, here we discuss the effect of the IDF on two more metrics related to depolarization: the depolarization index ( $P_d$ ), which is a global indicator of the depolarization produced by a sample and the degree of spherical purity ( $P_s$ ), which measures the contribution to depolarization that is not directly related to the dichroic properties [30,39].

We start by calculating the effect of the IDF on the IPP. The IPP are obtained as linear transformations of  $M$  and cannot be directly obtained from  $M$  elements, as these indices are linear combinations of the covariance matrix,  $H(M)$ , eigenvalues  $\lambda_i$ . [37,39,42]. The covariance matrix  $H$  is a Hermitian semi-definite matrix that can be obtained from  $M$  elements as follows:

$$H(M) = \frac{1}{4} \sum_{i,j=0}^3 m_{ij}(\sigma_i \otimes \sigma_j^*), \quad (9)$$

where  $m_{ij}$  represent the elements of Mueller matrix,  $\sigma$  are the Pauli matrices, and is the Kronecker product. The IPP arise from lineal combinations of  $H$  eigenvalues ( $\lambda_i$ ,  $i=0,1,2,3,4$ ):

$$P_1 = \frac{\lambda_0 - \lambda_1}{trH}, \quad P_2 = \frac{\lambda_0 + \lambda_1 - 2\lambda_2}{trH}, \quad P_3 = \frac{\lambda_0 + \lambda_1 + \lambda_2 - 3 + \lambda_3}{trH}, \quad (10)$$

where  $trH$  stands for the trace of the covariance matrix  $H$  where  $trH = m_{00}$  and the values of IPP are restricted between 0 and 1 following the relation ( $0 \leq P_1 \leq P_2 \leq P_3 \leq 1$ ).

Therefore, to obtain the filtered IPP we need to calculate the covariance matrix of  $M_a$  in Eq. (5), i.e.  $H(M_a)$ . Each element of the covariance matrix can be calculated as a linear combination of different elements of  $M$  as shown in Eq. (9), and importantly, the  $m_{00}$  element is only present on the diagonal of  $H$  (see Eq. (S1) of the Sup. doc.) [39]. Therefore, the diagonal elements of  $H$  will be the only ones affected by the filter, and  $H(M_a)$  can be obtained as:

$$H(M_a) = H(M) - (1 - P_3)m_{00}\mathbb{I}, \quad (11)$$

where  $\mathbb{I}$  is the identity matrix.

The next step is to obtain the eigenvalues of  $H(M_a)$ ,  $\lambda'_i$ , to calculate the filtered IPP (i.e.,  $P'_1$ ,  $P'_2$  and  $P'_3$ ). To this aim, we can relate the covariance matrix before,  $H(M)$ , and after,  $H(M_a)$ , the filter by using Eq. (11) through the diagonalization calculation:

$$H(M_a) - \lambda'\mathbb{I} = 0 \rightarrow H(M) - (1 - P_3)m_{00}\mathbb{I} - \lambda'\mathbb{I} = 0, \quad (12)$$

$$H(M) - (\lambda' + (1 - P_3)m_{00})\mathbb{I} = 0,$$

$$\lambda = \lambda_a + (1 - P_3)m_{00}, \quad (13)$$

where  $\lambda$  and  $\lambda'$  correspond to the eigenvalues of  $H(M)$  and  $H(M_a)$  respectively. Eq. (13) allows to calculate the relationship between IPP before and after the filtering. The IPP are defined as a function of the eigenvalues as follows (see Eq. (10)) [37,43]:

$$P_k = \frac{1}{trH} \sum_{k=1}^n k\Delta\lambda_k, \quad k = 1, 2, 3; \quad (14)$$

where  $\Delta\lambda_k = \lambda_{k-1} - \lambda_k$ . Therefore, regarding Eq. (12), the relation between eigenvalues,  $\lambda_i = \lambda'_i + P_3$  ( $i=0,1,2,3$ ), and the traces  $trH(M_a) = m'_{00} = P_3m_{00}$ , we can write the filtered IPP as:

$$P'_k = \frac{1}{trH(M_a)} \sum_{k=1}^n k\Delta\lambda_a = \frac{1}{P_3trH} \sum_{k=1}^n k\Delta\lambda'_k = \frac{1}{P_3trH} \sum_{k=1}^n k\Delta\lambda_k = \frac{1}{P_3} P_n, \quad (15)$$

$$P'_k(x, y) = \frac{P_k(x, y)}{P_3(x, y)},$$

where  $\Delta\lambda_a = (\lambda_{k-1} - P_3) - (\lambda_k - P_3) = \lambda_{k-1} - \lambda_k = \Delta\lambda_k$ . Inspecting Eq. (15) we can observe the same effect on the filtered variables than in Eq. (8); the value of the filtered index increases by an amount given by  $1/P_3(x, y)$ , in the same way as the parameters presented in Eq. (8).

In addition, we present the effect of the IDF on ( $P_d$ ) and ( $P_s$ ). Both of these metrics can be obtained directly from the components of  $M$  [39] and, the effect of the filter on these parameters is the same as for the IPP and the dichroic parameters:

$$P'_d(x, y) = \frac{P_d(x, y)}{P_3(x, y)}, \quad P'_s(x, y) = \frac{P_s(x, y)}{P_3(x, y)}. \quad (16)$$

## 2.3. Discussion

In secs. 2.2.1 and 2.2.2 we discussed how the visibility of images representing polarimetric observables [3–5,7], can be significantly improved using the proposed subtraction of the effect of isotropic depolarization. For most of these observables, their visibility is increased by a factor proportional to  $1/P_3$  when the IDF is applied. Thus, this contrast enhancement is particularly relevant for small values of  $P_3$ , which is the typical case for polarimetric images of biological tissues.



Under this scenario, the potential of the IDF for applications in biophotonics is discussed in the following Section 3 by analyzing the contrast enhancement (and biological structure unveiling capability) obtained when applying our proposed IDF for studying diverse examples of biological tissues of animal origin. As additional information, if the readers are interested in a more visual interpretation of the filter, we address them to the Supplementary material (sec. 3), where we provide a physical interpretation of the filter in terms of depolarizing spaces [41].

### 3. Filter application to the analysis of biological samples

As discussed in previous section, the contrast enhancement associated to the isotropic depolarization filter application on the study of a given sample, it is higher as lower the  $P_3$  value is. In other words, the IDF is specially suitable for samples showing rich isotropic depolarization behavior, which masks other polarimetric features of the sample. This scenario is common when dealing with biological samples, as for instance it is the case of soft tissues, usually presenting very low values for  $P_3$  metric (see Table 1 and Fig. S5 in the Supplementary material). For this reason, in this section we present different examples of the IDF benefits when applied for the study of different soft tissues.

In particular, in the following we present the application of the IDF for the study of two different tissues: sections of *ex-vivo* heart and brain measured at 625 nm and 470 nm, respectively. In Section 3.1, we provide a brief description of the samples and the motivation of this choice due to their importance in the field of medicine. The Mueller matrices,  $M_s$ , corresponding to the stated samples were experimentally obtained by means of a complete Mueller matrix image polarimeter described in the sec. 4 of the Supplementary document. In addition, for completeness, in the Supplementary material we also provide the results obtained for other polarimetric observables and some examples of other samples highlighting as well the potential of the filter for medical applications.

#### 3.1. Biological samples: description and interest

We have obtained excellent results in terms of image contrast enhancement after applying the filter to the polarimetric images of a number of soft tissue samples. For the sake of brevity, we will discuss two representative examples in this section: (1) heart and (2) brain tissue sections; both from *ex-vivo* animal. We have chosen these two examples because of their great interest in the medical field and because, there is currently no standard non-invasive gold technique to characterize certain structural features and/or pathological tissues associated to these samples.

In the case of the heart, cardiovascular disease is the number one cause of death in the world, leading to around the 15% of total worlds deaths and has increased in more than 6 million cases in the last 20 years [44]. The early diagnosis of structural cardiac abnormalities can help in the detection, prevention and treatment of heart malfunctioning and unfavorable cardiovascular events such as infarction [45]. Analyzing cardiac tissue remodeling at an early stage can be lifesaving. Currently, the gold standard technique for detecting myocardial fibrosis is the endomyocardial biopsy [45]. This technique is an invasive method, and it is practically infeasible in daily clinical routine [46]. In this sense, different studies have demonstrated the usefulness of polarimetry in the heart structural variations and in differentiating between healthy, infarcted and regenerated myocardial tissue [27,47]. Particularly, depolarization has arisen as an indicator of these structural changes, being directly correlated with the anisotropic structure of the heart tissue components [47]. Interestingly, the approach here presented also allows to follow the trajectories of the subepicardial coronary vessels and generate contrast between their walls and their lumens. This feature may be suitable for the clinical context, as it

would provide a tool for surgeons without the use of intra-surgical arteriography (see Fig. S8 of the Supplementary material).

In the case of the brain, the study of brain connectivity and its functional expression is probably the present frontier of applied neuroscience, as there is no gold-standard technique for pathway mapping apart from *peri-mortem* tract-tracing injections that are not ethically suitable for the study of human connectivity [48]. Techniques such as histology or ultrastructure-based methods can distinguish fiber orientation but are not useful for tracing long range tracts [49]. It has been demonstrated the ability of Mueller matrix polarimetry to classify large tracts that are known to have different orientations (internal capsule, cerebral peduncles, fimbria, medial lemniscus, optic tract) and to resolve the limits between gray and white matter [13,33].

Recently, polarimetry has demonstrated its capabilities to study in an easy and non-invasive way some of the above mentioned characteristics leading to promising results in the medical field, in particular to fundamental studies of sample components, characterization and early pathology detection. The filter we present would help to construct more powerful polarimetric techniques based on the Mueller matrix inspection by means of a simple mathematical treatment of  $M$ .

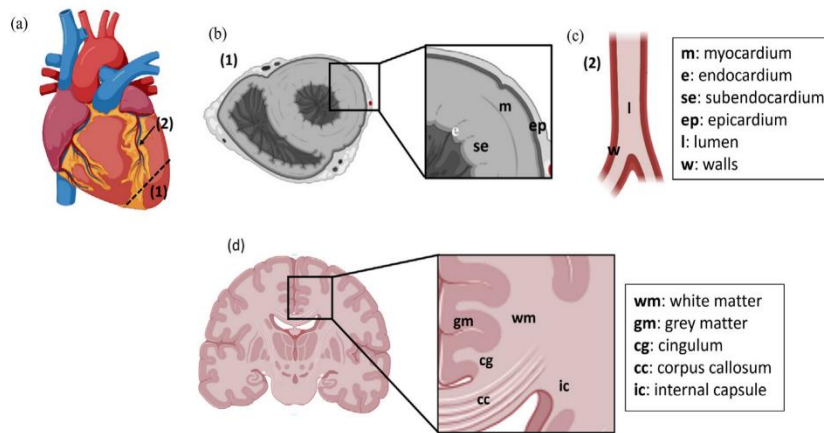
In the following, we present the results correspondent to a transverse section of an *ex-vivo* lamb heart sample and a coronal section across the frontal lobe of an *ex-vivo* cattle brain sample. In Fig. 1 we provide a schematic representation of the regions of the samples inspected. We demonstrate how, by means of applying the IDF to the experimentally obtained Mueller matrices, much more information of the structures of the samples can be obtained.

#### 3.2. Experimental results for the polarimetric analysis of a heart sample

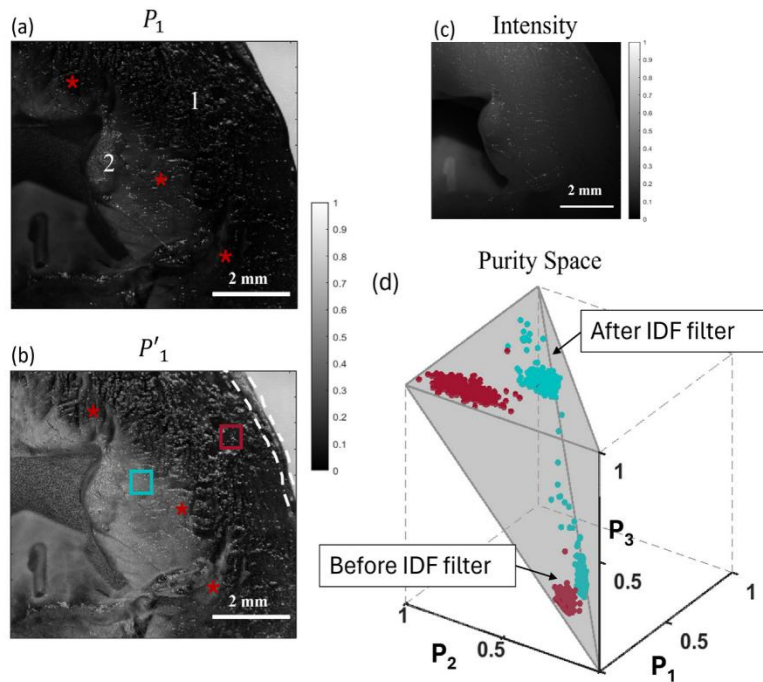
In this section, we present the results of applying the filter to the heart sample. The Mueller matrices,  $M_s$ , corresponding to the stated samples were experimentally obtained by means of a complete Mueller matrix polarimeter. Information related to the components, calibration and calculation of the experimental Mueller matrices are described in section 4 of the Supplementary document. In Fig. 2 we compare the standard intensity image (i.e., the non-polarimetric image; Fig. 2(c)) with the images obtained with a particular polarimetric observable, the  $P_1$  channel, before (see Fig. 2(a)) and after (see Fig. 2(b)) application of the IDF. We chose  $P_1$  for the analysis because, among all polarimetric observables studied, it was the most interesting metric in terms of contrast enhancement and structure unveiling. For the sake of clarity, in Fig. 2(d) we also present a visual interpretation of the effect of the filter on the heart sample data, in terms of the 3D Purity Space constructed by means of the IPP.

Fig. 2(a) to (c) show the images correspondent to the transverse section of the heart sample. In the conventional intensity image (unpolarized reflectance), the heart appears as an homogeneous and undifferentiated tissue (see Fig. 2(c)). However, by examining the depolarization response of the sample (through the  $P_1$  parameter) we are able to see a spatial dependence, showing different depolarization results for the inner (low gray levels mean low depolarization) and outer region (black means high depolarization). Interestingly, these regions correspond to different tissue types: (1) is myocardial tissue composed of concentrically arranged fascicles of myocardial muscle whereas (2) corresponds to subendocardial tissue, composed of loose connective tissue and Purkinje fibers. We show how polarimetric analysis reveals structures invisible to conventional techniques.

Filtering the isotropic depolarization component largely overcomes the performance of both the intensity image and the unfiltered  $P_1$  channel. The obtained filtered image is shown in Fig. 2(b), where the contrast between structures (1) and (2) is clearly enhanced compared to the  $P_1$  image (in particular, the contrast is enhanced by an amount of  $1/P_3$ ). Furthermore, the application of the IDF leads to the unveiling of new information that was obscured by the isotropic depolarization in the  $P_1$  image. In Fig. 2(b), the region corresponding to subendocardial



**Fig. 1.** (b), (c) and (d) correspond to the anatomical context for measurements showed respectively in Fig. 2, Fig. S8 of the Sup. doc. and Fig. 3, depicted in humanized schematic drawings. (a) frontal view of a mammalian heart showing the interventricular sulcus containing the interventricular branch of the left coronary artery surrounded by the subepicardial fatty tissue. (1) shows the direction of a section of both ventricles transverse to the heart axis resulting in an image close to the one depicted in (b). In this image the left ventricle appears lined by the endocardium (en) and surrounded by the subendocardium (se), the myocardium (m) and the epicardium (ep). (2) indicates the location of a longitudinal section of the coronary vessel, shown in (c), where (l) and (w) correspond to its lumen and walls respectively. Finally, an idealized drawing of a coronal section (d) of human brain is shown, demonstrating the equivalent areas to the ones analyzed in Fig. 3.



**Fig. 2.** Comparison of the polarimetric observable  $P_1$  before (a) and after (b) applying the IDF with intensity image (c). (1) and (2) in (a) indicate myocardial and subendocardial tissue, respectively; white dashed lines in (b) indicate the epicardial tissue and asterisks in (a) and (b) denote some regions where the filter is unveiling information hidden due to isotropic depolarization. (d) corresponds to the representation of the IPP values before and after IDF in the Purity Space; the regions of the sample selected for the Purity Space representation are indicated in (b), red and blue squares correspond to: myocardial and subendocardial tissue, respectively.

tissue is better defined than before the filter (see Fig. 2(a)). That is, in  $P'_1$  we are able to see the border and the two different structures present in this specimen with great contrast. In addition, the filtered image in Fig. 2(b) shows much clearer boundaries and transitions between myocardial and subendocardial tissue, and it is much richer in structural details, as can be seen, for example, in the regions highlighted by red asterisks. Finally, the boundaries between the epicardium (see white dashed lines in Fig. 2(b)) and the myocardial tissue are clearly differentiated, whereas they were almost invisible in both the intensity and  $P_1$  images.

Finally, we note that the IDF is not only useful for enhanced vision but also for data processing in applications such as tissue classification, as valuable data for training machine learning models. Fig. 2 (d), is a graphical representation of the effect of the filter on the values of the IPP represented in their corresponding Purity Space. Complementary information about Purity Spaces can be found in sec. 3 of the Supplementary material. Purity Spaces have been shown to be useful in applications related to image-based tissue or structure discrimination [10,43], therefore we find interesting to discuss the effect of the IDF in this framework. To do so, we selected two different regions



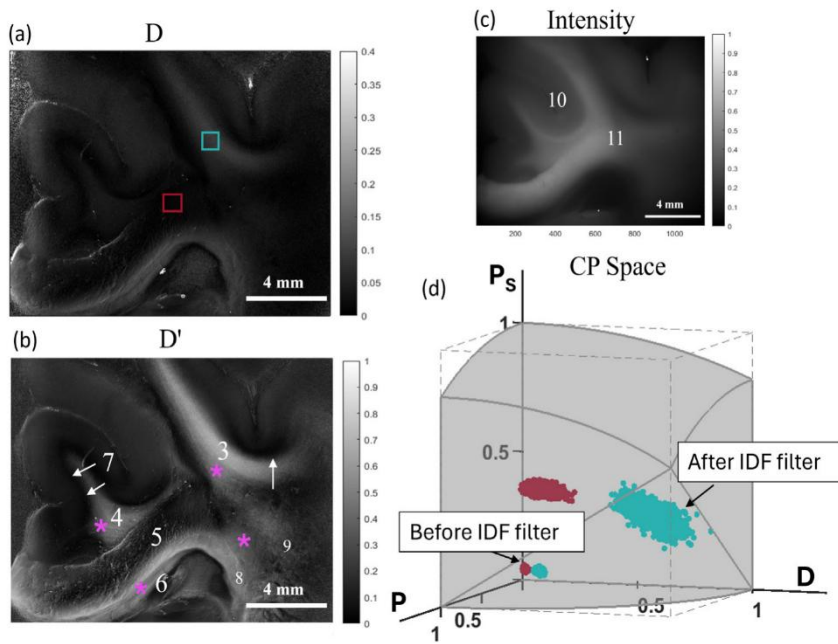


**Fig. 3.** Comparison of the polarimetric observable  $D$  before (a) and after (b) applying the IDF with the intensity image (c) in the coronal section across the frontal lobe of the brain. Numbers 3 to 9 in (b) correspond to different white matter tracts of interest. (10) and (11) in (c) denote regions formed by neocortical gray matter and subcortical white matter, respectively. (d) corresponds to the representation of the CP parameters before and after the filter in the CP Space; the regions of the sample selected for the CP Space representation are indicated in (a), red and blue squares represent different fiber tracts (coronal and rostro-caudal) within WM.

within the  $P'_1$  image, myocardial and subendocardial, these two regions corresponding to spatial zones of the sample where more information was unveiled after applying the IDF (see blue and red squares in Fig. 2(b)). The values for the pixels within these regions, before and after the filter, are represented in the Purity space with the same color code (see Fig. 2(d)). This representation gives us a visual way to understand the beneficial effect of the IDF in terms of data discrimination. Since the  $P_3$  parameter controls the height of the tetrahedron describing the Purity Space volume (Fig. 2(d)), and as the filter effect fixes all values of  $P_3$  to 1 (see Section 2), we can understand the effect of the filter as the projection of the data clouds, on the plane  $P_3 = 1$  (i.e., all filtered data is re-located to the top surface of the figure). As consequence of this transformation, we can see as the distances between the myocardial and subendocardial heart structures (blue and red datasets) are enlarged after the filter application, this resulting into the subsequent larger discrimination capability between the two regions of the tissue. Moreover, the spread of the points also increases when applying the filter, obtaining richer information of the regions when eliminating the isotropic part of the depolarization, as we shown in Fig. 2. This increase in the dispersion of the clouds can be quantified, particularly, the dispersion increases by a factor  $1/P_3$  (3.92 times larger for this case).

As a result of this first study case, we demonstrated how by removing the isotropic component of samples depolarization response, by applying the IDF, richer sample information, related to physiological information of tissues, is retrieved. This could be useful for studying myocardial tissue in a more accurate way, helping in the inspection and detection of myocardial tissue modification and leading to the early detection of cardiac diseases such as infarction.

### 3.3. Experimental results for the polarimetric analysis of a brain sample

We present a second example of the IDF potential by studying its interest for the characterization of a brain sample. Fig. 3 shows

the comparison between the diattenuation channel before ( $D$ , Fig. 3(a)) and after ( $D'$ , Fig. 3(b)) being filtered and the non-polarimetric intensity image (Fig. 3(c)). From all analyzed polarimetric observables images, we selected the diattenuation feature for comparison with standard intensity because it was the metric providing the best results in terms of image enhancement. This result is in agreement with recent studies [33] reporting the interest of diattenuation measurements to reveal very interesting information related to white matter (WM) fiber tracts, this allowing to inspect nerve fiber architecture and distinguish regions with different compositions difficult to detect by means of conventional techniques [49].

Regarding the intensity image of the brain section in Fig. 3(a), we show how the boundaries between neocortical gray matter (10) and subcortical white matter (11) are observed, but no further information of the sample is provided. In turn, when using diattenuation channel  $D$  (Fig. 3(b)), the visualization of brain structures is significantly improved, but the application of the filter on  $D$  (Fig. 3(c)), gives rise to the appearance of significant structures and details, and in particular, the WM tract identification is outstanding, both subcortical and within the corpus callosum (5,6). We also can see clear distinction between tracts following the plane of the section (i.e. coronal, or 'vertical'; 5,7) and tracts, either rostro-caudal (3,4) or medio-lateral (6,8), that do not follow the same plane. Thus, the filtered image allows the identification, in this particularly rich area of the WM, of a wide set of tracts: superior longitudinal fasciculus (3), cingulum (4), medio-dorsal callosal fibers (long-range interhemispheric U-shaped fibers, 5), ventro-lateral (left-right) callosal fibers (6), short-range U-shaped fibers and layer VIb (7, arrows) and ventro-striatal callosal fibers (8). Area termed 9 represents the coalescence between callosal fibers and the internal capsule [50]. Pink asterisks in Fig. 3(b) denote the regions where the filtering effect is revealing hidden information in the polarimetric observable before the filter, detecting information about the fiber directionality masked by isotropic depolarization.

The significant brain section visualization improvement achieved by the filtered diattenuation image,  $D'$  (Fig. 3(b)), with respect to the non-filtered image  $D$  (Fig. 3(a)), can be better understood by taking into

account the associated range of values. In this sense, as can be seen from the corresponding greybars, the diattenuation  $D$  values associated to the brain image are restricted between the range 0-0.4, corresponding this maximum value to the white. That is, the diattenuation response of the sample is low and the range of values that the parameter can reach is quite limited. This implies a lower capability of structure discrimination. Unlike this, when applying the filter, the range variation of the filtered diattenuation  $D'$  is largely increased, taking values almost covering the full range (0-1), this leading to the excellent structure unveiling shown in Fig. 3(b).

Further interpretation of the filter effect on the brain sample data is provided by using a depolarizing Space representation. In particular, Fig. 3(d) shows the filter effect (data clouds before and after applying the IDF) in terms of the 3D Components of Purity (CP) Space. We used the CP Space since the metric leading to the best results was the diattenuation ( $D$ ) channel, and the CP Space consists of three polarimetric observables, including the diattenuation (in particular, the Diattenuation,  $D$ , the Polarizance  $P$  and the Spherical Purity,  $P_s$ ) [39,51].

Note that ideal depolarizers (input light is fully depolarized independently of its state of polarization) are located at the point (0,0,0) of the CP Space. As brain data before being filtered presents very low values of the  $P_s$  metric, due to their high isotropic depolarizing performance, data clouds are concentrated very close to this point, both for the coronal (in red) and caudal WM fiber tracts (in blue) cases. However, after applying the IDF, isotropic depolarization is removed, so data clouds are displaced far from the fully depolarizing condition, increasing the discriminatory capability between tissues. In particular, when comparing the results before and after filtering represented in Fig. 3(d) we see outstanding results. The two different regions in the sample (labeled by the red and blue point clouds in the figure) are better discriminated after the application of the filter; not only the separation in the space between the clouds representing different structures is larger but also, the dispersion of the points increases. Also, in this case the variance of the points increases in a factor 7.57. This situation ensures excellent performance in terms of tissue discrimination and revealing information of intrinsic properties of the sample.

In summary, we have presented the impactful performance of the IDF for the polarimetric analysis of biological samples. The IDF is particularly useful for the case of soft tissues, where the  $P_s$  value is low ( $P_s$  images for the samples studied in this work are provided in section 5.2 of the Supplementary documents). However, it can be applied on any kind of sample fulfilling this condition. For the cases presented in this section, we have obtained impressive results, overtaking the response of conventional polarimetric methods. In the heart sample, we showed how the contrast between different structures (myocardial and subendocardial) is highly increased, whereas in the brain sample we even reveal invisible structures in the polarimetric images before filtering. These results pave the way to the application of this technique for the early detection of pathologies in heart and brain samples leading to changes in the myocardial structure or the fiber orientation/density, respectively. That could be possible due to the increase of sensitivity in detecting tissue changes that we can get in the filtered polarimetric observables.

#### 4. Conclusions

In this work we presented a digital filtering method that takes advantage of different sources of depolarization present in samples. Depolarization can be divided into two types: anisotropic and isotropic. While the former contains information about the physical microscopic constituents of matter, the second one is related with multiple scattering processes in the sample, and it can be regarded as a polarimetric white noise. It is important to note that the isotropic depolarization usually hides the anisotropic information contained in  $M$ , so it is interesting to isolate these two contributions. To do this, we inspect

the characteristic decomposition of  $M$  and see how it can be separated into four Mueller matrices representing different physical systems. In particular, the isotropic depolarization is related to the last term of the decomposition  $(1 - P_3)M_3$ ; where  $M_3 = \text{diag}(1, 0, 0, 0)$  is a perfect depolarizer and  $1 - P_3$  is the weight of the isotropic decomposition. The remaining elements of the decomposition represent the anisotropic properties of the samples. Recall that the proposed isotropic depolarization filter consists in removing this isotropic part of the raw  $M$ ; this leads to a new filtered  $M'$  where the anisotropic content is magnified.

The IDF has been applied to different soft tissues of animal origin, since these structures usually exhibit low  $P_s$  values (i.e., they have a high isotropic depolarization response), making them suitable candidates for a successful application of the filter. In particular, we focused the polarimetric analysis on heart and brain samples due to their interest and importance in the medical field, where we demonstrate the outstanding performance of the IDF in terms of structure unveiling and contrast enhancement. In recent years, the potential of polarimetry for biological tissue inspection has already been demonstrated, proving that polarimetric observables provide rich information about sample structure that is not visible with intensity images or conventional medical techniques. At this stage, with the presentation of this IDF, we aim to go one step further by outperforming existing polarimetric techniques. In particular, we show how the filtered polarimetric observables corresponding to the heart samples not only greatly increase the contrast between different tissues (myocardial and subendocardial), but also reveal structures hidden in the conventional polarimetric images in the filtered observables. In the case of the brain, we obtain very interesting results, revealing information about the directionality and identification of fiber tracts in the WM, which were not visible in the unfiltered polarimetric parameters. It is worth noting that we have presented a very simple filtering method for improved visualization of sample features, which can be implemented experimentally using a macroscopic and non-destructive technique.

Importantly, we want to note that the proposed IDF can be tested with other polarimetric observables than those used in this manuscript. In this sense, we have focused on a reduced set of commonly used observables as representative examples to demonstrate the performance of the filter. However, it could be applied to a large number of already proposed polarimetric observables and/or methods.

The results presented in this work highlight the interest of the filtering method for the study and characterization of biological samples, paving the way for new protocols in biomedical and clinical applications. For example, in the examined samples discussed throughout the manuscript, different structures of interest were revealed. In the case of the heart sample, not only the boundaries and the distinction between myocardial and subendocardial tissue are revealed by IDF, but also the trajectories of the subepicardial coronary vessels and the visualization enhancement of their walls and lumens are obtained. For the brain, we show how IDF can detect and classify tracts with different orientations and resolve the boundaries between gray and white matter. Interestingly, these results can be useful in several medical scenarios. For example, in the study of cardiac pathologies, the inspection and classification of tracts in the white matter can help shed light on the effect of some neuropathies and as a powerful tool for surgeons in the clinical context.

Finally, although we have focused our discussion on the biomedical field, we would like to note that the proposed methods are general and could be useful for a wide range of applications. Note that in all those samples where isotropic depolarization is a significant feature, which is a common situation in several scenarios. For this reason, we invite all researchers dealing with depolarizing samples to test the suitability of the proposed filter.



## CRediT authorship contribution statement

**Mónica Canabal-Carbia:** Writing – original draft, Methodology, Data curation, Conceptualization. **Irene Estévez:** Writing – review & editing, Writing – original draft, Supervision, Conceptualization. **Emilio González-Arny:** Writing – original draft, Investigation. **Ivan Montes-Gonzalez:** Writing – review & editing. **Jose J. Gil:** Writing – review & editing, Methodology, Conceptualization. **Anrau Barrera:** Data curation. **Enrique García-Caurel:** Writing – review & editing, Conceptualization. **Razvigor Ossikovski:** Writing – review & editing, Conceptualization. **Ignacio Moreno:** Writing – review & editing, Conceptualization. **Juan Campos:** Writing – review & editing, Supervision, Funding acquisition, Formal analysis, Conceptualization. **Angel Lizana:** Writing – review & editing, Writing – original draft, Supervision, Conceptualization.

## Funding sources

The authors acknowledge the financial support of Ministerio de Ciencia e Innovación and Fondos FEDER (PID2021-126509OB-C21 and PDC2022-133332-C21) and support of Generalitat de Catalunya, Spain (2021SGR00138).

IM acknowledge the financial support of Ministerio de Ciencia e Innovación and Fondos FEDER (PID2021-126509OB-C22).

## Declaration of competing interest

The authors declare no conflicts of interest.

## Appendix A. Supplementary data

Supplementary material related to this article can be found online at <https://doi.org/10.1016/j.optlastec.2025.112956>.

## Data availability

Data will be made available on request.

## References

- [1] F. Snik, C.U. Keller, Astronomical polarimetry: polarized views of stars and planets, in: *Planets, Stars and Stellar Systems*, in: *Astronomical Techniques, Software and Data*, vol. 2, 2013, p. 175, [http://dx.doi.org/10.1007/978-94-007-5618-2\\_4](http://dx.doi.org/10.1007/978-94-007-5618-2_4).
- [2] J.S. Tyo, D.L. Goldstein, D.B. Chenault, J.A. Shaw, Review of passive imaging polarimetry for remote sensing applications, *Appl. Opt.* 45 (22) (2006) 5453–5469, <http://dx.doi.org/10.1364/ao.45.005453>.
- [3] Z. Kong, T. Ma, Y. Cheng, R. Fei, Z. Zhang, Y. Li, L. Mei, A polarization-sensitive imaging lidar for atmospheric remote sensing, *J. Quant. Spectrosc. Radiat. Transfer* 271 (2021) 107747, <http://dx.doi.org/10.1016/j.jqsrt.2021.107747>.
- [4] I. Estévez, F. Oliveira, P. Braga-Fernandes, M. Oliveira, L. Rebouta, M.I. Vasilevski, Urban objects classification using mueller matrix polarimetry and machine learning, *Opt. Express* 30 (16) (2022) 28385–28400, <http://dx.doi.org/10.1364/OE.451907>.
- [5] B. Al Bugami, Y. Su, C. Rodríguez, A. Lizana, J. Campos, M. Dufort, R. Ossikovski, E. García-Caurel, Characterization of vine, *Vitis vinifera*, leaves by Mueller polarimetric microscopy, *Thin Solid Films* 764 (2023) 139594, <http://dx.doi.org/10.1016/j.tsf.2022.139594>.
- [6] C. Rodríguez, E. García-Caurel, T. Garnatje, M. Serra i Ribas, J. Luque, J. Campos, A. Lizana, Polarimetric observables for the enhanced visualization of plant diseases, *Sci. Rep.* 12 (1) (2022) 14743, <http://dx.doi.org/10.1038/s41598-022-19088-6>.
- [7] J.C. Ramella-Roman, I. Saytashev, M. Piccini, A review of polarization-based imaging technologies for clinical and preclinical applications, *J. Opt.* 22 (12) (2020) 123001, <http://dx.doi.org/10.1088/2040-8986/abbf8a>.
- [8] D. Ivanov, V. Dremín, E. Borisova, A. Bykov, T. Novikova, I. Meglinski, R. Ossikovski, Polarization and depolarization metrics as optical markers in support to histopathology of ex Vivo colon tissue, *Biomed. Opt. Express* 12 (7) (2021) 4560–4572, <http://dx.doi.org/10.1364/BOE.426713>.
- [9] M. Kupinski, M. Boffety, F. Goudail, R. Ossikovski, A. Pierangelo, J. Rehinder, J. Vizet, T. Novikova, Polarimetric measurement utility for pre-cancer detection from uterine Cervix specimens, *Biomed. Opt. Express* 9 (11) (2018) 5691–5702, <http://dx.doi.org/10.1364/BOE.9.005691>.
- [10] O. Rodríguez-Núñez, P. Schucht, E. Hewer, T. Novikova, A. Pierangelo, Polarimetric visualization of healthy brain fiber tracts under adverse conditions: ex Vivo studies, *Biomed. Opt. Express* 12 (10) (2021) 6674–6685, <http://dx.doi.org/10.1364/BOE.439754>.
- [11] M. Canabal-Carbia, A. Van Eeckhout, C. Rodríguez, E. González-Arny, I. Estévez, J.J. Gil, E. García-Caurel, R. Ossikovski, J. Campos, A. Lizana, Depolarizing metrics in the biomedical field: Vision enhancement and classification of biological tissues, *J. Innov. Opt. Heal. Sci.* (2023) 2330004, <http://dx.doi.org/10.1142/S1793545823300045>.
- [12] C. Rodríguez, A. Van Eeckhout, E. García-Caurel, A. Lizana, J. Campos, Automatic pseudo-coloring approaches to improve visual perception and contrast in polarimetric images of biological tissues, *Sci. Rep.* 12 (1) (2022) 18479, <http://dx.doi.org/10.1038/s41598-022-23330-6>.
- [13] J.J. Gil, I. San José, M. Canabal-Carbia, I. Estévez, E. González-Arny, J. Luque, T. Garnatje, J. Campos, A. Lizana, Polarimetric images of biological tissues based on the arrow decomposition of Mueller matrices, *Photonics* 10 (6) (2023) 669, <http://dx.doi.org/10.3390/photonics10060669>.
- [14] A. Van Eeckhout, A. Lizana, E. García-Caurel, J.J. Gil, A. Sansa, C. Rodríguez, I. Estévez, E. González, J.C. Escalera, I. Moreno, et al., Polarimetric imaging of biological tissues based on the indices of polarimetric purity, *J. Biophotonics* 11 (4) (2018) e201700189, <http://dx.doi.org/10.1002/jbio.201700189>.
- [15] A. Van Eeckhout, E. García-Caurel, R. Ossikovski, A. Lizana, C. Rodríguez, E. González-Arny, J. Campos, Depolarization metric spaces for biological tissues classification, *J. Biophotonics* 13 (8) (2020) e202000083, <http://dx.doi.org/10.1002/jbio.202000083>.
- [16] D. Ivanov, V. Dremín, T. Genova, A. Bykov, T. Novikova, R. Ossikovski, I. Meglinski, Polarization-based histopathology classification of ex Vivo colon samples supported by machine learning, *Front. Phys.* 9 (2022) 800, <http://dx.doi.org/10.3389/fphy.2021.814787>.
- [17] A. Majumdar, J. Lad, K. Tumanova, S. Serra, F. Queresby, M. Khorasani, A. Vitkin, Machine learning based local recurrence prediction in colorectal cancer using polarized light imaging, *J. Biomed. Opt.* 29 (5) (2024) 052915, <http://dx.doi.org/10.1117/1.JBO.29.5.052915>.
- [18] M. Sun, H. He, N. Zeng, E. Du, Y. Guo, S. Liu, J. Wu, Y. He, H. Ma, Characterizing the microstructures of biological tissues using Mueller matrix and transformed polarization parameters, *Biomed. Opt. Express* 5 (12) (2014) 4223–4234, <http://dx.doi.org/10.1364/BOE.5.004223>.
- [19] O. Sieryi, Y. Ushenko, V. Ushenko, O. Dubolazov, A.V. Syvokorovskaya, O. Vanchulyak, A.G. Ushenko, M. Gorsky, Y. Tomka, A. Bykov, et al., Optical anisotropy composition of benign and malignant prostate tissues revealed by Mueller-matrix imaging, *Biomed. Opt. Express* 13 (11) (2022) 6019–6034, <http://dx.doi.org/10.1364/BOE.464420>.
- [20] J. Chue-Sang, N. Holness, M. Gonzalez, J. Greaves, I. Saytashev, S. Stoff, A. Gandjbakhche, V.V. Chernomordik, G. Burkett, J.C. Ramella-Roman, Use of Mueller matrix colposcopy in the characterization of cervical collagen anisotropy, *J. Biomed. Opt.* 23 (12) (2018) 121605, <http://dx.doi.org/10.1117/1.JBO.23.12.121605>.
- [21] I. Pardo, S. Bian, J. Gomis-Brescó, E. Pascual, A. Canillas, S. Bosch, O. Arteaga, Wide-field Mueller matrix polarimetry for spectral characterization of basic biological tissues: Muscle, fat, connective tissue, and skin, *J. Biophotonics* (2023) e202300252, <http://dx.doi.org/10.1002/jbio.202300252>.
- [22] Y. Dong, J. Qi, H. He, C. He, S. Liu, J. Wu, D.S. Elson, H. Ma, Quantitatively characterizing the microstructural features of breast ductal Carcinoma tissues in different progression stages by Mueller matrix microscope, *Biomed. Opt. Express* 8 (8) (2017) 3643–3655, <http://dx.doi.org/10.1364/BOE.8.003643>.
- [23] Y. Wang, H. He, J. Chang, C. He, S. Liu, M. Li, N. Zeng, J. Wu, H. Ma, Mueller matrix microscope: a quantitative tool to facilitate detections and fibrosis scorings of liver cirrhosis and cancer tissues, *J. Biomed. Opt.* 21 (7) (2016) 071112, <http://dx.doi.org/10.1117/1.JBO.21.7.071112>.
- [24] A.G. Clark, D.M. Vignjevic, Modes of cancer cell invasion and the role of the microenvironment, *Curr. Opin. Cell Biol.* 36 (2015) 13–22, <http://dx.doi.org/10.1016/j.cceb.2015.06.004>.
- [25] A. Keikhosravi, Y. Liu, C. Drifka, K.M. Woo, A. Verma, R. Oldenbourg, K.W. Ellicei, Quantification of collagen organization in histopathology samples using liquid crystal based polarization microscopy, *Biomed. Opt. Express* 8 (9) (2017) 4243–4256, <http://dx.doi.org/10.1364/BOE.8.004243>.
- [26] S. Sugiyama, Y.-J. Hong, D. Kasaragod, S. Makita, S. Uematsu, Y. Ikuno, M. Miura, Y. Yasuno, Birefringence imaging of posterior eye by multi-functional Jones matrix optical coherence tomography, *Biomed. Opt. Express* 6 (12) (2015) 4951–4974, <http://dx.doi.org/10.1364/BOE.6.004951>.
- [27] M.F. Wood, N. Ghosh, M.A. Wallenberg, S.-H. Li, R.D. Weisel, B.C. Wilson, R.-K. Li, I.A. Vitkin, Polarization birefringence measurements for characterizing the myocardium, including healthy, infarcted, and stem-cell-regenerated tissues, *J. Biomed. Opt.* 15 (4) (2010) 047009, <http://dx.doi.org/10.1117/1.3469844>.

- [28] A. Pierangelo, A. Benali, M.-R. Antonelli, T. Novikova, P. Validire, B. Gayet, A. De Martino, Ex-Vivo characterization of human colon cancer by Mueller polarimetric imaging, *Opt. Express* 19 (2) (2011) 1582–1593, <http://dx.doi.org/10.1364/OE.19.001582>.
- [29] E. Du, H. He, N. Zeng, M. Sun, Y. Guo, J. Wu, S. Liu, H. Ma, Mueller matrix polarimetry for differentiating characteristic features of cancerous tissues, *J. Biomed. Opt.* 19 (7) (2014) 076013, <http://dx.doi.org/10.1117/1.JBO.19.7.076013>.
- [30] R. Chipman, W.S.T. Lam, G. Young, *Polarized Light and Optical Systems*, CRC Press, 2018, <http://dx.doi.org/10.1201/9781351129121>.
- [31] N. Ghosh, I.A. Vitkin, Tissue polarimetry: concepts, challenges, applications, and outlook, *J. Biomed. Opt.* 16 (11) (2011) 110801, <http://dx.doi.org/10.1117/1.3652896>.
- [32] C. Rodríguez, I. Estévez, E. González-Arnan, J. Campos, A. Lizana, Optimizing the classification of biological tissues using machine learning models based on polarized data, *J. Biophotonics* 16 (4) (2023) e202200308, <http://dx.doi.org/10.1002/jbio.202200308>.
- [33] M. Menzel, M. Axer, K. Amunts, H. De Raedt, K. Michielsen, Diattenuation imaging reveals different brain tissue properties, *Sci. Rep.* 9 (1) (2019) 1939, <http://dx.doi.org/10.1038/s41598-019-38506-w>.
- [34] I. Shtein, Y. Shelef, Z. Marom, E. Zelinger, A. Schwartz, Z.A. Popper, B. Bar-On, S. Harpaz-Saad, Stomatal cell wall composition: distinctive structural patterns associated with different phylogenetic groups, *Ann. Botany* 119 (6) (2017) 1021–1033, <http://dx.doi.org/10.1093/aob/mcw275>.
- [35] M. Canabal-Carbia, I. Estévez, E. Nabadda, E. Garcia-Caurel, J. Gil, R. Ossikovski, A. Márquez, I. Moreno, J. Campos, A. Lizana, Connecting the microscopic depolarizing origin of samples with macroscopic measures of the indices of polarimetric purity, *Opt. Lasers Eng.* 172 (2024) 107830, <http://dx.doi.org/10.1016/j.optlaseng.2023.107830>.
- [36] J.J. Gil, Polarimetric characterization of light and media: physical quantities involved in polarimetric phenomena, *Eur. Phys. J.- Appl. Phys.* 40 (1) (2007) 1–47, <http://dx.doi.org/10.1051/epjap:2007153>.
- [37] I. San José, J.J. Gil, Invariant indices of polarimetric purity: generalized indices of purity for  $n \times n$  covariance matrices, *Opt. Commun.* 284 (1) (2011) 38–47, <http://dx.doi.org/10.48550/arXiv.0807.2171>.
- [38] J.J. Gil, On optimal filtering of measured Mueller matrices, *Appl. Opt.* 55 (20) (2016) 5449–5455, <http://dx.doi.org/10.1364/AO.55.005449>.
- [39] J.J. Gil, R. Ossikovski, *Polarized Light and the Mueller Matrix Approach*, CRC Press, 2022, <http://dx.doi.org/10.1201/9780367815578>.
- [40] J.J. Gil, Structure of polarimetric purity of a Mueller matrix and sources of depolarization, *Opt. Commun.* 368 (2016) 165–173, <http://dx.doi.org/10.1016/j.optcom.2016.01.092>.
- [41] J.J. Gil, Components of purity of a three-dimensional polarization state, *J. Opt. Soc. Amer. A* 33 (1) (2016) 40–43, <http://dx.doi.org/10.1364/JOSAA.33.000040>.
- [42] S.R. Cloude, Group theory and polarisation algebra, *Opt. (Stuttgart)* 75 (1) (1986) 26–36.
- [43] R. Ossikovski, J. Vizet, Eigenvalue-based depolarization metric spaces for Mueller matrices, *J. Opt. Soc. Amer. A* 36 (7) (2019) 1173–1186, <http://dx.doi.org/10.1364/JOSAA.36.001173>.
- [44] World Health Organization, The top 10 causes of death, 2020, URL <https://www.who.int/news-room/fact-sheets/detail/the-top-10-causes-of-death>. (Accessed on 22 March 2024).
- [45] T.D. Karamitsos, A. Arvanitaki, H. Karvounis, S. Neubauer, V.M. Ferreira, Myocardial tissue characterization and fibrosis by imaging, *Cardiovasc. Imaging* 13 (5) (2020) 1221–1234, <http://dx.doi.org/10.1016/j.jcmg.2019.06.030>.
- [46] M.P. Graham-Brown, A. Patel, D. Stensel, D.S. March, A.-M. Marsh, J. McAdam, G.P. McCann, J.O. Burton, et al., Imaging of myocardial fibrosis in patients with end-stage renal disease: current limitations and future possibilities, *BioMed. Res. Int.* 2017 (2017) <http://dx.doi.org/10.1155/2017/5453606>.
- [47] I. Ahmad, Review of the emerging role of optical polarimetry in characterization of pathological myocardium, *J. Biomed. Opt.* 22 (10) (2017) 100901, <http://dx.doi.org/10.1117/1.JBO.22.10.100901>.
- [48] C.J. Charvet, Mapping human brain pathways: challenges and opportunities in the integration of scales, *Brain Behav. Evol.* 98 (2023) 194–209, <http://dx.doi.org/10.1159/000530317>.
- [49] A. Agrawal, J.P. Kapfhammer, A. Kress, H. Wichers, A. Deep, W. Feindel, V.K. Sonntag, R.F. Spetzler, M.C. Preul, Josef Klingler's models of white matter tracts: influences on neuroanatomy, neurosurgery, and neuroimaging, *Neurosurgery* 69 (2) (2011) 238–254, <http://dx.doi.org/10.1227/NEU.0b013e318214ab79>.
- [50] E. Mandonnet, S. Sarubbo, L. Petit, The nomenclature of human white matter association pathways: proposal for a systematic taxonomic anatomical classification, *Front. Neuroanat.* 12 (2018) 94, <http://dx.doi.org/10.3389/fnana.2018.00094>.
- [51] A. Van Eeckhout, J.J. Gil, E. Garcia-Caurel, J.G. Romero, R. Ossikovski, I. San José, I. Moreno, J. Campos, A. Lizana, Unraveling the physical information of depolarizers, *Opt. Express* 29 (23) (2021) 38811–38823, <http://dx.doi.org/10.1364/OE.438673>.